

Synthesis and biological evaluation of small molecule GLUT inhibitors that cause glucose starvation in cancer

Dissertation

For the achievement of the academic degree of the
Doctor in Natural Sciences
(Dr. rer. nat.)

Submitted to
Faculty of Chemistry and Chemical Biology
TU Dortmund University
by

Elena Sabrina Reckzeh

from Hilden, Germany

Dortmund 2019

Die vorliegende Arbeit wurde zwischen März 2015 und Mai 2019 unter der Anleitung von Prof. Dr. Dr. h.c. Herbert Waldmann und Dr. Slava Ziegler an der Fakultät für Chemie und Chemische Biologie der Technischen Universität Dortmund und an dem Max-Planck Institut für Molekulare Physiologie Dortmund angefertigt.

Dekan: Prof. Dr. Stefan M. Kast

1. Gutachter: Prof. Dr. Dr. h.c. Herbert Waldmann

2. Gutachter: Prof. Dr. Daniel Summerer

Results presented in this thesis contributed to the following publications:

Ceballos J, Karageorgis G, Schwalfenberg M, Reckzeh ES, Sievers S, Ostermann C, Pahl A, Ziegler S, Waldmann H, “Synthesis and Biological Evaluation of Indomorphan Pseudo Natural Products”, *submitted*.

Schwalfenberg M[#], Ceballos J[#], Reckzeh ES, Karageorgis G, Sellstedt M, Nowacki J, Carnero Corrales MA, Wilke J, Laraia L, Tschapalda K, Metz M, Sehr DA, Rahmann S, Winklhofer K, Janning P, Ziegler P, Waldmann H, “A Dual-Specific GLUT-1- and GLUT-3 Inhibitor Potently Suppresses Cancer Cell Growth”, *submitted*.

Reckzeh ES, Karageorgis G, Schwalfenberg M, Ceballos J, Nowacki J, Stroet MCM, Binici A, Knauer A, Brand S, Strohmann C, Ziegler S, Waldmann H. “Inhibition of Glucose Transporters and Glutaminase Synergistically Impairs Tumor Cell Growth.” *Cell Chemical Biology*, *in press*.

Reckzeh ES, Brockmeyer A, Metz M, Waldmann H, Janning P, “Target Engagement of Small Molecules: Thermal Profiling Approaches on Different Levels”, *Methods in Molecular Biology, Systems Chemical Biology*, Ed. Ziegler S, Ed. Waldmann H, New York: Humana Press, **2019**, Vol. *1888*, 73-98.

Karageorgis G, Reckzeh ES, Ceballos J, Schwalfenberg M, Sievers S, Ostermann C, Pahl A, Ziegler S, Waldmann H. Chromopyrones are “Pseudo Natural Product” Glucose Uptake Inhibitors Targeting Glucose Transporters GLUT-1 and -3” *Nature Chemistry*, **2018**, *10*, 1103-11.

1 Table of content

1	TABLE OF CONTENT	1
2	ACKNOWLEDGEMENT	4
3	SUMMARY	6
4	ZUSAMMENFASSUNG	8
5	INTRODUCTION	10
5.1	CANCER	10
5.2	THE WARBURG EFFECT	11
5.3	GLUCOSE TRANSPORTERS	13
5.3.1	<i>Glucose uptake inhibitors</i>	<i>17</i>
5.4	METABOLIC REWIRING	21
5.4.1	<i>KRas in metabolic rewiring</i>	<i>22</i>
5.4.2	<i>Metabolic flexibility and glutamine</i>	<i>24</i>
5.5	FURTHER APPLICATIONS OF GLUCOSE UPTAKE INHIBITORS	25
6	AIM OF THE THESIS	26
7	EXPERIMENTAL PART	27
7.1	EXPERIMENTAL PART – CHEMISTRY	27
7.1.1	<i>Materials</i>	<i>27</i>
7.1.2	<i>Instrumentation</i>	<i>27</i>
7.1.3	<i>Methods</i>	<i>28</i>
7.1.3.1	<i>Preparative HPLC-MS</i>	<i>28</i>
7.2	EXPERIMENTAL PART – BIOLOGY	32
7.2.1	<i>Material</i>	<i>32</i>
7.2.2	<i>Instruments and software</i>	<i>40</i>
7.2.3	<i>Cell biology methods</i>	<i>42</i>
7.2.4	<i>Biochemical methods</i>	<i>53</i>

Table of content

7.2.5	<i>Methods to study target engagement of small molecules</i>	57
7.2.6	<i>Compound absorbance and fluorescence spectra</i>	59
7.2.7	<i>Data analysis</i>	60
8	RESULTS	62
8.1	IDENTIFICATION OF SMALL-MOLECULE INHIBITORS OF GLUCOSE UPTAKE	62
8.2	CHEMICAL INVESTIGATION OF THE PIPERAZIN-2-ONE CLASS	64
8.2.1	<i>Confirmation of the glucose uptake inhibitory activity of 1a</i>	64
8.2.2	<i>Synthesis of a piperazin-2-one-based compound library</i>	66
8.2.3	<i>Structure-activity relationship (SAR) studies of the piperazin-2-ones</i>	69
8.3	BIOLOGICAL INVESTIGATION OF GLUTOR	77
8.3.1	<i>Mode of action of Glutor</i>	77
8.3.2	<i>Drug-likeness of Glutor</i>	79
8.3.3	<i>Influence of Glutor on cancer cell growth</i>	80
8.3.4	<i>Glutor induces cell death in physiologically relevant spheroids</i>	86
8.3.5	<i>Metabolic profiles of different cell lines correlate with Glutor sensitivity</i>	87
8.3.6	<i>GLUT-1, GLUT-2 and GLUT-3 are targets of Glutor</i>	89
8.3.7	<i>Cancer cells upregulate GLUT-1 and GLUT-3 to escape glucose starvation</i>	94
8.3.8	<i>Nutrient dependencies of HCT116 cells</i>	99
8.3.9	<i>Influence of co-treatment on growth of HCT116 cells</i>	110
8.4	BIOLOGICAL CHARACTERIZATION OF OTHER GLUT INHIBITORS	119
8.4.1	<i>(+)-Glupin-1</i>	119
8.4.2	<i>Chromopyrones</i>	129
8.4.3	<i>BAY-876</i>	135
9	DISCUSSION	148
9.1	STRUCTURAL OPTIMIZATION OF GLUTOR	149
9.2	GLUT ISOFORM SELECTIVITY	152
9.2.1	<i>Target identification, validation and off-targets</i>	153
9.3	RESCUE EFFECT	154

Table of content

9.3.1	<i>Regulation of B2M</i>	156
9.4	CANCER CELL GROWTH INHIBITION	157
9.5	RAS MUTATION AND GLUCOSE ADDICTION	160
9.6	METABOLIC FLEXIBILITY AND COMBINATORY TREATMENT APPROACH	162
9.6.1	<i>Other combinatorial treatments</i>	164
9.7	FURTHER INDICATIONS AND APPLICATIONS OF GLUCOSE UPTAKE INHIBITORS	167
10	OUTLOOK	170
11	ABBREVIATIONS	171
12	LITERATURE	175
13	APPENDIX	187
13.1	SUPPLEMENTARY FIGURES	187
13.2	SUPPLEMENTARY TABLES	194
13.3	COMPOUND CHARACTERIZATION	204
14	CURRICULUM VITAE	243
15	PUBLICATION LIST	246

2 Acknowledgement

Throughout all my studies I could not wait to dive deep into a project and start to take on responsibility, as well as to follow own ideas. The PhD phase was the most exciting and enriching time of my education and I truly enjoyed every day of it. I would like to thank all people that contributed to this important phase of my life.

First and foremost, I would like to thank Prof. Dr. Dr. h.c. Herbert Waldmann for the opportunity to obtain my PhD in his group. The versatile project, the independent way of working as well as the access to high-end equipment and the excellent academic environment contributed to my scientific maturation. I truly appreciate all the support that I received to grow on so many levels.

I am sincerely grateful to Dr. Slava Ziegler, my co-supervisor and group-leader, who was always helpful during professional and personal hurdles. Her valuable, constructive input contributed to the success of this project. Moreover, the personal feedback I received throughout these years clearly motivated me to always give my very best.

I would like to thank Prof. Dr. Daniel Summerer for taking over the function of the second examiner.

My personal thanks go to the students, Jessica Nowacki, Marc Stroet and Aylin Binici, that I supervised throughout these past four years during their Bachelor and Master thesis and who were always extremely dedicated to participating in this project with their scientific work and creative ideas. Moreover, I thank the talented trainees Laura Ney and Alexandra Brause for their assistance. I would also like appreciate my gratitude to Beate Schölermann for her support during the last months of my PhD.

I would like to thank Melanie Schwalfenberg, Dr. Javier de Ceballos and Dr. George Karageorgis who worked together with me on this project. I would also like to thank Julian Wilke, Dr. Silke Brand and Lena Knauer who contributed some of the experiments. Furthermore, I appreciated all

Acknowledgement

discussions with the people from the Lead Discovery Center about this project and sharing their knowledge and expertise.

I would like to particularly thank the mass spectrometry team of Dr. Petra Janning, Malte Metz, Jens Warmers and Andreas Brockmeyer for measuring samples, analyzing data and for their constructive feedback on experimental design and analysis. I am very thankful to the Compound Management and Screening Center, particularly Dr. Sonja Sievers, Claude Ostermann and Dr. Axel Pahl for their support in all compound screenings, compound handling and computational analysis. I furthermore appreciate the continuous help in all administrative issues from Brigitte Rose.

I would like to express my gratitude for the financial, personal and scientific support that I received during my time in the International Max Planck Research School in Chemical and Molecular Biology. Here my special thanks go to Christa Hornemann and Dr. Lucia Sironi who were always highly encouraging and motivating and make the graduate school an outstanding place to grow.

The nice working atmosphere in the department would not have been possible without Elisabeth Hennes, Julian Wilke, Prof. Dr. Luca Laraia, Dr. Luis Bering, Beate Schölermann, Dr. Sumersing Patil, Dr. Lea Kremer, Prof. Dr. Shobhna Kapoor, Dr. Tim Förster, Michael Winzker, Andreas Christoforow, Dr. Hélène Adihou, Stefan Zimmermann, Jens Warmers, Annina Burhop, Tabea Schneidewind, Dr. Marjorie Rummelt, Melanie Schwalfenberg, Dr. Javier de Ceballos, Dr. Kirsten Tschapalda, Dr. Janine Schulte-Zweckel and Dr. Guillaume Garivet.

My deepest and heartfelt appreciation goes to my husband and best friend Michael Reckzeh for all the support, understanding and encouragement as well as exciting journeys that will always continue. All my achievements would not have been possible without my parents, Roland and Barbara Heider, who supported me throughout my life in the best way imaginable. I also thank my siblings, Janina and Damian Heider, as well as Markus Geimer for being my family.

3 Summary

Deregulation of cellular energy metabolism has been well established as a hallmark of cancer. Increased aerobic glycolysis, termed the Warburg effect, is associated with an overexpression of different glucose transporter isoforms, especially GLUT-1 (ubiquitously expressed). To date, numerous GLUT inhibitors have been reported to reduce cancer growth, albeit improvement of selectivity and efficacy as well as unspecific toxicity of such inhibitors remain to be major challenges. In order to identify compounds that block glucose uptake of cancer cells, a cell-based screen that monitors 2-deoxy-*D*-glucose (2-DG) uptake by cancer cells was employed. This led to the discovery and further investigation of three distinct substance classes of which one was investigated in-depth within this dissertation. Chemical investigation of the main compound class, the piperazin-2-ones, involved detailed planning and execution of compound synthesis to improve potency and physicochemical properties and establish a conclusive structure-activity relationship (SAR). The thereby generated most potent, enantiomerically pure compound, termed Glutor, inhibited glucose uptake and reduced the glycolysis rate of cancer cells with low nanomolar potency. In a panel of 94 cell lines Glutor impeded the growth of 44 different cancer cell lines with an $IC_{50} < 100$ nM, while non-malignant cells were unaffected. Interestingly, among the most sensitive cancer cells, mutations in KRas were enriched. Spheroids were employed to investigate the cellular potency in a physiologically more relevant cell model. Thereby, Glutor induced a strong increase in cytotoxic events after 24 hours of treatment, which even outreached the compound effect on monolayer-cultured cells.

Furthermore, among the class I GLUTs, a GLUT-1/-2/-3 isoform selectivity was determined for Glutor by employing overexpression experiments of the respective isoform, which lead to partial rescue of 2-DG uptake inhibition and verification by cellular thermal shift assays (CETSA®). Subsequent studies revealed an upregulation of GLUT-1 and GLUT-3 expression levels under glucose starvation conditions. This proved the necessity of a GLUT-1/-3 selectivity profile to

achieve a full inhibitory effect on glucose uptake. Numerous reports describe the dependence of *in vitro* cultured cancer cells on glutamine to maintain catabolism and viability. Therefore, the effect of varying extracellular glutamine concentrations on glucose dependence as well as Glutor treatment was investigated and revealed that physiological glutamine concentrations (0.5 mM) increased the potency of both compound treatment and glucose deprivation. In line with this, a strong synergistic effect in a combinatory treatment using the glutaminase inhibitor CB-839 was uncovered. These experiments prove the possibility of novel combinatory treatment approaches for anti-cancer therapy. In the scope of this dissertation, derivatives of the other two substance classes, (*R,R*)-Chromopynone-1/2 and (+)-Glupin-1, were investigated as well. Thereby, several findings made for Glutor could be determined as general for glucose uptake inhibitors.

The new small molecular GLUT inhibitors may ultimately pave the way for the investigation of glucose uptake inhibition as a new therapeutic anti-cancer strategy or in a combinatory treatment approach with other drugs.

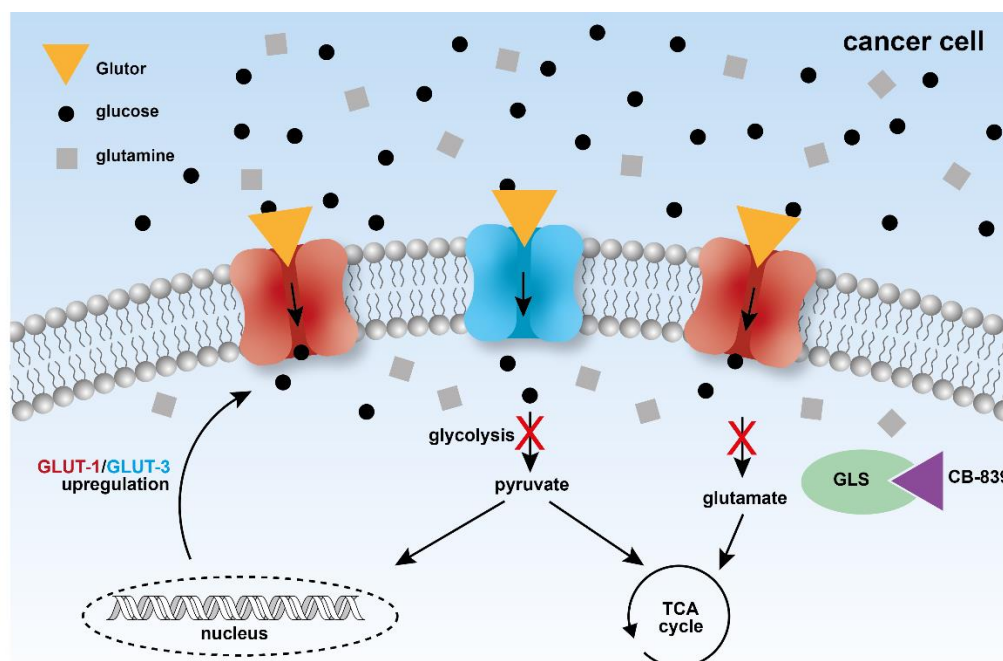


Figure 1 Graphical abstract indicates the synergistic effect between Glutor and the glutaminase inhibitor CB-839 as well as the observed rescue effect upon glucose starvation. GLS: glutaminase kidney isoform, TCA: tricarboxylic acid cycle, GLUT: facilitative glucose transporter.

4 Zusammenfassung

Die Veränderung des zellulären Metabolismus ist ein Hauptmerkmal von Krebserkrankungen. Diese schließt die aeroben Glykolyse ein, auch Warburg-Effekt genannt, die zur vermehrten Expression von Glukose-Transportern (GLUTs), insbesondere GLUT-1, führt und dadurch zur erhöhten Glukoseaufnahme in Krebszellen. Um die Glukosezufuhr von Krebszellen zu unterbinden, wurden bereits einige GLUT-Inhibitoren entwickelt, die jedoch mangelnde Selektivität, Wirksamkeit sowie unspezifischen Nebenwirkungen aufweisen. Um neue niedermolekulare Glukoseaufnahme-Inhibitoren zu identifizieren, wurde ein Zell-basiertes Testsystem eingesetzt, das die Aufnahme von 2-Desoxy-*D*-Glukose (2-DG) in Krebszellen nachweist. Aus einer Bibliothek von über 150.000 niedermolekularen Substanzen wurden drei Substanzklassen identifiziert, welche die 2-DG-Aufnahme im niedrigen mikromolaren Bereich inhibieren. Eine dieser Substanzklassen, die Piperazin-2-one, wurde im Rahmen dieser Arbeit näher untersucht. Mithilfe organisch synthetischer Methoden wurden weitere Piperazin-2-on-Derivate generiert, um die Wirksamkeit sowie physikochemische Eigenschaften verbessert. Durch eine umfassende Strukturwirkungsbeziehung konnte die aktivste Verbindung, das Enantiomer Glutor, identifiziert werden. Glutor hemmte die Glukoseaufnahme und reduzierte die Glykolyserate von Krebszellen im niedrigen nanomolaren Bereich. Zudem unterband Glutor das Wachstum von diversen Krebszelllinien mit einem $IC_{50} < 100$ nM, wobei nicht entartete Zellen unbeeinflusst blieben. Auffällig war hierbei eine Anreicherung von KRas-Mutationen unter den sensitiven Zelllinien. In physiologisch relevanteren, dreidimensionalen Sphäroiden führte die Behandlung mit Glutor bereits nach 24 Stunden zu einem, im Vergleich zu einlagig kultivierten Zellen, stärkeren Anstieg der Zytotoxizität.

Die Überexpression von GLUT-1/-2 und -3 verringerte die Glutor-vermittelte Inhibition der 2-DG-Aufnahme, was auf die Inhibition der Isoformen GLUT-1/-2/-3 hindeutet. Zudem erhöhte Glutor die Schmelztemperatur von GLUT-3 in Zelllysaten, was die Bindung an GLUT-3 und somit GLUT-

3 als Zielprotein bestätigte. Unter Glukoseentzug konnte zudem ein Anstieg der GLUT-1- und GLUT-3-Expression verzeichnet werden. Dieser Befund verdeutlicht die Relevanz eines GLUT-1/3-Selektivitätsprofils, um eine vollständige Hemmung der Glukoseaufnahme von Krebszellen zu garantieren. *In vitro* kultivierte Zellen sind auf extern hinzugefügtes Glutamin angewiesen, und viele Krebszellen sind Glutaminabhängig. In Übereinstimmung damit wies Glutor eine erhöhte Wirksamkeit bei geringerer, physiologischer Glutaminkonzentration von 0,5 mM auf. Die kombinatorische Anwendung von Glutor und dem Glutaminase-Inhibitor CB-839 zeigte einen klaren synergistischen, inhibitorischen Effekt auf das Zellwachstum. Dies könnte einen wirkungsvollen, kombinatorischen Behandlungsansatz für die Krebsbekämpfung darstellen. Im Rahmen dieser Arbeit wurden auch Derivate der zwei weiteren identifizierten Substanzklassen, (*R,R*)-Chromopynone-1/-2 und (+)-Glupin-1, näher untersucht. Viele der Erkenntnisse, die durch die Untersuchungen mit Glutor gewonnenen wurden, konnten als allgemeingültig für Glukoseaufnahme-Inhibitoren bestätigt werden.

Die im Rahmen dieser Arbeit untersuchten niedermolekularen Inhibitoren haben das Potential, den Grundstein für den therapeutischen Einsatz von Glukoseaufnahme-Inhibitoren in der Krebsforschung allein oder in Kombination mit anderen Medikamenten zu legen.

5 Introduction

5.1 Cancer

Cancer is a collective term for a large group of diseases that can affect any tissue of the body. It is characterized by uncontrolled cell proliferation that arises from numerous genetic alterations and most often results in tumor formation. Cancer cells invade the surrounding healthy tissue and can migrate to distal sites through the blood stream to form new tumors (metastasis). These metastases are usually the cause of death. Cancer is the second leading cause of death worldwide, while 70% of the associated deaths occur in low- and middle-income countries because of limited access to diagnostic and treatment opportunities.^{1,2}

Traditional cancer treatments include the operative removal of the tumor, radiation and chemotherapy or a combination of these. Since all three procedures entail a large degree of side effects, modern research focuses on two main areas: immunooncology and targeted cancer therapy. The aim of immunooncology is to reactivate the patient's immune system to antagonize the cancer, whereas the latter focuses on the (molecular) differences between normal and cancer cells to selectively kill cancer. These differences have been grouped by Hannahan and Weinberg in 2000 as the seven hallmarks that enable cells to evolve into a malignant state. These hallmarks include resisting cell death, sustaining proliferative signaling, evading growth suppressors, activating invasion and metastasis, enabling replicative immortality and inducing angiogenesis.² Further studies have revealed a second layer of complexity which is combined in the second generation of hallmarks published by Hannahan and Weinberg in 2011 (Figure 2). Hannahan and Weinberg added two enabling characteristics (genome instability and tumor-promoting inflammation) and two emerging characteristics (avoiding immune destruction and deregulating cellular energetics).³ The adapted energy metabolism of cancer is one hallmark that is recently gaining more attention for targeted cancer therapy and is the focus of this thesis.

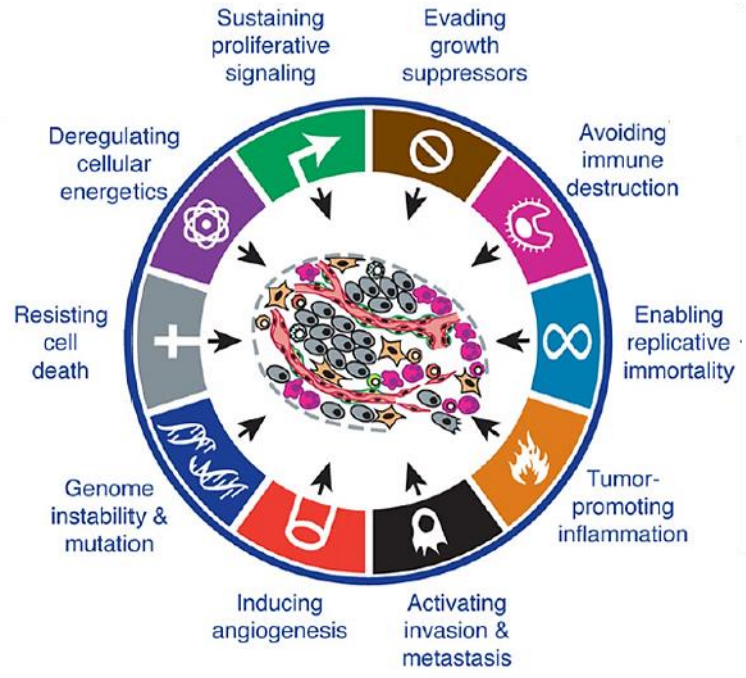


Figure 2 The second generation hallmarks of cancer as postulated by Hanahan and Weinberg.³

5.2 The Warburg effect

Non-malignant, resting cells convert the highly abundant nutrient glucose during glycolysis to pyruvate. Pyruvate subsequently enters the tricarboxylic acid (TCA) cycle and mitochondrial oxidative phosphorylation to generate 36 mol adenosine triphosphate (ATP) per mole glucose that is consumed by the cell (Figure 3a). In the absence of oxygen, cells convert glucose into pyruvate, which is fermented into lactate, generating 2 mol ATP per mole glucose. In 1924, Otto Warburg was the first scientist to observe that cancer cells perform glycolysis regardless of oxygen availability (Figure 3b).⁴ Thus, this observation is also known as the Warburg effect or aerobic glycolysis.

At first glance, this adaptation is counterintuitive since cancer cells require energy for their rapid proliferation and generate 9-fold less ATP during aerobic glycolysis (since mitochondria remain functional and oxidative phosphorylation occurs at low levels aerobic glycolysis generates ~4 mol

ATP/mol glucose).^{3,5} However, the rate of glycolysis is 10-100 times higher than the rate of oxidative phosphorylation, which compensates for the low ATP yield per mole glucose.⁶ The faster kinetics of glycolysis provide an advantage, when cancer cells compete with surrounding stroma cells for glucose.⁶

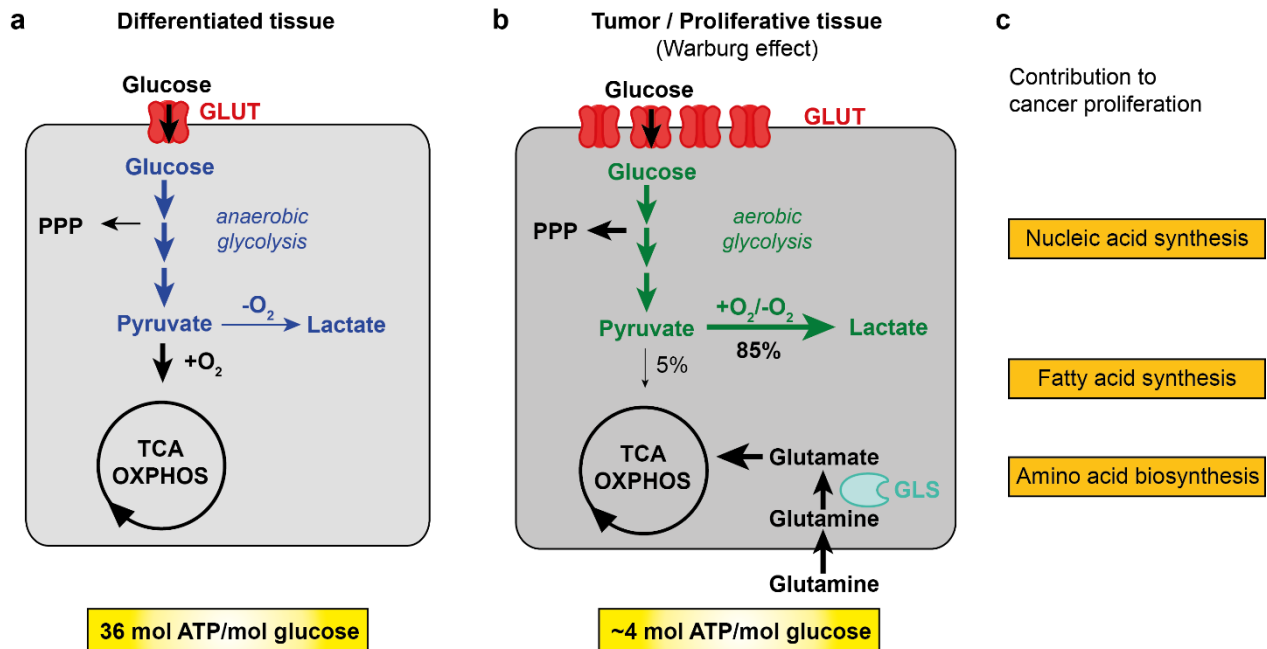


Figure 3 Metabolism of differentiated tissue and tumor cells. Schematic representation of the metabolic phenotypes of differentiated tissue (a) and tumor cells (b). The contribution of the metabolic pathways to proliferation is depicted in c). PPP=pentose-phosphate pathway, TCA=tricarboxylic acid cycle, OXPHOS=oxidative phosphorylation, GLUT=facilitative glucose transporter, GLS=glutaminase kidney isoform.

Another hypothesis for this metabolic adaptation is that intermediates, which are generated during glycolysis, serve as a starting material for e.g. nucleoside biosynthesis using the pentose-phosphate pathway and are therefore essential for DNA replication and division.⁶ Also, the need for reducing equivalents NADPH is much higher than ATP demand. NADPH is produced in high amounts through the pentose phosphate pathway, which is a pathway branch of glycolysis (Figure 3b). Thus, until today the exact reason why cancer cells perform aerobic glycolysis remains controversial.⁶

To accelerate glucose uptake and thereby the rate of glycolysis, cancer cells overexpress the facilitative glucose transporters (GLUTs). High expression levels of the isoform GLUT-1 have been associated with poor patient prognosis and advanced tumor stages, which is why GLUT-1 was proposed as diagnostic marker.⁷⁻⁹ This phenomenon is now applied for tumor localization and diagnosis. Patients receive the glucose derivative 2-deoxy-2-(¹⁸F)fluoro-*D*-glucose (FDG) intravenously, which is rapidly taken up by all tissues with high glucose consumption, such as tumors, within the human body.¹⁰ These can be detected with positron emission tomography (PET). 2-Deoxy-*D*-glucose (2-DG) itself reduces the glycolytic rate by means of hexokinase inhibition and is investigated in multiple clinical trials alone (trial I/II) and together with other anti-cancer treatment strategies, *i.e.* the chemotherapeutic agent docetaxel or radiotherapy.¹¹⁻¹³ Naturally, targeting anaerobic glycolysis is a promising approach for cancer therapy. To date, no medication targeting metabolic differences in cancer cells has been introduced to the market, which underscores the high need for new therapeutic entities. In 2014, the Food and Drug Administration (FDA) approved the drug Enasidenib (AG-221), which inhibits a metabolic target. This small molecule targets the cancer-associated mutated form of isocitrate dehydrogenase (IDH) 2 in order to reduce the production of the oncometabolite 2-hydroxyglutarate (2-HG) and does not target any metabolic adaptation of cancer directly.¹⁴

5.3 Glucose transporters

Glucose is a hydrophilic molecule that cannot pass the plasma membrane of cells. Therefore, glucose is transported via two main protein families, either via passive diffusion (facilitative glucose transporters – GLUTs) or together with sodium by an electrochemical gradient (sodium-dependent co-transporters - SGLTs). GLUTs are integral membrane proteins that passively transport glucose according to the prevalent glucose gradient. There are 14 GLUT isoforms known so far that are expressed in a tissue-specific manner and which are involved in central metabolic processes, *e.g.*

basal glucose uptake (GLUT-1). The isoforms are divided into three distinct protein classes I-III according to their amino acid similarity (Figure 4).¹⁵

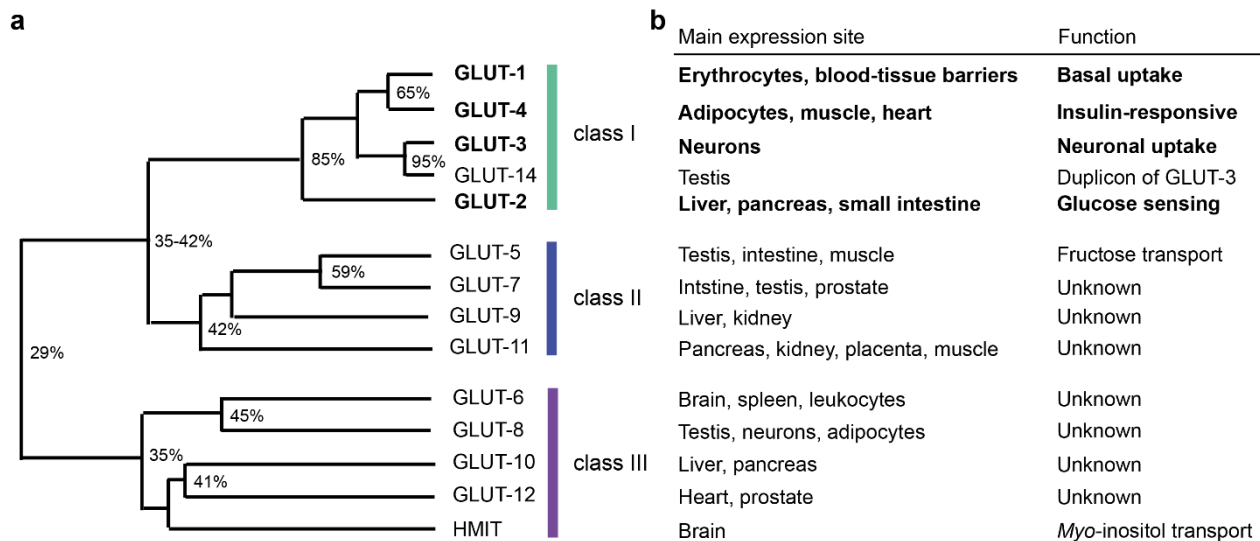


Figure 4 GLUT isoforms of class I-III. a) CLUSTAL multiple alignment revealed amino acid sequence similarities between GLUT isoforms. Adapted from Scheepers *et al.*¹⁵ b) Function and main expression sites of all GLUTs.^{16,17}

Class I GLUTs are the most studied isoforms and comprise five different proteins: GLUT-1, GLUT-2, GLUT-3, GLUT-4 and GLUT-14, which is a duplicon of GLUT-3 and has not gained much attention. The function of most other GLUTs (class II and III) is still a matter of debate or unknown. GLUT-1 is mainly expressed in erythrocytes and blood-tissue barriers to ensure glucose uptake from the blood stream into organs. Furthermore, GLUT-1 is ubiquitously expressed and ensures basal glucose supply of nearly all somatic cells. GLUT-2 is involved in glucose sensing in the pancreas and GLUT-2-mediated glucose uptake is coupled to insulin secretion. Due to GLUT-2's low glucose affinity (Table 1), its major purpose is the postprandial glucose consumption.¹⁸ GLUT-3 has the highest affinity for glucose and is expressed primarily in neurons. GLUT-4 is mainly expressed in insulin-responsive tissues such as muscle or fat. Most expressed GLUT-4 transporters are stored in vesicles when insulin is absent. Upon insulin secretion GLUT-4 membrane translocation is induced.

Table 1 Overview of substrate specificity and affinity for the GLUT isoforms 1-4.^{18,19}

GLUT isoform	GLUT-1	GLUT-2	GLUT-3	GLUT-4
Characteristics	High affinity	Low affinity High capacity High velocity	High affinity High capacity	High affinity
K_m Glc	3-7 mM	17 mM	1.4 mM	6.6 mM
K_m 2-DG	5 mM		~ 1.4 mM	
K_m Fru	no	~ 76 mM	yes	
K_m Gal	~ 17 mM	~ 92 mM	~ 8.5 mM	
K_m Man	yes	~ 125 mM	yes	
K_m GlcN		0.8 mM	yes	3.9 mM
K_m 3-OMe-Glc	~ 20 mM			
DHA	yes		yes	yes
Others	GalN		Maltose, Xyl	

Highest substrate affinity is highlighted in grey. 2-DG=2-deoxy-*D*-glucose, Glc=glucose, Man=mannose, Mt=maltose, Xyl=xylose, DHA=dehydroascorbic acid, GlcN=glucosamine, Fru=fructose, GalN=galactosamine.

The structures of human GLUT-1²⁰ (inward-open conformation) and GLUT-3²¹ (outward-open conformation) have been solved by means of X-ray crystallography. Other human GLUT isoform structures are based on computer homology models of the large-conductance mechanosensitive ion channel (MscL) from *Mycobacterium tuberculosis*, glycerol-3-phosphate transporter GlpT and GLUT-1-4 homologs of *Escherichia coli*.²² The sequences of GLUT-1-4 are highly conserved (Figure 4, Figure 5a) and the glucose binding site exhibits 100% sequence identity among GLUT-1-4 (Figure 5b). Different substrate affinities for glucose or susceptibility for other sugars (Table 1) must therefore originate from the surrounding amino acids. Variation between the amino acid sequences of these four isoforms occur within each of the 12 transmembrane helices. Interestingly, GLUT-1 possesses unique sequence stretches in comparison to GLUT-2-4 at the intracellular helix and within the extracellular loops (Figure 5a).

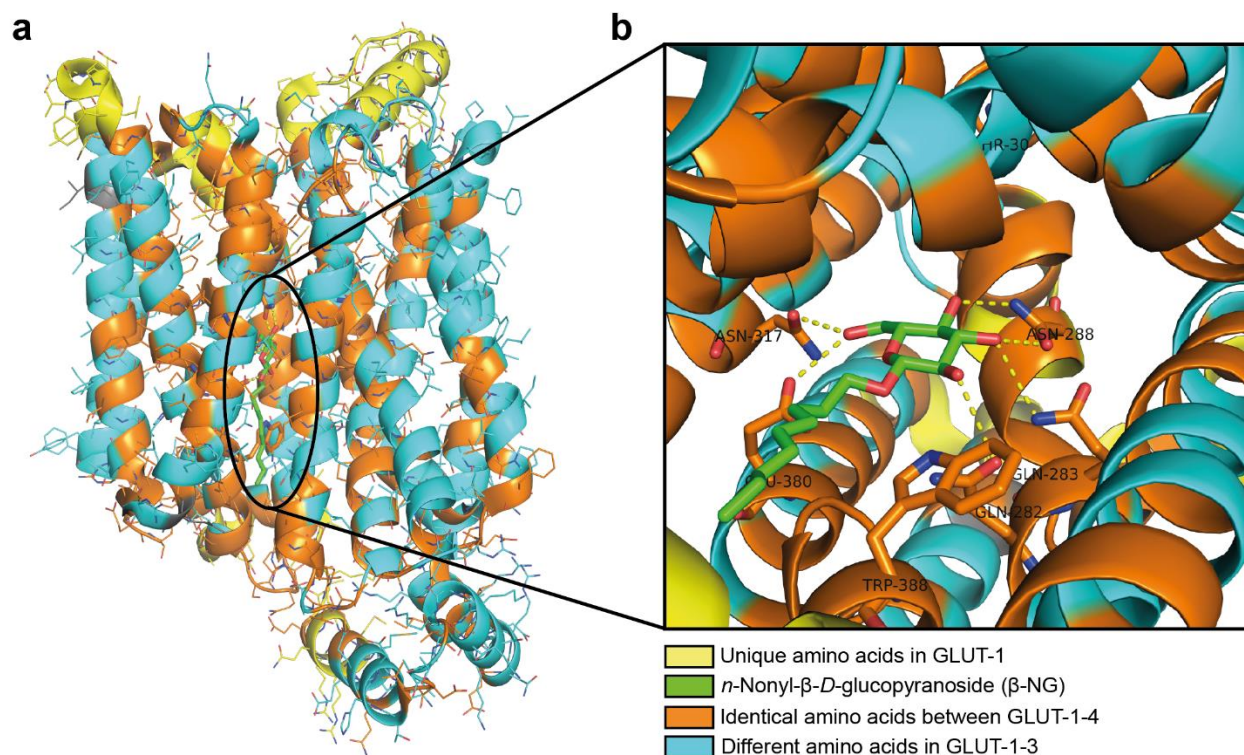


Figure 5 Crystal structure of GLUT-1 and similarity to GLUT-2-4. Structural similarity of GLUT-1-4 isoforms as illustrated on the inward-open crystal structure of GLUT-1 as overview (a) and within the glucose binding site (b). Amino acid alignment of GLUT-1-4 was reported by Zhao *et al.*²³ PDB: 4PYP²⁰.

The overexpression of all isoforms GLUT-1-4 has been described for cancers, mostly associated with the tissue of their respective site of expression.¹⁸ The GLUT-1 isoform is upregulated in nearly all malignant cells. The development of GLUT-1-selective inhibitors for targeted cancer therapy was therefore a long standing goal that was only recently addressed by Siebeneicher *et al.*²⁴ However, high expression levels of GLUT-3 were also determined in a wide range of cancer types, among others endometrial and breast cancers, head and neck tumors, thyroid carcinomas, colon and pancreatic, and non-small cell lung cancer.^{25–30} The required isoform selectivity profile of GLUT inhibitors to potently target glucose uptake in cancer remains therefore uncertain. Multiple selective and unselective inhibitors have been reported and will be discussed in the following chapter.

5.3.1 Glucose uptake inhibitors

The basis of targeted cancer therapy is the discovery of molecules that perturb a biological process that is prevalent in cancer. Such molecules are identified in a process called chemical genetics. Compared to the traditional genetics approaches where certain genes are interrupted to elucidate their function via phenotype analysis, chemical genetics makes use of compounds that disrupt the same process. One disadvantage of the classical genomics approach is the poor transferability to human cells due to their complex genome and their slow reproduction rate compared to e.g. yeast and bacterial cells. Compounds that are utilized in chemical genetics can be natural products, peptides or small molecules. In order to identify compounds that selectively disrupt these biological processes, two main approaches are applied: forward chemical genetics and reverse chemical genetics (Figure 6).^{31,32}

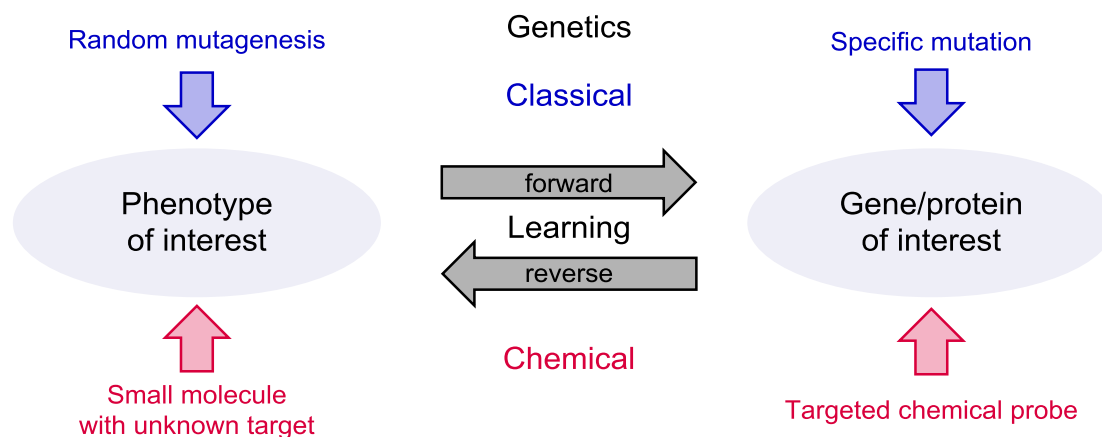


Figure 6 Overview of the classical genetics approach (top) and the chemical genetics approach (bottom). Both approaches can be performed in a forward or a reverse fashion. Figure adapted from Lehar *et al.*³²

In a forward chemical genetics approach, the identification of small molecules that induce a certain phenotype stands in focus (Figure 6, left to right). Usually phenotypic cell-based assays are conducted in the presence of a large compound library to identify such hit compounds. Target identification approaches are subsequently applied to determine the protein whose (altered) function is responsible for phenotype induction. This way, novel interesting proteins and protein

functions can be elucidated. The reverse chemical genetics approach employs biochemical or cellular assays that investigate the manipulation of a specific gene or protein activity by means of small molecules. Subsequent studies deal with the investigation of the thereby caused phenotype (Figure 6, right to left).

Regardless of the approach, the discovery and further development of small molecules that can be used to perturb biological systems is of extreme importance not only to generate novel tool compounds, but also to pave the way for therapeutic applications. The year of 2018 broke all records for the Food and Drug Administration (FDA)-approved drugs: 59 new drugs (42 New Chemical Entities (NCE) and 17 biologics) were introduced to the drug market.³³ Out of the 42 NCE, 47% are small molecules whereas 16% are natural products.³³ This underscores the tremendous potential that lies in the discovery of novel small molecular tool compounds.

Glucose uptake inhibitors from diverse chemical classes have been investigated since the late 20th century (Figure 7, Table 2). Cytochalasin B, a fungal metabolite that was originally described to inhibit cytokinesis, cell motility and disturbance of cell shape, was shown to inhibit glucose uptake by Estensen *et al.* in 1972 (Figure 7, Table 2).³⁴ Since then, this compound was utilized as an unselective tool compound for glucose uptake inhibition in numerous studies.^{35–37} However, Cytochalasin B inhibits actin polymerization, which makes the compound unattractive for further clinical investigation due to the fundamental reliance of the human organism on this process.³⁸ In the 21st century, the systematic development of more specific glucose uptake inhibitors began. Wang *et al.* reported a small molecule, compound 30, that inhibited glucose uptake and reduced the viability of the prostate carcinoma cell line LNCaP with low micromolar IC₅₀ value (Figure 7, Table 2).³⁹ Lui *et al.* discovered the tool compound WZB-117 that inhibits glucose uptake with submicromolar potency (Figure 7, Table 2).¹⁶ Even though after 48 h of treatment the effect on proliferation of the human lung cancer cell line A549 was rather weak (IC₅₀=10 µM), WZB-117

reduced the growth of A549 mouse xenograft models by 70% after daily intraperitoneal injection of WZB-117 at 10 mg/kg for 10 weeks.¹⁶

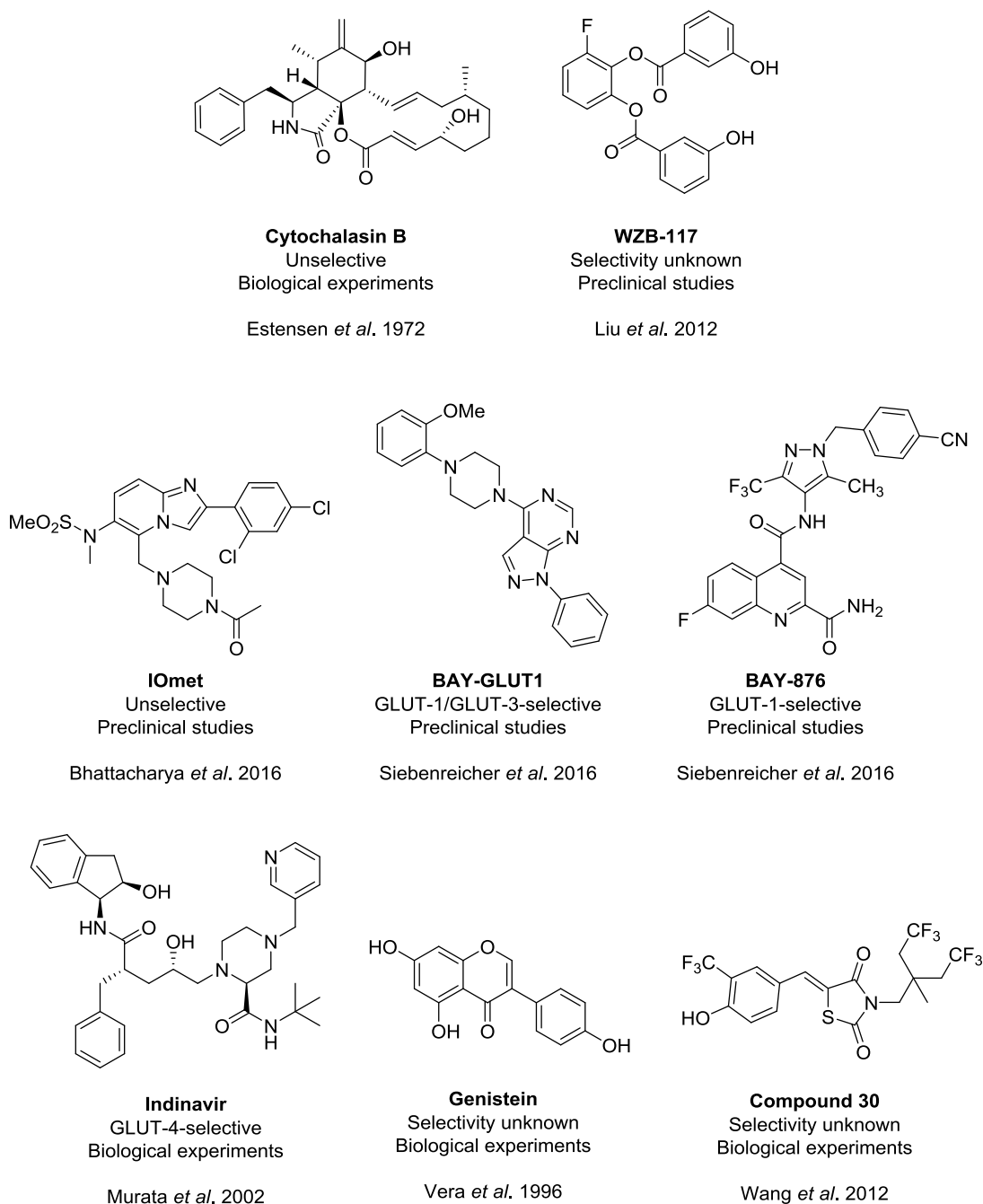


Figure 7 Selection of small molecule GLUT inhibitors. The potencies of all depicted compounds can be found in Table 2.

IOMET Pharma Ltd. filed a patent for GLUT inhibitors in 2014. One highly potent but unselective compound, herein referred to as IOMET, is illustrated in Figure 7 (Table 2).⁴⁰ One described IOMET analog reduced lactate excretion and inhibited growth of A549 cells with nanomolar potency.⁴⁰ In 2016, the Bayer corporation published two novel chemotypes, BAY-GLUT1 and BAY-876, that were discovered based on a high-throughput screening for inhibition of glycolysis-dependent ATP production (Figure 7, Table 2).^{24,41} BAY-876 was the first and until now the only GLUT-1-selective and highly potent ($IC_{50}=2$ nM for DLD-1 cells) glucose uptake inhibitor.

Table 2 Chemical class, potency and GLUT isoform selectivity of selected glucose uptake inhibitors (Figure 7).

Compound	Class	IC ₅₀ (μM)	Assay	Cell line	GLUT selectivity	Comment
WZB-117 ¹⁶	Polyphenol	0.5	³ H-2DG	A549	-	Xenograft studies
BAY-GLUT1 ⁴¹	Pyrazolopyrimidine	0.019	ATP depletion ^a	DLD-1	GLUT-1/-3	
BAY-876 ²⁴	Quinoline	0.002	ATP depletion ^a	DLD-1	GLUT-1	
Cytochalasin B ³⁴	Alkaloid	<4	¹⁴ C-2-DG ^b	N1S1-67	Unselective	Actin polymerization inhibitor
IOMET ⁴⁰	Imidazopyridine	<1	³ H-2DG	HEK293 ^c	Unselective	385 analogues with different selectivity profiles
Genistein ⁴²	Flavonoid	~10	³ H-2DG	HL-60	-	>6 reported flavonoid-based GLUT inhibitors
Compound 30 ³⁹	Thiazolidinedione	2.5	³ H-2DG	LNCaP	-	
Indinavir ⁴³	Peptide analog	10-15	2-DG	Primary rat adipocytes	GLUT-4	HIV protease inhibitor

^aATP depletion in the presence of Rotenone; ^bincorporation of ¹⁴C into lactate; ^cHEK293 cells overexpress human GLUT-1, GLUT-2, GLUT-3 or GLUT-4 transiently.

Over the past three decades, 15 flavonoids have been identified to inhibit glucose uptake. Among these are Phloretin⁴⁴, Fasentin³⁵, Silybin⁴⁵, Apigenin⁴⁶ and Genistein⁴² (Figure 7, Table 2).⁴⁷⁻⁴⁹ Genistein inhibited 2-DG uptake with micromolar potency. The HIV protease inhibitor Indinavir

was recently described as selective GLUT-4 inhibitor, which stopped 2-DG uptake with micromolar potency in primary rat adipocytes (Figure 7, Table 2).⁴³

None of the above-mentioned GLUT inhibitors are currently investigated in clinical trials. Thus, there is still a high demand to develop novel GLUT inhibitors, which will pave the way for drug discovery.

5.4 Metabolic rewiring

Metabolic adaptations in cancer have been associated with the activation of proto-oncogenes such as the GTPase KRas (KRas), dysfunction of tumor suppressors like the cellular tumor antigen p53 (p53) and von Hippel-Lindau disease tumor suppressor (VHL), dysregulated expression of the Myc proto-oncogene protein (Myc) and stabilization of hypoxia-inducible factor 1-alpha (HIF-1- α).^{50–52} HIF-1- α regulates the transcription of different glycolytic enzymes, including GLUTs. Under normoxic conditions, HIF-1- α is hydroxylated via prolyl hydroxylases which increases the affinity to VHL, a E3 ubiquitin ligase, that induces the proteasomal degradation of HIF-1- α . Hypoxic conditions and mutations in VHL therefore stabilize HIF-1- α . Also, phosphatidylinositol-4,5-bisphosphate 3-kinase (PI3K) signaling that acts via RAC-alpha serine/threonine-protein kinase (AKT1) and serine/threonine-protein kinase mTOR (mTOR) activation as well as accumulation of reactive oxygen species (ROS) are associated with HIF-1- α stabilization.⁵³

Inhibitors of glucose metabolism reduce growth of xenograft tumors that are derived from Myc- or KRas-driven cancer cells.^{54–56} Therefore, targeting metabolism as an effector of signaling pathways that control cell growth might be an effective strategy to address cancers that are driven by these genetic alterations and cannot be targeted directly.⁵⁷ Of note, several factors that are involved in glucose addiction, such as Myc, also drive glutaminolysis. Thereby, cancer gains the

flexibility to switch between the two metabolic pathways, depending on the availability of glucose and glutamine.

5.4.1 KRas in metabolic rewiring

Mutated Ras is present in ca. 25% of all human cancers,⁵⁸ with a strong accumulation in colorectal cancers (CRC) (40% KRas mutated)⁵⁹, pancreatic ductal adenocarcinoma (PDAC) (>90% KRas mutated)⁶⁰ and non-small cell lung cancer (NSCLC).⁵ In general, the Ras isoform KRas is mutated most frequently (85%), whereas GTPase NRas (NRas) (11%) and GTPase HRas (HRas) (4%) are mutated less often.⁶¹ KRas, which is mostly associated with deregulation of cellular energetics, but also HRas and NRas, are considered “undruggable”. This turns (K)Ras into the holy grail of targeted cancer therapeutics. Associated metabolic transformations include enhanced nutrient uptake, increased glycolysis (through expression of proteins involved in rate limiting steps of glycolysis such as GLUT-1, hexokinase and lactate dehydrogenase)⁶⁰ and upregulated glutaminolysis (Figure 8). Furthermore, increased fatty acid and nucleotide synthesis, altered expression of mitochondrial genes and reduced mitochondrial activity as well as increased generation of ROS have been related to KRas mutation (Figure 8).^{2,54,58,62,63} Moreover, mutated KRas funnels glucose intermediates into the hexosamine biosynthesis pathway (HBP) for O-glycosylation of proteins and into the pentose phosphate pathway (PPP) to generate necessary building blocks for nucleotide biosynthesis (Figure 8).⁶⁰ However, the degree of metabolic rewiring depends on the genetic background and on the tissue type.^{64–66} Kerr *et al.* reported that the level of glucose addiction correlates with the copy number of KRas, specifically the heterozygous or homozygous presence or a copy gain of mutated KRasG12D.⁶⁵ Davidson *et al.* revealed that NSCLC cells cultured *in vitro* exhibit high glutamine dependence, whereas the same NSCLC cell line was highly glucose-addicted in a mouse xenograft model.⁶⁴ The metabolic consequences in cancers that carry NRas mutation remains unclear, even though about 20% of all melanomas are affected and often display a highly glycolytic phenotype.^{67,68}

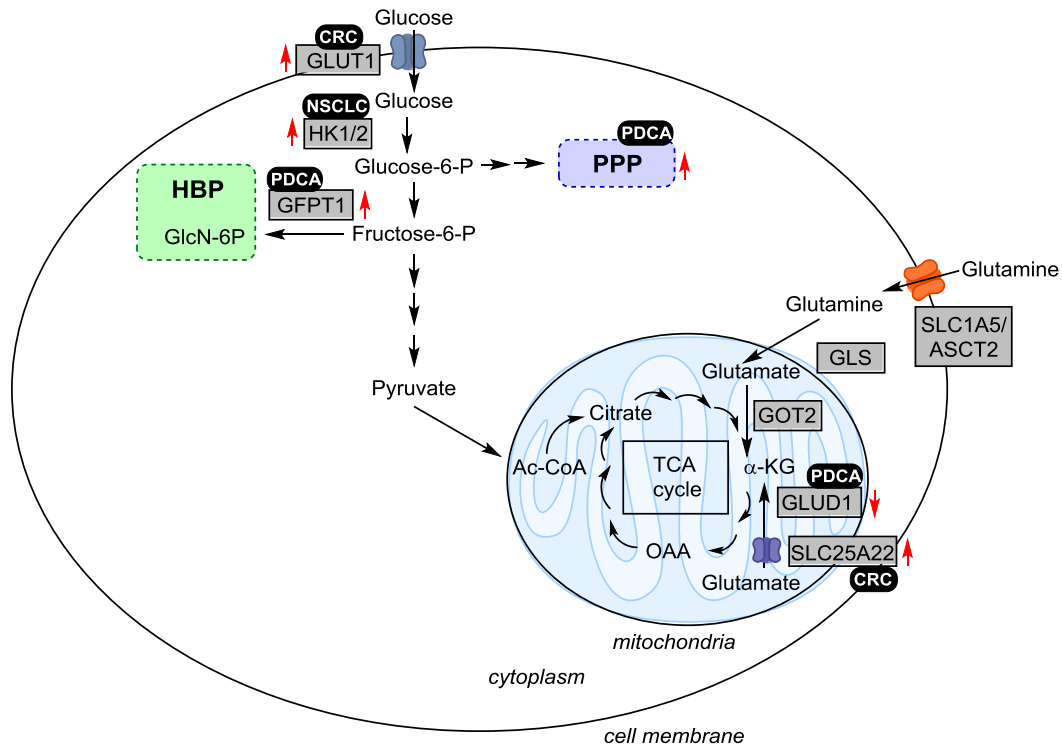


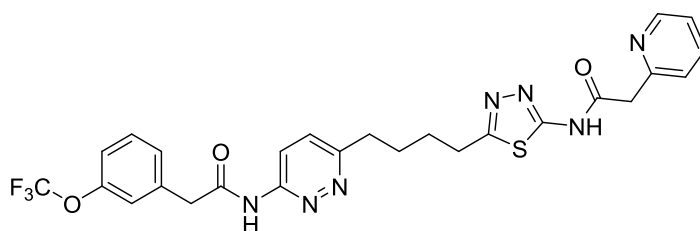
Figure 8 Metabolic rewiring in KRas-driven cancers. Schematic representation of selected metabolic pathways. Black box=cancer type, red arrows=change in expression level, grey boxes=enzymes; GLUT1: Glucose transporter 1, HK1/2: hexokinase 1/2, GFPT1: glucosamine-fructose-6-phosphate aminotransferase-1, GlcN: glucosamine, GLS: glutaminase kidney isoform, GLUD1: glutamate dehydrogenase 1, GOT: glutamate-oxaloacetate transaminase, α-KG: α-ketoglutarate, OAA: oxaloacetate, Ac-CoA: Acetyl-CoA, SLC: solute carrier, P: phosphate, BP: bisphosphate, ASCT2: alanine, serine, cysteine-preferred transporter 2, HBP: hexosamine biosynthesis pathway, PPP: pentose phosphate pathway, TCA: tricarboxylic acid, PDCA: pancreatic ductal cell carcinoma, CRC: colorectal cancer, NSCLC: non-small cell lung cancer. Adapted from Kawada *et al.*⁶²

How mutated KRas coordinates the metabolic shift in cancer remains largely unknown.⁶² KRas is a small GTPase that cycles between the active guanosine triphosphate (GTP)-bound and the inactive guanosine diphosphate (GDP)-bound state. When activated, KRas mainly acts through the RAF proto-oncogene serine/threonine-protein kinase (RAF) /mitogen-activated protein kinase (MEK)/extracellular-signal-regulated kinase (ERK) signaling and the PI3K/AKT1/mTOR pathway, which regulate distinct cellular processes such as proliferation, motility and survival.⁶⁹ Independent of oxygen availability, KRas can influence the expression level of HIF-1-α as well.^{52,70,71} Furthermore, Gaglio *et al.* reported a decoupling between glucose and glutamine metabolism in KRas-mutated cancers.⁷² Conclusively, Ras-, especially KRas-mutated cancers, are largely

influenced in their metabolic phenotype, which drives nutrient, especially glucose addiction and makes them a highly attractive target for metabolic disruption via small molecules.

5.4.2 Metabolic flexibility and glutamine

It was long believed that cancer cells acquire an aerobic glycolytic metabolism and that they are disabled from performing oxidative phosphorylation. Recent evidence has emerged that some cancer cells possess a rather flexible metabolic phenotype and that the tumor itself is composed of cells with highly heterogeneous nutrient dependencies according to their perfusion.^{73,74} The most relevant nutrient besides glucose is the most abundant amino acid glutamine (Figure 3a).⁷⁵ Glutamine fulfills a rather anabolic role in the biosynthesis of proteins, nucleotides, fatty acids and serves as a precursor to fuel the TCA cycle for energy production and for redox control. Furthermore, glutamine is important for the uptake of essential amino acids.^{76,77} Under normal conditions, glutamine is considered a non-essential amino acid since it can be generated *in cellulo* from glucose.⁷⁸ However, the necessity for biosynthetic building blocks during stress and proliferation can increase the demand for glutamine, which outpaces glutamine availability, thus rendering glutamine an essential amino acid.⁷⁹ After cellular uptake via transporter proteins (SLC1A5/ASCT2) (Figure 8), glutamine is converted to glutamate by glutaminase kidney isoform (GLS), which fuels into the respective anabolic pathways (Figure 3a). Therefore, cancer dependence on glutamine suggests the disruption of amidohydrolysis by glutaminase in order to cut the glutamine supply. Indeed, a potent small molecule (CB-839) has been developed that inhibits the cancer-specific glutaminase kidney isoform (GLS) in triple-negative breast cancer (TNBC) cells (Figure 9).⁸⁰ Also, cancer cell growth is reduced by CB-839 with low nanomolar potency in the same cell lines.⁸⁰ However, until now CB-839 has been investigated in multiple clinical studies exclusively in co-administration with other cancer treatments, suggesting that interrupting glutaminolysis alone is not sufficient to target this adaptive disease.⁸¹



CB-839
GLS-selective
Clinical phase I & II

Gross *et al.* 2014

Figure 9 Chemical structure of the inhibitor CB-839 against the glutaminase kidney isoform (GLS).

Targeting metabolic plasticity of cancer by disrupting glutamine and glucose supply simultaneously is therefore an attractive novel anti-cancer strategy. Low expression levels of GLUT-1 have already been associated with a sensitizing effect on lung cancer cells when glutamine is limited.⁸² Unspecific disruption of the glutamine supply via transaminase inhibition with aminooxyacetate (AOA) revealed a beneficial effect on growth inhibition of ovarian cancer when administered together with 2-DG.⁸³ Therefore, a co-treatment approach with CB-839 and a GLUT inhibitor offers an attractive strategy to target metabolic flexibility in cancer.

5.5 Further applications of glucose uptake inhibitors

An adapted metabolism is found not only in cancer but also in other diseases that are associated with stress or proliferation. Especially immunological diseases that involve the over-activation of immune cells (e.g. T cells), infections or abnormal cell growth are associated with a strong glucose dependence.⁵ This Warburg effect-like adaptation was observed for psoriasis (cytokine-driven, inflammatory skin disease associated with hyperplasia),⁸⁴ host cells infected with intracellular bacteria such as *Legionella pneumophila*,⁸⁵ fibrosis,⁸⁶ graft-versus-host disease,⁸⁷ colitis,⁸⁷ systemic lupus erythomatheus,⁸⁸ rhinoviral infections⁸⁹ and persistence of the human immunodeficiency virus (HIV).⁹⁰ This broadens the potential applicability of glucose uptake inhibitors for therapeutic indications.

6 Aim of the thesis

Curing cancer is a long-standing goal for which the development of novel therapeutics is necessary. Since cancer exhibits an altered metabolism and most often glucose addiction, glucose uptake inhibitors have the potential to be an effective cancer treatment.

An in-house medium throughput cancer cell-based screening was conducted in order to identify small molecules that inhibit glucose uptake. The piperazin-2-one hit substance class (Figure 10a,b) was selected according to its potency and structure. This small molecule class should be chemically and biologically investigated.

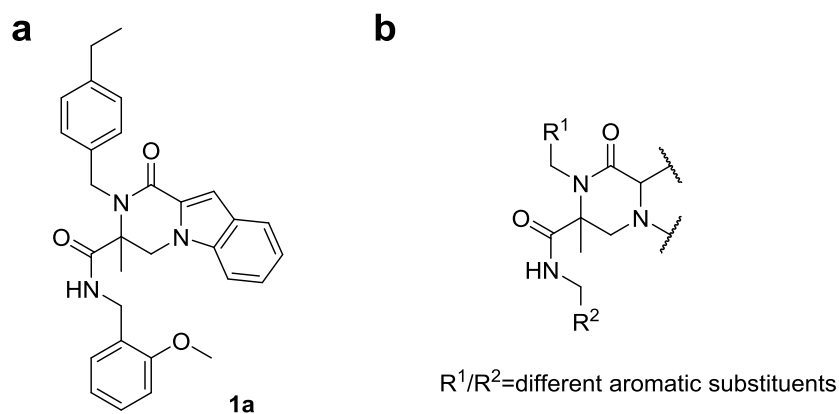


Figure 10 Chemical structure of the piperazin-2-one hit compound 1a (a) and general chemical structure of the piperazin-2-one substance class (b).

Chemical investigation should include the synthesis of a hit substance-based compound library. Assessment of the biological activity of all derivatives should lead to subsequent analysis of the structure-activity relationship (SAR). The proposed protein target class and isoform selectivity within class I glucose transporters should be confirmed using well established, label-free methods. Furthermore, the sensitivity of different cancer cell types towards a potent inhibitor as well as the underlying reasons should be elucidated. Metabolic adaptations of cancer cell lines and potential co-treatment opportunities should be explored.

7 Experimental part

7.1 Experimental part – chemistry

7.1.1 Materials

All chemicals were obtained from Acros Organics, Activate Scientific, Alfa Aesar or Sigma-Aldrich and used as provided, unless otherwise indicated. Dry solvents were stored over activated molecular sieves (MS 4 Å beads) and purchased from Sigma-Aldrich or Acros Organics.

7.1.2 Instrumentation

Proton and carbon nuclear magnetic resonance (^1H - and ^{13}C -NMR) spectra were recorded on *Varian Mercury 400* (400 MHz), *Bruker Avance DRX 500* (500 MHz), *INOVA 500* (500 MHz), *Bruker AV600* (600 MHz) and *Bruker AV700* (700 MHz) NMR spectrometer at ambient temperature. Proton chemical shifts are indicated as parts per million (ppm, δ -scale) and are referenced to residual protium in the NMR solvent (CHCl_3 , $\delta 7.26$ ppm; CH_2Cl_2 , $\delta 5.30$ ppm; $(\text{CH}_3)_2\text{SO}$, $\delta 2.50$ ppm)⁹¹. Data are represented as follows: chemical shift, multiplicity (s = singlet, bs = broad singlet, d = doublet, dd = doublet of doublets, ddd = doublet of doublet of doublets, dt = doublet of triplets, t = triplet, td = triplet of doublets, q = quartet, m = multiplet), coupling constant (J) in Hertz (Hz) and integration. Carbon chemical shifts are expressed in parts per million (ppm, δ -scale) and are referenced to the carbon resonances of the NMR solvent (CDCl_3 , $\delta 77.16$ ppm; CD_2Cl_2 , $\delta 53.84$ ppm; $(\text{CH}_3)_2\text{SO}$, $\delta 39.52$ ppm). All NMR spectra were analyzed using MastReNova Version 12.0.0. High resolution mass spectra (HR-MS) were recorded on a LTQ Orbitrap mass spectrometer 5 coupled to an Acceka HPLC-System (HPLC column: Hypersyl GOLD, 0 m x 1 mm, particle size 1.9 μm , ionization method: electron spray ionization). Systematic names for molecules according to IUPAC rules were generated using ChemDraw Professional version 16.0.

7.1.3 Methods

7.1.3.1 Preparative HPLC-MS

Separations were performed by means of mass-directed preparative HPLC (Agilent Series, 1100/LC/MSD VL) using reversed-phase C18 column with a constant flow of 20.0 mL/min. Solvent A: water +0.1% v/v TFA; solvent B: acetonitrile +0.1% v/v TFA.

7.1.3.2 Separation of enantiomers from racemic mixture

Chiral separation was performed by means of solid phase separation via an Ultimate 3000 HPLC (Dionex, Thermo Fisher) employing an IC column (CHIRALPAK IC, column no. IC00CG-MA004) column. An isocratic gradient was used to separate both enantiomers (elute: isohexane / DCM/MeOH(5%)).

7.1.3.3 General experimental procedures

Reactions were carried out in standard laboratory glassware. Organic solutions were volatilized by rotary evaporation at 40 °C. Analytical thin-layer chromatography (TLC) was performed using aluminum plates pre-coated with silica gel (Silica gel 60₂₅₄, Merck KGaA, Darmstadt, DE KGA). Compounds were visualized on the TLC plates by exposure to ultraviolet light (UV). TLC plates were stained by submersion in aqueous ninhydrin solution or aqueous potassium permanganate solution (KMnO₄) followed by brief heating by a heat gun to visualize primary amines or unsaturated carbohydrates. Ninhydrin solution was prepared as follows: 1.5 g ninhydrin in 100 ml of n-butanol +3.0 ml acetic acid. KMnO₄ solution was prepared as follows: 1.5 g potassium permanganate +10 g potassium carbonate +1.25 ml 10% (w/v) sodium hydroxide in 200 ml water. Flash column chromatography was performed either using an automatic column with prepacked silica columns purchased from Buchi (Reveleris columns) or manually using silica gel Acros Organics 60 (particle size 0.035–0.070 mm).

7.1.3.4 General procedure 1A: Modified Leuckart-Wallach reaction

General procedure for conventional heating: A microwave vial was charged with the corresponding aldehyde (3.6 mmol, 1 equiv.) dissolved in formamide (36 mmol, 10 equiv.) and formic acid (18 mmol, 5 equiv.). The reaction mixture was vigorously stirred at 180 °C for 2-4 h. After cooling the mixture to room temperature, the crude reaction was mixed with water (25 mL) and extracted thrice with DCM (25 mL). The combined organic layers were dried over Na₂SO₄ or MgSO₄, filtered and the filtrate was concentrated under reduced pressure. Subsequently the remains were purified by silica gel column chromatography (elute as indicated) to yield the corresponding formamide.⁹²

General procedure for microwave irradiation: A microwave vial was charged with the corresponding aldehyde (0.4 mmol, 1 equiv.) and dissolved in a mixture of formamide (18.4 mmol, 50 equiv.) and formic acid (1.8 mmol, 5 equiv.). The reaction mixture was irradiated in a microwave oven for 30 sec at 180 °C. The crude reaction was quenched with 10 mL water and extracted thrice with DCM (15 mL). The combined organic layers were dried over Na₂SO₄ or MgSO₄ and filtered. The filtrate was concentrated under reduced pressure and residual formamide was removed *in vacuo*. The crude reaction was purified by means of silica gel column chromatography (elute as indicated) to yield the corresponding formamide.⁹²

7.1.3.5 General procedure 2: Modified Ugi reaction

The bifunctional carboxylic acid/ketone (0.20 mmol, 1.0 equiv.) and the amine (0.20 mmol, 1.0 equiv. or 0.18 mmol, 0.9 equiv.) were dissolved in MeOH (1 mL). The reaction mixture was vigorously stirred for 30 min at room temperature to let the imine form and the isocyanide (0.20 mmol, 1.0 equiv.) was added subsequently. The mixture was vigorously stirred at 40 °C until full conversion of the starting material was observed by TLC. The solvent was removed under reduced pressure. The remains were mixed with water (25 mL) and extracted thrice with dichloromethane (25 mL). The combined organic layers were dried over Na₂SO₄ or MgSO₄, filtered

and the filtrate was concentrated under reduced pressure. The product was purified by silica gel column chromatography (eluate: petroleum ether / EtOAc or DCM / MeOH).⁹³

7.1.3.6 General procedure 3A: Modified Ugi reaction with in situ isocyanide formation using phosgene

The reaction was performed as described by Neochoritis *et al.*⁹² The corresponding formamide (0.06 mmol, 1.0 equiv.) was dissolved in DCM (1 mL) and cooled to 0 °C. Triethylamine (0.15 mmol, 2.5 equiv.) was added and the mixture was vigorously stirred for 10 min. Triphosgene (0.02 mmol, 0.3 equiv.) dissolved in DCM (1 mL) was added dropwise over a period of approximately 30 min. After consumption of the formamide (monitored by TLC), the bifunctional carboxylic acid/ketone (0.07 mmol, 1.2 equiv.) and the amine (0.06 mmol, 1.0 equiv.) were added and the reaction mixture was vigorously stirred for 5-72 h. The crude mixture was concentrated under reduced pressure. The remains were mixed with water (50 mL) and extracted thrice with DCM (50 mL). The combined organic layers were dried over NaSO₄, filtered and the filtrate was concentrated under reduced pressure. The crude reaction was purified by silica gel column chromatography using the indicated elute.

7.1.3.7 General procedure 3B: Modified Ugi reaction with in situ isocyanide formation using Burgess reagent

The reaction was performed as described by Creedon *et al.*⁹⁴ Briefly, an oven-dried Schlenck tube was charged with the corresponding formamide (220 μmol, 1 eq) which was dissolved in dry acetonitrile under argon atmosphere. Burgess reagent (348 μmol, 1.5-2 eq) was added and the reaction mixture was stirred for 0.5-2 h at room temperature. The reaction progress was monitored by TLC. The amine (198 μmol, 0.9 eq) and bifunctional compound (220 μmol, 1 eq) were combined in MeOH and stirred for approximately 10 min. This mixture was added to the *in situ* formed isocyanide. The reaction mixture was vigorously stirred at room temperature for 1-5 days. Saturated NaHCO₃ (50 mL) was added to the reaction mixture and the product was extracted

thrice with DCM (50 mL). The combined organic layers were dried over Na₂SO₄ or MgSO₄ and filtered. The filtrate was concentrated under reduced pressure and the remains were purified by silica gel column chromatography or recrystallization from MeOH as indicated.

7.1.3.8 *Single crystal X-ray structure analyses*

Structure determination was performed by Lena Knauer, TU Dortmund. For data collection, the Bruker D8 Venture four-circle diffractometer (Bruker AXS GmbH) was employed. The area detector PHOTON100 CMOS (Bruker AXS GmbH) was utilized. To generate the X-ray radiation, the microfocus sources I μ S Cu or Mo (Incoatec GmbH) with HELIOS mirror optics and a single-hole collimator (Bruker AXS GmbH) was used. Data collection was undertaken using the software APEX 3 Suite (v.2017.3-0) that included the programs SAINT for integration and SADABS for adsorption correction (Bruker AXS GmbH). The structures were determined using Olex2⁹⁵ and employing the software ShelXT⁹⁶ using intrinsic phasing and structure refinement was conducted with the XL refinement package⁹⁷ using least squares minimization.

7.2 Experimental part – biology

7.2.1 Material

7.2.1.1 Eukaryotic cell lines

The medium composition is given in chapter 7.2.1.8.

Cell line	Specification	Medium	Order number	Supplier
BxPC-3	Human pancreatic adenocarcinoma	DMEM complete	ACC760	DSMZ GmbH, DE
DLD-1	Human colorectal adenocarcinoma	RPMI1640	PAR-086	Horizon Discoveries, UK
DLD-1 GLUT1(-/-)	Human colorectal adenocarcinoma	RPMI1640	R00-024	Horizon Discoveries, UK
HCT116	Human colorectal carcinoma	DMEM complete	ACC581	DSMZ GmbH, DE
MIA PaCa-2	Human pancreatic carcinoma	DMEM complete	CRM-CRL-1420	ATCC, USA
MDA-MB-231	Human mammary gland adenocarcinoma	DMEM complete +1% NEAA	ACC-732	DSMZ GmbH, DE
SW480	Human colorectal adenocarcinoma	Leibovitz's L-15	CCL-228	ATCC, USA
UM-UC-3	Human urothelial transitional cell carcinoma	MEM Eagle	CRL-1749	ATCC, USA
UO-31	Human renal carcinoma	RPMI1640	MTA 1-4488-14	NCI, USA
CHO	Chinese hamster ovary	DMEM complete	CRL-9618	ATCC, USA

NEAA=Non-essential amino acids, DSMZ=Deutsche Sammlung von Mikroorganismen und Zellkulturen, ATCC=American Type Culture Collection, NCI=National Cancer Institute.

7.2.1.2 Antibodies

Antibody	Host	Dilution for immunoblotting	Order number	Supplier
Primary antibodies				
Anti-GLUT1	Mouse	1:5,000	Ab40084	Abcam, UK
Anti-GLUT2	Rabbit	1:200	Sc-9117	Santa Cruz, US
Anti-GLUT3	Rabbit	1:5,000	Ab191071	Abcam, UK
Anti-GLUT3	Rabbit	1:5,000	Sc-74399	Santa Cruz, US
Anti-GLUT4	Rabbit	1:500	07-1404	Millipore, USA
Anti-Na ⁺ -K ⁺ -ATPase	Rabbit	1:10,000	Ab76020	Abcam, UK
Anti-Vinculin	Mouse	1:10,000	Sc-59803	Santa Cruz, USA
Secondary antibodies				
Anti-rabbit 680RD	Donkey	1:5,000	926-68071	LI-COR Biosciences, DE
Anti-rabbit 800CW	Donkey	1:5,000	926-3221300	LI-COR Biosciences, DE
Anti-mouse 680RD	Donkey	1:5,000	926-68072	LI-COR Biosciences, DE
Anti-mouse 800CW	Donkey	1:5,000	926-32212	LI-COR Biosciences, DE
Anti-rabbit HRP	Goat	1:100,000	31430	Pierce, USA (Thermo Scientific)
Anti-mouse HRP	Goat	1:10,000	31460	Pierce, USA (Thermo Scientific)

HRP=Horseradish peroxidase

7.2.1.3 Plasmids

Plasmid	Order number	Supplier
GLUT-1	pTCN(BC121804)	transOMIC, USA
GLUT-2	pTCV(BC060041)	transOMIC, USA
GLUT-3	pCMV-SPORT 6	Dharmacon, USA
GLUT-4	pTCN(BC121804)	transOMIC, USA
pTCN empty vector	pTCN	transOMIC, USA
pCMV empty vector	pCMV	Dharmacon, USA

7.2.1.4 Oligonucleotides

Gene	Forward Primer (5'-3')	Reverse Primer (5'-3')	Product Size, bp	Efficiencies
<i>GLUT1</i>	TTGCAGGCTTCTCCAACCTGGAC	CAGAACCAGGAGCACAGTGAAG	112	104.8%
<i>GLUT2</i>	ATGTCAGTGGGACTTGTGCTGC	AACTCAGCCACCATGAACCAGG	130	99.9%*
<i>GLUT3</i>	TGCCTTTGGCACTCTCAACCAG	GCCATAGCTCTTCAGACCCAAG	97	104.9%
<i>GLUT4</i>	CCATCCTGATGACTGTGGCTCT	GCCACGATGAACCAAGGAATGG	137	89.2%*
<i>ACTB</i>	CACCATTGGCAATGAGCGGTTTC	AGGTCTTTGCGGATGTCCACGT	134	100.7%
<i>B2M</i>	CCACTGAAAAAGATGAGTATGCCT	CCAATCCAAATGCGGCATCTTCA	126	102.0%
<i>TUBB</i>	CTGGACCGCATCTCTGTGTACT	GCCAAAAGGACCTGAGCGAACA	116	100.8%
<i>ATP1A1</i>	GGCAGTGTTCAGGCTAACCCAG	TCTCCTTCACGGAACCACAGCA	118	100.2%

The primer efficiencies for amplicon duplication were measured in DLD-1 wt lysates or with isoform specific plasmids (*).

7.2.1.5 Chemicals and reagents

Reagent	Supplier
α -D-Glucose	Sigma-Aldrich Chemie GmbH, DE
[³ H]-2-Deoxy- α -D-glucose ([³ H]-2DG)	PerkinElmer LAS, DE
2-Deoxy- α -D-glucose (2-DG)	Santa Cruz Biotechnology Inc., DE
3-Bromopyruvate	Alfa Aesar, USA
Agarose, UltraPure™	Invitrogen Thermo Fisher Scientific, USA
Bradford assay reagent	Bio-Rad Laboratories GmbH, DE
Bovine albumin fraction V (BSA)	AppliChem GmbH, DE
Calcium chloride dihydrate (CaCl ₂ ·H ₂ O)	Sigma-Aldrich Chemie GmbH, DE
Caspase-3/7 green apoptosis assay reagent, 5 mM	Essen BioScience, USA
Cell dissociation solution	Sigma-Aldrich Chemie GmbH, DE
CellTiter-Glo® reagent	Promega Corporations, USA
Chameleon™ duo pre-stained protein ladder	LI-COR Biosciences, DE
(3-[3-Cholamidopropyl]-dimethyl-ammonio]-1-propansulfonat (CHAPS)	Carl Roth GmbH, DE
Diaphorase, <i>Clostridium kluyvery</i>	Sigma-Aldrich Chemie GmbH, DE
Dimethyl sulfoxide (DMSO)	Sigma-Aldrich Chemie GmbH, DE
DNA ladder, 1 kb	Fermentas GmbH, DE
DNA ladder, 100 bp plus	Thermo Fisher Scientific, USA
Dodecyl- β -D-maltoside (DDM)	Carl Roth GmbH, DE
Dithioerythritol (DTE)	GERBU Biotechnik GmbH, DE
Emulsifier-Safe™ scintillation liquid	PerkinElmer LAS, DE
Ethylenediaminetetraacetic acid (Na ₂ EDTA)	GERBU Biotechnik GmbH, DE
Fetal bovine serum (FBS)	Gibco®, Thermo Fisher Scientific, USA
Glucose-6-phosphate dehydrogenase	Sigma-Aldrich Chemie GmbH, DE
GlutaMAX™, 200 mM	Gibco®, Thermo Fisher Scientific, USA
4-(2-Hydroxyethyl)-1-piperazineethanesulfonic acid (HEPES)	GERBU Biotechnik GmbH, DE
Hydrochloric acid (HCl), 1M	VWR International GmbH, DE
Insulin, bovine	Sigma-Aldrich Chemie GmbH, DE
Iodacetamide	AppliChem GmbH, DE
L-Glutamine, 200 mM	PAN Biotech GmbH, DE
Lipofectamine® 3000	Thermo Fisher Scientific, USA
Magnesium sulfate (MgSO ₄)	J.T. Baker, Avantor, USA
Milk, skimmed	Sigma-Aldrich Chemie GmbH, DE
Non-essential amino acid solution (MEM-NEAA), 100x	PAN Biotech GmbH, DE
Nicotinamide adenine dinucleotide phosphate (NADP ⁺)	AppliChem GmbH, DE
Nonidet P-40 (NP-40) alternative	Merck-Calbiochem, DE
Odyssey® blocking buffer, PBS-based	LI-COR Biosciences, DE
PAGE Ruler™ plus prestained protein ladder	Fermentas GmbH, DE
Penicillin, 10,000 U/mL; streptomycin, 10 mg/mL	PAN Biotech GmbH, DE
Ponceau S, 0.2% (w/v)	SERVA Electrophoresis GmbH, DE
Potassium chloride (KCl)	J.T. Baker, Avantor, USA
Potassium dihydrogen phosphate (KH ₂ PO ₄)	Merck KGaA, DE

Experimental part

Reagent	Supplier
Propidium iodide (PI)	Sigma-Aldrich Chemie GmbH, DE
Protease inhibitor cocktail, EDTA-free	Roche Diagnostics GmbH, DE
Resazurin	Acros Organics, Thermo Fisher Scientific, USA
RNase-free water	Invitrogen Thermo Fisher Scientific, USA
SsoAdvanced™ SYBR® green mix	Bio-Rad Laboratories GmbH, DE
Sodium chloride (NaCl)	VWR International GmbH, DE
Sodium hydroxide (NaOH), 2M	Waldeck GmbH & Co. KG, DE
Sodium pyruvate, 100 mM	PAN Biotech GmbH, DE
SuperSignal™ west pico chemiluminescent	Thermo Fisher Scientific, USA
SuperSignal™ femto maximum sensitivity substrate	Thermo Fisher Scientific, USA
Tris(2-carboxyethyl)phosphine (TCEP·HCl)	Sigma-Aldrich Chemie GmbH, DE
Triethylammonium bicarbonate (TEAB) buffer, 1 M	Sigma-Aldrich Chemie GmbH, DE
Tandem Mass Tag (TMT) 10plex™	Thermo Fisher Scientific, USA
Tris	Carl Roth GmbH, DE
Trypan blue, 0.4% (w/v)	Invitrogen Thermo Fisher Scientific, USA
Trypsin, 0.05% (w/v); EDTA, 0.02% (w/v)	PAN Biotech GmbH, DE
Trypsin, proteomics grade	Sigma-Aldrich Chemie GmbH, DE
Tween®-20	Sigma-Aldrich Chemie GmbH, DE
WST-1	Roche Diagnostics GmbH, DE

7.2.1.6 Consumables

Consumable	Supplier
96-well plate, clear, conical	Sarstedt AG & Co, DE
96-well plate, clear, flat, UV	Santa Cruz Biotechnology Inc., DE
96-deep well plate, opaque	Greiner Bio-One GmbH, DE
96-well plate, black, flat, non-binding	Greiner Bio-One GmbH, DE
96-well plate, black, flat, clear-bottom	Corning Inc., USA
384-well plate, black, flat	Corning Inc., USA
384-well plate, black, flat, clear-bottom	Corning Inc., USA
384-well plate, white, flat	Greiner
Cannula	B.Braun, DE
Cell culture dish, 10 cm	Sarstedt AG & Co, DE
Cell culture flasks, 75 cm ² , 175 cm ²	Sarstedt AG & Co, DE
Cell culture plate, clear, 6-, 12-, 96-well	Sarstedt AG & Co, DE
Cell counter chambers, disposable	Invitrogen Thermo Fisher Scientific, USA
Cell scratcher	Falcon®, Corning Inc., USA
Cryovials	VWR International GmbH, DE
Cuvettes	Sarstedt AG & Co, DE
Hemocytometer	Paul Marienfeld GmbH & C. KG, DE
iCycler iQ® PCR plates, 96 well	Bio-Rad Laboratories Ltd., UK
Membrane filter	Thermo Fisher Scientific, USA
PCR tubes, 0.2 mL	Sorenson BioScience, Inc., USA
PCR plate	Bio-Rad Laboratories Ltd., UK

Experimental part

Consumable	Supplier
PCR Sealers™, Microseal® 'B' Film	Bio-Rad Laboratories Ltd., UK
Pipette tips, 10 µL	Sarstedt AG & Co, DE
Pipette tips, 200 µL, 1,000 µL	Diagonal, DE
Pipette tips, protein low-binding, 10 µL, 200 µL, 1000 µL	Sorenson BioScience, Inc., USA
Pipette tips, RNase-free, 10 µL, 200 µL, 1000 µL	Biozym Scientific GmbH, DE
Polycarbonate tubes, 0.5 mL	Beckman Coulter, USA
Syringes, 10 mL, 20 mL, 50 mL	B.Braun, DE
Tubes, 0.5 mL, 1.5 mL, 2.0 mL	Eppendorf AG, DE
Tubes, protein low-binding 0.5 mL, 1.5 mL, 2.0 mL	Eppendorf AG, DE
Tubes, 15 mL, 50 mL	Sarstedt AG & Co, DE
Seahorse cell culture plate, 8-well	Agilent, USA
Serological pipettes 1 mL, 5 mL, 10 mL, 25 mL	Sarstedt AG & Co, DE
Sterile filter, 0.2 µm	Sarstedt AG & Co, DE
Parafilm® M	Bemis® Company, Inc., USA
Polyvinylidene difluoride membrane (PVDF)	Merck KGaA, DE
QiaShredda column	Qiagen GmbH, DE
Whatman® 3MM Paper	Whatman GmbH, DE

7.2.1.7 Buffers and solutions

Buffer	Composition
Standard buffers	
Phosphate buffered saline (PBS)	2.7 mM KCl 1.5 mM KH ₂ PO ₄ 136.9 mM NaCl 8.1 mM Na ₂ HPO ₄ pH 7.4
SDS separating gels	
5% Stacking gel (1 mL)	0.68 mL H ₂ O 0.17 mL 30% (w/v) acrylamide 0.13 mL 1.0 M Tris (pH 6.8) 0.01 mL 10% (w/v) SDS 0.01 mL 10% (w/v) ammonium peroxodisulfate 0.001 mL <i>N,N,N,N</i> -tetramethylethylenediamine
6% Resolving gel (5 mL)	2.6 mL H ₂ O 1.0 mL 30% (w/v) acrylamide 1.3 mL 1.5 M Tris (pH 8.8) 0.05 mL 10% (w/v) SDS 0.05 mL 10% (w/v) ammonium peroxodisulfate 0.004 mL <i>N,N,N,N</i> -tetramethylethylenediamine

Experimental part

Buffer	Composition
SDS running buffer (10x)	250 mM Tris 2.5 M glycine 35 mM SDS
SDS sample buffer (5x)	0.5 M Tris-HCl (pH 6.8) 40% (v/v) glycerol 277 mM SDS 400 mM DTE 0.3 mM bromophenol blue
Transfer buffer	25 mM Tris 188 mM glycine 20% (v/v) methanol
PBS-T	PBS 0.1% (v/v) Tween®-20
TBS (10x)	500 mM Tris-HCl (pH 7.5) 1.5 M NaCl
TBS-T	TBS (1x) 0.1% Tween®-20
2-DG uptake assay	
2-DG solution	4 mM 2-DG in ddH ₂ O
Enzyme mix	125 mM Tris-HCl (pH 8.4) 0.1% (w/v) BSA 16 U/mL glucose-6-phosphate dehydrogenase 0.2 U/mL diaphorase 0.1 mM NADP ⁺ 2.5 µL/mL resazurin solution in ddH ₂ O
Krebs-Ringer buffer (KRB)	20 mM HEPES 5 mM KH ₂ PO ₄ 1 mM MgSO ₄ 1 mM CaCl ₂ 136 mM NaCl 4.7 mM KCl pH 7.4 0.1% (w/v) BSA
Acidic lysis buffer	0.06 M HCl 1% (w/v) CHAPS
Tris-based neutralizing solution	0.5 M Tris in ddH ₂ O
Resazurin solution	1 mg/ml resazurin in ddH ₂ O

Experimental part

Buffer	Composition
Hexokinase assay	
Radioimmunoprecipitation assay (RIPA) buffer (50 mL)	10 mM Tris-HCl (pH 8.0) 1 mM EDTA 1% (v/v) Triton X-100 0.1% (w/v) sodium deoxycholate 0.1% (w/v) SDS 140 mM NaCl 1 mM phenylmethylsulfonyl fluoride (PMSF) 1 tablet protease inhibitor cocktail
ATP solution	3 mM ATP in ddH ₂ O
Enzyme mix	100 mM Tris-HCl 5 mM MgCl ₂ pH 8.5 0.1 mM NADP ⁺ 16 U/mL G6PDH
Lactate assay	
Precipitation solution	0.6 M HClO ₄ in ddH ₂ O
KHCO ₃ -based neutralization solution	2 M KHCO ₃ in ddH ₂ O
CETSA® / TPP	
NP40-based lysis buffer (50 mL)	PBS 0.4% (v/v) NP40 alternative 1 tablet protease inhibitor cocktail (CETSA®)
Dilution buffer	100 mM TEAB (from 1 M TEAB buffer)
Reducing reagent solution	200 mM TCEP 200 mM TEAB (from 1 M TEAB buffer)
Alkylating reagent solution	375 mM iodacetamide 200 mM TEAB (from 1 M TEAB buffer)
Trypsin stock solution	0.4 µg/mL trypsin in 10 mM HCl
Tryptic digest solution	28 ng/mL (from trypsin stock solution) in dilution buffer
Quenching solution	5% (w/v) hydroxylamine
TMT labeling solution	0.976 mg/mL in anhydrous acetonitrile
Lysis buffers	
Lysis buffer for rescue experiment	2% (w/v) dodecyl-β-D-maltoside in ddH ₂ O
Agarose gel	

Experimental part

Buffer	Composition
Agarose gel	3% (w/v) agarose in 1x TEA buffer
TEA 5x	0.2 M Tris-HCl (pH 8.5) 5 mM Na ₂ EDTA 0.1 M glacial acetic acid

7.2.1.8 Cell culture media and supplements

Medium	Supplements	Order number	Supplier
DMEM medium full w/o sodium pyruvate	10% (v/v) FBS 1 mM sodium pyruvate 100 U/mL penicillin 0.1 mg/mL streptomycin	P04-03550	PAN Biotech GmbH, DE
DMEM medium w/o D-glucose w/o L-glutamine w/o sodium pyruvate	10% (v/v) FBS 100 U/mL penicillin 0.1 mg/mL streptomycin	P04-01548S1	PAN Biotech GmbH, DE
DMEM medium w/o D-glucose w/o L-glutamine w/o sodium pyruvate w/o phenol red	10% (v/v) FBS 100 U/mL penicillin 0.1 mg/mL streptomycin	P04-01548	PAN Biotech GmbH, DE
Leibovitz's L-15	10% (v/v) FBS 100 U/mL penicillin 0.1 mg/mL streptomycin	P04-27500	PAN Biotech GmbH, DE
MEM Eagle	10% (v/v) FBS 100 U/mL penicillin 0.1 mg/mL streptomycin	P04-08500	PAN Biotech GmbH, DE
Opti-MEM™		11058-021	Gibco™, Thermo Fisher Scientific, USA
RPMI1640	10% (v/v) FBS 100 U/mL penicillin 0.1 mg/mL streptomycin	P04-18047 P04-16500	PAN Biotech GmbH, DE
Seahorse XF base medium DMEM w/o phenol red	2 mM GlutaMAX™	103335-100	Agilent, USA

7.2.1.9 Kits

Kit	Supplier
Amplite™ fluorometric L-lactate	AAT Bioquest, USA
DC™ protein assay	Bio-Rad Laboratories Ltd., UK
QuantiTect® reverse transcription	Qiagen GmbH, DE
RNA 6000 nano kit	Agilent, USA
RNeasy® mini kit	Qiagen GmbH, DE
Seahorse XF glycolysis stress test	Agilent, USA
Seahorse mito stress test	Agilent, USA

7.2.2 Instruments and software

Instrument/Software	Specification	Supplier
Cell counter, automatic	Countess II	Invitrogen Thermo Fisher Scientific, USA
Cell washer, automatic	Eix405	BioTek Instruments, Inc., USA
Centrifuge	Centrifuge 5702 Centrifuge 5417R Centrifuge 5424R Centrifuge 5430 Centrifuge 5810R Minispin	Eppendorf AG, DE
Cooling chamber	Unichromat 900	Uniequip GmbH, DE
Data analysis software	Excel Prism 5/7	Microsoft Office, USA GraphPad, USA
Freezing container	Mr. Frosty™	Thermo Fisher Scientific, USA
High-performance liquid chromatography (HPLC)	HPLC Nano HPLC-MS/MS	Thermo Fisher Scientific, USA
Immunoblot imager	Odyssey® CLx imaging system Odyssey® Fc imaging system	LI-COR Biosciences, DE
Immunoblot analysis	Image Studio 5.2	LI-COR Biosciences, DE
Incubator	NuAire CO ₂ Air-Jacket MCO-230AICUVH-P INE400	NuAire, USA PHCbi, Panasonic, JP Memmert GmbH & Co. KG, DE
Laminar flow hood	NuAire HERA Safe MSC-ADVANATEG 1.2	NuAire, USA Thermo Fisher Scientific, USA Thermo Fisher Scientific, USA
Liquid handler	ECHO® 520	Labcyte Ltd, UK
Liquid dispenser	Multidrop® Combi	Thermo Fisher Scientific, USA
Live-cell imaging device	IncuCyte® ZOOM IncuCyte® S3	Essen BioScience, USA
Live-cell imaging software	IncuCyte® ZOOM 2015/2016A IncuCyte® S3 2017A	Essen BioScience, USA

Experimental part

Instrument/Software	Specification	Supplier
Microliter syringe	Hamilton, 100 µL	Hamilton, USA
Microscope	Leitz Labovert DM IRB PrimoVert	Leitz Labovert Mikroskop, FR Leica Camera AG; DE Carl Zeiss AG, DE
Multichannel pipette	8-Channel, 100 µL, 300 µL	Eppendorf AG, DE
PCR cyclers	Mastercycler epgradient S	Eppendorf AG, DE
Pipettes	2.5 µL, 10 µL, 100 µL, 200 µL, 1,000 µL	Eppendorf AG, DE
Pipetting aid	- -	INTEGRA Biosciences AG, CH Brand GmbH & Co. KG, DE
Plate reader	Tecan Infinite® M200 Tecan Spark® SpectraMax® Paradigm Multi-Mode Microplate Reader Deelux-LED96 DTX 880	Tecan Trading AG, CH Tecan Trading AG, CH Molecular devices, LLC., USA Deelux Labortechnik GmbH, DE Beckman Coulter, USA
Plate shaker	Thermomix comfort	Eppendorf AG, DE
Quantitative proteomics software	MaxQuant (v.1.5.3.30) ⁹⁸	Jürgen Cox <i>et al.</i>
Real-time qPCR cyclers	iCycler iQ™5 CFX96 Real-Time System	Bio-Rad Laboratories GmbH, DE
Real-time qPCR analysis	CFX Manager	Bio-Rad Laboratories GmbH, DE
RNA integrity measurement	Bioanalyzer	Agilent, USA
Scintillation counter	Wallac 1409 scintillation counter	PerkinElmer LAS, DE
SDS gel electrophoresis chamber	-	Bio-Rad Laboratories GmbH, DE
Semi-dry electrophoretic device	Trans-Blot® SD semi-dry transfer cell	Bio-Rad Laboratories GmbH, DE
Sonifier	Bandelin	Sonoplus GmbH & Co. KG, DE
Spectrophotometer	BioPhotometer 6131	Eppendorf AG, DE
Thermoshaker	ThermoMixer C Thermoblock MTP	Eppendorf AG, DE
UV workstation	UVC/T-M-AR	Biosan, LV
Test tube shaker	Vortex-Genie 2	Scientific Industries, Inc., USA
Tube rolling device	TRM 50	IDL GmbH & Co. KG, DE
Ultracentrifuge	Optima MAX-XP ultracentrifuge	Beckman Coulter, USA
Ultracentrifuge rotor, fixed angle	TLA-120.1	Beckman Coulter, USA
Vacuum concentrator	Concentrator plus	Eppendorf AG, DE
Water bath	Memmert	Memmert GmbH & Co. KG, DE

7.2.3 Cell biology methods

7.2.3.1 *Thawing of cell lines*

Cell lines that were cryopreserved in liquid nitrogen (chapter 7.2.3.4) were rapidly thawed using a 37 °C warm water bath. The cell suspension was transferred to a fresh 15 mL tube containing 10 mL of the respective prewarmed full cell culture medium and centrifuged at 0.2 x g for 5 min at room temperature. The supernatant was removed and the cell pellet was resuspended in 12 mL fresh, prewarmed full medium. The cell suspension was transferred to a fresh 75 cm² cell culture flask and the cells were cultured at 37 °C and 5% CO₂ in humidified atmosphere using an incubator until further sub-cultivation (chapter 7.2.3.2).

7.2.3.2 *Sub-cultivation of adherent cell lines*

Adherent cells were sub-cultured once a confluence of about 90% was reached. The cell culture medium was removed and the cells were washed with 5 mL prewarmed, sterile PBS. The cells were detached using 1.2 mL trypsinization solution containing EDTA and incubated for 5 min to 15 min at 37 °C and 5% CO₂ in humidified atmosphere. The degree of detachment was monitored periodically using a microscope. Gentle taping of the cell culture flask ensured successful detachment of all cells. The trypsin was inactivated upon addition of 10 mL fresh, prewarmed full medium followed by separation of clotted cells using a serological pipette. Depending on the growth rate of the used cell line, 1-3 mL of the generated cell suspension was transferred to a fresh cell culture flask supplemented with 10 mL fresh, prewarmed full medium.

7.2.3.3 *Cell counting and seeding of cells*

To seed adherent cells in a desired cell density, cells were detached and suspended after trypsin inactivation (chapter 7.2.3.2). The cell suspension was centrifuged at 0.2 x g for 5 min to separate dead, floating cells. After removal of the supernatant, the cell pellet was resuspended in 10 mL fresh, prewarmed full medium. The cell suspension was mixed 1:1 with trypan blue to visualize

dead cells. 10 μL of the resulting mixture were either pipetted in a disposable cell counting chamber for automated cell counting or placed in a hemocytometer. The automated cell counter provides a cell density (cells/mL) as well as viability (%) of the cell suspension. To count cells with the hemocytometer, the chamber was prepared beforehand by humidifying the cover glass and pressing it gently on the hemocytometer. The accurate volume of the chamber between cover glass and hemocytometer was reached when the Newton's rings could be observed. After placing 10 μL of the trypan blue-cell suspension mixture in the chamber, viable (non-blue) cells were counted within each of the four 16-square corners. After calculating the mean value, the number was multiplied by 20,000 (dilution factor 2, conversion factor 10,000 to reach from 100 μL to 1 mL) to assess the cell number/mL. The cell suspension was diluted with fresh, prewarmed medium to generate a new cell suspension with the desired cell density. The cell suspension was transferred into a 96-well plate using an eight- or twelve-channel pipet (100 μL /well) or into a 12- (1 mL/well) or 6-well (3 mL/well) plate using a serological pipet. The outer wells within the cell culture plates were filled with sterile PBS if unused to avoid excessive medium evaporation.

7.2.3.4 Cryopreservation of cells

In order to cryopreserve cells, a cell suspension was generated (chapter 7.2.3.2) and the cell density was determined as described in 7.2.3.3. The resulting cell suspension was diluted to reach a cell density of approximately 1×10^6 cells/mL and supplemented with 5% (v/v) DMSO to avoid excessive damage of the cell membranes by ice crystals. 1 mL of the DMSO-supplemented cell suspension was transferred in one cryovial, which was afterwards placed in a Mr. Frosty™ freezing container to ensure slow temperature reduction and freezing at $-80\text{ }^\circ\text{C}$ overnight. The following day, the cryovials were transferred on dry ice in a liquid nitrogen tank and stored until further usage.

7.2.3.5 *Compound treatment and controls*

All compounds were dissolved in dimethyl sulfoxide (DMSO) and maintained as 10 mM stock solution at -20 °C. The stock solutions were aliquoted to avoid multiple freeze-thaw cycles. Cellular experiments that involved compound treatment included a control, *i.e.*, cells were treated with the same DMSO concentration as compound-treated cells. DMSO concentration was always below 0.5% (v/v). Experiments involving the treatment with varying nutrient concentrations included cells treated with glucose- or glutamine-depleted medium as a control (DMEM medium). The usage of known inhibitors as controls is indicated in each experiment.

7.2.3.6 *Generation of cell lysates*

Whole cell lysates for cellular thermal shift assay (CETSA®) and Thermal proteome profiling (TPP) (chapter 7.2.5.1): SW480 cells were grown to confluence in 175 cm² cell culture flasks. After washing with PBS once, the adherent cells were detached by addition of trypsinization solution or cell dissociation buffer followed by an incubation period of 20-30 min at 37 °C. Cells were suspended in 20 mL PBS (or medium in case of trypsin detachment) and transferred in 50 mL tubes followed by two centrifugation steps (290 x g, 4 °C, 5 min) and two washing steps with 20 mL PBS. The cell pellet was resuspended in approximately 1.0 mL PBS supplemented with 0.4% (v/v) NP40 alternative and protease inhibitor and transferred to a fresh non-protein binding tube. For Thermal Proteome Profiling (TPP, chapter 7.2.5.1), protease inhibitor cocktail was excluded from the lysis buffer. The cells were subjected to four freeze-and-thaw cycles and one short sonification step (10 s). Insoluble material was removed by ultracentrifugation at 100,000 xg and 4 °C for 20 min. The supernatant was transferred to a fresh protein low-binding tube and the protein concentration was determined by means of the Bradford method (chapter 7.2.4.1). The lysates were snap frozen in liquid nitrogen and stored at -80 °C until further usage.

Whole cell lysates for hexokinase activity assay (chapter 7.2.5.2): HCT116 cells were grown in 175 cm² cell culture flasks until a confluence of approximately 95% was reached. The adherent

cells were washed thrice with 5 mL ice-cold PBS. Cell lysis was performed using 300 μ L RIPA buffer containing protease inhibitor cocktail followed by incubation on ice for 5 min. The cell lysates were collected using a cell scraper and transferred to a fresh tube. After centrifugation at 500 x g for 10 min at 4 °C the supernatant was transferred into a fresh 1.5 mL tube. The protein concentration was determined by means of Bradford method (chapter 7.2.4.1) and the lysates were snap frozen in liquid nitrogen and stored at -80 °C until further usage.

Rescue experiment (chapter 7.2.3.14): After 24 h or 48 h of treatment (chapter 7.2.3.14), the DLD-1 cells were washed once with PBS and detached using cell dissociation solution. The cells were suspended in PBS and transferred to a fresh tube followed by centrifugation at 1,200 rpm at 4 °C for 5 min. The pellet was resuspended in PBS containing 2% (w/v) dodecyl- β -D-maltoside (DDM) and lysed on ice for 15 min. The cell lysates were centrifuged at 20,800 x g at 4 °C for 15 min and the supernatant was transferred into 1.5 mL protein low-binding tubes. The protein content was determined by means of DCTM protein assay (chapter 7.2.4.2) or Bradford method (chapter 7.2.4.1). The lysates were either snap frozen in liquid nitrogen and stored at -80 °C until further usage or directly separated using SDS-PAGE according to the general procedure (chapter 7.2.4.4).

7.2.3.7 Resazurin-coupled 2-DG uptake assay

Cells were seeded in complete medium with a density of 40,000 cells/well using a 96-well plate (black, clear bottom) (chapter 7.2.3.3). After 24 h at 37 °C and 5% CO₂ in humidified atmosphere, cells were washed thrice with Krebs-Ringer bicarbonate (KRB) buffer supplemented with 0.1% (w/v) bovine albumin fraction V (BSA) that was prepared freshly before use. The cells were treated with the respective compound and incubated for 30 min at room temperature in the presence of 1 mM 2-DG. After removal of the supernatant, the cells were washed thrice with ice-cold KRB buffer supplemented with 0.1% (w/v) BSA to stop cellular 2-DG uptake. Cells lysis was performed in 60 μ L acidic lysis buffer for 15 min at 65 °C followed by a cooling period at room

temperature of around 30 min. The lysates were neutralized using 20 μ L neutralizing buffer and 60 μ L of resazurin-supplemented enzyme mix was added. After 2 h of incubation at room temperature in the dark, resorufin (reduction product of resazurin) fluorescence intensity was assessed using the Tecan Infinite® M200 plate reader (ex/em 535 nm/590 nm, bottom read-out). For data normalization, the background (no 2-DG) was subtracted from the raw values followed by normalization to the value of DMSO-treated cells. IC₅₀ values were calculated by means of non-linear regression fit with variable slope (four parameters) using GraphPad Prism 5 or 7.

Compound screening was performed by employing the aforementioned 2-DG uptake assay in semi-automated fashion in collaboration with the Compound Management and Screening Center (COMAS), Dortmund. Implementation of the assay to higher throughput was performed by Melanie Schwalfenberg and included the following variations: HCT116 cells were seeded (chapter 7.2.3.3) in DMEM full medium in 15,000 cells/well using 384-well black-walled, clear bottom plates and incubated overnight at 37 °C supplemented with 5% (v/v) CO₂ in humidified atmosphere. For compound library screening compounds were tested at 30 μ M or for IC₅₀ determination in serial dilution starting from 30 μ M. An acoustic nanoliter dispenser (ECHO® 520) was used to generate the compound dilutions. Fluorescence intensity (ex/em 535 nm/590 nm) was measured using a SpectraMax® Paradigm Multi-Mode Microplate Reader (bottom read-out) employing Rhodamine filter setting.

7.2.3.8 Cell viability after 2-DG uptake assay (semi-automated)

To validate hit compounds from the 2-DG uptake inhibition screen, hit compounds were tested for their influence on cell viability employing the CellTiter-Glo® reagent after 30 min treatment of HCT116 cells. Cells were seeded with 12,000 cells/well or 7,500 cells/well in a white 384-well cell culture plate and incubated for 24 h or 48 h, respectively, at 37 °C with 5% (v/v) CO₂ and humidified atmosphere (chapter 7.2.3.3). Cells were washed thrice with 75 μ L KRB buffer supplemented with 0.1% (w/v) BSA before the compound (30 μ M or for IC₅₀ determination in serial

dilution starting from 30 μM) and 1 mM 2-DG were added. After 30 min of incubation, the cells were washed twice with 75 μL KRB buffer supplemented with 0.1% (w/v) bovine albumin fraction V (BSA). CellTiter-Glo® reagent (15 μL) was added to the cells, mixed for 2 min on an orbital shaker and incubated for 10 min at room temperature before luminescence was recorded using a SpectraMax® Paradigm Multi-Mode Microplate Reader. All steps involving liquid handling were performed using automated cell washer or a multidrop device. *The assessment of cellular viability was conducted by the Compound Management and Screening Center (COMAS), Dortmund.*

7.2.3.9 [³H]-2DG uptake assay

Cells were seeded into a 24-well cell culture plate and grown to about 80% confluence (chapter 7.2.3.3). Cells were washed thrice with Krebs-Ringer Bicarbonate (KRB) buffer supplemented with 0.1% (w/v) BSA followed by incubation with the compound and 1 $\mu\text{Ci/mL}$ [³H]-2DG for 30 min at room temperature. Residual [³H]-2DG was removed and the cells were washed thrice with ice-cold KRB buffer supplemented with 0.1% (w/v) BSA. Cell lysis was performed using 200 μL 0.1 M NaOH followed by 30 min incubation at room temperature. 2 mL Emulsifier-Safe™ scintillation liquid were mixed with 195 μL cell lysate and radioactivity was measured using Wallac 1409 scintillation counter. Protein content was assessed using 5 μL of the cell lysate by means the Bradford method (chapter 7.2.4.1) and radioactivity was normalized to cellular protein concentration.

7.2.3.10 Lactate excretion assay

30,000 cells were seeded in a 96-well plate 24 h prior to the experiment (chapter 7.2.3.3). 12 h before the treatment cells were starved of glucose (0 mM). Compound treatment (chapter 7.2.3.5) was performed in 120 μL medium with 2 mM glucose for the indicated time periods. DMSO-treated cells or cells incubated in the absence of glucose served as a control. Afterwards, 100 μL of the medium was collected and stored at -20 °C until further usage. Prior to the lactate assay, the supernatant was thawed on ice and proteins were precipitated according to the method described

by McLellan *et al.*⁹⁹ Briefly, 200 μL 0.6 M ice-cold perchloric acid was added to the supernatant, mixed vigorously and stored on ice for 10 min. The precipitate was separated by means of centrifugation (6000 x g, 10 min, 4 °C). The supernatant was transferred to a fresh tube and neutralized using 65 μL 2 M KHCO_3 . The thereby generated KClO_4 precipitate is separated via centrifugation (6000 x g, 5 min, 4 °C). Lactate was detected in a 384-well plate using the Amplite™ fluorometric *L*-lactate assay kit (AAT Bioquest) according to the manufacturer's instructions. In this assay, the amount of *L*-lactate in the supernatant is quantified by conversion using NADPH-generating, supplemented enzymes. The amount of NADH is detected using a fluorogenic NADH sensor. After incubation in the dark for 30 min to 2 h, fluorescence intensity of the generated fluorophore was detected spectrophotometrically (ex/em 540/590 nm) using the plate reader Tecan Infinite® M200. For each time point, the values were normalized to the value of DMSO-treated cells.

7.2.3.11 Sulforhodamine B cell viability

The growth behavior of 94 cell lines was assessed by Oncolead (Germany) using a Sulforhodamine B assay¹⁰⁰. After 72 h of incubation with the compound, the cells were fixed with 10% trichloroacetic acid (TCA) for adherent cells or 50% TCA for semi-adherent or suspension cells for 1 h at 4 °C. The cells were washed twice with 400 μL ddH₂O and dried at ambient temperature. The cells were stained with 100 μL of 0.04% (w/v) Sulforhodamine B and incubated for at least 30 min at room temperature. The dye Sulforhodamine B binds to basic amino acids of cellular proteins. Unbound dye was washed away six times using 1% (v/v) acetic acid and the samples were dried at ambient temperature. The immobilized dye was extracted by addition of 100 μL of 10 mM Tris and the absorbance at 510 nm was measured using the LED96 plate reader (Deelux, Germany). The cell panel was commissioned by the Lead Discovery Center, Dortmund.

7.2.3.12 Glycolysis stress test

HCT116, UM-UC-3 and BxPC-3 cells were seeded with 6,000 cells/well and MDA-MB-231 with 250,000 cells/well in 80 μ L DMEM full medium in 8-well Seahorse XFp microplates and were incubated at 37 °C with 5% CO₂ in humidified atmosphere (chapter 7.2.3.3). The outer two wells served as controls and were filled with sterile PBS. The reservoirs around the wells were filled with sterile PBS to avoid excessive evaporation. After 24 h, the medium was removed and exchanged for glucose-free Seahorse XF base medium (0.5 mM or 2 mM GlutaMAX™) and the cells were incubated for 45 min at 37 °C without CO₂ supply. The glycolysis stress test was performed using the glycolysis stress test from Agilent: compound addition was performed after the first three measurement cycles (3x 6 min) followed by a 30 min incubation step (5x 6 min). Afterwards, the assay was performed according to the manufacturer's instructions. The data was analyzed using the suitable supplier's Wave software. The oxygen consumption rate (OCR) and the extracellular acidification rate (ECAR) were normalized to the time point before compound addition (18 min after beginning of the experiment). For the generation of a metabolic profile, the glycolytic reserve, glycolytic capacity and OXPHOS reduction were calculated from the second of three measurements from one experiment phase (e.g. after addition of glucose).

7.2.3.13 Mito stress test

HCT116 cells were seeded with a density of 20,000 cells/well in 80 μ L DMEM full medium and incubated overnight at 37 °C and 5% (v/v) CO₂ in humidified atmosphere (chapter 7.2.3.3). The medium was removed and 180 μ L prewarmed assay medium (Seahorse XF base DMEM, 25 mM glucose, 2 mM GlutaMax™, 1 mM sodium pyruvate) were added to the cells. The cells were incubated at 37 °C without CO₂ for 45-60 min, before the Mito stress test was initiated. After the first three measurement cycles (3x 6 min), BAY-876 or DMSO was added in the respective concentration to the cells and incubated for 30 min (5x 6 min). Oligomycin (1 μ M), carbonyl cyanide 4-(trifluoromethoxy) phenylhydrazone (FCCP) (500 nM) and Rotenone/Antimycin A

(1 μM) were added consecutively followed by three measurement cycles (3 x 6 min) before the next compound addition. The data was analyzed using the suitable supplier's Wave software and the OCR and ECAR were normalized to the third measurement right before addition of BAY-876 (18 min after beginning of the experiment). *This experiment was performed by Julian Wilke.*

7.2.3.14 Rescue experiment

DLD-1 or HCT116 cells were seeded in full medium with a density of 63,000 cells/well (48 h of treatment) or 31,500 cells/well (24 h of treatment) in a 12-well cell culture plate for mRNA expression analysis (chapter 7.2.4.3) and with a density of 30,600 cells/well (24 h of treatment) or 15,300 cells/well (48 h of treatment) in a 6-well cell culture plate for immunoblot analysis (chapter 7.2.4.4). The cells were incubated for 24 h at 37 °C with 5% CO₂ in humidified atmosphere (chapter 7.2.3.3). The medium was removed, the cells were washed once with prewarmed glucose- and glutamine-free medium and treated with the compound (RPMI1640 medium) or different glucose concentrations (DMEM medium) for the indicated time. The cells were harvested for mRNA expression analysis (chapter 7.2.4.3) or for immunoblot analysis (chapter 7.2.4.4).

7.2.3.15 GLUT-1-4 overexpression in CHO cells

CHO cells were seeded with a seeding density of 100,000 cells/mL in a 10 cm cell culture dish (10 mL) and allowed to attach overnight at 37 °C with 5% CO₂ in humidified atmosphere (chapter 7.2.3.3). Transient transfection with the different GLUT isoforms 1-4 was performed using the respective plasmids (chapter 7.2.1.3) and Lipofectamine® 3000 as the manufacturer instructed. Briefly, 100 μg plasmid DNA was mixed 1:2 with Lipofectamine® in OptiMEM™ and added to the monolayer cultured CHO cells. Cells that were transfected with the insulin-responsive GLUT-4 isoform were treated with 100 $\mu\text{g}/\text{mL}$ insulin. The cells were incubated for 48 h and reseeded at 40,000 cells/ well in 96-well plates to perform the resazurin-dependent 2-DG uptake assay (chapter 7.2.3.7) or lysed to monitor the protein expression level by means of immunoblotting (chapter 7.2.4.4). *This experiment was performed by Dr. George Karageorgis.*

7.2.3.16 WST-1 assay

The WST-1 assay is based on the detection of the cleavage of the tetrazolium salt WST-1 to formazan by mitochondrial dehydrogenase. Thereby, the metabolic viability of cells can be assessed. Cells were seeded with 5,000 cells/well in a clear 96-well cell culture plate and incubated for 24 h at 37 °C, 5% CO₂ in humidified atmosphere (chapter 7.2.3.3). As control, cell-free wells were implemented and treated accordingly to the cells. After the indicated treatment duration, 10 µL WST-1 reagent was added to the cells and after 10 min (glucose concentrations) or 30 min (compound treatment) incubation at 37 °C the absorbance of the formed formazan dye was monitored spectrophotometrically at 450 nm using the plate reader DTX 880 (Beckman Coulter) or Infinite® M200 (Thermo Scientific). The background at 620 nm (reference wavelength) for all wells and 450 nm (cell-free wells) were subtracted from all values. The absorbance was normalized to the values of DMSO-treated cells and plotted against the compound/glucose concentration.

7.2.3.17 Real-time live-cell imaging

Cells were seeded with the indicated seeding density in a 96-well cell culture plate and incubated for 24 h at 37 °C with 5% CO₂ in humidified atmosphere (chapter 7.2.3.3). Cells were washed with prewarmed, sterile PBS before compound addition in the respective medium. In case of altered nutrient concentrations, glutamine- and glucose-depleted DMEM medium was supplemented with the desired nutrient concentration without the addition of sodium pyruvate. Unless otherwise indicated, 100 µL medium were used during cell treatment with the exception of the experiment determining the glutamine dependence of HCT116 cells, in which 200 µL of medium were used. Cell growth was monitored in real-time for 48 h to 120 h by means of the IncuCyte® ZOOM or IncuCyte® S3. To evaluate cell growth behavior, the image-based cell confluence was analyzed using the provided software IncuCyte® ZOOM 2016B or IncuCyte® S3 2017A.

7.2.3.18 Apoptosis induction during live-cell imaging analysis

To monitor apoptosis induction during live-cell imaging (chapter 7.2.3.17), the green Caspase-3/7 reagent (2.5 μM) was added together with the compound to the cells. The reagent is a DNA-intercalating dye coupled to a peptidic sequence which is cleaved by caspases 3 and 7 that are activated during onset of apoptosis. The cleaved dye can intercalate into the DNA, which results in green fluorescent nuclei. To assess the level of apoptotic cells, the image-based cell confluence as well as the green fluorescence confluence was determined using the provided software IncuCyte® ZOOM 2016B or IncuCyte® S3 2017A. The *green confluence* (%) was normalized to the overall *cell confluence* (%).

7.2.3.19 3D vs. 2D cell culture

HCT116 cells were seeded with a cell density of 750 cells/200 μL /well (to obtain 380 μm \varnothing spheroids) or 10,000 cells/200 μL /well (for 800 μm \varnothing spheroids) in monolayer or in ultra-low attachment (ULA) plates for spheroid generation using prewarmed full DMEM medium (chapter 7.2.3.3). Half of the medium of the large spheroids (and respective monolayer control) was exchanged for 100 μL fresh, prewarmed full medium after 48 h of incubation at 37 °C with 5% CO_2 in humidified atmosphere. Spheroids and monolayer-cultured cells were treated 72 h after seeding with compound or different glucose and glutamine concentration (DMEM medium, w/o phenol red) and in the presence of 0.02 mg/mL propidium iodide to monitor cell death. To ensure the correct nutrient concentration in the medium, 100 μL old medium was exchanged six times against 100 μL fresh medium with the desired final nutrient concentration. Compound addition in full medium was performed by exchanging 100 μL old medium against 100 μL fresh medium containing 2x the final concentration of the compound. Live-cell imaging was performed using IncuCyte® S3 and quantification of cell growth and cytotoxicity (PI staining) was calculated using the respective software IncuCyte® S3 2017A. PI is a red fluorescent DNA intercalator which can only pass the porous cell membrane of dead cells. To assess the cytotoxicity of monolayer-cultured cells *red*

confluence (%) was used as a measure, whereas *bright-field objects red mean intensities (RCU)* was used to assess toxicity of spheroids. The corresponding half maximal effective concentration (EC_{50}) values were calculated using a non-linear regression fit with variable slope and four parameters (GraphPad Prism 5 or 7).

7.2.3.20 Mitochondrial toxicity assay

The utilization of galactose for glycolysis requires 2 mol ATP. Since the glycolysis yields 2 mol ATP, the net ATP yield in the presence of galactose instead of glucose is zero. Thus, ATP needs to be produced via mitochondrial oxidative phosphorylation. In the presence of mitochondrial inhibitors, the cells cannot generate ATP in the presence of galactose which makes the cells more sensitive to the inhibitor. This phenomenon was used to assess mitochondrial toxicity according to Marroquin *et al.*¹⁰¹ HCT116 cells were seeded in prewarmed, full medium with a seeding density of 5,000 cells/well and incubated for 24 h at 37 °C with 5% CO₂ at humidified atmosphere prior to treatment (chapter 7.2.3.3). The medium was removed and the cells were washed once with sterile, prewarmed PBS. Cells were treated with compound using glucose- and glutamine-free DMEM medium supplemented either with 25 mM glucose or 10 mM galactose and 4 mM *L*-glutamine. Oligomycin inhibits the mitochondrial ATP synthase and was used as a control. Cell growth was monitored by means of live-cell imaging employing the IncuCyte® ZOOM. Half-maximal growth inhibition (GI_{50}) values were generated (chapter 7.2.7.1) to compare the effects of the compounds on the cell growth.

7.2.4 Biochemical methods

7.2.4.1 Determination of protein concentrations with Bradford method

Bradford assay reagent (5x) was diluted 1:4 with ddH₂O according to the manufacturer's instructions. BSA was dissolved in the respective lysis buffer in a concentration range between

0.05-2 mg/mL for determination of a standard curve. The BSA standard solution or the sample (1 μ L) was added to 999 μ L Bradford assay reagent in a cuvette, sealed with parafilm and mixed thoroughly by inverting. The BSA standard was prepared as technical duplicates and all samples as technical triplicates. Bradford assay reagent contains Coomassie Brilliant Blue G-250 ($A_{\text{max}}=470$ nm) that binds to basic and aromatic amino acids of proteins and thereby deprotonates the dye ($A_{\text{max}}=595$ nm). Therefore, the absorbance at 595 nm is proportional to the protein content of the sample. After 5 min incubation, the absorption was measured spectrophotometrically at 595 nm. The standard absorbance curve of the BSA standard was determined and the protein concentration of the samples was calculated using the thereby generated formula. The absorbance of the samples should lie within the linear range of the BSA standard (0.05-2 mg/mL), otherwise the samples were prediluted before mixing with the Bradford assay reagent.

7.2.4.2 Determination of protein concentrations with DCTM protein assay

BSA was dissolved in the respective lysis buffer in a concentration range between 0.05-2 mg/mL for determination of a standard curve. The BSA standard or each sample (5 μ L) was added to one well within a 96-well plate (clear bottom) in technical duplicates or triplicates, respectively. Reagent S (20 μ L) was added to reagent A (980 μ L) to generate working reagent A. Working reagent A (25 μ L) was added to each well, followed by addition of 200 μ L reagent B. The plate was incubated for 20 min in the dark before the absorbance was measured spectrophotometrically at 750 nm. The standard absorbance curve of the BSA standard was determined and the protein concentration of the samples was calculated using the thereby generated formula.

7.2.4.3 Reverse transcription-quantitative PCR (RT-qPCR)

After treatment for the indicated time points (chapter 7.2.3.14), total RNA was isolated from DLD-1 or HCT116 cells using RNeasy® mini kit (Qiagen) according to the manufacturer's instructions and eluted using RNase-free water. One random replicate of DLD-1 treated cells was analyzed for its RNA integrity using the Bioanalyzer (Agilent) and the corresponding RNA 6000 nano kit

(Agilent) to ensure a high quality of the sample. Here the manufacturer's instructions were followed precisely using 625 µg sample. The RNA Integrity Number (RIN) provides an objective measure (RIN=0-10) for the integrity of the RNA within the sample. A RIN value ≥ 7 represents sufficient quality of the sample with 10 indicating highly intact RNA. The assessment of the integrity is based on the ratio of the ribosomal 18S and 28S bands as well as evaluation of the signal intensity of the background. The QuantiTect® reverse transcription kit (Qiagen) was used to eliminate genomic DNA and reverse transcribe the RNA in the corresponding cDNA and the instruction of the manufacturer were followed. Before reverse transcription of the samples, linear cDNA synthesis was assured using different concentrations of isolated RNA of untreated DLD-1 cells. For reverse transcription, equal RNA amounts (226-911.6 ng) were used within one biological replicate. The final concentration depended on the sample with the lowest RNA concentration. Before RT-qPCR was conducted, the dynamic range of the primers in RT-qPCR was assured using a serial dilution of cDNA (8.3 fg/µL-83.3 ng/µL) of untreated DLD-1 cells. Furthermore, the primer efficiency was tested by conducting the RT-qPCR with different concentrations (0.0005-50 ng/µL) of either cDNA of untreated DLD-1 cells or, in case of too low mRNA levels (*GLUT2* and *GLUT4*), of gene-specific plasmids (chapter 7.2.1.3). The determined primer efficacies are given in chapter 7.2.1.4. Additionally, the reverse and the forward primers of one primer pair were titrated against each other in a RT-qPCR using cDNA of untreated DLD-1 cells to determine the best concentration for each primer where no additional amplicon products were generated. The final primer concentration for all in here utilized primers was 0.5 µM. The amplicon sizes were verified using a 3% (w/v) agarose gel and employing the DNA ladder 1 kb or 100 bp plus as size standard control. For all conducted RT-qPCRs, a master mix which included 5 µL SsoAdvanced™ SYBR® green mix (Bio-Rad), 0.5 µL forward and 0.5 µL reverse primer and 1 µL RNase-free water (per sample/well) was mixed beforehand and pipetted to the qPCR plates before 3 µL cDNA sample (diluted 1/6) was added to each well. The plates were sealed with PCR Sealers™. After short mixing and centrifugation for 10 sec, the RT-qPCR was conducted using the thermal cycler iCycler

iQTM5 (Bio-Rad). The RT-qPCR program included an activation step of the polymerase (30 sec, 95 °C), followed by 50 iterative cycles including a denaturation step (10 sec, 95 °C) and an annealing/extension step (30 sec, 60 °C). Data was analyzed using CFX Manager (Bio-Rad). *GLUT1-4* and *B2M* levels were normalized to mRNA levels of *ACTB*, *TUBB* and *ATP1A1* using the method $\Delta\Delta C_t^{102}$.

7.2.4.4 Immunoblotting

General: Samples were diluted 4:1 in 5x SDS sample buffer. For protein separation, 6% (w/v) SDS gels were prepared and the separation was conducted at a constant voltage of 80 V for about 1.5 h using SDS running buffer. ChameleonTM duo pre-stained protein ladder or PAGE RulerTM plus prestained protein ladder served as size standard control. The SDS gel, Whatman® paper and a methanol-activated polyvinylidene difluoride (PVDF) membrane were incubated for 10 min in transfer buffer at 4 °C: The proteins were transferred from the SDS gel on the PVDF membrane using a semi-dry electrophoretic device. Protein transfer was verified by staining the PVDF membranes with Ponceau S for 30 sec, followed by washing with ddH₂O until the solution became colorless. The membrane was loaded in a 50 mL tube and unspecific binding sites were blocked using 10 mL PBS-based Odyssey® blocking buffer for 1 h at ambient temperature under constant rotation. GLUT isoforms or reference proteins were detected using specific primary antibodies, which were diluted in Odyssey® blocking buffer beforehand (chapter 7.2.1.2). Detection of reference proteins Na⁺-K⁺-ATPase (GLUT-1) or Vinculin (GLUT-3) served as internal normalization when possible (chapter 7.2.1.2). The membranes were incubated with the primary antibody overnight at 4 °C under constant rotation. The antibody solution was collected, stored at -20 °C and was used up to three times. The blot was washed thrice with PBS for 10 min at room temperature under constant rotation. The secondary, infrared dye-labeled antibodies were used for detection. 800CW-labeled antibodies were used to detect the protein of interest, whereas 680RD-labeled antibodies were used to detect the reference protein. The secondary antibodies were diluted in Odyssey® blocking buffer (chapter 7.2.1.2) and incubated for at room temperature

under constant rotation in the dark. After 1 h, the secondary antibody was removed and the membrane was washed twice with 10 mL PBS-T and once with 10 mL PBS for 10 min at room temperature and constant rotation in the dark. The detection of the fluorescent bands was conducted using Odyssey® CLx imaging system. Densitometric analysis for protein quantification was performed using Image Studio Ver. 5.2.

GLUT-1-4 overexpression in CHO cells: The transiently transfected CHO cells (chapter 7.2.3.15) were lysed using 1.5x SDS sample buffer without supplementing bromophenol blue and the protein concentration was determined by means of DC™ protein assay (chapter 7.2.4.2). The proteins underwent separation by means of SDS-PAGE followed by semi-dry mediated transfer on PVDF membranes. Unspecific binding sites were blocked using 5% (w/v) skimmed milk in TBS-T for 1 h at ambient temperature. Incubation of the primary antibody was performed at 4 °C overnight. After washing the membranes thrice with TBS-T, the secondary horseradish peroxidase-labeled antibody was applied and incubated for 1 h at room temperature. Visualization of specific protein content was conducted using SuperSignal™ west pico chemiluminescent or femto maximum sensitivity substrate using the Odyssey® Fc imaging system. Quantification of protein content was performed by means of densitometric analysis using the software Image Studio Ver. 5.2. *This experiment was performed by Dr. George Karageorgis.*

7.2.5 Methods to study target engagement of small molecules

7.2.5.1 Cellular Thermal Shift Assay (CETSA®) and Thermal Proteome Profiling (TPP)

SW480 cell lysates were thawed on ice (chapter 7.2.3.6) and diluted with lysis buffer to a protein concentration of 2 mg/mL with 3 mL total volume using lysis buffer with 0.4% (v/v) NP-40 alternative. The lysates were divided into two separate reaction tubes (1.4 mL each). One fraction was treated with the compound, the other fraction was treated with the equivalent amount of

DMSO. The lysates were incubated for 10 min at ambient temperature and divided into 10 different fractions with 120 μL each (20 fractions total). Each compound-treated lysate fraction was exposed to a different temperature within a temperature gradient between 36.9 and 67 $^{\circ}\text{C}$ for 3 min followed by an infinite cooling step at 4 $^{\circ}\text{C}$. DMSO-treated control lysates were subjected to the same temperature gradient. Unfolded, aggregated proteins were separated by ultracentrifugation (100,000 \times g, 4 $^{\circ}\text{C}$, 20 min). The soluble fraction (100 μL) was transferred to a fresh protein low-binding tube and snap frozen in liquid nitrogen and stored at -80 $^{\circ}\text{C}$ until further usage.

CETSA[®]: If necessary, the cell lysates were thawed on ice and 25 μL lysate was separated on an SDS-PAGE followed by transfer and immobilization to the PVDF membrane (chapter 7.2.4.4). The amount of soluble proteins was assessed by means of immunoblotting with the desired antibodies (chapter 7.2.1.2). After densitometric analysis, melting curves were generated by normalization to the soluble protein fractions at the first temperature (*i.e.* 36.9 $^{\circ}\text{C}$).

TPP: If necessary, the lysates were thawed on ice and the protein disulfide bridges were reduced using tris(2-carboxyethyl)phosphine (TCEP) using 7.5 μL reducing reagent solution for 1 h at 55 $^{\circ}\text{C}$. The thereby generated thiols were alkylated using 7.5 μL alkylating reagent solution followed by incubation for 30 min at ambient temperature protected from light. The proteins were precipitated using 900 μL prechilled acetone (-20 $^{\circ}\text{C}$) and the lysates were stored at -20 $^{\circ}\text{C}$ overnight. After centrifugation at 8000 \times g at 4 $^{\circ}\text{C}$ for 10 min the supernatant was removed and the pellets were dried under laminar flow at ambient temperature. The pellets were solubilized in 107.5 μL tryptic digest solution and vortexed vigorously. Tryptic digest was facilitated by incubation at 37 $^{\circ}\text{C}$ overnight using a thermoblock and at constant shaking (300 rpm). *Sample preparation, measurement and data analysis were performed by the mass spectrometry group of the MPI Dortmund, namely Jens Warmers, Andreas Brockmeyer, Malte Metz and Petra Janning.* Each sample was labeled with one out of ten TMT10plex[™] labeling reagents (41 μL) according to the exposed temperature within the temperature gradient using a gas-tight syringe. The samples

were mixed and incubated for 2 h at room temperature. Subsequently, the reaction was quenched with 8 μL quenching solution and incubated for 15 min at ambient temperature. All compound-treated and all DMSO-treated samples were combined, respectively and dried using a vacuum concentrator. The samples were dissolved in 120 μL 20 mM NH_4COO (pH 11) and prefractionated by means of HPLC. After evaporating the samples, the pellets were dissolved in 10 μL 0.1% (v/v) TFA using a nanoHPLC-MS/MS. Data analysis was performed by employing MaxQuant (v.1.5.3.30)⁹⁸ and an in-house programmed MS Excel macro¹⁰³ to generate the corresponding melting curves. The fitting was performed by means of Boltzmann fit.

7.2.5.2 Hexokinase activity assay

HCT116 whole cell lysates (chapter 7.2.3.6) were thawed in ice. A serial dilution between 0 mM and 15.6 mM 2-DG in assay buffer was generated freshly before the assay. All assay components were pipetted in a black, flat 96-well plate: 10 μL HCT116 lysate (conc. 0.04 mg/mL), 0.3 mM ATP, 10 μL 2-DG in respective dilution, 43 μL enzyme mix, 10 μL compound in the respective concentration and were filled up to 100 μL volume with assay buffer. The plate was incubated at 37 °C for 40 min in the dark. Fluorescence intensity of the generated $\text{NADPH}+\text{H}^+$ (ex/em 340 nm/445 nm) was measured using the Tecan Infinite® M200 or Sparks plate reader. After background subtraction (no 2-DG), all values were normalized to the highest hexokinase activity (15.6 mM 2-DG) or to the prevalent 2-DG concentration (3.1 mM) at compound addition. 3-Bromopyruvate¹⁰⁴, a known hexokinase 2 inhibitor, served as a control.

7.2.6 Compound absorbance and fluorescence spectra

The compound was diluted in ddH₂O to 100 μM and 100 μL of the solution was transferred into a 96 well plate (UV compatible). An absorbance spectrum (230 nm-1000 nm) was recorded using the Infinite® M200 spectrometer (Tecan). The background (DMSO absorbance) was subtracted from the compound absorbance values at each wavelength to generate the compound

absorbance spectrum. The emission spectrum of the compound was recorded at the respective excitation wavelength that was identified as the absorption maximum in the absorbance spectrum.

7.2.7 Data analysis

7.2.7.1 Growth curve determination during live-cell imaging analysis

To assess the growth rate of compound-treated cells, HCT116, UM-UC-3, UO-31 and MIA PaCa-2 cells were seeded in 96-well cell culture plates with a seeding density of 5,000 cells/well (chapter 7.2.3.3). DLD-1 cells were seeded with a density of 10,000 cells/well (chapter 7.2.3.3). After completion of the experiment, growth curves were determined by analyzing the cell confluence using the provided software IncuCyte® ZOOM 2016B or IncuCyte® S3 2017A (chapter 7.2.3.17). The growth rate was calculated by linear regression of the exponential growth phase (e.g. 24-74 h). The growth rates were plotted against the compound concentration to determine the half maximal growth inhibition value (GI_{50}) employing a non-linear dose-response fit (variable slope) using GraphPad Prism 5 or 7.

7.2.7.2 Validation of synergism during combinatory treatment

To validate synergism during co-treatment of Glutor and CB-839 or **(S)-5n** and Aumitin, the open-source software combenefit¹⁰⁵ was employed. Growth rates of compound-treated HCT116 cells were determined during live-cell imaging experiments and normalized to DMSO-treated cells (chapter 7.2.3.17, chapter 7.2.7.1). All models were employed to generate synergism scores over three biological replicates ($n=3 \pm s.d.$).

Definition of implemented synergy models (combenefit): a=compound A, b=compound B, a_u =concentration compound A, b_u =concentration compound B, R_{AB} =reference effect of compounds A and B, E=compound efficacy.

Loewe model:¹⁰⁶ The concentration a_u and b_u , at which the efficacy of both compounds A and B is equal, is determined to calculate the reference effect R_{AB} for the combination of the compounds.

$$R_{AB_Loewe}(a,b) = E(a_u) = E_B(b_u)$$

In case of different maximum effects of compound A and B the following extension is implemented:

$$R_{AB_Loewe}(a,b) = E(b_u) = E_B(b)$$

Bliss model:¹⁰⁷ The efficacy of compound A and B is multiplied at the concentrations to calculate the reference effect R_{AB} for the combination of the compounds.

$$R_{AB_Bliss}(a,b) = E_A(a) \times E_B(b)$$

The efficacy of compound A (or compound B) corresponds to the unaffected fraction of the cell population.

HSA model:¹⁰⁸ The greatest efficacy difference between compound A and B when given alone is determined to calculate the reference effect R_{AB} of the combination of the compounds.

$$R_{AB_HSA}(a,b) = \text{MIN}(E_A(a), E_B(b))$$

7.2.7.3 Statistical analysis

Biological replicates (n) are given as mean values \pm standard deviation (s.d.) or as median including the interquartile range. When appropriate, statistical significance was evaluated. For the rescue experiments (chapter 7.2.3.14) that included RT-qPCR (chapter 7.2.4.3) and immunoblot analysis (chapter 7.2.4.4), an unpaired two-tailed t-test with Welch's correction was employed using GraphPad Prism 5 or 7. Welch's correction was chosen due to normalization to the respective control of DMSO-treated cells and therefore assuming unequal standard deviation. *:p<0.05; **:p<0.01; ***:p<0.001. To evaluate the relation between two conditions, linear regression analysis was performed. N: technical replicates; n: biological replicates.

8 Results

8.1 Identification of small-molecule inhibitors of glucose uptake

A cell-based assay (Figure 11a) was employed to identify small-molecule inhibitors of glucose uptake from a compound library of over 150,000 substances. The library was composed of different commercially available substances as well as synthesized compounds from different academic sources. The compounds were selected according to chemical diversity and drug likeness. sp^3 -rich compounds obtained from Elderis were additionally included in the library.

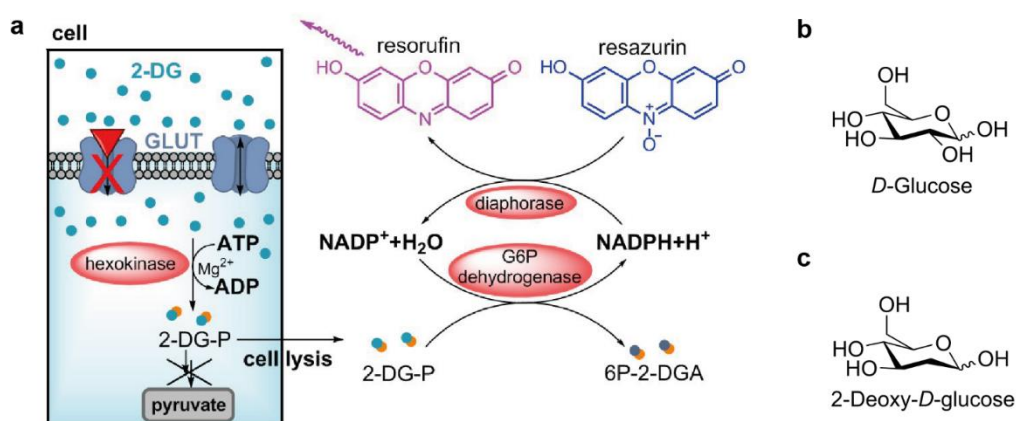


Figure 11 Schematic representation of the 2-deoxy-*D*-glucose (2-DG) uptake assay. a) 2-DG is consumed by cells via glucose transporters (GLUTs), followed by phosphorylation through the endogenous hexokinase to 2-DG-6-phosphate (2-DG-P), which is trapped inside the cells. After cell lysis, a supplemented glucose-6-phosphate dehydrogenase (G6PDH) oxidizes 2-DG-P to 6-phospho-2-deoxyglucuronic acid (6P-2-DGA) and thereby reduces $NADP^+$. Supplemented diaphorase uses the generated $NADPH+H^+$ to reduce the dye resazurin to the fluorophore resorufin. Fluorescence intensity (ex/em 530/590 nm) is directly proportional to the consumed 2-DG. Red triangle=compound. b) Structure of *D*-glucose. c) Structure of glucose analogue 2-DG.

For the assay, the human colorectal carcinoma cell line HCT116 was incubated with the glucose analogue 2-deoxy-*D*-glucose (2-DG) (Figure 11b,c) and the compound of interest. 2-DG is transported by facilitative glucose transporters (GLUTs) inside the cell followed by phosphorylation at the 6-position to 2-DG-6 phosphate (2-DG-P). 2-DG-P is trapped inside the cell and cannot be metabolized further within the glycolytic cascade. After 30 min, the compound and excessive 2-DG are removed and cells are washed and lysed. Supplemented glucose-6-phosphate

dehydrogenase oxidizes 2-DG-P to 6-phospho-2-deoxyglucuronic acid (6P-2-DGA), whereby NADP⁺ is reduced to NADP+H⁺. Diaphorase, which is added to the mixture, reduces the supplemented dye resazurin to the fluorophore resorufin in the presence of previously generated NADP+H⁺. The fluorescence intensity of resorufin is measured, which is proportional to the amount of 2-DG in the cell.

With this assay in hand, structurally distinct compound classes were identified to potently inhibit 2-DG uptake in HCT116 cells (Figure 12). The hit substances of these compound classes, namely the piperazin-2-ones, the indomorphans and the chromane-tetrahydropyriminones, possessed IC₅₀ values within the submicromolar to nanomolar concentration range.

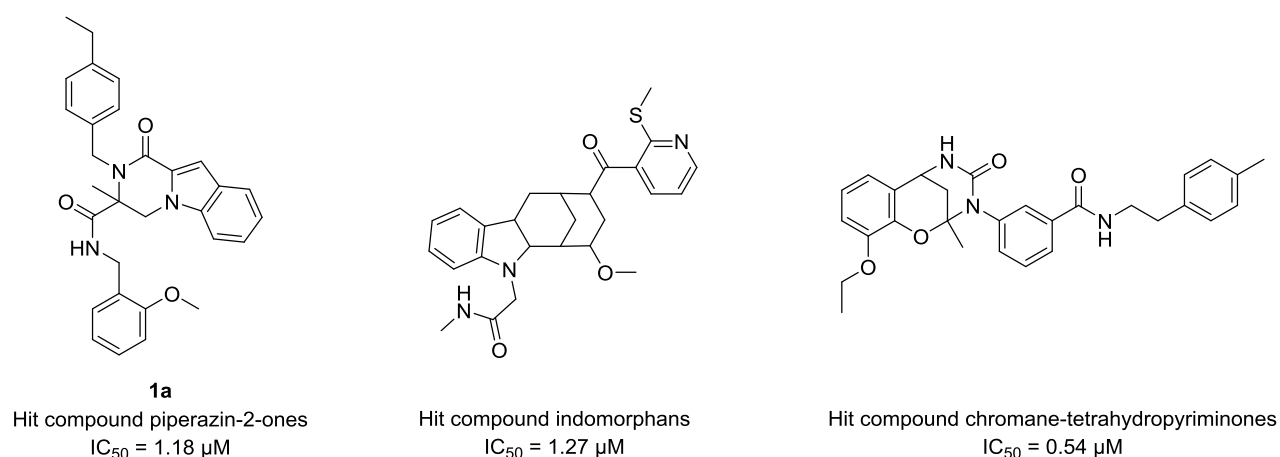


Figure 12 Chemical structures of the hit compounds identified as glucose uptake inhibitor classes. Data show the IC₅₀ values as obtained in the initial compound screening employing the semi-automated resazurin-coupled 2-DG uptake assay (n=1, N=3). The screening was performed by the Compound management and screening center (COMAS), Dortmund.

All substance classes were structurally optimized and biologically characterized further. Only part of the biological characterization of the indomorphans, with its most active derivative (+)-Glupin-1 (GLucose Uptake Inhibitor, chapter 8.4.1), and the chromane-tetrahydropyriminones, with its derivatives (*R,R*)-Chromopynone-1 and -2 (fused CHROMane- and tetrahydrOPYrimiNONE natural product fragments, chapter 8.4.2), are elucidated within the framework of this dissertation. *In depth characterization of the indomorphane substance class was conducted within the doctoral*

thesis of Dr. Javier de Ceballos and Melanie Schwalfenberg. The chromane-tetrahydropyriminones were investigated by Dr. Geroge Karageorgis.¹⁰⁹

8.2 Chemical investigation of the piperazin-2-one class

8.2.1 Confirmation of the glucose uptake inhibitory activity of 1a

The inhibition of 2-DG uptake by the hit compound **1a** was confirmed using the resazurin-coupled 2-DG uptake assay (Figure 13b). Thereby, an IC_{50} value of $588.0 \pm 143.3 \mu\text{M}$ was determined in HCT116 cells, which is in line with the activity determined in the semi-automated assay ($1.18 \mu\text{M}$, Figure 12).

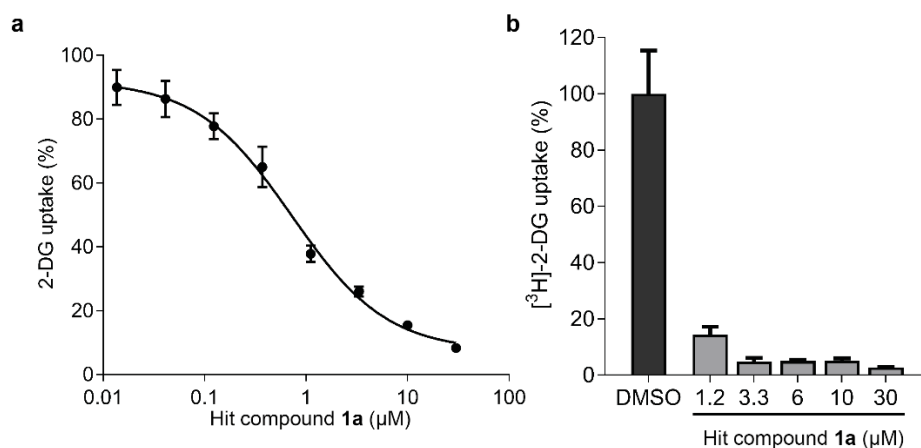


Figure 13 Confirmation of 2-DG uptake inhibition by hit compound 1a. a) Hit compound **1a** inhibits 2-DG uptake in the resazurin-coupled assay in HCT116 cells. Data are representative values \pm s.d. of $n=3$ ($N=3$). b) Hit compound **1a** inhibits $[^3\text{H}]-2\text{-DG}$ uptake. Radioactivity was assessed in HCT116 cells using a scintillation fluid and monitored using a scintillation counter. Shown are mean values \pm s.d. of $n=2$ (30 μM) or $n=1$ (1.2, 3.3, 6, 10 μM) in technical duplicates.

Furthermore, an orthogonal assay monitoring the uptake of $[^3\text{H}]-2\text{-DG}$ was employed to confirm the inhibition of glucose uptake (Figure 13c). The hit compound **1a** inhibited the uptake of $[^3\text{H}]-2\text{-DG}$ down to about 20% residual uptake at low micromolar concentrations. Moreover, **1a** did not

Results

reduce the viability of HCT116 cells after 30 min compound incubation as monitored by a CellTiter-Glo® counterscreen to exclude a cytotoxic effect.

A reduction of the resorufin emission in the employed 2-DG uptake assay (Figure 13a) or a decrease in radioactivity in the [³H]-2-DG uptake assay (Figure 13b) can also arise from an inhibitory effect on the endogenous hexokinase (Figure 11a). Therefore, an assay monitoring the endogenous hexokinase activity within HCT116 whole cell lysates was employed (Figure 14a, Figure 14b).

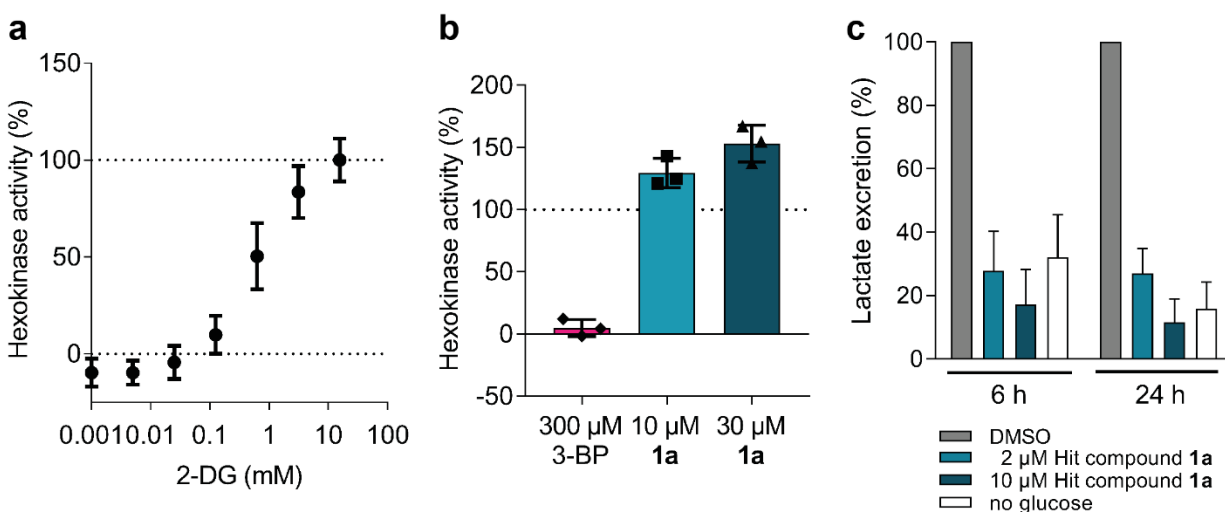


Figure 14 Hit compound 1a did not inhibit endogenous hexokinase activity and lowers lactate excretion in HCT116 cells. a,b) Endogenous hexokinase activity was monitored in the absence (a) or in the presence of the hit compound **1a** (b) using whole HCT116 cell lysates. 2-DG was added to the lysates and NADPH+H⁺ production through supplemented glucose-6-phosphate-dehydrogenase was monitored at ex/em 340/445 nm after incubation at 37 °C for 40 min. Hit compound **1a** or the hexokinase 2 inhibitor 3-bromopyruvate (3-BP)¹¹⁰ were added at 3.12 mM 2-DG (b). Data are mean values ±s.d. (n=3, N=3). Data is normalized to the highest hexokinase activity at 15.56 mM 2-DG (a) or to 3.12 mM 2-DG (b). c) To monitor lactate excretion after compound treatment, HCT116 cells were starved of glucose for 12 h followed by treatment with the hit compound **1a** in the presence of 2 mM glucose or in glucose absence. The supernatant was assayed for the presence of lactate using Amplitude™ fluorometric L-lactate assay kit (AAT Bioquest). Fluorescence was monitored at ex/em 540/590 nm. DMSO served as controls. Data show mean values ±s.d. (n=3, N=3).

While conversion of 2-DG to 2-DG-6-phosphate (2-DG-6P) by hexokinase increased with rising 2-DG concentration (Figure 14a), the presence of 10 μM or 30 μM **1a** did not lower hexokinase activity (Figure 14b). A slight signal increase can be explained by the autofluorescence of **1a**. The compound has an absorption peak at 312 nm and an emission peak (ex 312 nm) at 364 nm

(Appendix, Figure 88a). 3-Bromopyruvate, a known hexokinase 2 inhibitor¹¹⁰, abolished hexokinase activity in this assay.

Aerobic glycolysis leads to pyruvate formation which is fermented to lactate and subsequently excreted in the extracellular environment (chapter 5.2). To ensure downstream inhibition of glycolysis, **1a** was tested in a lactate excretion assay using HCT116 cells. Lactate excretion was reduced after 6 h and 24 h of compound treatment to similar levels as in glucose-starved cells, which confirms inhibition of the glycolytic pathway by **1a** (Figure 14b).

8.2.2 Synthesis of a piperazin-2-one-based compound library

For analysis of the underlying structure-activity relationship for 2-DG uptake inhibition of the piperazin-2-one-based compound class, a small-molecule collection was generated by collecting commercially available analogues and by employing organic synthetic strategies. The synthesis followed the general synthetic route depicted in Figure 15 that employs a modified four component Ugi reaction to form the compound core in the last step (*part of this work was performed by Marc Stroet and Jessica Nowacki as part of their graduation work or Master thesis*).⁹³

A carboxylic ester-substituted pyrazole derivative (**2a/2b**) is *N*-alkylated resulting in a mixture of constitutional isomers **3**. The desired 2-*N*-alkylated product (**3a-c**) is preferentially formed at high reaction temperatures. Subsequently, the ester is hydrolyzed under basic conditions to form the free carboxylic acids (**4a-c**). The bifunctional ketone/carboxylic acid **4a-c** is combined together with a primary amine (**9a-g**) and an isocyanide (**8a-m**) in a modified four component Ugi reaction as described by Ilyn *et al.*⁹³

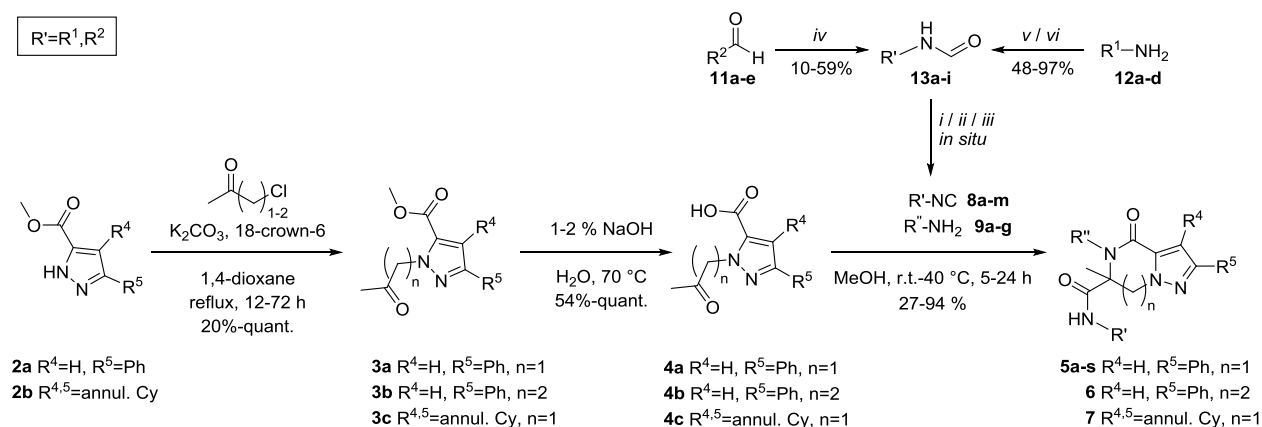


Figure 15 Overview of synthetic scheme for a piperazin-2-one-based compound library. *i*) Triphosgene, ACN, 0 °C, 0.5-2 h;⁹²; *ii*) Burgess reagent, ACN / MeOH (5:1), rt, 2 h;⁹⁴; *iii*) Benzenesulfonyl chloride, trioctylamine, 80 °C, 2 h.¹¹¹; *iv*) HCONH₂, HCO₂H, 180 °C, conventional heating 0.5-2 h or microwave 3 min;⁹²; *v*) HCO₂Et, 60 °C, 24 h;¹¹²; *vi*) HCONH₂, H₂NOH⁺HCl, toluene, 110 °C, 24 h;¹¹³. R¹=heteroaromatic, R²=alkyl, aromatic, heteroaromatic, R'=R¹, R², R''=aromatic. annul. Cy=annulated cyclohexane. An overview of all used amines and isocyanides can be found in the Appendix Table 21.

The required isocyanides were either purchased or synthesized *in situ* from the corresponding formamides (**13a-i**) by employing either Burgess reagent⁹⁴, triphosgene⁹² or benzenesulfonyl chloride¹¹¹. Hydrophobic formamides were synthesized from the corresponding aldehydes **11a-d** using a modified Leuckart-Wallach reaction.⁹² Most hydrophilic, heterocycle-containing formamides could not be synthesized using this reaction, but were generated from the corresponding primary amines **12a-c** through a transamidation reaction.^{112,114}

Derivatization of the final piperazin-2-one derivatives included *N*-methylation at the exocyclic amide of **5a** to generate **13** (Figure 16). Furthermore, the propargyl-substituted piperazin-2-one derivative **5m** was modified via click reaction with different azides to yield compounds **14** and **15** (Figure 17).

Results

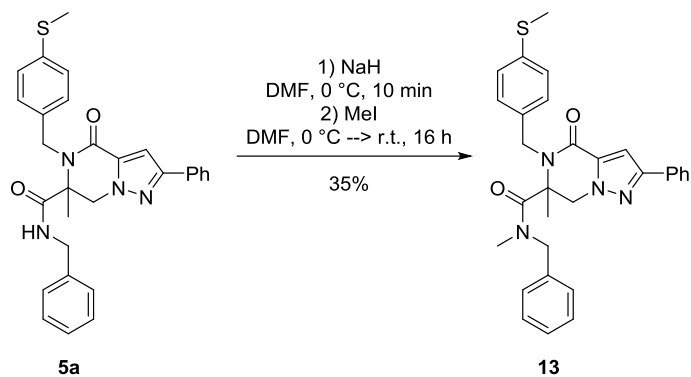


Figure 16 Derivatization I for generation of *N*-methylated piperazin-2-one derivative **13**.

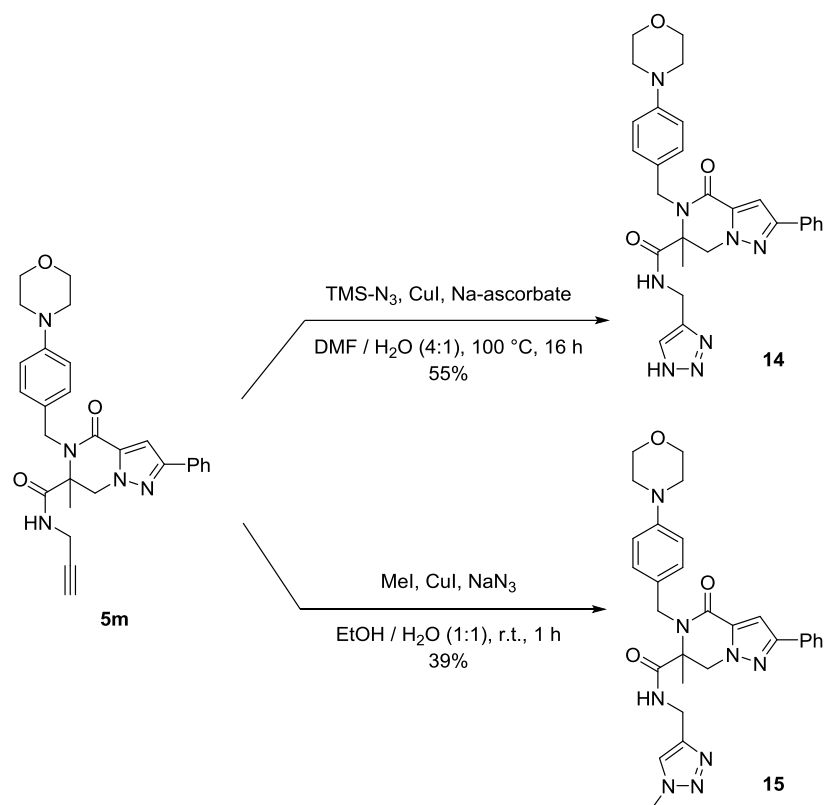


Figure 17 Derivatization II for generation of triazole-substituted piperazin-2-one derivatives **14** and **15**.

Deprotection of the *tert*-butyl-substituted piperazin-2-one derivative **5l** yielded the free amine **16**.

This was further substituted using a chloro-substituted pyridine to yield **17** (Figure 18). The final

piperazin-2-one-based compound library was composed of 95 structurally distinct molecules (Appendix, Table 22, Table 23).

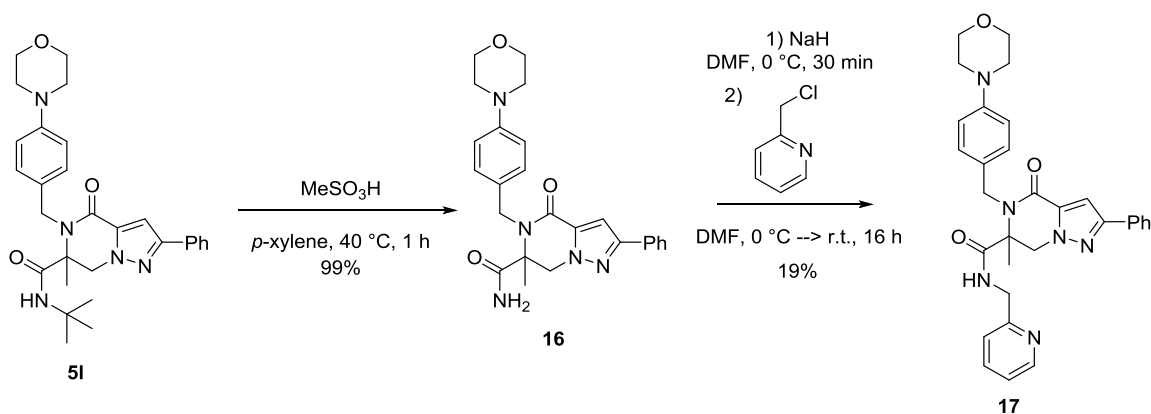


Figure 18 Derivatization III for generation of the free amine piperazin-2-one 16 and the 2-pyridine substituted piperazin-2-one 17.

8.2.3 Structure-activity relationship (SAR) studies of the piperazin-2-ones

In order to investigate the structure-activity relationship (SAR) of the piperazin-2-one substance class, a total of 27 analogues were synthesized as described earlier. Additionally, 68 analogues were obtained commercially (ChemDiv, USA).

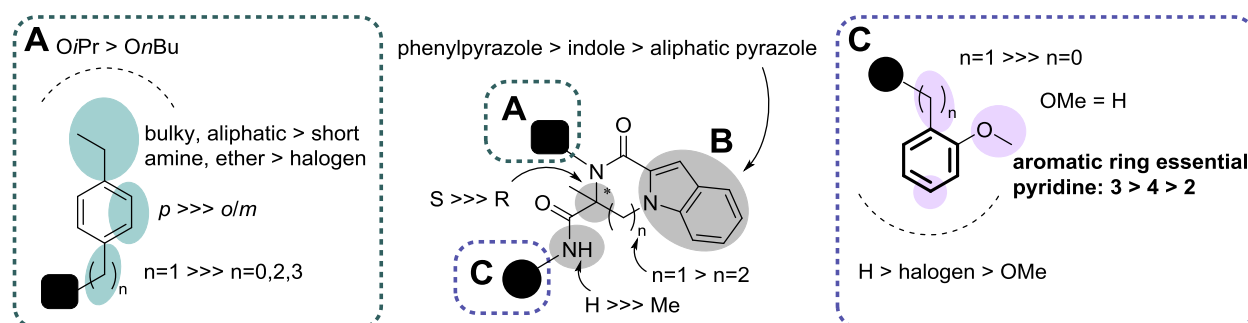


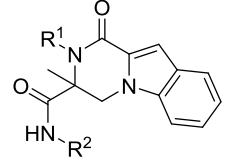
Figure 19 Summary of structure-activity relationship (SAR) for the piperazin-2-one inhibitor class. A condensed SAR is visualized on the structure of hit compound 1a. Circles describe variation in the chemical structure. Black square A indicates the substitution of the cyclic amide, black circle C indicates the substitutions on the exocyclic amide. B marks the central core of the piperazin-2-one derivative.

Results

To ensure consistency, the activity of all analogues was determined employing the semi-automated resazurin-coupled 2-DG uptake assay using HCT116 cells (Appendix, Table 22 and Table 23; *the screening assay results were obtained by the Compound Management and Screening Center (COMAS), Dortmund*). The SAR is summarized in Figure 19.

Investigation of the *N*-benzyl amide **A** of the hit compound **1a** ($IC_{50}=3.29\pm 2.04\ \mu\text{M}$) revealed that replacement of the 4-ethyl substituent by 4-methoxy (**1c**) did not alter the biological activity ($IC_{50}=3.67\pm 1.40\ \mu\text{M}$) (Table 3, compare entry 1 and 3), whereas substitution of the 4-ethyl to a 4-methyl (**1b**) reduced the IC_{50} to $10.7\pm 5.92\ \mu\text{M}$ (Table 3, compare entry 1 and 2). Introduction of the methoxy group in 3- (**1d**) or 2-position (**1e**) led to a ca. 7-fold activity reduction ($IC_{50}=25.6\pm 4.37\ \mu\text{M}$) or complete inactivation of the compound (Table 3, compare entry 3 with entry 4 and 5). Replacement of the substituent in 2-, 3- or 4-position by a chloride or fluoride led to activity loss of the compound in all cases (Table 3, compare entries 1-5 with entries 6-9). Also, exchange of the *N*-benzyl **A** (**1a**) by an *N*-CH₂-(2-furyl) (**1j**) or a *N*-CH₂-(3-pyridyl) (**1k**) reduced the biological activity by nearly 10-fold (Table 3, compare entry 1 with entries 10-11). Replacement of the *N*-benzyl **A** (**1a**) by an *N*-phenyl (**1l**) led to complete loss of activity (Table 3, compare entry 1 and entry 12). Also, compounds that contain long linkers between the nitrogen and a phenyl-group, namely C₂H₄ (**1m**) or C₃H₆ (**1n**), possessed no biological activity (Table 3, entries 13 and 14).

Table 3 Structure-activity relationship (SAR) of the indole-based compound collection.

	Structure-activity relationship (SAR) of the indole-based compound collection.							
	entry	compd	R ¹	IC ₅₀ (±s.d.) ⁿ / μM	entry	compd	R ¹	IC ₅₀ (±s.d.) ⁿ / μM
	1	1a	- 4-Et-Bn	3.29(±2.04) ¹²	9	1i	- 2-Cl-Bn	n.a. ³
	2	1b	- 4-Me-Bn	10.7(±5.92) ¹⁵	10	1j	- CH ₂ -(2-furyl)	25.9(±4.10) ⁶
	3	1c	- 4-OMe-Bn	3.67(±1.40) ¹²	11	1k	- CH ₂ -(3-pyridyl)	>30 ⁶
	4	1d	- 3-OMe-Bn	25.6(±4.37) ¹²	12	1l	- 4-Et-Ph	n.a. ³
	5	1e	- 2-OMe-Bn	n.a. ³	13	1m	- C ₂ H ₄ -Ph	n.a. ³
	6	1f	- 4-F-Bn	n.a. ³	14	1n	- C ₃ H ₆ -Ph	n.a. ³
	7	1g	- 4-Cl-Bn	n.a. ³	15	1o	- 4-Et-Bn	3.64(±1.73) ¹⁸
	8	1h	- 3-Cl-Bn	n.a. ³	16	1p	- 4-Et-Bn	>30 ³

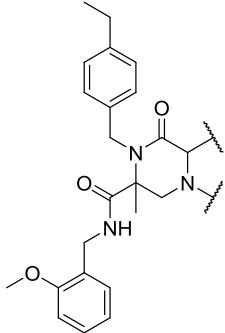
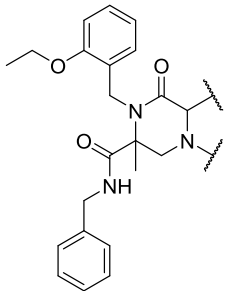
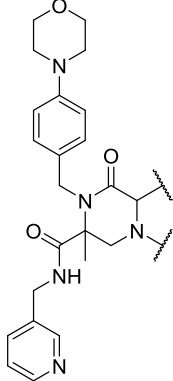
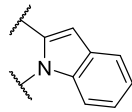
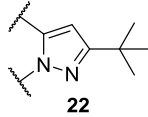
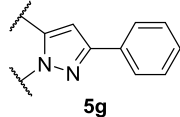
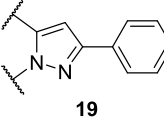
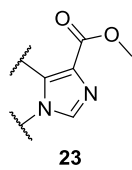
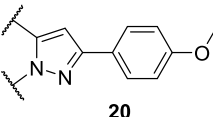
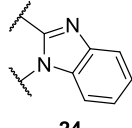
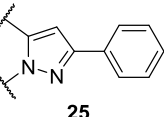
1a-n R² = -2-OMe-Bn
1o R² = -Bn
1p R² = -C₃H₆O*i*Pr

IC₅₀ values for 2-DG uptake inhibition were determined via semi-automated 2-DG uptake assay. Values are mean ±s.d. of n=3-18 (as indicated). compd=compound; n.a.=no inhibition at 30 μM.

Results

Elimination of the 2-methoxy substituent at the *N*-benzyl amide **C** (**1a**) to give the unsubstituted benzyl (**1o**) did not influence the activity of the compound ($IC_{50} = 3.64 \pm 1.73 \mu\text{M}$) (Table 3, compare entry 1 and entry 15). However, substitution of the *N*-benzyl **C** (**1a**) by a *N*- $\text{C}_3\text{H}_6\text{O}$ -*iso*-propyl ether (**1p**) rendered the molecule nearly inactive (Table 3, compare entry 1 and 16).

Table 4 Structure-activity relationship (SAR) of the piperazin-2-one core scaffold B.

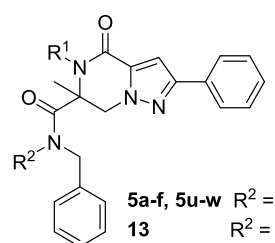
entry	cmpd	$IC_{50} \pm \text{s.d.}^n$ (μM)	entry	cmpd	$IC_{50} \pm \text{s.d.}^n$ (μM)	entry	cmpd	$IC_{50} \pm \text{s.d.}^n$ (μM)
1		5.09 ± 1.40^{15}	5		n.a. ³	10		14.04 ± 2.32^3
2		3.29 ± 2.04^{12}	6		$>30^3$	11		0.03 ± 0.01^{12}
3		0.82 ± 0.59^{18}	7		$>30^3$			
4		0.81 ± 0.28^{21}	8		15.22 ± 5.10^{15}			
			9		8.04 ± 1.47^8			

IC_{50} values for 2-DG uptake inhibition were determined via semi-automated 2-DG uptake assay. Values are mean \pm s.d. of $n=3-21$ (as indicated). cmpd=compound; n.a.=not active at $30 \mu\text{M}$.

Variation of the core scaffold **B** revealed that the phenyl pyrazole scaffold (**19**, **25**, **5g**) contributes most to the biological activity (Table 4, entries 3, 9, 11, columns are sorted by increasing activity). Hereby, the addition of a *para*-methoxy group (**20**, $IC_{50}=0.81\pm 0.28\ \mu\text{M}$) did not alter the activity of the unsubstituted phenyl **19** ($IC_{50}=0.82\pm 0.59\ \mu\text{M}$) (Table 4, compare entry 3 and 4). Annulation of the aromatic ring to the *N*-heterocycle altered the conformation in such a way that it strongly reduced the potency of the compound (Table 4, compare entries 1 and 2 with entries 3 and 4, compare entries 5 and 8 with entry 9). Substitution of the phenyl ring of **25** by an aliphatic residue, such as *tert*-butyl (**22**) or methyl-carboxylate (**23**), decreased the activity of the compound to $IC_{50}>30\ \mu\text{M}$ (Table 4, compare entry 9 with entries 6 and 7). Annulated, saturated ring structures led to a nearly 500-fold activity reduction from $IC_{50}=0.03\pm 0.01\ \mu\text{M}$ (**5g**) to $14.04\pm 2.32\ \mu\text{M}$ (**7**) (Table 4, compare entry 10 and 11). Therefore, the phenyl-pyrazole core scaffold was used for subsequent SAR studies as most active core scaffold **B**.

Further investigation of the substitution pattern of the *N*-benzyl amide (**A**) revealed, that replacement of the 4-ethyl of the 3-phenylpyrazole **1o** by either di-substituted amines (**5b**, **5c**) or ethyl ether (**5u**) did not influence the biological potency of the compound (compare Table 3 entry 15 and Table 5 entries 4, 5 and 9).

Table 5 Structure-activity relationship (SAR) of the phenylpyrazole-based compound collection I.

	entry		R ¹		IC ₅₀ (±s.d.) ⁿ / μM					
		1	5a	-	4-SMe-Bn	1.65(±1.10) ²¹	7	5e	-	4-Et-Bn
	2	(S)-5a	-	4-SMe-Bn	0.88(±0.23) ¹²	8	5f	-	4-(CCH)-Bn	6.77(±1.39) ³
	3	(R)-5a	-	4-SMe-Bn	n.a. ⁶	9	5u	-	4-OEt-Bn	0.46(±0.27) ¹⁵
	4	5b	-	4-NEt ₂ -Bn	0.33(±0.09) ³	10	5v	-	4- <i>Or</i> Bu-Bn	1.94(±1.60) ¹⁵
	5	5c	-	4-NMe ₂ -Bn	0.42(±0.27) ¹²	11	5w	-	CH ₂ -(4-OEt-Bn)	>30 ³
	6	5d	-	4- <i>Oi</i> Pr-Bn	0.19(±0.06) ¹²	12	13	-	4-SMe-Bn	n.a. ³

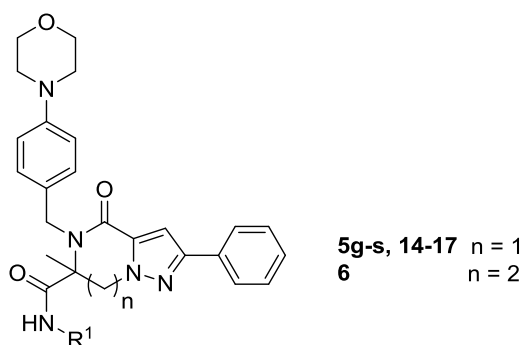
IC_{50} values for 2-DG uptake inhibition were determined via semi-automated 2-DG uptake assay. Values are mean ±s.d. of n=3-21 (as indicated). compd=compound; n.a.=not active at 30 μM.

Substitution by a thio-ether on the other hand slightly decreased biological activity by 4-fold (Table 5, compare entries 4, 5, and 9 with entry 1). More bulky substituents such as *iso*-propoxy (**5d**) or

Results

morpholino (**5n**) increased the potency of the compound by ca. 10-fold from $IC_{50}=1.65\pm 1.10\ \mu\text{M}$ to $IC_{50}=0.19\pm 0.06\ \mu\text{M}$ and $0.16\pm 0.09\ \mu\text{M}$, respectively (compare Table 5 entry 6 and Table 6 entry 13 with Table 5 entry 1). Exchange of the bulky substituents in **5d** or **5n** to linear aliphatic substituents such as *On*-butyl (**5v**) or propargyl (**5f**) decreased the activity to $IC_{50}=1.94\pm 1.60\ \mu\text{M}$ and $6.77\pm 1.39\ \mu\text{M}$ (compare Table 5 entry 6 and Table 6 entry 13 with Table 5 entries 8 and 10). Thus, the morpholino group (**5n**) was kept in 4-position of the *N*-benzyl amide **A** for further optimization studies.

Table 6 Structure-activity relationship (SAR) of the phenylpyrazole-based compound collection II.



entry	cmpd	R ¹	IC ₅₀ (±s.d.) ⁿ / μM	entry	cmpd	R ¹	IC ₅₀ (±s.d.) ⁿ / μM
1	5g	- CH ₂ -(3-pyridyl)	0.03(±0.01) ¹²	12	5m	- CH ₂ -CCH	>30 ⁶
2	(S)-5g	- CH ₂ -(3-pyridyl)	0.019(±0.002) ¹²	13	5n	- Bn	0.16(±0.09) ⁹
3	(R)-5g	- CH ₂ -(3-pyridyl)	n.a. ⁹	14	(S)-5n	- Bn	0.38(±0.12) ¹⁸
4	5h	- CH ₂ -(5-Me-3-pyridyl)	0.48(±0.09) ⁶	15	(R)-5n	- Bn	n.a. ³
5	5i	- CH ₂ -(4-pyridyl)	0.12(±0.01) ⁶	16	5o	- 4-F-Bn	2.98(±0.09) ⁶
6	17	- CH ₂ -(2-pyridyl)	21.82(±2.14) ³	17	5p	- 3-F-Bn	1.15(±0.60) ³
7	5j	- CH ₂ -(3-pyrimidyl)	4.00(±1.31) ³	18	5q	- 4-F-Ph	n.a. ⁹
8	5k	- CH ₂ -(4-3-Me-3 <i>H</i> -imidazol)	0.75(±0.02) ⁶	19	5r	- 4-OMe-Bn	19.2±(9.53) ⁹
9	14	- CH ₂ -(4-1 <i>H</i> -1,2,3-triazole)	18.0(±3.03) ³	20	16	- H	n.a. ³
10	15	- CH ₂ -(4-1-Me-1 <i>H</i> -1,2,3-triazole)	6.64(±0.91) ⁶	21	5s	- CH ₂ -(2-furyl)	1.17(±0.05) ⁶
11	5l	- <i>t</i> Bu	n.a. ³	22	6	- CH ₂ -(3-pyridyl)	1.33(±0.05) ⁶

IC₅₀ values for 2-DG uptake inhibition were determined via semi-automated 2-DG uptake assay. Values are mean ±s.d. of n=3-12 (as indicated). cmpd=compound; n.a.=not active at 30 μM.

Methylation of the exocyclic amide in **5a** (**13**) as well as enlargement of the piperazin-2-one scaffold in **5g** from a 6- to a 7-membered ring (**6**) inactivated or largely decreased the biological

activity of the compound, respectively (Table 5, compare entry 1 and 12; Table 6, compare entry 1 and 22). Thus, no further modification on the basic core structure was undertaken.

Additional fluoride substituents in 4-position (**5o**) or 3-position (**5p**) of **5n** (**C**) led to a 20-fold and 10-fold decrease in activity to $IC_{50}=2.98\pm0.09\ \mu\text{M}$ and $1.15\pm0.60\ \mu\text{M}$, respectively (Table 6, compare entries 16 and 17 with entry 13). Substitution of the 4-fluorobenzyl (**5o**) by a 4-fluorophenyl (**5q**) led to complete activity loss (Table 6, compare entry 16 and 18). Exchange of the 4-fluoride substituent (**5o**) by 4-methoxy (**5r**) led also to decreased biological activity to $IC_{50}=19.2\pm9.53\ \mu\text{M}$ (Table 6, compare entry 16 and entry 19). Exchange of the phenyl (**C**) of **5n** by the 5-membered aromatic heterocycle furyl (**5s**) led to a 10-fold decreased biological activity to $IC_{50}=1.17\pm0.05\ \mu\text{M}$ (Table 6, compare entry 13 with entry 21). Complete deletion of the benzyl (**C**) of **5n**, giving the free amide **16**, led to loss of biological activity (Table 6, compare entry 20 with entry 13). Also, introduction of aliphatic substituents such as *tert*-butyl (**5l**) or propargyl (**5m**) led to inactive or nearly inactive compounds (Table 6, compare entries 11 and 12 with entry 13).

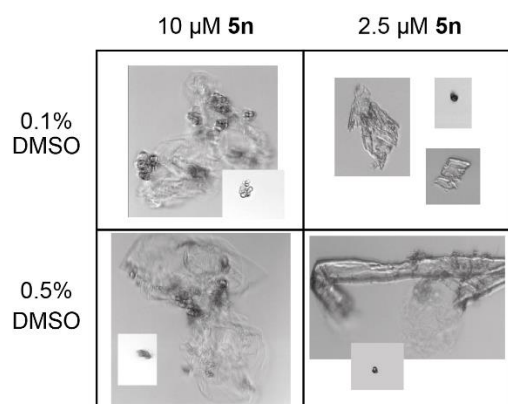


Figure 20 Precipitation of compound (**S**)-**5n**. Piperazin-2-one derivative (**S**)-**5n** was dissolved in full DMEM medium and incubated for 12 h at 37 °C to mimic conditions of cellular experiments. Magnification 20x.

Due to observed solubility problems of the most active analogue **5n** ($IC_{50}=0.16\pm0.09\ \mu\text{M}$) in aqueous cell culture media (Figure 20, (**S**)-**5n**), a nitrogen was introduced in 3-position of the *N*-benzyl amide **C** (**5g**). Notably, the 3-pyridyl did not only significantly improve the solubility of the compound, but furthermore increased the potency by nearly one order of magnitude to $IC_{50}=0.03\pm0.01\ \mu\text{M}$ to yield the most active derivative **5g** (Figure 14, compare entry 13 and entry

1). Exchange of the 3-pyridyl to a 4- (**5i**) or 2-pyridyl (**17**) reduced the potency by 4-fold and 30-fold to $IC_{50}=0.12\pm 0.01\ \mu\text{M}$ and $21.82\pm 2.14\ \mu\text{M}$, respectively (Figure 14, compare entries 5 and 6 with entry 1). A potential interaction between the nitrogen of the 3-pyridyl with the hypothesized GLUT target protein could not be stabilized by introduction of a second, adverse nitrogen to give a pyrimidyl **5j** or by introduction of an adverse methyl group (**5h**). Both structural alterations reduced the biological activity by over 10-fold (**5h**) or even over 100-fold (**5j**) from $IC_{50}=0.03\pm 0.01\ \mu\text{M}$ to $0.48\pm 0.09\ \mu\text{M}$ and $4.00\pm 1.31\ \mu\text{M}$, respectively (Figure 14, compare entries 4 and 7 with entry 1). Exchange of the 3-pyridyl (**5g, C**) against a smaller aromatic *N*-containing heterocycle (imidazole, **5k**) reduced the activity to $IC_{50}=0.75\pm 0.02\ \mu\text{M}$ (Table 6, compare entries 8 with entry 1). Reduction to $IC_{50}=18.0\pm 3.03\ \mu\text{M}$ and $6.64\pm 0.91\ \mu\text{M}$ was observed when 3-pyridyl (**5g, C**) was substituted for a triazole (**14**) or an *N*-methylated triazole (**15**), respectively (Table 6, compare entries 9-10 with entry 1).

The racemic mixture of the most active analogue **5g** was separated by means of chiral preparative HPLC and revealed that the (+)-enantiomer inhibited 2-DG uptake with an IC_{50} of $19\pm 2\ \text{nM}$, whereas the (-)-enantiomer was completely inactive at a concentration of $30\ \mu\text{M}$ (Table 6, compare entries 2 and 3 with entry 1). Analysis of the crystal structure of the (-)-enantiomer of a heavy atom-containing analogue (**R**)-**5a** unambiguously proved that the inactive enantiomer was *R*-configured (Figure 21, Table 5 entry 3). By analogy, the (+)-enantiomer was assigned an (*S*)-configuration. Hence, the most active enantiomeric derivative that was developed from the SAR studies of the piperazin-2-one substance class was (**S**)-**5g**, which was termed Glutor (GLucose Uptake inhibiTOR) (Figure 22a). In the CellTiter-Glo® counterscreen, Glutor did not reduce the viability of HCT116 cells after 30 min of treatment. In a manually performed glucose uptake assay, Glutor inhibited 2-DG uptake of HCT116 cells with high potency ($IC_{50}=10.8\pm 5.3\ \text{nM}$, Figure 22b), whereas the racemate **5g** showed a 2-fold activity reduction ($IC_{50}=21.6\pm 10.5\ \text{nM}$) as expected (Figure 22b).

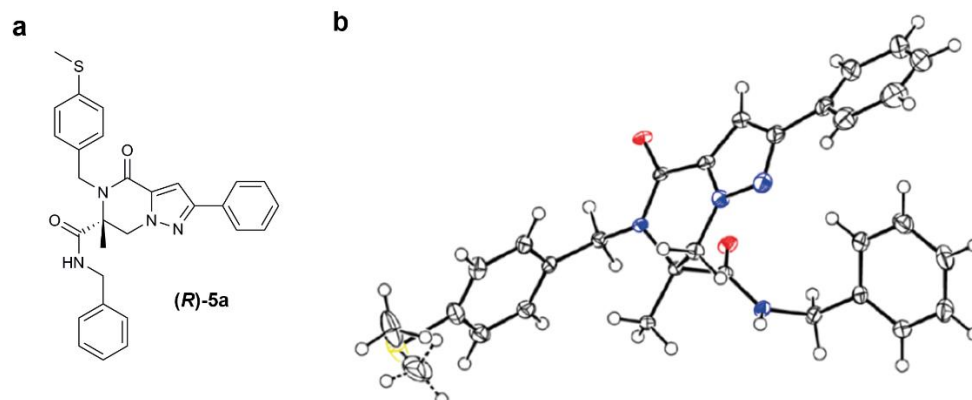


Figure 21 Crystal structure of the piperazin-2-one derivative (*R*)-5a. a) Chemical structure of compound (*R*)-5a. b) Plot for X-ray crystal structure of (*R*)-5a. Structure determination was performed by Lena Knauer, TU Dortmund.

Glutor inhibited 2-DG uptake with similar potency also in other malignant cell lines (*part of the Bachelor thesis of Aylin Binici*). MIA PaCa-2 (pancreatic adenocarcinoma) cells exhibited an IC_{50} towards Glutor of 1.07 ± 0.25 nM, UM-UC-3 (urinary bladder carcinoma) of 8.32 ± 2.04 nM and the kidney carcinoma cell line UO-31 an IC_{50} value of 3.60 ± 1.51 nM (Figure 22c).

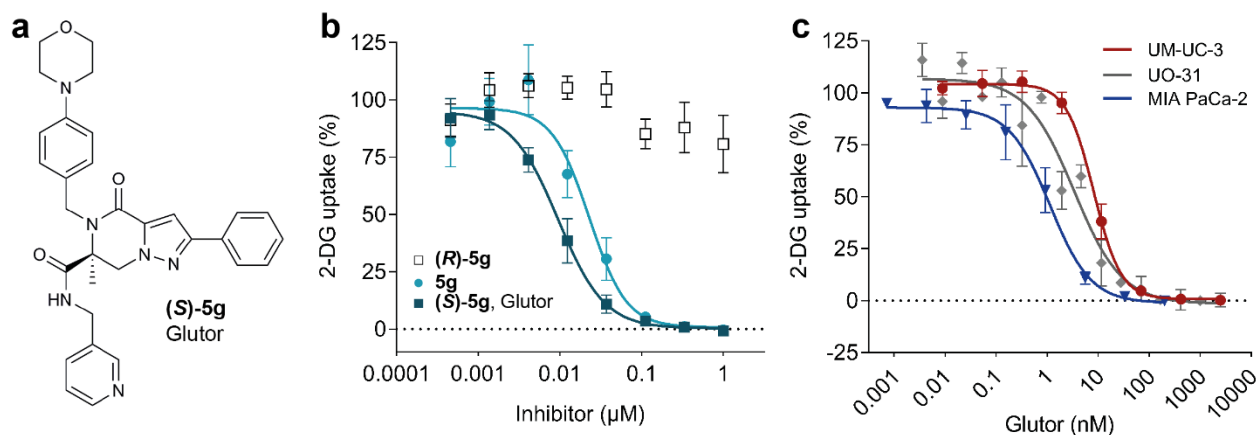


Figure 22 Glutor inhibited 2-DG uptake in different cell lines with nanomolar potency. a) Chemical structure of Glutor ((*S*)-5g). b,c) Glutor (b,c), its inactive (*R*)-enantiomer (*R*)-5g (b) and the respective racemic mixture 5g (b) were tested in the resazurin-coupled 2-DG uptake assay employing different cancerous cell lines such as HCT116 (b), UM-UC-3 (c), UO-31 (c) and MIA PaCa-2 (c). Data show mean values \pm s.d. of $n=3$ (HCT116, MIA PaCa-2, UM-UC-3) or $n=4$ (UO-31).

8.3 Biological investigation of Glutor

8.3.1 Mode of action of Glutor

As mentioned earlier, endogenous hexokinase inhibition may lead to false positive results in the resazurin-coupled 2-DG uptake assay. Therefore, Glutor was subjected to the hexokinase assay (Figure 23a,b). Glutor did not inhibit hexokinase activity in HCT116 whole cell lysates at concentrations of 10 μ M, 30 μ M and 300 μ M (Figure 23b). Treatment with a known hexokinase 2 inhibitor (3-bromopyruvate¹¹⁰) led to complete inhibition of the hexokinase (Figure 23b).

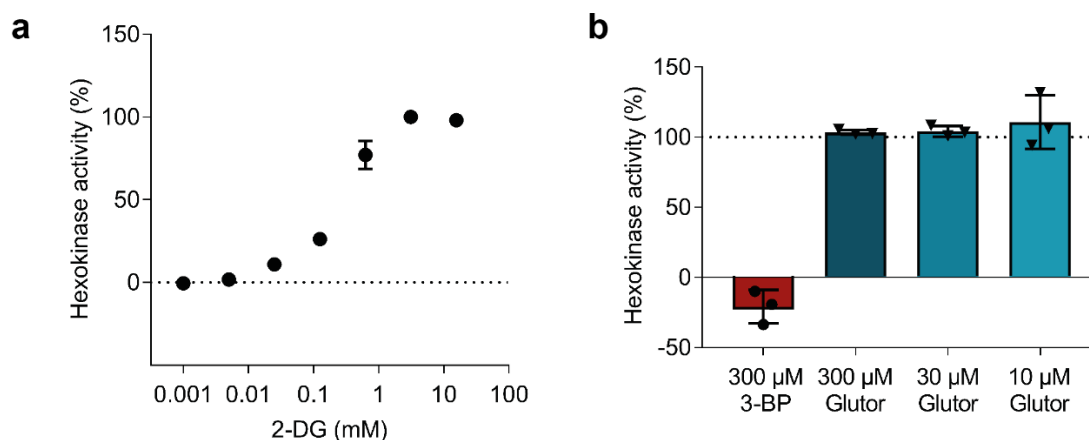


Figure 23 Glutor did not inhibit endogenous hexokinase activity in HCT116 cell lysates. NADP⁺ and glucose-6-phosphate dehydrogenase were supplemented to HCT116 whole cell lysates and NADPH+H⁺ generation was monitored at ex/em 340 nm/445 nm in the presence increasing 2-DG concentrations (a). b) Glutor or DMSO was added to the cell lysates in the presence of 3.12 mM 2-DG. 3-Bromopyruvate (3-BP)¹¹⁰ served as a control. Data is normalized to the highest concentration of hexokinase activity at 15.56 mM 2-DG (a) or the prevalent 2-DG concentration at compound addition (3.12 mM, b). Data show mean values \pm s.d. (n=3, N=3).

Further investigations revealed that Glutor inhibited glycolysis in HCT116 cells using a glycolytic stress test employing a Seahorse XFp instrument (Figure 24a). The Seahorse instrument determines the extracellular acidification rate (ECAR, Figure 24a) as a measure of glycolytic flux and the oxygen consumption rate (OCR, Figure 24b) as measure of respiration. Thereby, the cellular metabolic activity can be monitored in real-time. After glucose starvation for 1.5 h, the compound was added followed by a 30 min incubation period in analogy to the 2-DG uptake

assay. Addition of 10 mM glucose increased the ECAR in the absence of the compound. Reduction of glycolysis was observed in the presence of 50 nM Glutor and glycolytic arrest in the presence of 250 nM Glutor. At the same time, respiration decreased in the absence of the compound due to a metabolic switch from oxidative phosphorylation to glycolysis, which is not observed in the presence of 250 nM Glutor. Here, respiration was performed at a constant rate. Oligomycin inhibits the ATP synthase at the end of the respiratory chain which causes a steep decrease in OCR.¹¹⁵ In the absence of Glutor, HCT116 cells increased the glycolytic rate as soon as respiration was impeded by Oligomycin. In the presence of 50 nM Glutor glycolysis increased only slightly after addition of Oligomycin, whereas a decrease in ECAR was observed in the presence of 250 nM Glutor. Finally, the addition of 2-DG completely blocked glycolysis in HCT116 cells and did not influence OCR (Figure 24).

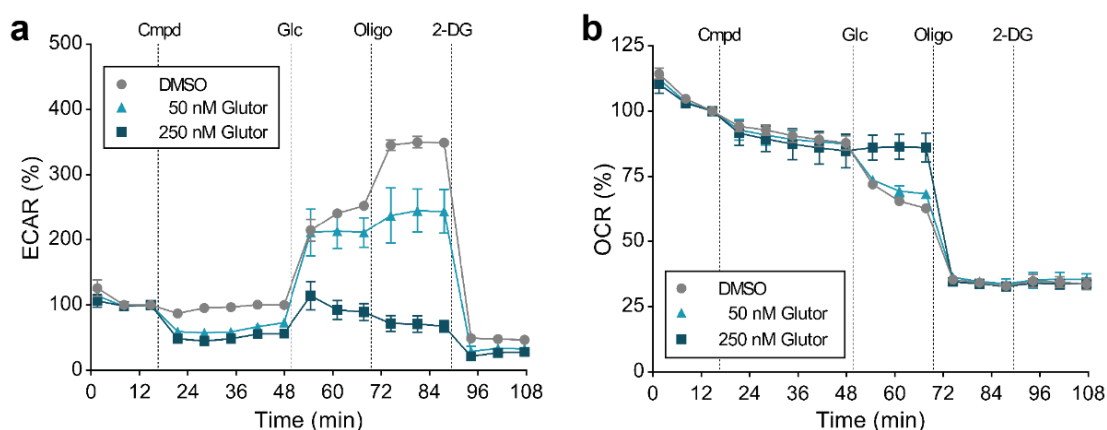


Figure 24 Glutor reduced the glycolysis rate in HCT116 cells. HCT116 cells were starved of glucose for 1.5 h and subjected to a glycolysis stress test (Seahorse XFp, Agilent). The extracellular acidification rate (ECAR, a) as measure of glycolysis and the oxygen consumption rate (OCR, b) as measure of respiration were monitored. Data show mean values \pm s.d. (n=3, N=2). Cmpd=compound, Glc=10 mM glucose, Oligo=2.5 μ M Oligomycin; 2-DG=50 mM 2-deoxy-D-glucose.

Since mitochondrial toxicity is one reason for the withdrawal of drugs from the market or failure of clinical candidates during clinical trials¹¹⁶, mitochondrial liability of HCT116 cells was assessed. A proposed routine screen described by Marroquin *et al.*¹⁰¹ involves the compound treatment of cancer cells in the presence of 25 mM glucose or 10 mM galactose (Figure 25). Since 2 mol ATP

are necessary for galactose to enter glycolysis and the ATP yield during glycolysis is also 2 mol, the net ATP of glycolysis in the presence of galactose is zero. Then, functional oxidative phosphorylation and therefore intact mitochondria are essential for cell survival. This enables the fast detection of compound-induced mitochondrial impairment. Glutor inhibits the growth of HCT116 cells equally in the presence of glucose and galactose, which excludes a mitotoxic effect (Figure 25a). In contrast, Oligomycin reduces the growth rate of HCT116 cells stronger in the presence of galactose than in the presence of glucose, which clearly demonstrates a mitotoxic effect, as expected from an ATP synthase inhibitor (Figure 25b).

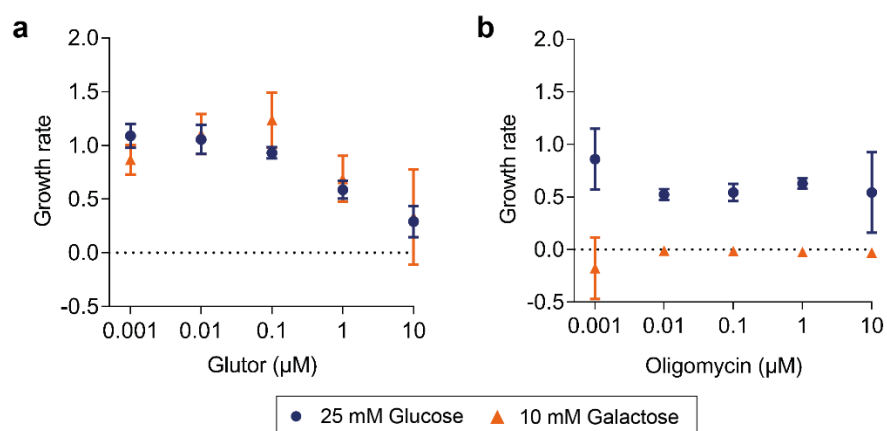


Figure 25 Glutor did not impede mitochondrial function. HCT116 cells were treated with Glutor (a) or Oligomycin (b) in the presence of either 25 mM glucose or 10 mM galactose. Growth was monitored using the live-cell imaging device IncuCyte® ZOOM. Growth rates were calculated and normalized to DMSO-treated cells. Data show mean values \pm s.d. ($n=3$, $N=3$).

8.3.2 Drug-likeness of Glutor

The drug-likeness of the chemical structure of Glutor was assessed by implementing the Quantitative Estimate of Drug-Likeness (QED) (Table 7). Glutor possessed a QED score of 0.39 (0-1), which resembles a medium-high score. This is expected from a tool compound that was structurally not optimized for lead structure and drug development. The partial contribution of the structural characteristics indicates that the values that positively influenced the QED score were the AlogP^{117} value (negative decadic logarithm of the calculate octanol-water partition coefficient,

3.32) and the amount of hydrogen bond donors (HBD, 1 hydrogen bond donor). The values that negatively influenced the outcome of the QED score were the molecular weight (MW) of Glutor (536.25 g/mol) and the aromaticity of the compound (Arom., 4 aromatic rings).

Table 7 Drug-likeness score of Glutor.

QED (0-1)	QED MW	QED ALogP	QED HBA	QED HBD	QED PSA	QED RotB	QED Arom	QED Alert
0.39	0.11	0.98	0.52	0.99	0.76	0.53	0.03	0.84
	MW (g/mol)	ALogP	HBA	HBD	PSA	RotB	AromRings	LogD
	536.25	3.32	9	1	92.59	7	4	3.32

QED = Quantitative Estimate of Drug-Likeness as described by Bickerton *et al.*¹¹⁸ All other QED values indicate the partial contribution of the characteristic to the overall QED score. A score of 1 indicates perfect drug likeness according to the aforementioned model. HBA/HBD=H-bond acceptor/donor as defined by Lipinski *et al.*¹¹⁹; AlogP=negative decadic logarithm of the calculated octanol-water partition coefficient as described by Ghose *et al.*¹¹⁷; LogD=ALogP at pH 7.4; PSA=Polar surface area as described by Ertl *et al.*¹²⁰ Arom=aromaticity; AromRings=aromatic rings; RotB=rotatable bonds; MW=molecular weights. Red-blue=low-high QED score. *The computational tool was provided by Dr. Axel Pahl, COMAS.*

8.3.3 Influence of Glutor on cancer cell growth

As the identification of glucose uptake inhibitors is relevant to cancer drug discovery, Glutor was investigated for its potential to inhibit the growth of the used model cell line HCT116 (Figure 26). Cell growth was monitored by means of live-cell imaging using the IncuCyte® ZOOM (Figure 26a). The confluence of the cells was calculated via a cell-specific algorithm that recognizes cells contrast-dependently (Figure 26b). To generate a quantitative measure of cell growth, the growth rate of HCT116 cells was calculated by linear regression of the exponential growth phase (e.g. 30-80 h). The generated growth rates were plotted against the Glutor concentration and the half-maximal growth inhibition (GI_{50}) value for HCT116 cells was determined to be $470.1 \pm 81.0 \mu\text{M}$ (Figure 26c). *Part of this work was reported in the Bachelor thesis of Aylin Binici.*

Results

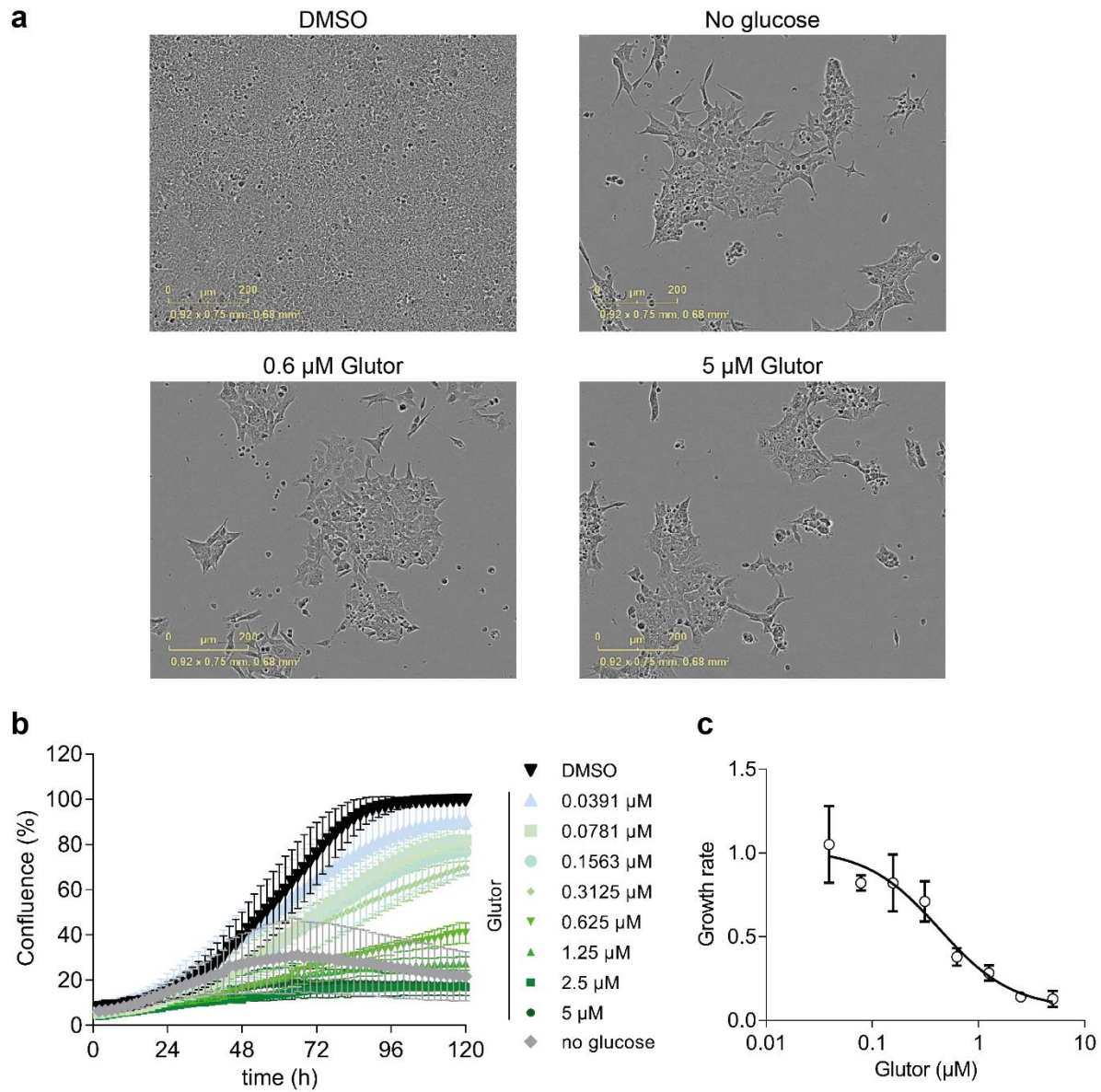


Figure 26 Glutor impaired the growth of the HCT116 cells. Cell growth was monitored via live-cell imaging over 120 h using the IncuCyte® ZOOM. Cells were treated with different Glutor concentrations in the presence of 25 mM glucose. Glucose-starved cells served (no glucose) as a control. a) Representative images of HCT116 after 96 h of treatment. b) The cell confluence was determined over the time. Data show mean values \pm s.d. (n=3, N=3). c) The slope (growth rate) of the exponential growth phase was calculated using linear regression to determine the GI_{50} value. Data show mean values \pm s.d. (n=3, N=3).

In order to investigate the impact of Glutor treatment on cancer, the growth of a panel of 94 cell lines in the presence of Glutor was explored (Figure 27).

Results

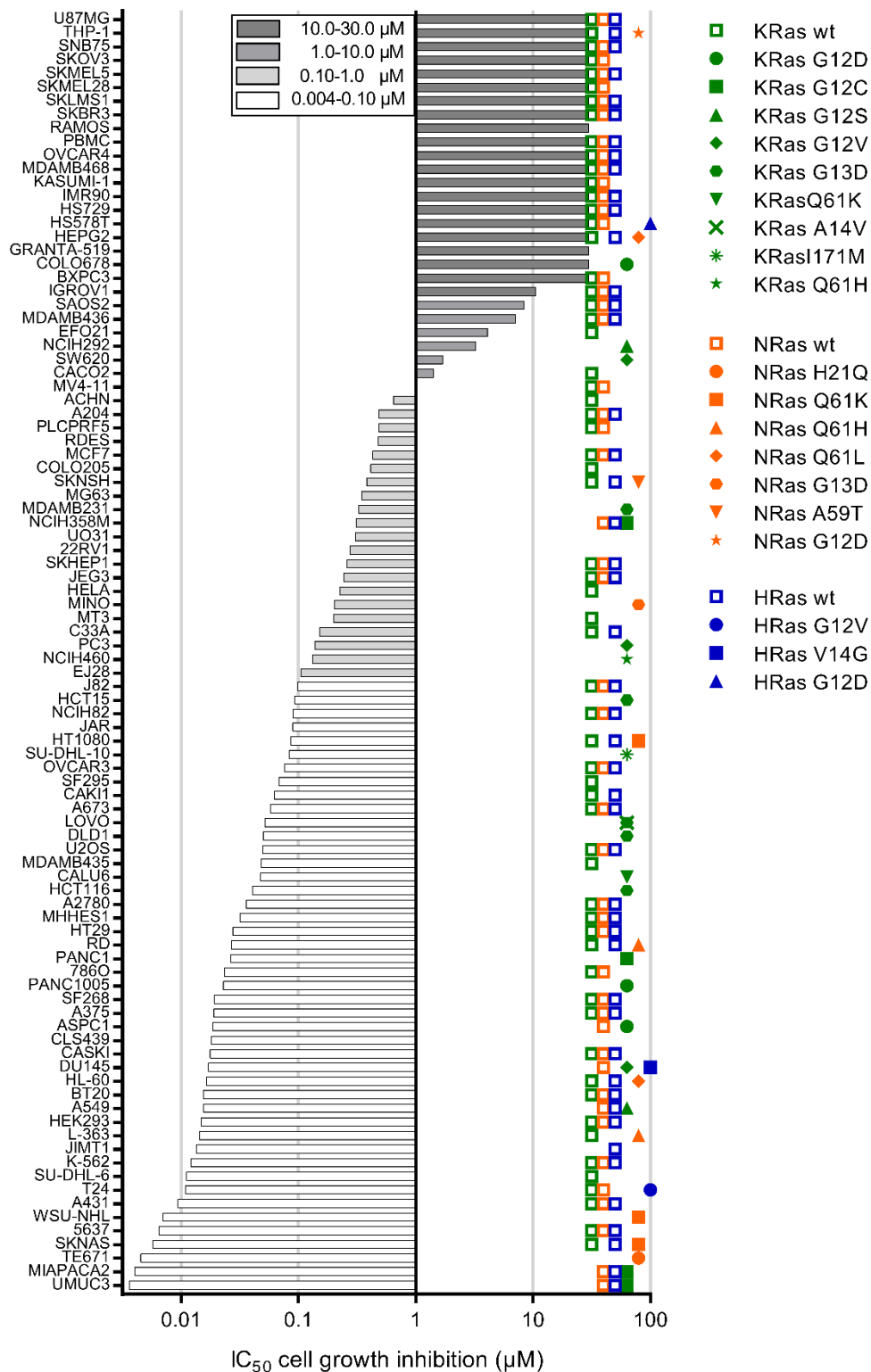


Figure 27 Growth inhibition by Glutor of various cancer cell lines. A panel of 94 cell lines was subjected to Sulforhodamine B assay after 72 h of Glutor treatment. IC_{50} values were determined after 72 h. The symbols indicate the mutational status of KRas, NRas and HRas as described in the Catalogue Of Somatic Mutations In Cancer (COSMIC)¹²¹. *Sulforhodamine B* assay was performed by Oncolead, Germany.

This cell panel included mostly cancerous human cell lines from various tissue origin as well as two non-malignant cell lines (IMR-90, HEK-293) and PBMCs. The cells were treated for 72 h with different Glutor concentrations, before protein content was determined by means of a Sulforhodamine B assay as a measure of cell viability, for IC₅₀ determination. The growth of nearly half of the cell lines was inhibited with IC₅₀ values below 100 nM Glutor concentration, 21 cell lines exhibited an IC₅₀ value between 100 nM and 1 μM, 8 cell lines showed a moderate IC₅₀ value between 1 μM and 10 μM, whereas 20 cell lines were resistant (IC₅₀>30 μM) against Glutor treatment (Figure 27).

Among the resistant cells were the non-malignant cell line IMR-90 (embryonic kidney cells) as well as non-malignant peripheral blood mononuclear cells (PBMCs). The second non-malignant cell line HEK-293 showed a high sensitivity towards compound treatment (IC₅₀=15 nM). Even though the HEK-293 cell line originates from non-malignant tissue, this cell line cannot be considered a normal cell line due to its instable genome.¹²² These genomic changes could have led to glucose addiction rendering this cell line sensitive to Glutor treatment. The cell lines that were influenced most in their viability were the urinary bladder carcinoma cell line UM-UC-3 and the pancreatic carcinoma cell line MIA PaCa-2. Both exhibit an IC₅₀ value of 4 nM. Of note, both originating tissues (pancreas and urinary bladder) were overrepresented among the cell lines with the highest sensitivity towards Glutor treatment. Also, no urinary bladder carcinoma cell line and just one pancreatic cancer cell line (BxPC-3) showed Glutor resistance. Overall, the sensitivity did not correlate with the tissue source (Appendix, Table 18), the origin (metastatic, primary tumor, Appendix, Table 18), expression level of the main upregulated GLUT isoforms in cancer, i.e. *GLUT1* and *GLUT3* mRNA expression (Figure 28) or with known driver mutations that are involved in glucose dependence (i.e. KRas).⁶²

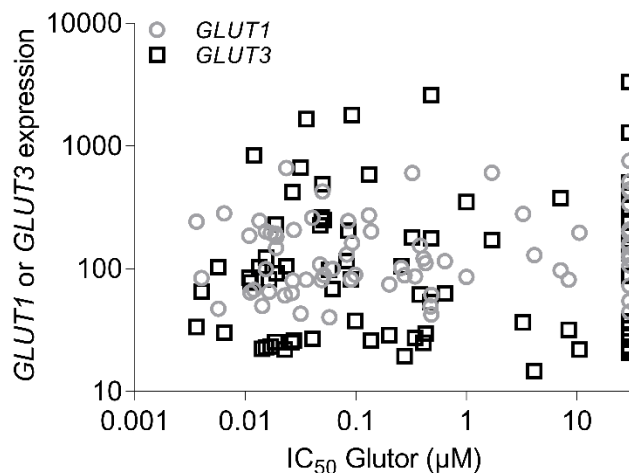


Figure 28 Glutor sensitivity did not correlate with the *GLUT1* or *GLUT3* expression level. The level of *GLUT1* and *GLUT3* were extracted from the Cancer Cell Lines Encyclopedia.¹²³ The IC₅₀ value was determined using the Sulforhodamine B assay (Figure 27).

Of note, all cancer cells within the panel that were resistant to Glutor (IC₅₀>30 µM) possess the wild type proto-oncogene GTPase KRas (KRas) (Figure 27). Hence, a mutation in KRas induced vulnerability towards glucose deprivation by Glutor. However, Glutor sensitivity did not correlate with KRas mutation since numerous sensitive cell lines express the wild type protein. KRas is involved in metabolic adaptation in cancer (Metabolic rewiring, chapter 5.4.1).^{5,124} These findings suggest that targeting glucose import may be a viable approach to inhibit cancer cell growth, especially of cancer types that possess oncogenic KRas such as pancreatic ductal adenocarcinoma (PDAC).¹²⁵ Investigation of the other Ras isoforms NRas and HRas confirmed an overrepresentation of oncogenic mutations among the Glutor sensitive cell lines. Hereby, 21 out of 44 malignant cell lines (48%) that exhibit an IC₅₀ value below 100 nM harbored a Ras mutation, whereas only 4 out of 19 malignant cell lines (21%) with an IC₅₀ value >10 µM show a mutation in one of the three Ras isoforms.

The influence of compound treatment on cell growth was further determined using kinetic live-cell analysis using IncuCyte® ZOOM (Figure 29, Table 8). The strongest growth reduction was observed for the bladder carcinoma cell line UM-UC-3 (Figure 29a, Table 8), which was in line

Results

with the results from the Sulforhodamine B assay (Figure 27). DLD-1 cells possessed an IC_{50} value of 50 nM in the Sulforhodamine B assay, which could be confirmed during live-cell analysis ($GI_{50}=30.7\pm 8.1$ nM) (Figure 29c). Slight discrepancies between the Sulforhodamine B (Figure 27, Table 8) and live-cell analysis results (Figure 29b,d, Figure 26, Table 8) were observed for the MIA PaCa-2, HCT116 and UO-31 cells. MIA PaCa-2 were inhibited with an IC_{50} of 4 nM in the Sulforhodamine B assay and possessed a GI_{50} of 58.4 ± 30.5 nM in the live-cell analysis, UO-31 an IC_{50} value of 304 nM and a GI_{50} of 14.7 ± 10.3 nM and HCT116 cells exhibited an IC_{50} value of 40 nM and a GI_{50} value of 470.1 ± 81.0 nM (Table 8). GLUT-1 and GLUT-3 protein expression was determined for selected cell lines and did not correlate with the sensitivity of the cancer cell lines as determined via Sulforhodamine B nor live-cell imaging analysis (Appendix, Figure 89).

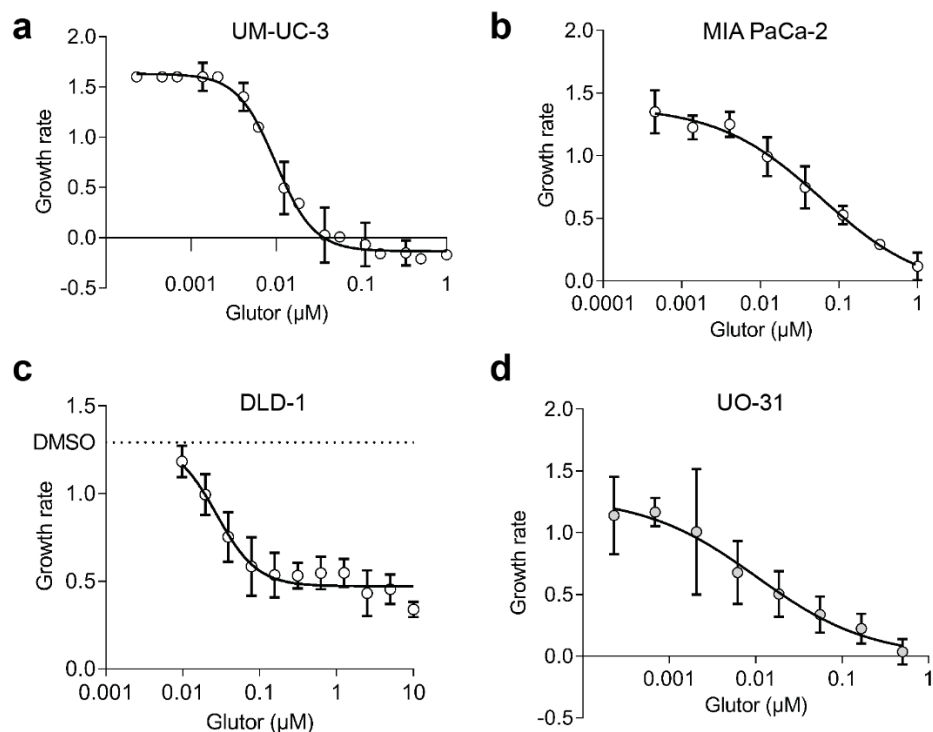


Figure 29 Glutator inhibited growth of different cancer cell lines in live-cell imaging experiments. Growth inhibition curves of UM-UC-3 (a), MIA PaCa-2 (b), DLD-1 (c) and UO-31 (d) upon Glutator treatment as monitored during live-cell imaging by means of IncuCyte® ZOOM. Data show mean values \pm s.d. of $n=3$, $N=3$ (a,c,d) and $n=4$, $N=3$ (b). Top constrain set to DMSO growth rate for DLD-1.

Table 8 Comparison between growth inhibition and 2-DG uptake assay.

Cell line	UM-UC-3	MIA PaCa-2	HCT116	DLD-1	UO-31
GI ₅₀ (nM) ⁿ IncuCyte®	10.2 ± 1.2 ³	58.4 ± 30.5 ⁴	470.1 ± 81.0 ³	30.7 ± 8.1 ³	14.7 ± 10.3 ³
IC ₅₀ (nM) SRB	4	4	40	50	304
IC ₅₀ (nM) ⁿ 2-DG uptake	8.3 ± 2.0 ³	1.1 ± 0.3 ³	3.3 ± 0.8 ⁶	35.5 ± 4.8	3.6 ± 1.5 ⁴

SRB = Sulforhodamine B assay (Figure 27). n=number of biological replicates. The GI₅₀ values and the IC₅₀ values (IncuCyte®) are given as mean values ±s.d. (n=3).

8.3.4 Glutator induces cell death in physiologically relevant spheroids

The utilization of monolayer cultured cancer cells is under debate to not adequately represent the physiological status of a disease. Therefore, alternative cell culture models such as spheroids find more recognition at early drug discovery stages. The 3D shape of the spheroid mimics the natural tumor shape more accurately and therefore gives a stronger indication for compound utilization in *in vivo* systems since compound penetration can be largely influenced in spheroids.¹²⁶ HCT116 cells were cultured as monolayer (2D) or as spheroids (3D) in the presence of different Glutator concentrations and of propidium iodide (PI) in order to monitor cell toxicity (Figure 30a). Glucose-depleted cells were used as a control. Onset of cytotoxic events (PI staining) was observed after 24 h in 2D and 3D. Formation of a necrotic core in the spheroid was observed after 48 h of Glutator treatment. Here, the diameter of the necrotic core was strongly dependent on the Glutator concentration. Spheroids treated with 1 μM Glutator and spheroids that were incubated in glucose-free environment exhibited a similar diameter of the necrotic core (Figure 30a). Quantification of PI staining was used to calculate the half-maximal effective concentration (EC₅₀) values of cell death induction (Figure 30b). The EC₅₀ values of the monolayer-cultured cells and spheroid-cultured cells were in a similar range. However, cell death induction by Glutator was slightly more effective in spheroids (81.7±3.1 nM) than in monolayer-cultured cells (EC₅₀=192.9±34.4 nM). In

conclusion, the potency of Glutor was not impaired when physiologically more relevant spheroid-cultured HCT116 cells were employed.

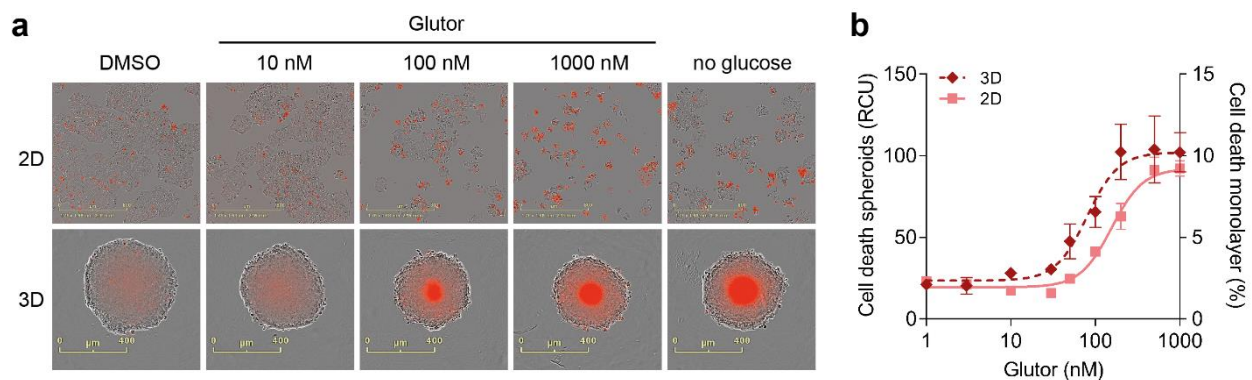


Figure 30 Glutor induced cell death of monolayer and spheroid cultured HCT116 cells. HCT116 cells were seeded with the same cell density and cultured as monolayer or as spheroids and treated after 72 h with different Glutor concentrations (in the presence of 25 mM glucose). Cells treated with glucose-depleted media served as a control. Cell integrity was monitored using propidium iodide (PI) staining. a) Representative images of Glutor-treated cells after 72 h of treatment. b) Quantification of PI staining after 72 h of treatment. All brightfield object red mean intensity served as measure of spheroid toxicity and red object confluence as measure of toxicity of monolayer-cultured cells. Data show representative values \pm s.d. (n=3, N=8).

8.3.5 Metabolic profiles of different cell lines correlate with Glutor sensitivity

Metabolic plasticity in cancer has a great impact on the sensitivity towards metabolic drugs with regard to cell viability. It is known that cancer cells do not only increase aerobic glycolysis upon malignant transformation, but rather also accelerate oxidative phosphorylation to adapt quickly to environmental changes.⁷³ In order to investigate if metabolic flexibility is one reason for the different sensitivities towards Glutor treatment, the most sensitive cell line UM-UC-3 (Figure 31a,b) and a resistant BxPC-3 cell line (Figure 31c,d) were investigated in the Seahorse XFP analyzer using a glycolysis stress test. The glycolysis rate (ECAR) was reduced by Glutor in both cell lines to a similar extent (Figure 31a,c). Major differences between both cell lines were observed in the untreated controls when comparing glycolytic reserve, glycolytic capacity and the reduction of the respiratory rate (OCR) upon glucose addition (Figure 31, Figure 32). Here, glucose addition in UM-UC-3 cells led to a strong reduction in OCR, while ECAR increased (Figure 31a,b). In contrast,

the Glutor-resistant cell line BxPC-3 also increased the glycolytic rate but kept the respiratory rate at a constant high level (Figure 31c,d). Upon mitochondrial impairment (Oligomycin addition), BxPC-3 could still increase glycolysis by 213% in order to rescue the energy-depleted state (in the absence of the GLUT inhibitor) (Figure 31c). This led to a total difference of about 250% between the glycolytic capacity in UM-UC-3 and BxPC-3 cells (Figure 32a).

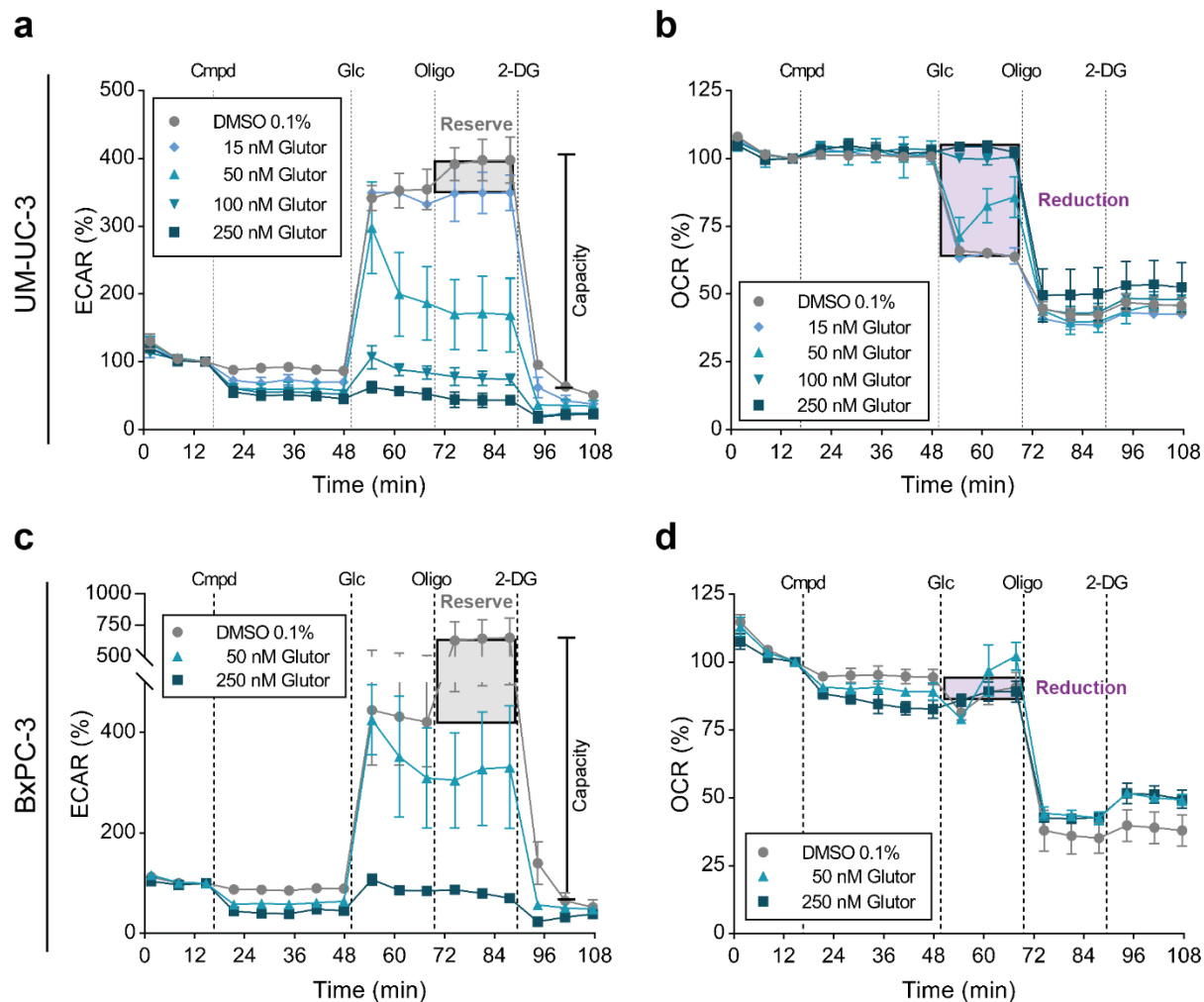


Figure 31 Glutor impaired glycolysis in UM-UC-3 and BxPC-3 cells. UM-UC-3 (a,b) and BxPC-3 cells (c,d) were subjected to a glycolysis stress test after incubation with glucose-free (0 mM) medium for 45 min. The extracellular acidification rate (ECAR; a,c) and the oxygen consumption rate (OCR; b,d) were measured using a Seahorse XFP instrument. Data show mean values \pm s.d. (n=3, N=2). Glycolytic reserve (a,c), glycolytic capacity (a,c) and OXPHOS reduction (b,d) are highlighted within the graphs. Cmpd=compound/DMSO; Glc=10 mM glucose; Oligo=2.5 μ M Oligomycin; 2-DG=50 mM 2-deoxy-D-glucose.

To analyze whether this observation is statistically relevant, the glycolytic reserve and the OXPHOS reduction of UM-UC-3, BxPC-3 and the model cell line HCT116 were plotted against the IC_{50} values obtained in the Sulforhodamine B assay (Figure 32c). Indeed, a strong correlation was observed between the sensitivity towards Glutor treatment (IC_{50}) and the glycolytic reserve ($R^2=0.98$) and the OXPHOS reduction ($R^2=0.95$), respectively (Figure 32c). Therefore, the data suggests that the metabolic plasticity of the investigated cell lines correlate with the sensitivity towards glucose starvation through Glutor treatment.

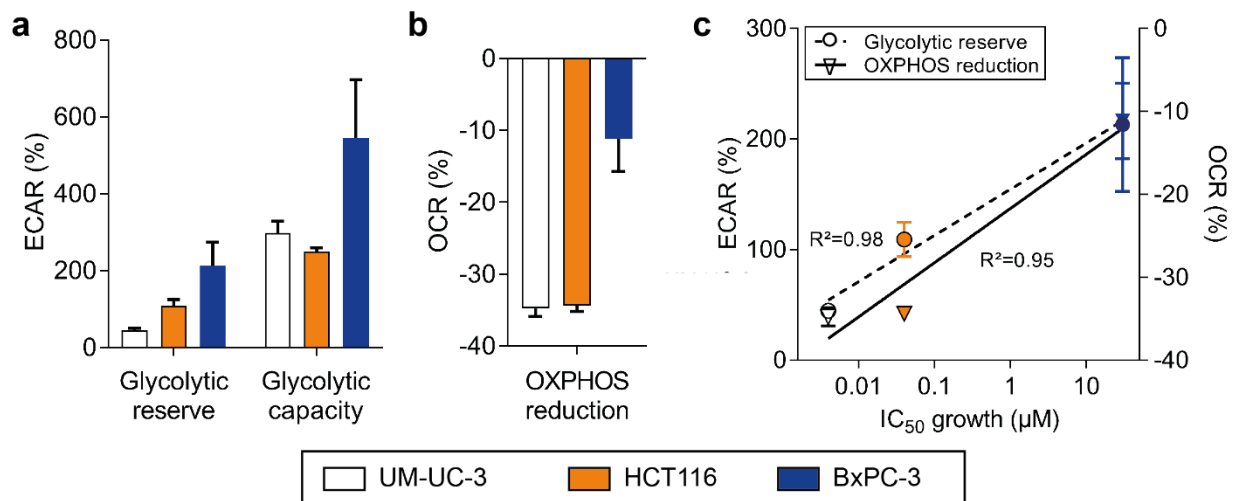


Figure 32 Metabolic profiles of different cancer cell lines with different Glutor sensitivities during glycolysis stress test. UM-UC-3, HCT116 and BxPC-3 cells were subjected to glycolysis stress test after 45 min of glucose starvation (Figure 24, Figure 31). a,b) Glycolytic reserve, glycolytic capacity and OXPHOS reduction were calculated using the second of three measurements within one measurement cycle (illustrated in Figure 31). Data show mean values \pm s.d. (n=3, N=2). c) Correlation between cell line sensitivity towards Glutor treatment in the Sulforhodamine B assay (Figure 27) and glycolytic reserve (a) and OXPHOS reduction (b). The correlation coefficient (R^2) was determined using a linear regression model. Data show mean values \pm s.d. (n=3, N=2).

8.3.6 GLUT-1, GLUT-2 and GLUT-3 are targets of Glutor

As mentioned in chapter 5.3, all class I GLUT isoforms have distinct tissue distribution and mainly GLUT-1, but also GLUT-3 overexpression are associated with cancer. To determine the isoform selectivity of Glutor, CHO cells (hamster ovary) were transfected with plasmids encoding one of the specific human isoforms GLUT-1-4 or an empty vector control 72 h before performing the 2-

DG uptake assay (Figure 33a-d). The immunoblots to assess the relative increase of GLUT-isoform expression are shown in Figure 34.

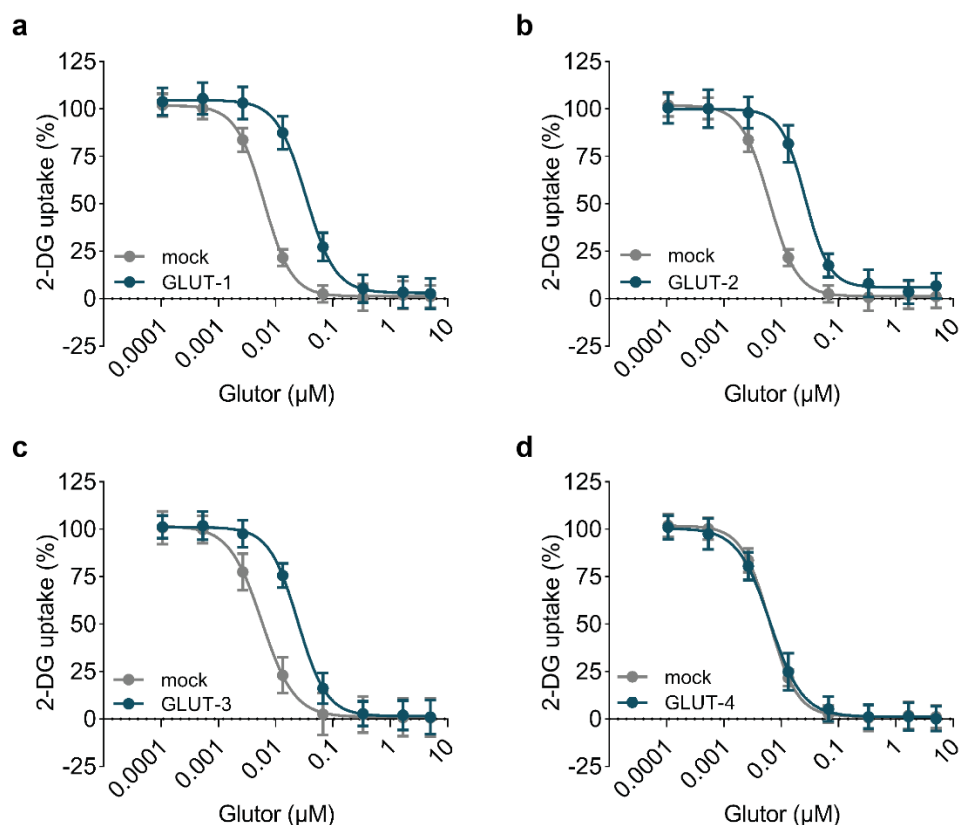


Figure 33 Overexpression of GLUT-1-3 partially rescues 2-DG uptake inhibition of Glutor. CHO cells were transfected with plasmids coding for GLUT-1 (a), GLUT-2 (b), GLUT-3 (c) or GLUT-4 (d) or the corresponding empty vector control (mock) 72 h before the 2-DG uptake assay. Glutor activity was assessed via resazurin-coupled 2-DG uptake assay. Data show mean values \pm s.d. ($n=3$, $N=3$). *Experiments and data analysis were conducted by Dr. George Karageorgis.*

A 4- to 6-fold decrease in Glutor potency was observed for CHO cells that overexpress the GLUT isoforms GLUT-1-3 from $\text{IC}_{50}=6.2\pm 1.2$ nM to 34 ± 3.5 nM (GLUT-1) and 26 ± 2.9 nM (GLUT-2), and from 5.9 ± 1.6 nM to 24 ± 2.6 nM (GLUT-3) (Figure 33a-c, Table 9). In contrast, GLUT-4 overexpression did not result in a change in IC_{50} value for 2-DG uptake (Figure 33d, Table 9). In conclusion, GLUT-1-3 seem to be the GLUT isoforms that are inhibited by Glutor, whereas GLUT-4 is most likely no target of the compound.

Results

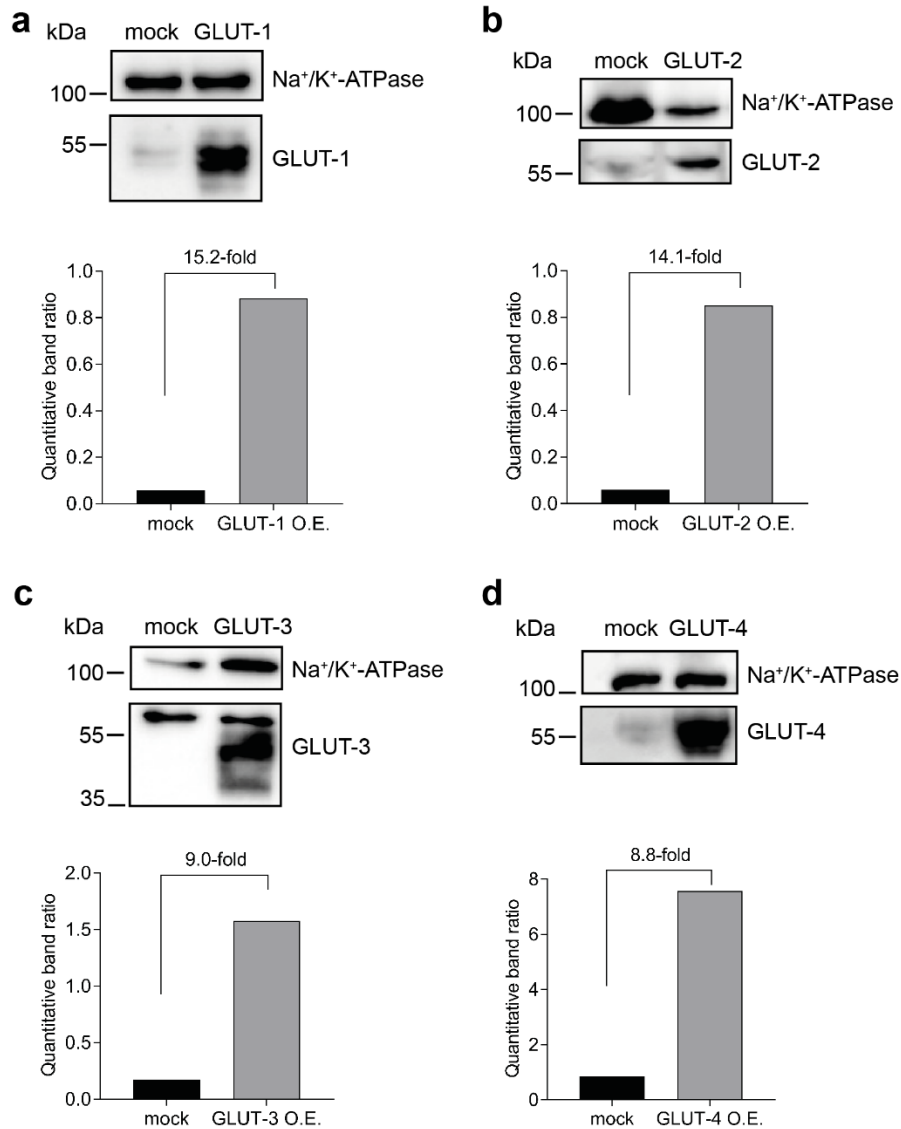


Figure 34 Overexpression of GLUT-1-4 in CHO cells. Protein levels were assessed for GLUT-1 (a), GLUT-2 (b), GLUT-3 (c) and GLUT-4 (d) overexpressing CHO cells and the respective mock-transfected control 48 h post transfection using immunoblotting. Representative blots and the quantitative band ratios between GLUT isoform and respective house-keeping control for mock- and GLUT-transfected CHO cells are shown (n=3). *Experiment was performed by Dr. George Karageorgis.*

To confirm this observation, DLD-1 cells that mainly express GLUT-1 (Figure 35b) and DLD-1 (-/-) cells that mainly express GLUT-3 (Figure 35c), were analyzed for their 2-DG uptake inhibition sensitivity (Figure 35a, Table 9). 2-DG uptake was inhibited in both cell lines, indicating that both isoforms, GLUT-1 and GLUT-3, are targets of Glutor.

Results

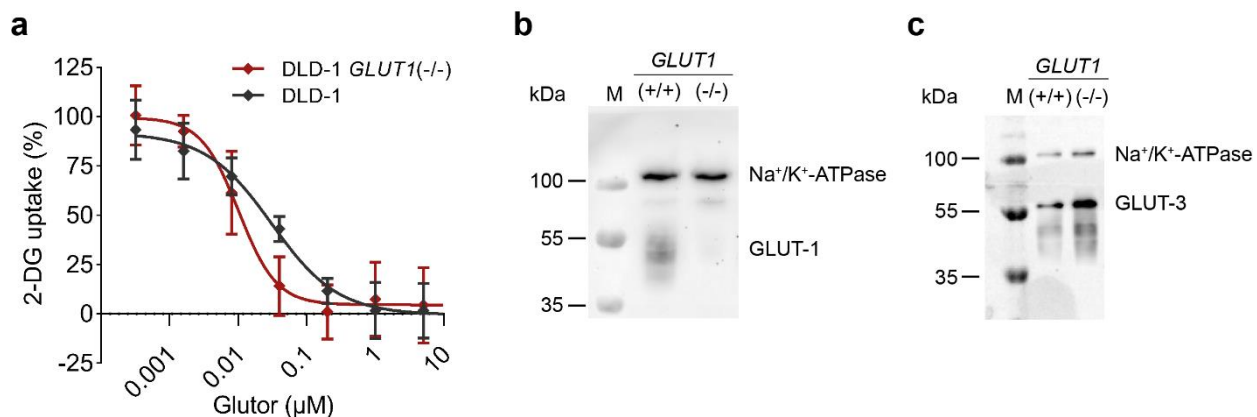


Figure 35 Glutor inhibited 2-DG uptake in DLD-1 wt and DLD-1 *GLUT1(-/-)* cells. a) DLD-1 wt and *GLUT1(-/-)* cells were tested for 2-DG uptake in the presence of Glutor. Data show mean values \pm s.d. (n=3, N=3). b,c) GLUT-1 (b) and GLUT-3 (c) protein level of DLD-1 wt and *GLUT1(-/-)* cells were analyzed by means of immunoblotting. Na⁺/K⁺-ATPase served a reference protein. M=Protein standard. *The experiments were performed by Dr. George Karageorgis.*

Table 9 Overview of 2-DG uptake during overexpression (Figure 33) and *GLUT1(-/-)* experiments (Figure 35).

CHO	IC ₅₀ (GLUT-1)	IC ₅₀ (GLUT-2)	IC ₅₀ (GLUT-3)	IC ₅₀ (GLUT-4)	DLD-1	IC ₅₀
Mock	6.2 \pm 1.2 nM	6.2 \pm 1.2 nM	5.9 \pm 1.6 nM	6.2 \pm 1.2 nM	wt	35.5 \pm 4.8 nM
O.E.	34 \pm 3.5 nM	26 \pm 2.9 nM	24 \pm 2.6 nM	6.4 \pm 1.7 nM	<i>GLUT1(-/-)</i>	9.8 \pm 1.4 nM
Increase	6.5 x	4.2 x	4.1 x	1.0 x	Decrease	3.6 x

O.E.=overexpression, wt=wild type.

Since GLUT-1 and GLUT-3 are the targets that are mainly overexpressed in cancer, cellular thermal shift assays (CETSA®) were performed using SW480 cell lysates, which show a high degree of GLUT-1 and GLUT-3 expression (Figure 36, Appendix Figure 89).¹²⁷ CETSA® is a cell-based target engagement method that can be performed using unmodified small molecules. The assay is based on the thermal destabilization and hence denaturation of proteins upon heat treatment. An interaction between a compound and its protein target may lead to a thermal (de)stabilization of the protein target and, therefore, to a shift in the melting curve and melting temperature (T_m) compared to the untreated control.¹²⁸ The presence of specific proteins can be subsequently assessed in complex whole cell lysates via immunoblotting. Therefore, the melting behavior of GLUT-1 and GLUT-3 as Glutor targets (Figure 36a,b) as well as Na⁺-K⁺-ATPase and vinculin as controls (Figure 36c,d) were investigated.

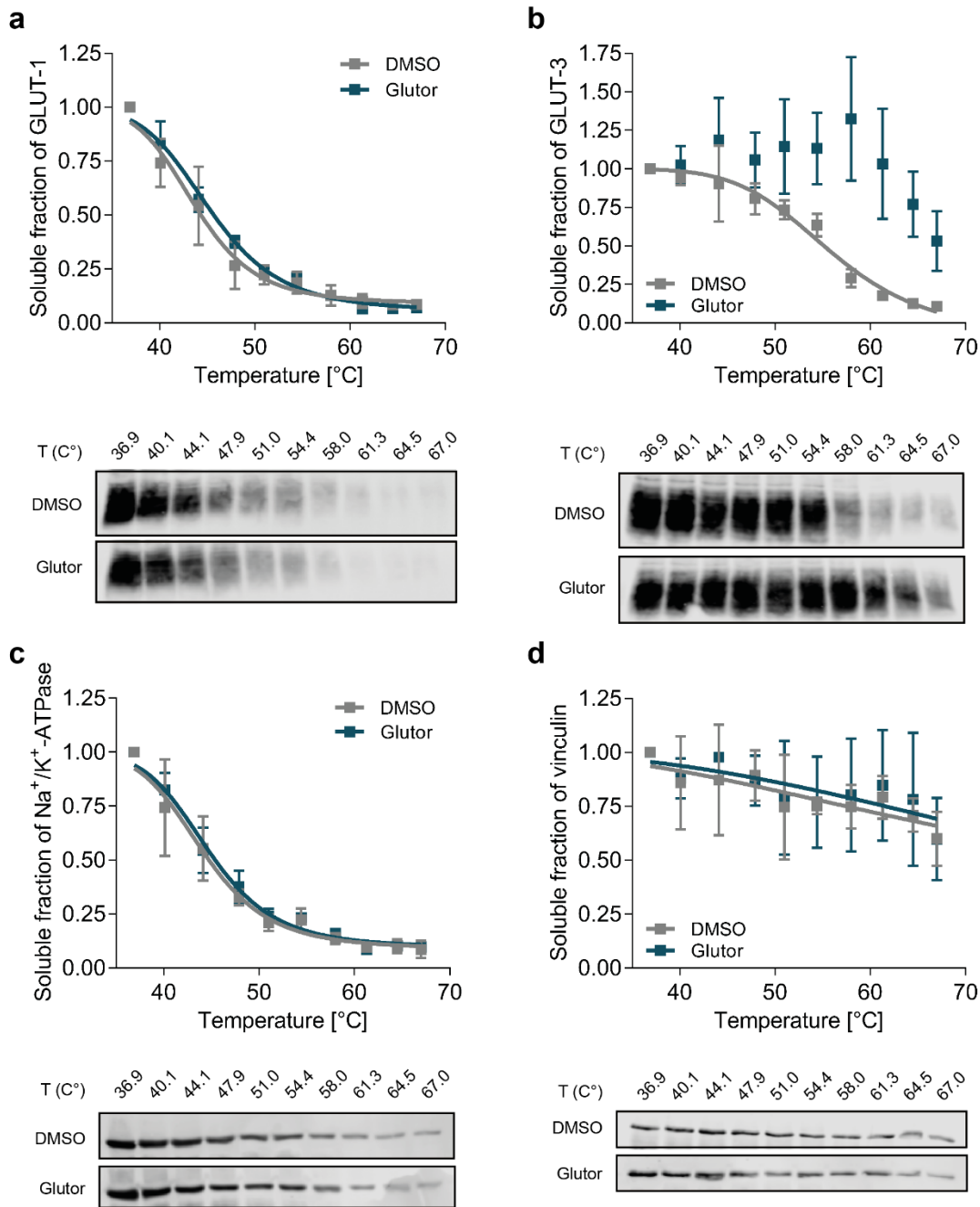


Figure 36 Glutor stabilized GLUT-3 in a Cellular Thermal Shift Assay (CETSA®). SW480 whole cell lysate was subjected to ten different temperatures in the presence of 10 μ M Glutor or DMSO. After ultracentrifugation, the supernatant was analyzed for GLUT-1 (a), GLUT-3 (b), Na⁺/K⁺-ATPase (c) or vinculin (d) by means of immunoblotting and protein amount was quantified via densitometric analysis. Protein amount was normalized to the first temperature within the temperature gradient, *i.e.* 36.9 °C. The data was fitted using the Boltzmann equation. Data show mean values \pm s.d. (n=3). Immunoblots are representative images of n=3.

The presence of Glutor does not influence the thermal stability of GLUT-1 (ΔT_m 1.1 \pm 1.4 °C), whereas a clear thermal stabilization was observed for GLUT-3 that led to an increase in T_m of

>10 °C (Figure 36a,b, Table 10). The control transmembrane protein Na⁺-K⁺-ATPase and cytosolic protein vinculin were not influenced in their thermal stability by Glutor (Figure 36c,d, Table 10). Due to insufficient melting of vinculin at high temperatures (only 25% of the protein melted) and high variance within the protein quantification, vinculin should not be used as control protein in CETSA® experiments, but rather proteins like Na⁺-K⁺-ATPase with a suitable melting behavior.

Table 10 Overview of melting temperatures from CETSA® experiments with Glutor.

T _m (°C)	GLUT-1	GLUT-3	Na ⁺ /K ⁺ -ATPase	Vinculin
Glutor	44.0±0.8	-	43.6±1.1	-
DMSO	42.9±1.6	55.1±1.1	42.9±1.9	-
ΔT _m	1.1±1.4	>10	0.7±2.9	-

Melting temperatures were determined using Boltzmann fit. Data show mean values ±s.d. of n=3. T_m=melting temperature; ΔT_m=delta T_m, -=data could not be fitted.

8.3.7 Cancer cells upregulate GLUT-1 and GLUT-3 to escape glucose starvation

In phases of glucose depletion, rat neurons (*in vitro*) and mice brain tissue (*in vivo*) upregulate the expression of the high affinity and high capacity transporter GLUT-3 (K_m=1.4 mM for 2-DG)¹⁸ to increase glucose consumption.¹²⁹ First indications that cancer adapts this rescue effect under low glucose concentrations were reported by Marín-Hernández *et al.* when MCF7 and HeLa cells were cultured at 2.5 mM glucose. This increased GLUT-1 and GLUT-3 protein expression after 24 h.¹³⁰ This potential rescue mechanism involving transcriptional upregulation of *GLUT1-4* mRNA was investigated in this thesis under glucose starvation conditions (0-1 mM glucose), physiological glucose concentration (5 mM)¹³¹ and normal cell culture condition (25 mM) after 24 h and 48 h (Figure 37). DLD-1 cells upregulated *GLUT1* and *GLUT3* mRNA levels after 24 h under low glucose conditions (0 mM, 1 mM) and after 48 h even to a significant extent by about 2-fold, whereas *GLUT4* mRNA was not influenced. Physiological glucose concentration did not influence the level of *GLUT1*, *GLUT3* and *GLUT4*. *GLUT2* was transcribed at such low levels that it could

Results

not be detected in any sample and was also not increased to detectable levels upon glucose starvation. Interestingly, *B2M*, which served as reference gene, showed similar upregulation (up to 1.6-fold) under glucose starvation conditions (0 mM) as *GLUT1* and *GLUT3* after 48 h (Figure 37a,b).

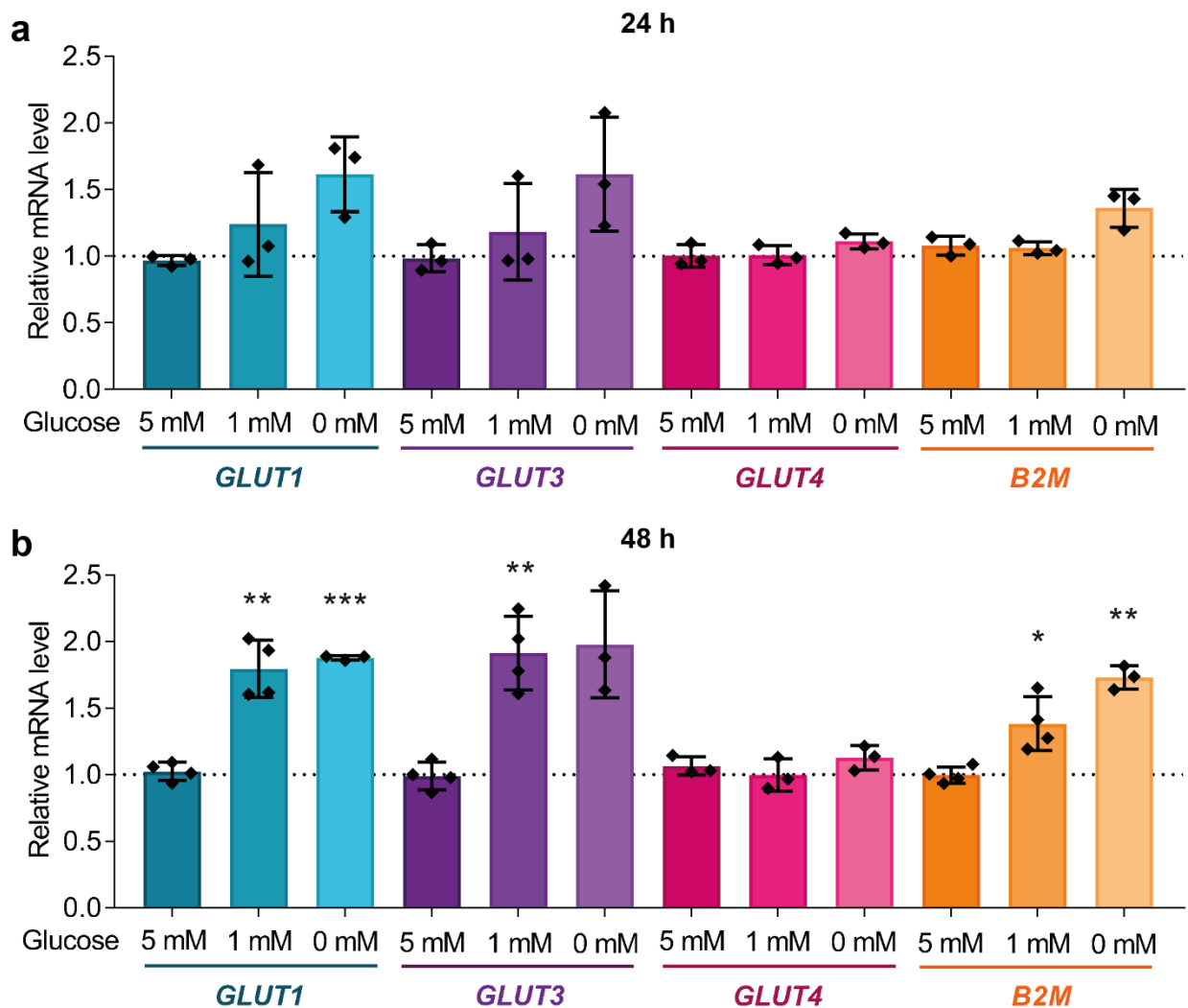


Figure 37 *GLUT1*, *GLUT3* and *B2M* upregulation was induced by glucose starvation conditions. DLD-1 cells were cultured in the presence of different glucose concentrations over 24 h (a) or 48 h (b) before extraction of total RNA for reverse transcription and RT-qPCR. *GLUT1,3,4* and *B2M* mRNA levels were normalized to the levels of *ATP1A1*, *ACTB* and *TUBB* and related to standard cell culture glucose level (25 mM glucose, which were set to 1). Data show mean values \pm s.d. (n=3-4). Statistical analysis was performed using an unpaired t-test with Welch's correction. *= $p < 0.05$; **= $p < 0.01$; ***= $p < 0.001$.

Results

Treatment of DLD-1 cells with 0.5 μ M Glutor mirrored the observed rescue effect in DLD-1 cells under glucose-depleted conditions (Figure 38). Here, a significant difference in *GLUT1*, *GLUT3* and *B2M* expression could be already observed after 24 h (Figure 38a). *GLUT4* mRNA level was not influenced after 24 h (Figure 38a) and showed a significant reduction after 48 h (Figure 38b).

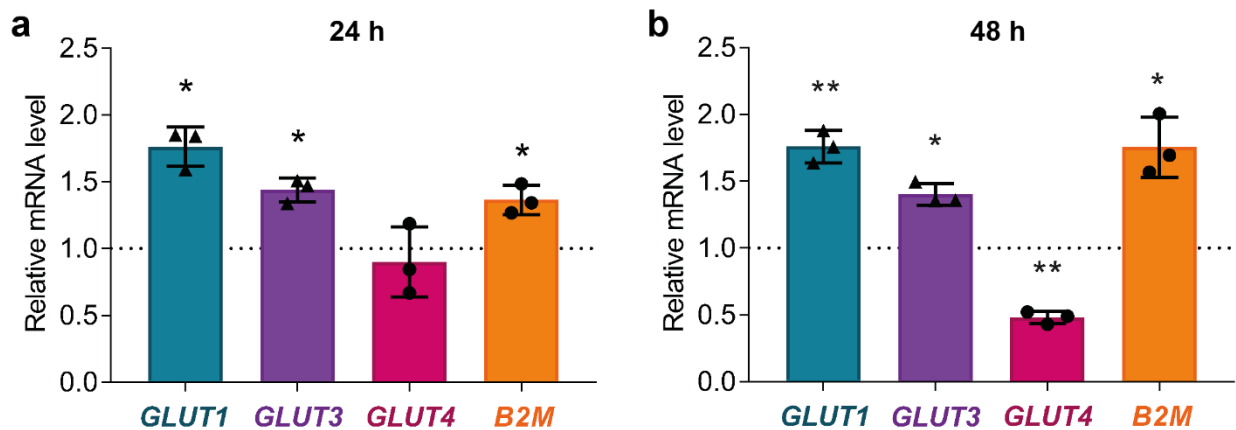


Figure 38 Glutor induced upregulation of *GLUT1*, *GLUT3* and *B2M*. DLD-1 cells were cultured in the presence of 0.5 μ M Glutor over 24 h (a) or 48 h (b) in the presence of 25 mM glucose prior to extraction of total RNA for reverse transcription and RT-qPCR. *GLUT1,3,4* and *B2M* mRNA levels were normalized to the levels of *ATP1A1*, *ACTB* and *TUBB* and related the value of DMSO-treated cells (which were set to 1) Data show mean values \pm s.d. (n=3). Statistical analysis was performed using an unpaired t-test with Welch's correction. *= $p < 0.05$; **= $p < 0.01$.

To confirm the observations described above, GLUT-1 and GLUT-3 protein levels were investigated by means of immunoblotting (Figure 39) as part of the Master thesis of Jessica Nowacki. On the protein level, GLUT-1 and GLUT-3 were ca. 2-fold upregulated after 24 h under glucose starvation conditions (0 mM) (Figure 39a,c). After 48 h, reduced glucose levels (1 mM) led to a significant 2-fold increase of GLUT-1, whereas glucose starvation conditions (0 mM) induced a significant 3.2-fold upregulation (Figure 39b). GLUT-3 was upregulated to even higher levels of 2.2-fold under reduced glucose conditions (1 mM) and 4.1-fold under glucose-depleted (0 mM) conditions (Figure 39d).

Results

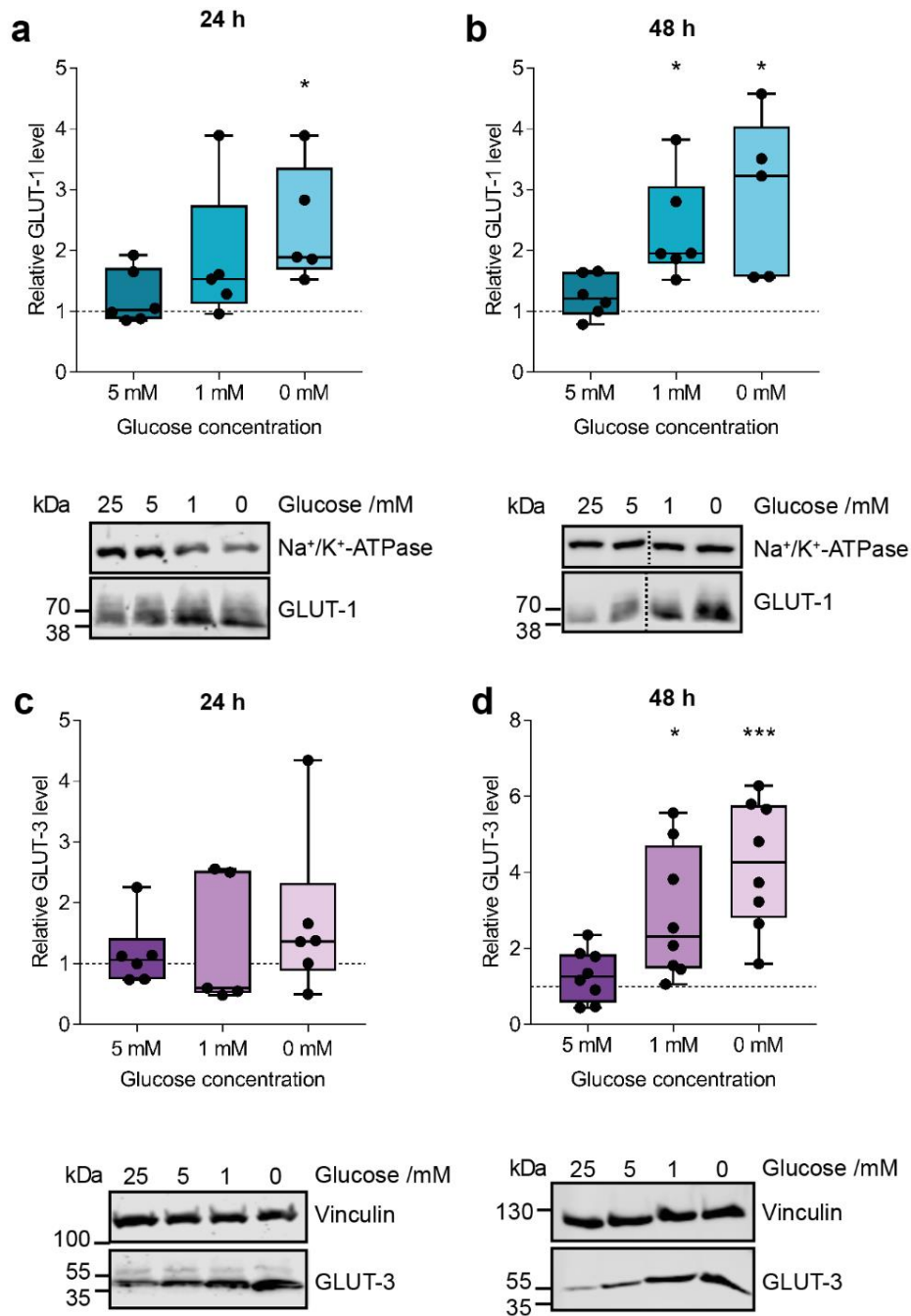


Figure 39 GLUT-1 and GLUT-3 protein levels were increased upon glucose starvation. DLD-1 cells were cultured for 24 h (a,c) or 48 h (b,d) in the presence of different glucose concentrations before protein lysates were generated for SDS-PAGE analysis and immunoblotting. Na⁺/K⁺-ATPase (a,b) and vinculin (c,d) served as reference genes for GLUT-1 (a,b) and GLUT-3 (c,d), respectively. Quantification was performed by means of densitometric analysis and protein levels were normalized to the respective reference gene and related to values of cells cultured in the presence of 25 mM glucose (which were set to 1). Data show median values with interquartile range of n=6 (a,b,c) or n=8 (d). Representative immunoblots are depicted below each graph. Dashed lines indicate cropped images from the same blot. Statistical analysis was performed using an unpaired t-Test with Welch's correction. **p*<0.05; ****p*<0.001.

Results

On the protein level, the presence of 0.5 μM Glutor induced an upregulation of the glucose transporters GLUT-1 and GLUT-3 after 24 h by about 2-fold (Figure 40). A significant upregulation was observed after 48 h by about 3-fold for GLUT-1 and even up to 6-fold for GLUT-3 (Figure 40).

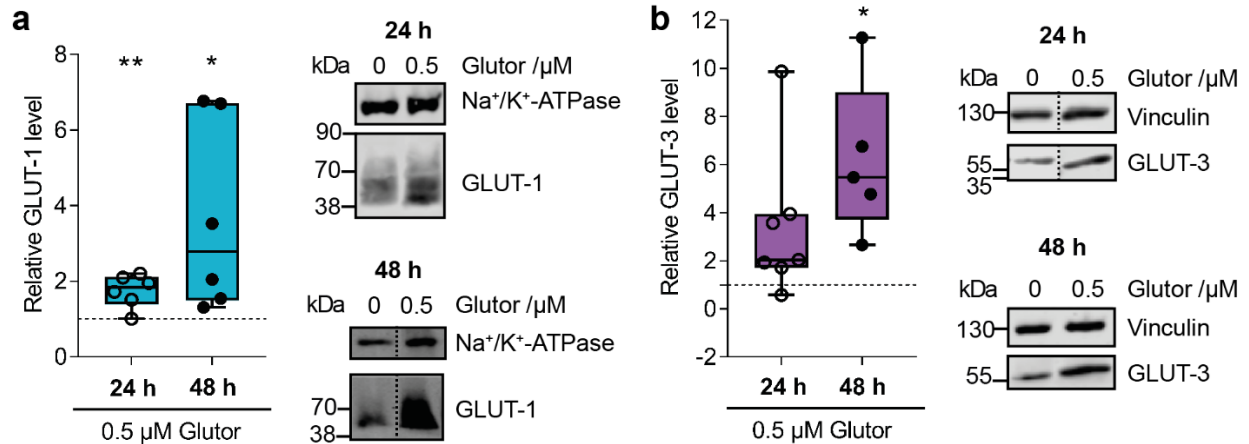


Figure 40 Glutor treatment induced upregulation of GLUT-1 and GLUT-3. DLD-1 cells were cultured for 24 h or 48 h in the presence of 0.5 μM Glutor and 25 mM glucose before protein lysates were generated for SDS-PAGE and immunoblotting. Na⁺/K⁺-ATPase (a) and vinculin (b) served as reference genes for GLUT-1 (a) and GLUT-3 (b), respectively. Quantification was performed by means of densitometric analysis. Protein levels were normalized to the respective reference gene and related to values of DMSO-treated cells (which were set to 1). Data show median values with interquartile range of n=6 (a) or n=7 (b). Representative immunoblots are depicted on the right side of each graph. Dashed lines indicate cropped images from the same blot. Statistical analysis was performed using an unpaired t-Test with Welch's correction. *= $p < 0.05$; **= $p < 0.01$.

Thus, cancer cells upregulate GLUT-1 and to an even higher extent GLUT-3 under glucose starvation conditions that are either induced by incubation in glucose-depleted medium or by the presence of a glucose uptake inhibitor with GLUT-1-3 isoform selective profile. This allows the tumor to increase the glucose consumption even under low glucose concentration to cope with phases of nutrient (glucose) shortage.

To confirm the observed rescue mechanism, HCT116 cells were incubated for 48 h with different glucose concentrations (0 mM, 1 mM, 5 mM, 25 mM) or treated with 0.5 μM Glutor (in presence of 25 mM glucose) (Figure 41). RT-qPCR revealed a significant increase in *GLUT3* mRNA under 0 mM and 1 mM glucose by 1.3- and 1.6-fold, respectively. A 1.5-fold increase in *GLUT3* mRNA was detected in the presence of 0.5 μM Glutor. This confirms the observed rescue mechanism in

HCT116 cells that results in *GLUT3* upregulation. The *GLUT1* mRNA level was unaltered under hypoglycemic conditions induced by different glucose concentrations or Glutor treatment, whereas *GLUT4* mRNA increased by 1.5-fold under glucose deprivation (0 mM) and by 1.3-fold during Glutor treatment and to significant extent (Figure 41). Analog to DLD-1 cells, *GLUT2* mRNA could not be detected in HCT116 cells under none of the implemented conditions.

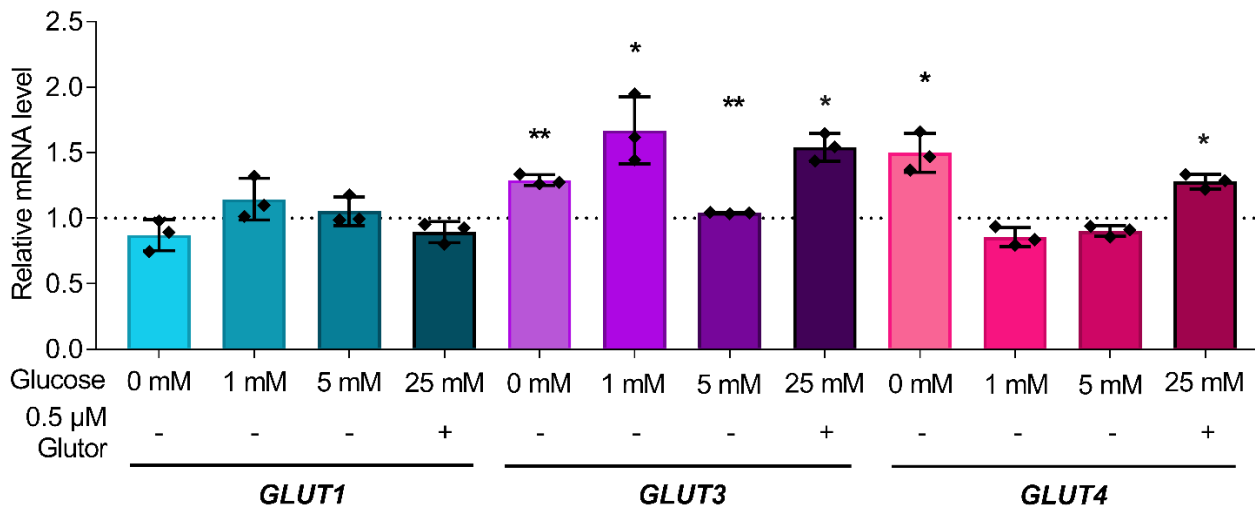


Figure 41 Glutor treatment increased GLUT3 and GLUT4 mRNA in HCT116 cells. HCT116 cells were cultured in the presence of different glucose concentrations (0 mM, 1 mM, 5 mM, 25 mM) or 0.5 μM Glutor and 25 mM glucose over 48 h before extraction of total RNA for reverse transcription and RT-qPCR. *GLUT1,3,4* mRNA levels were normalized to the levels of *ATP1A1*, *ACTB* and *TUBB* and related to standard cell culture glucose level (25 mM glucose, which were set to 1). Data show mean values \pm s.d. (n=3-4). Statistical analysis was performed using an unpaired t-test with Welch's correction. *= $p < 0.05$; **= $p < 0.01$.

8.3.8 Nutrient dependencies of HCT116 cells

The growth and viability of the model cancer cell line HCT116 was investigated in the presence of different glucose concentrations by means of live-cell imaging and confluence as a measure of cell growth as part of the Bachelor thesis of Jessica Nowacki (Figure 42a,b).

Results

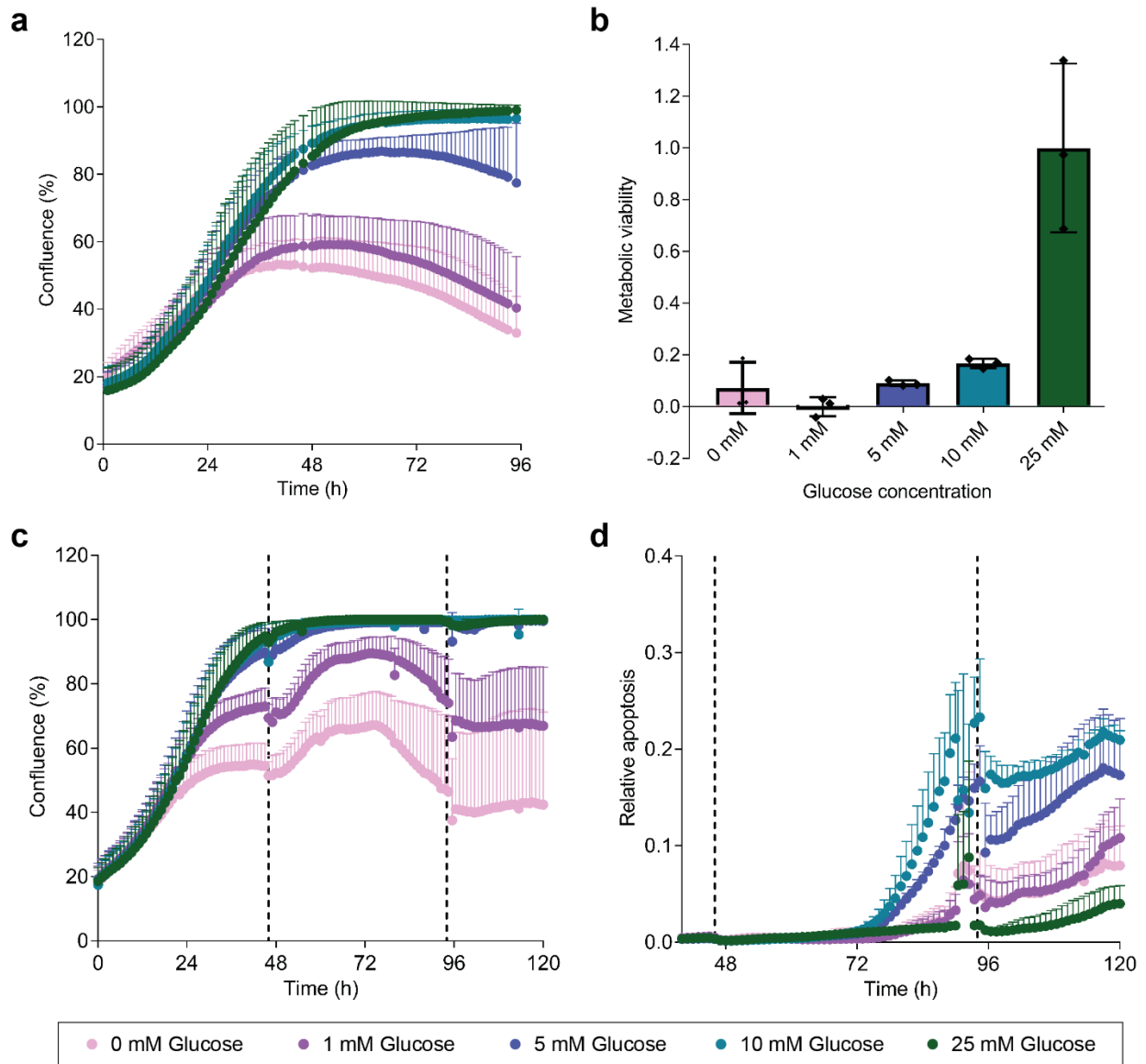


Figure 42 Glucose dependence of HCT116 cells. HCT116 cells were cultured over 96 h without medium exchange (a) or for 120 h with medium exchange every 48 h (c,d) and monitored by means of live-cell imaging using the IncuCyte® ZOOM. b) Viability was assessed after 72 h of incubation employing a WST-1 assay. Data is normalized to the value of cells cultured at 25 mM glucose. d) Apoptosis induction was monitored during the time course of the experiment depicted in c). The relative induction of apoptosis is given as a ratio between green confluence (apoptosis induction) and total cell confluence. Medium exchange is illustrated as dashed line. All values show mean values \pm s.d. (n=3, N=3).

Cells cultured under normal glucose concentration (25 mM) and reduced glucose concentration (10 mM) showed a normal growth behavior (Figure 42a). In contrast, physiological glucose concentration (5 mM) reduced growth such that the cells did not reach full confluence (Figure 42a). Low glucose concentrations (1 mM glucose) and glucose depletion (0 mM glucose) strongly

impacted cell growth (Figure 42a). Cell viability was assessed after 72 h of treatment employing a WST-1 assay (Figure 42b). This assay monitors the bioreduction capacity which is highly dependent on glycolytic NAD(P)H production and therefore the metabolic viability of the cells. HCT116 cells cultured in the presence of 25 mM glucose showed the highest metabolic activity (Figure 42b). The metabolic viability was already lowered in the presence of 10 mM glucose and was reduced by half or further when less than 10 mM glucose was available (Figure 42b).

In order to investigate if it is possible to culture this cell line under lower glucose concentrations (1 or 5 mM glucose), the medium was exchanged for fresh medium with the respective glucose concentration every 48 h. Indeed, fresh glucose supply rescued the cells for the first 12 h after medium exchange from growth retardation (Figure 42c). However, cells cultured under low glucose concentrations were still not able to grow to full confluence. Apoptosis was monitored during the time course of the experiment using a caspase-3/-7 sensitive reagent (Figure 42d). The lowest level of apoptosis was measured in the presence of 25 mM glucose (Figure 42d). Lowering the glucose concentration to 10 mM revealed the highest degree of apoptosis. Low glucose levels (0, 1, 5 mM glucose) reduced apoptosis as compared to cells cultured at 10 mM glucose. Since cells cultured under 10 mM and 5 mM glucose still underwent rapid cell proliferation and were confluent before medium exchange after 48 h, many cells compete for the limited nutrient glucose. Under lower glucose concentration (0, 1 mM glucose), the cell confluence was much lower and less cells were able to undergo cell division under glucose depletion. Therefore, there are fewer that could undergo apoptosis. Furthermore, medium exchange after 48 h and 96 h led to a short rescue period from apoptosis (Figure 42d), which is in line with the result obtained during live-cell growth analysis (Figure 42c).

Glutamine is the most abundant amino acid in the human body and in most cell culture media.^{132,133} Not only the dependence of cancer on glucose but also on glutamine was revealed *in vitro* and the glutamine metabolism is an attractive pathway in targeted cancer therapies.⁷³ In order to

Results

investigate the nutrient dependence of the model cancer cell line HCT116, the cells were cultured in glucose-free and glutamine-free medium and growth was monitored by means of live-cell imaging (Figure 43). The strongest reduction in cell growth was observed in the absence of both nutrients. Nonetheless, glutamine depletion had a stronger influence on cell growth than glucose depletion (Figure 43).

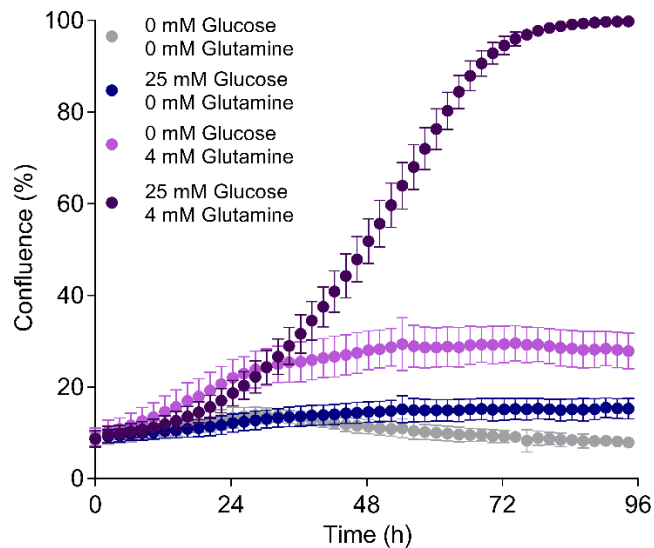


Figure 43 HCT116 cells were strongly dependent on glutamine for cell growth. HCT116 cells were cultured under glucose or glutamine starvation conditions over 96 h. Cell growth was monitored by means of live-cell microscopy and cell confluence was analyzed. Data are mean values \pm s.d. (n=3, N=3).

To investigate a co-dependence on both nutrients, the concentration of glucose (5 mM, 10 mM, 25 mM) and glutamine (0 mM, 0.05 mM, 0.5 mM, 4 mM) were varied simultaneously and cell growth (Figure 44a) as well as apoptosis (Figure 44b) were monitored in real-time as *part of the Bachelor thesis of Jessica Nowacki*. Irrespectively of the prevalent glucose concentration, cells cultured in the presence of a high (4 mM) glutamine concentration grew comparably, whereas cells cultured at low glutamine concentrations (0.05 mM, 0 mM) were strongly impeded in their cell growth at all glucose concentrations (Figure 44a). Interestingly, at the physiological glutamine concentration of 0.5 mM¹³⁴, an influence on the cell growth was observed in the presence of

Results

varying glucose concentrations (Figure 44a,c). More precisely, in the presence of only 5 mM glucose the cell confluence decreased in the presence of physiological glutamine concentration (see the arrow, Figure 44a).

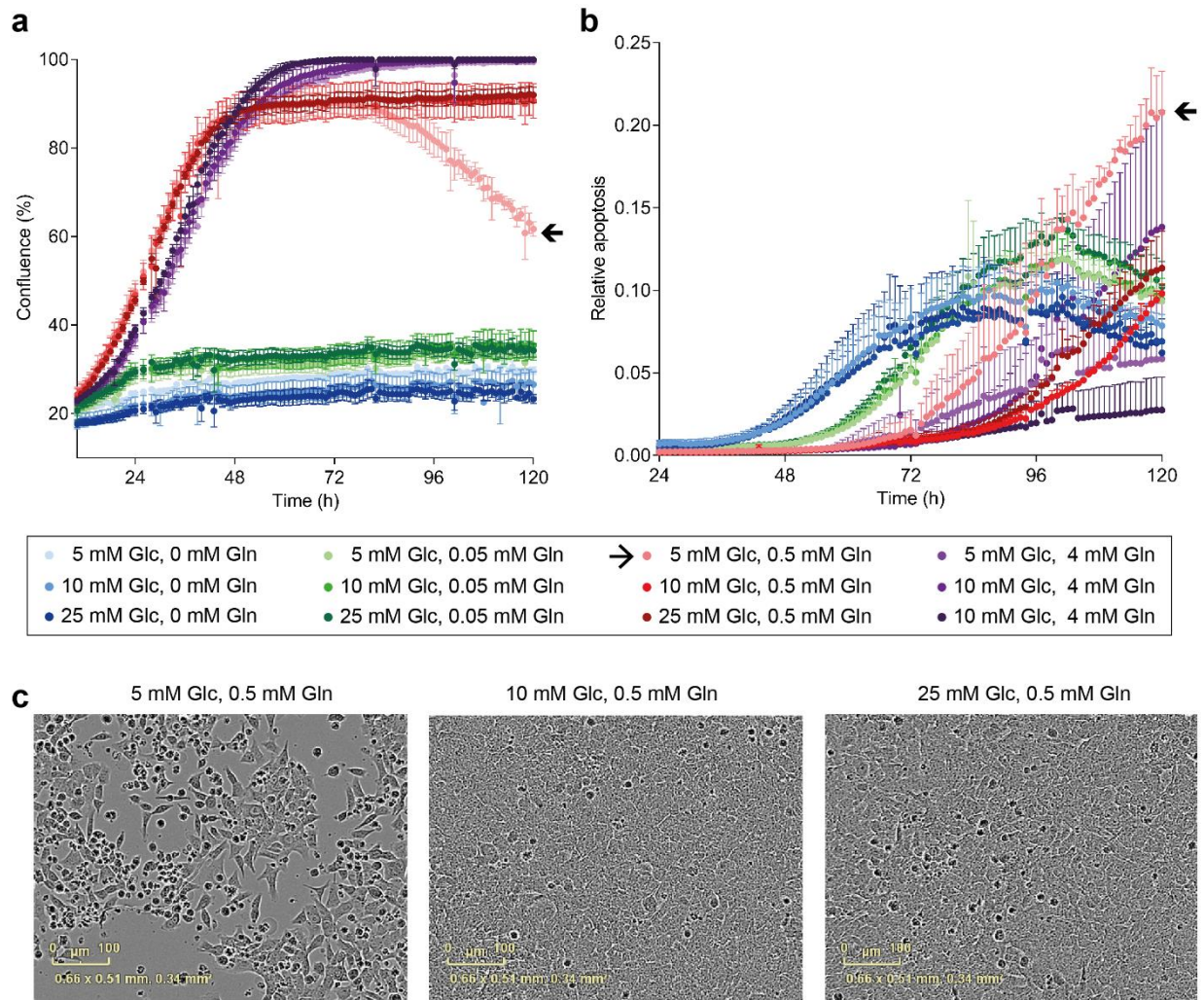


Figure 44 HCT116 cells depended strongly on glutamine for cell growth and viability. HCT116 cells were cultured under glucose or glutamine starvation conditions (a) or under different glutamine and glucose concentrations (b) over 96 h (a) or 120 h (b). Cell growth was monitored by means of live-cell microscopy and cell confluence was analyzed. c) Apoptotic events were monitored using caspase-3/-7 reagent and green fluorescence was monitored along with cell confluence (b) by means of live-cell imaging. Data are mean values \pm s.d. (n=3, N=3) (b) or show a representative replicate (a) (n=3, N=3). c) Representative images after 120 h of treatment. Glc=glucose, Gln=glutamine.

Apoptosis was induced after 40 h in glutamine-depleted medium and after 60 h in the presence of 0.05 mM glutamine (Figure 44b), regardless of the prevalent glucose concentration. At high glutamine concentration (4 mM) onset of apoptosis was detected earliest after 72 h with different

degrees of apoptosis depending on the prevalent glucose concentration (Figure 44b). Cells cultured under 25 mM glucose and 4 mM glutamine were highly viable with only few apoptotic events. Compared to cells cultured under 4 mM glutamine and reduced glucose (5 mM), the presence of 10 mM glucose (and 4 mM glutamine) led to a 2.6-fold increase in apoptosis. These differences are most likely due to different cell densities and therefore a different demand for absolute glucose amount. The strongest difference in apoptosis induction was observed, similar to the results in the cell growth experiment (Figure 44a), when the glucose concentration (5 mM, 10 mM, 25 mM) was varied at a constant glutamine level of 0.5 mM. Physiological glucose and glutamine concentration (5 mM glucose, 0.5 mM glutamine) led to apoptosis induction after 72 h and to the highest degree of apoptosis. As soon as the glucose level was increased to 10 mM or 25 mM, onset of apoptosis was shifted to 96 h and reached only half of the relative apoptosis level at 5 mM glucose.

Thus, a co-dependence of cell growth and viability on glutamine and glucose was observed when glutamine was applied to the cell culture medium at physiological concentration (0.5 mM glutamine) while the concentration of glucose was varied. When medium was exchanged after 48 h (Figure 45), no co-dependence could be observed anymore. With respect to apoptosis induction, the major differences were observed at high glutamine concentrations (4 mM) and varying glucose concentrations (Figure 45b). Here, in analogy to the experiment without medium exchange, cells treated with 10 mM glucose and 4 mM glutamine showed the highest degree of apoptosis. However, this observation did not match the results obtained during confluence analysis, since the cells exhibited a normal growth behavior (Figure 45a).

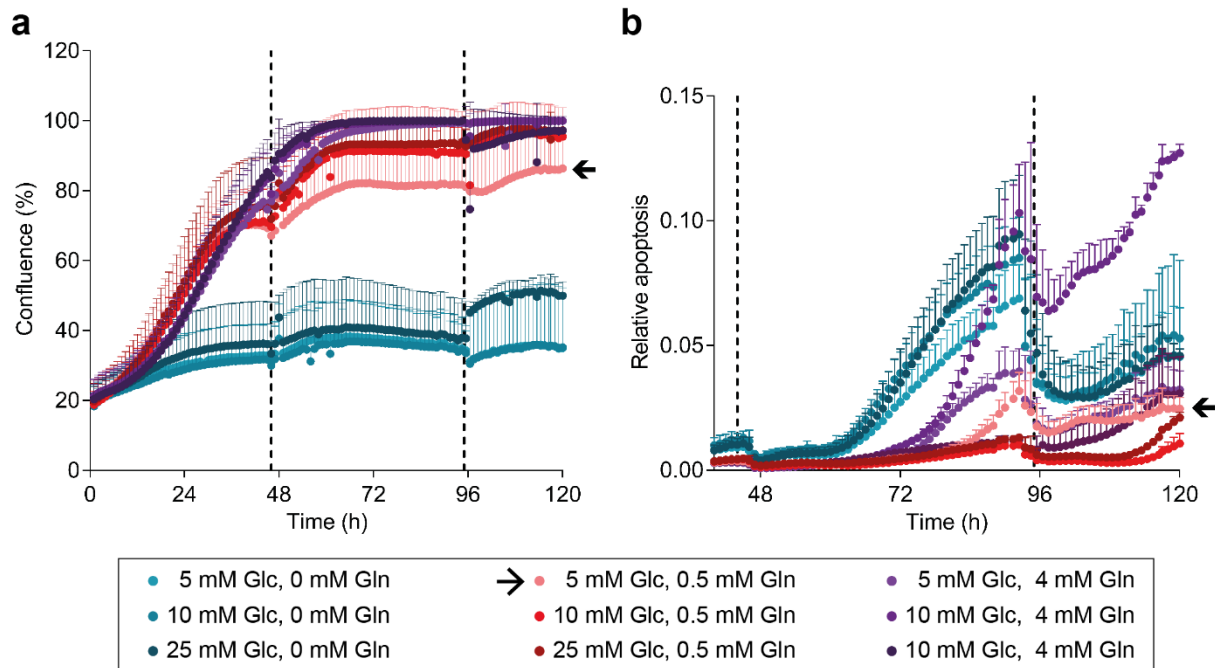


Figure 45 HCT116 cell growth was rescued with fresh glutamine supply during medium exchange. HCT116 cells were cultured in the presence of different nutrient concentrations (25 mM, 10 mM or 5 mM glucose and 4 mM, 0.5 mM or 0 mM glutamine) and cell growth (a) as well as apoptosis (b) was monitored via live-cell imaging over 120 h. a) Cell growth was assessed by analysis of the cell confluence by means of image-based analysis. b) Apoptosis was monitored via addition of a caspase-3/-7 reagent (green fluorescence) and green confluence was normalized to the total cell confluence. Medium exchange is illustrated as dashed line. All data show mean values \pm s.d. (n=3, N=3). Glc=glucose; Gln=glutamine.

Due to the earlier described co-dependence of HCT116 cell growth on glucose and glutamine, HCT116 cells were treated with the glucose uptake inhibitor Glutor at different glutamine concentrations (0.5 mM and 4 mM) and high glucose concentration (25 mM), to investigate potential differences in compound potency *as part of the Master thesis of Jessica Nowacki* (Figure 46). The concentration-dependent effect of Glutor on the growth of HCT116 cells at 4 mM glutamine (Figure 46a) could be clearly increased in the presence of physiological glutamine concentrations of 0.5 mM (Figure 46b). This observation is in line with the results obtained in the nutrient dependence assays (Figure 44). For quantitative comparison, the growth rates at four different glutamine concentrations (4 mM, 2 mM, 0.5 mM, 0.25 mM) were plotted against the Glutor concentration and GI_{50} values were calculated (Figure 46c, Table 11). Although no difference between the GI_{50} values and curves at 4 mM and 2 mM glutamine was observed, lower

Results

glutamine levels (0.5 mM, 0.25 mM) clearly increased Glutor potency by 3-fold from $GI_{50}=604.1\pm 290.7$ nM (4 mM glutamine) to 210.4 ± 43.7 nM (0.5 mM glutamine) (Table 11). One reason for similar GI_{50} values of cells treated in the presence of 4 mM or 2 mM glutamine and in the presence 0.5 mM or 0.25 mM glutamine might lay in the minor difference between the glutamine concentrations (Table 11). Hence, a 2-fold reduction in the extracellular glutamine level might be too small for a strong impact on Glutor potency.

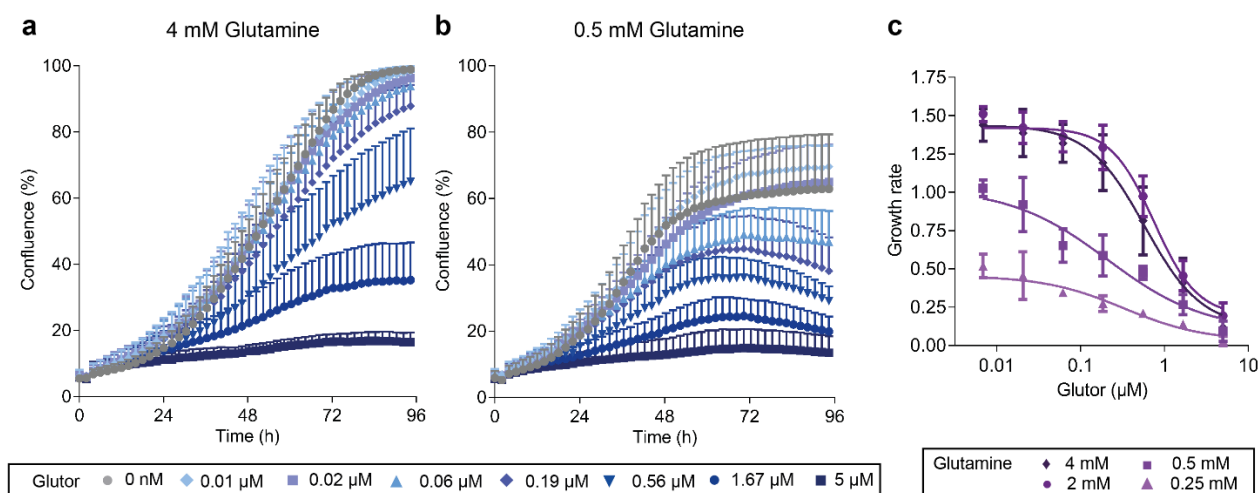


Figure 46 Glutor potency on cancer cell growth inhibition depended on the extracellular glutamine concentration. HCT116 cells were treated with different Glutor concentrations at 4 mM (a,c), 2 mM (c), 0.5 mM (b,c) or 0.25 mM (c) glutamine and 25 mM glucose over 96 h (b). Cell growth was monitored by means of live-cell microscopy and cell confluence was determined as a measure of cell growth (a,b). The growth rates (c) were determined by calculating the slope of the exponential growth phase to obtain GI_{50} values. Data show mean values \pm s.d. ($n=3$, $N=3$).

Table 11 GI_{50} values after treatment of HCT116 cells with Glutor at different glutamine concentrations.

Glutamine	4 mM	2 mM	0.5 mM	0.25 mM
GI_{50} (nM)	604.1 ± 290.7	639.0 ± 84.0	210.4 ± 43.7	222.2 ± 73.9

To exclude a rapid effect of glutamine on the cellular metabolism, a glycolysis stress assay (Seahorse XFP) was performed in the presence of 2 mM and 0.5 mM glutamine (Figure 47). Here, HCT116 cells, which were incubated for 1.5 h without glucose and with varying glutamine concentrations (0.5 mM and 4 mM), did not show a different response towards glucose uptake

Results

inhibition by means of Glutor treatment. This indicates a long-term effect as suggested by the previous conducted nutrient dependence assays (Figure 44). Furthermore, lower glutamine concentrations (0.5 mM) did not affect glycolytic (Figure 47a) or respiratory function (Figure 47) stronger than in presence of 4 mM glutamine.

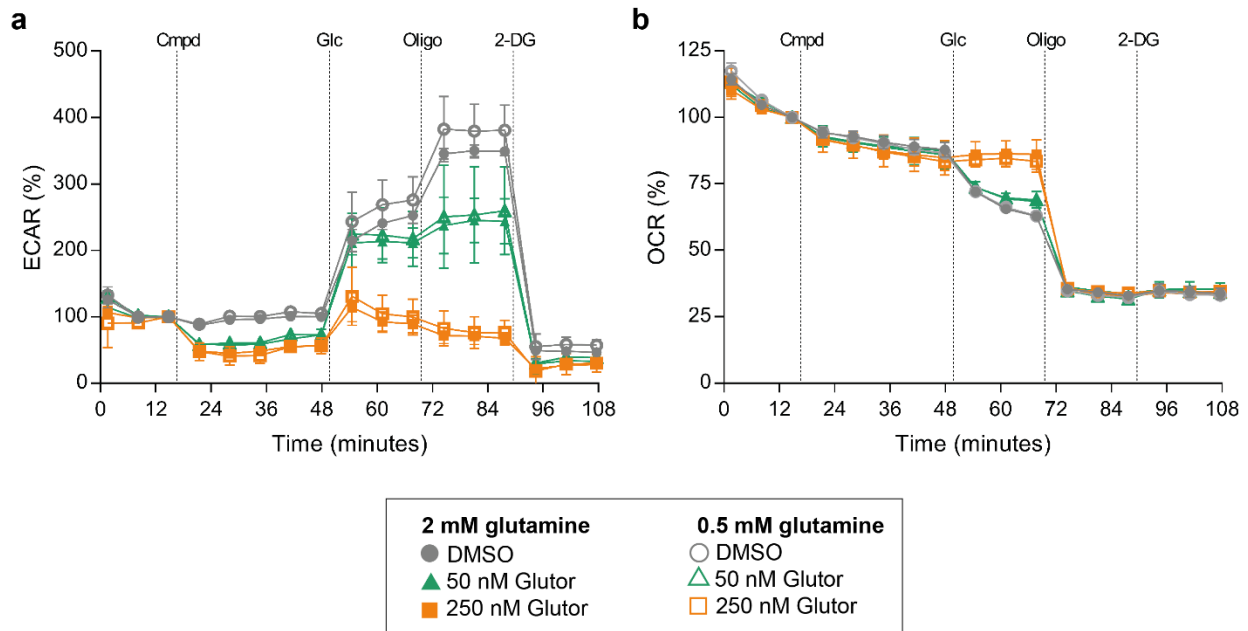


Figure 47 Extracellular glutamine levels had no short-term effect on glycolysis and respiration. HCT116 cells were subjected to a glycolysis stress test after 45 min glucose starvation in the presence of different glutamine levels (2 mM or 0.5 mM). The extracellular acidification rate (ECAR, a) and the oxygen consumption rate (OCR, b) were monitored using a Seahorse XFp analyzer. Data show mean values \pm s.d. ($n=3$, $N=2$). Cmpd=compound/DMSO; Glc=10 mM glucose; Gln=glutamine; Oligo=2.5 μ M Oligomycin; 2-DG=50 mM 2-deoxy-*D*-glucose.

Since nutrient dependence can vary according to the used cell culture model (monolayer cultured cells, spheroids, mouse xenograft models)^{64,135}, spheroids of the model cell line HCT116 were investigated for their glucose and glutamine dependence by means of live-cell imaging (Figure 48a). Large spheroids (800 μ m) were employed since an increased spheroid diameter results in a stronger nutrient gradient in comparison to smaller (400 μ m) spheroids that were employed previously (Figure 30).¹²⁶ At high glutamine concentration (4 mM) and high glucose concentration (25 mM), spheroids show an intact, round shape and the formation of a small necrotic core as visualized by weak propidium iodide (PI) staining. Physiological glucose concentration led to the

Results

development of a large necrotic core after 24 h of treatment and glucose depletion resulted even in spheroid bursting (Figure 48a, upper row). This response is in line with the results obtained in previous experiments (Figure 30). The variation of the extracellular glutamine concentration did not change the response of the spheroid (Figure 48a, lower row). Thus, glutamine depletion seems to have a lower impact on spheroid viability than glucose depletion, which is the opposite result to that obtained from the monolayer cultured cells described in chapter 8.3.8 (Figure 44).

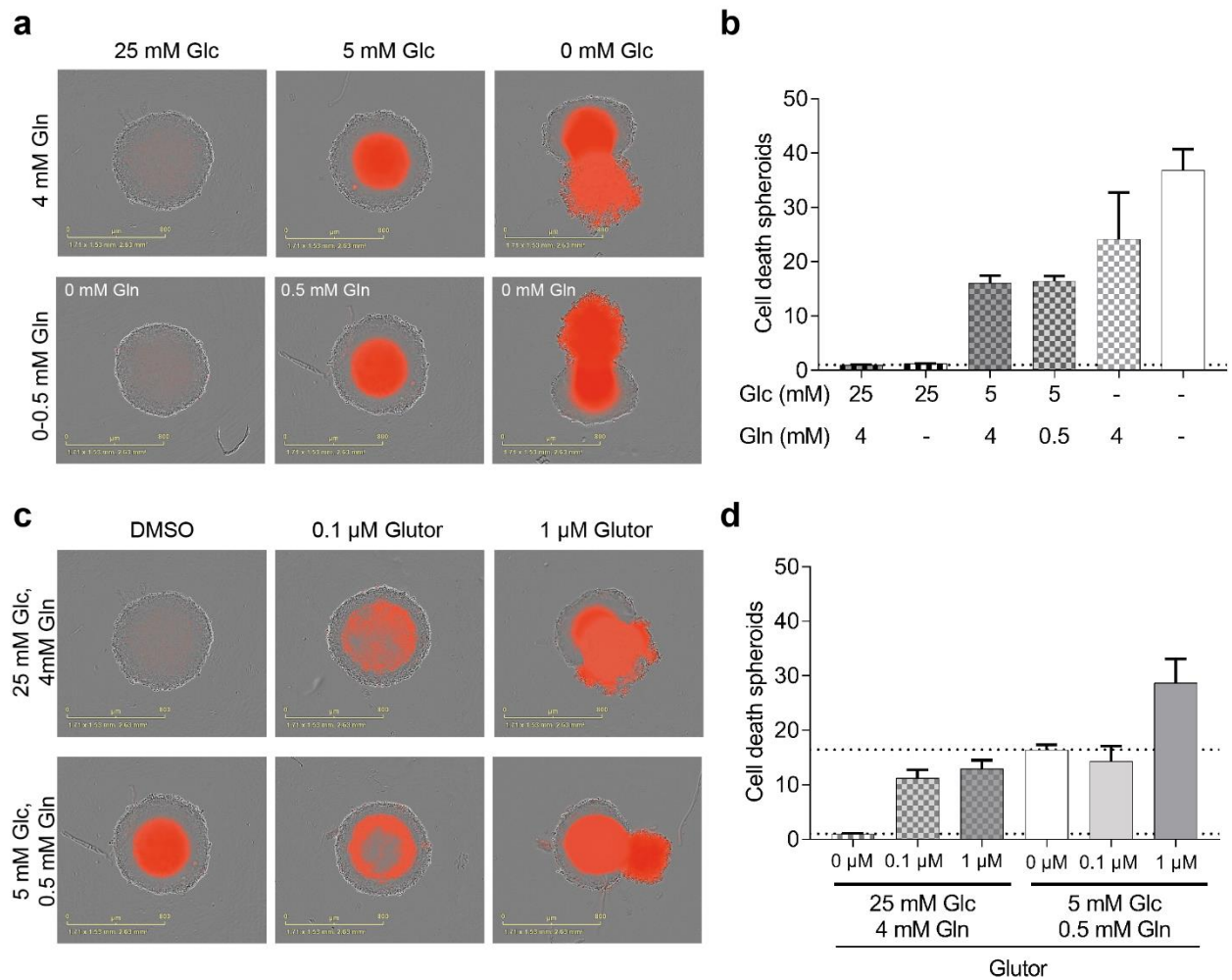


Figure 48 Glutator treatment and glucose withdrawal led to formation of necrotic core and spheroid bursting. HCT116 cells were cultured as spheroids and treated with compound or under nutrient varying conditions for 72 h. Cell integrity was monitored with propidium iodide (PI) staining. a,c) Representative images after 24 h of treatment under the indicated conditions. b,d) Quantification of PI staining after 24 h of treatment. Data is normalized to the value of cells cultured in presence of 25 mM glucose and 4 mM glutamine (which were set to 1) and show mean values \pm s.d. (n=3, N=8). Glc=glucose, Gln=glutamine.

Quantification of the PI intensity confirmed that no difference in the level of cytotoxicity was detected when the glutamine concentration (0-0.5 mM vs. 4 mM glutamine) was varied in the presence of 25 mM or 5 mM glucose (Figure 48b). Slight changes in spheroid viability were observed in the absence of glucose (0 mM) and varying glutamine concentrations (0 mM vs. 4 mM glutamine) (Figure 48b). An increased glutamine dependence was reported for a KRas-driven lung cancer cell line cultured *in vitro* compared to mouse xenograft models of the same cell lines.⁶⁴ The results described in this work confirm the observation that the cell culture model can have a great impact on nutrient dependence.

Furthermore, the spheroids were treated with different Glutor concentrations under cell culture conditions (25 mM glucose, 4 mM glutamine) or physiological glucose (5 mM) and glutamine (0.5 mM) concentrations (Figure 48c). Similar to the variation in glucose concentration (Figure 48a), treatment with 100 nM Glutor in the presence of 25 mM glucose and 4 mM glutamine induced the formation of a large necrotic core and 1 μ M Glutor led, as under glucose deprivation conditions, to spheroid bursting (Figure 48c). Untreated spheroids revealed that viability was affected stronger under physiological conditions compared to normal cell culture conditions, whereas only minor differences were observed when the cells were treated with Glutor in the presence of different nutrient concentrations (Figure 48c). Quantification of the PI intensity revealed that control cells (25 mM glucose, 4 mM glutamine) showed very low cytotoxicity, but treatment with 0.1 μ M or 1 μ M Glutor at normal cell culture conditions induced necrosis to a similar degree (Figure 48d). When the concentrations of glucose and glutamine are reduced to physiological level (5 mM glucose, 0.5 mM glutamine), the effect of 0.1 μ M Glutor on the viability of the spheroids is not impeded stronger. Nonetheless, 1 μ M Glutor increased the level of cytotoxicity by nearly 2-fold (Figure 48d). Thus, the usage of a physiologically more relevant cell culture model suggests that the glucose dependence is higher than the glutamine dependence in the model cell line HCT116 in 3D cell culture. Nonetheless, low glutamine concentrations still increased the effect of Glutor on spheroid viability.

8.3.9 Influence of co-treatment on growth of HCT116 cells

8.3.9.1 Synergism with GLS inhibitor CB-839

Since the experiments described above revealed that glutamine reduction increases cellular sensitivity towards Glutor treatment, the possibility of applying a combinatory treatment approach was investigated. The glutaminase inhibitor CB-839⁸⁰ is a nanomolar inhibitor of the glutaminase kidney isoform GLS (IC_{50} =20-30 nM) as tested in a biochemical assay employing GLS expressing kidney and brain homogenates.⁸⁰ Furthermore CB-839 inhibits the growth of triple-negative breast cancer (TNBC) cells with an IC_{50} value of 20-55 nM.⁸⁰ The compound is currently investigated in clinical trials in combination with different anticancer drugs such as the tyrosine kinase inhibitor Cabozantinib, the immune checkpoint (PD-L1/2) inhibitor Nivolumab and the chemotherapeutic cytidine analogue Azacitidin.⁸¹ CB-839 was employed to interrupt glutamine metabolism and reduce one possible nutrient supply of the TCA cycle. CB-839 was administered at three different concentrations (0.05 μ M, 0.5 μ M, 5 μ M) in the presence of 25 mM glucose and 4 mM glutamine with increasing concentration of Glutor (Figure 49) in HCT116 cells. The concentration-dependent effect of Glutor on HCT116 cell growth increased with rising CB-839 concentration (Figure 49a-d). In order to quantify the observed effect, the growth rates and the respective GI_{50} values of compound-treated HCT116 cells were determined (Figure 50a). These data revealed that the addition of CB-839 decreases the GI_{50} value of Glutor in HCT116 cells from 428 ± 157.3 nM down to 61.0 ± 16.2 nM in the presence of 0.05 μ M CB-839 and to 40.4 ± 10.5 nM in the presence of 0.5 μ M CB-839 (Figure 50a). The co-treatment of Glutor and 5 μ M CB-839 lowered the GI_{50} of Glutor by 40-fold down to 10.4 ± 0.8 nM compared to cells treated only with the glucose uptake inhibitor (Figure 50a).

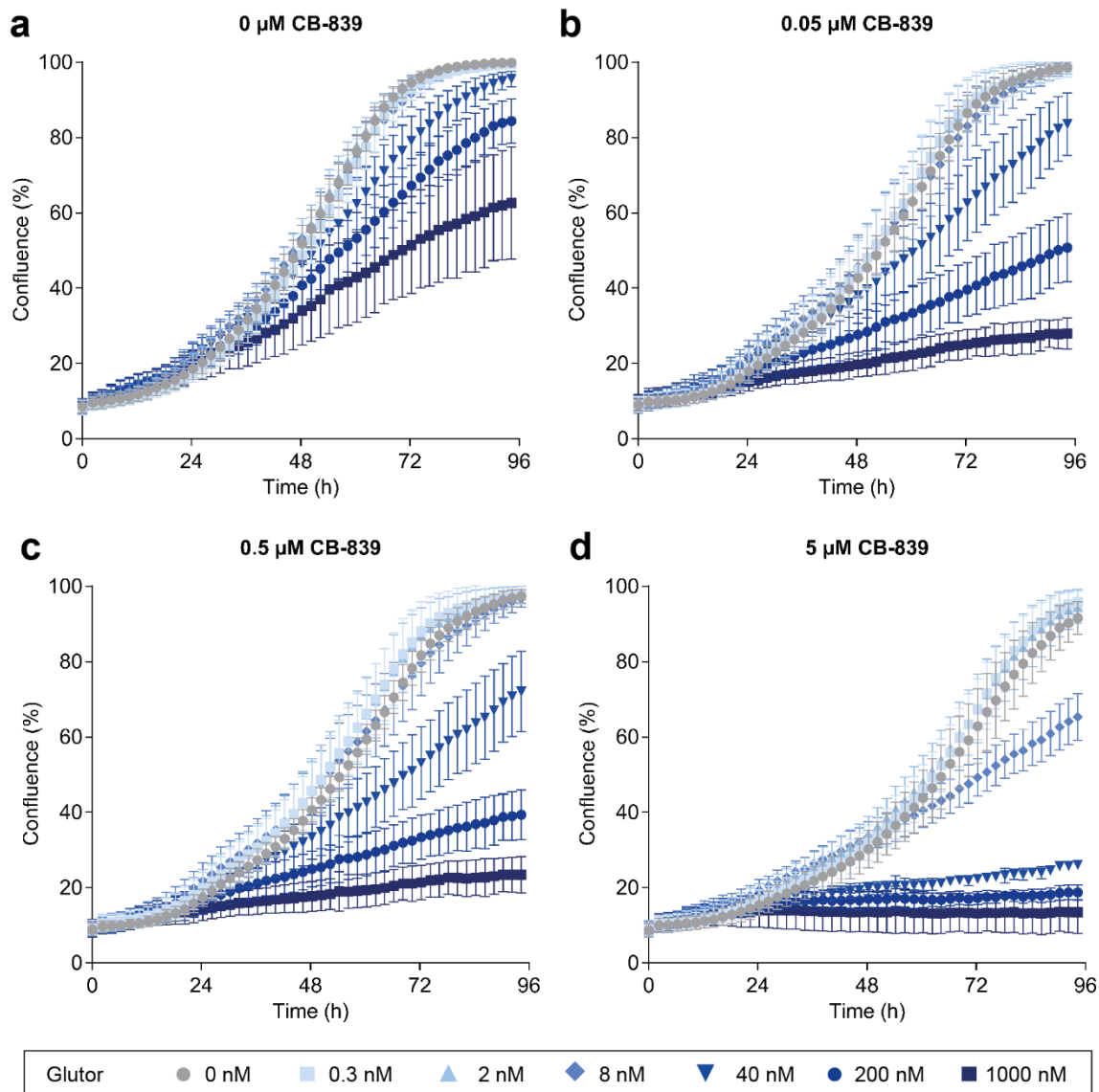


Figure 49 Co-treatment of HCT116 cells with Glutator and glutaminase inhibitor CB-839 revealed a beneficial effect on growth inhibition. HCT116 cells were treated for 96 h simultaneously with Glutator and glutaminase inhibitor CB-839. Cell growth was monitored via live-cell imaging using the IncuCyte® ZOOM to determine the cell confluence as a measure of cell growth. Data show mean values \pm s.d. ($n=3$, $N=3$).

In order to assess if the observed effect is due to a synergistic action of both compounds, the open source software combenefit¹⁰⁵ was employed. Combenefit combines different established models, namely Loewe,¹⁰⁶ HSA¹⁰⁸ and Bliss,¹⁰⁷ that are used to determine synergy and antagonism scores.

Results

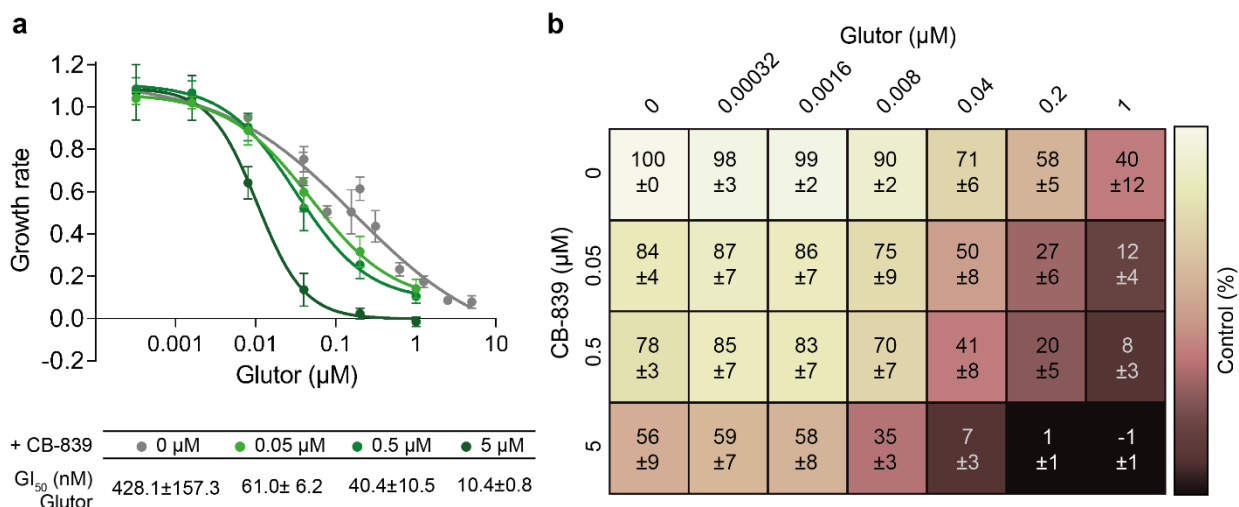


Figure 50 Growth rate inhibition during co-treatment experiments with Glutor and CB-839 in HCT116 cells. Growth rates were calculated via determination of the linear regression during the exponential growth phase (Figure 49). a) Dose-response curves were normalized to DMSO. GI_{50} values are given in the adjacent table. Data show mean values \pm s.d. of $n=3$, $N=3$ (0.05 μM , 0.5 μM , 5 μM Glutor) or $n=6$, $N=3$ (0 μM , Figure 26c). b) Growth rates were normalized to the value of DMSO-treated cells. Values were used for calculation of a potential synergistic effect (Figure 53). Data show mean values \pm s.d. ($n=3$, $N=3$).

For data analysis, all growth rate values were normalized to DMSO-treated cells (Figure 50b) to generate graphs that display the dose-response shifts during co-treatment (Figure 51). Single agent dose-response curves were generated to determine the interpolated IC_{50} values for Glutor (3.05 μM) and CB-839 (35.6 μM) (Figure 52).

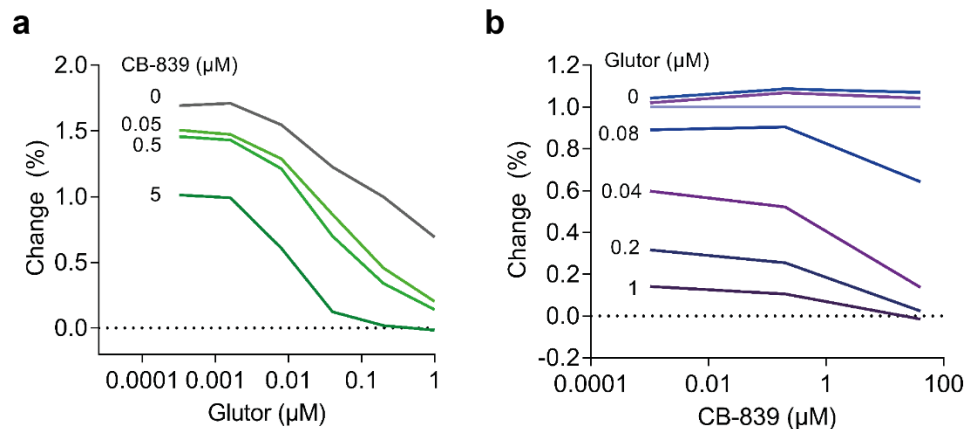


Figure 51 Dose-response shifts for co-treatment with Glutor and CB-839. Growth rates as determined in Figure 50 b for Glutor (a) or CB-839 (b).

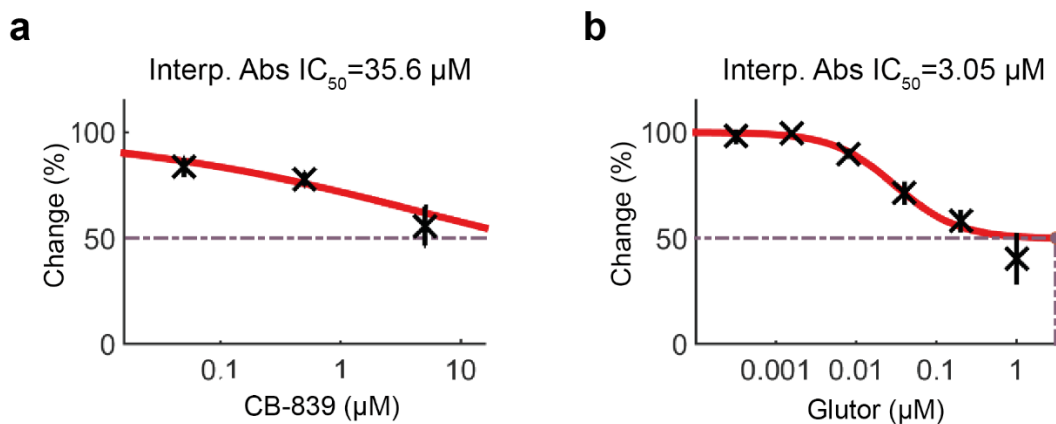


Figure 52 Single agent dose-response curves during treatment of HCT116 cells with Glutor or CB-839. Interpolated IC_{50} values were determined from the changes in growth rates (Figure 50b) using the software combenefit.¹⁰⁵ Graphs show mean values \pm s.d. ($n=3$, $N=3$). Interp.=interpolated, Abs=absolute.

Calculation of the synergy and antagonism scores during co-treatment revealed a strong synergistic effect of CB-839 and Glutor as calculated by all three independent models (Figure 53a-f). All models calculated the strongest synergy between 0.04 μ M and 1 μ M Glutor and 0.5 μ M and 5 μ M CB-839, whereas the synergy scores calculated with the Bliss model were lower (Figure 53e) than the scores calculated with the HSA and Loewe models (Figure 53a,c). Thus, cell sensitivity towards Glutor treatment can be increased by cutting another important nutrient source that fuels the TCA cycle. This can be achieved by means of a combinatorial treatment approach employing the GLS inhibitor CB-839 and might reveal a novel therapeutic anti-cancer strategy.

Results

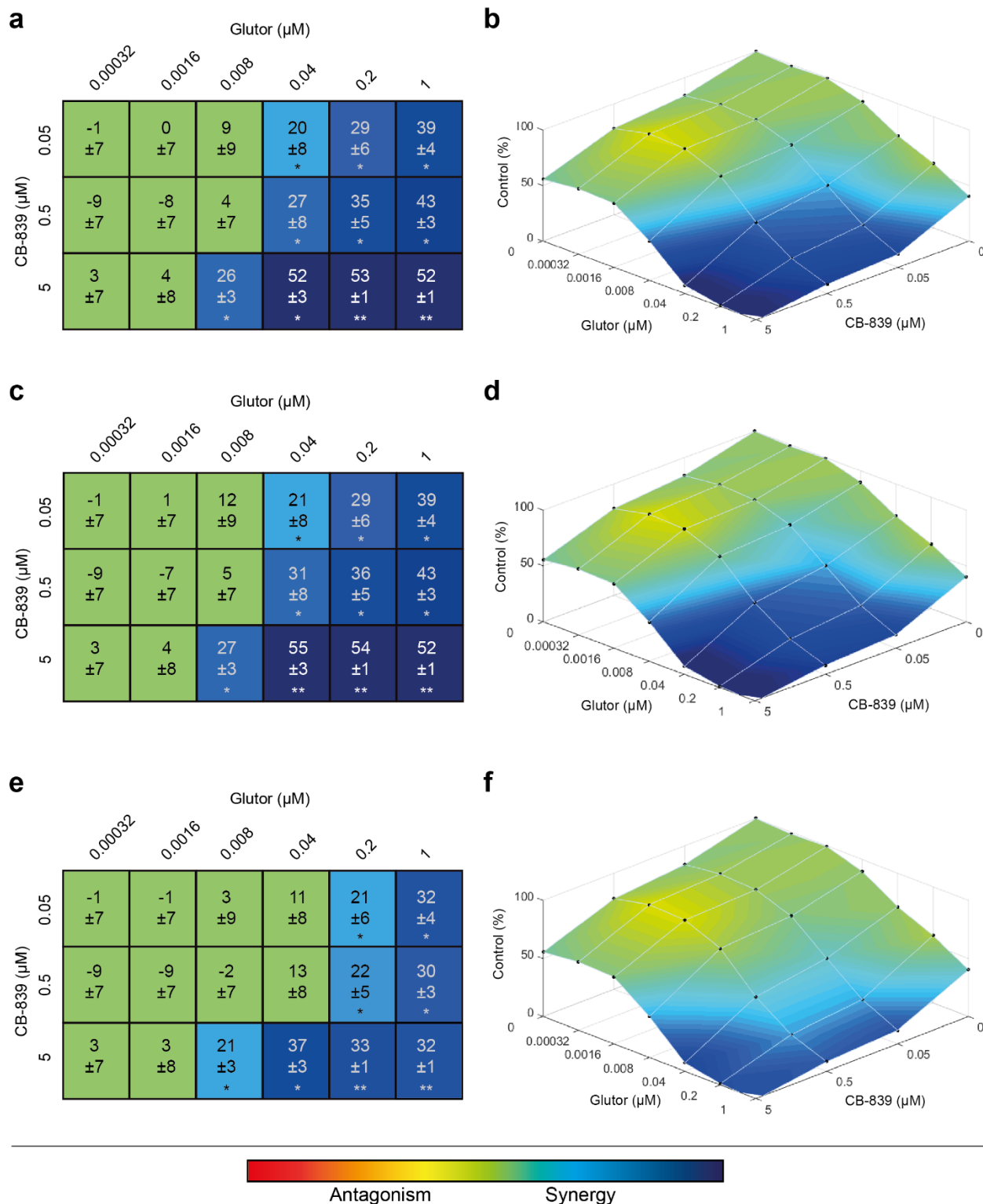
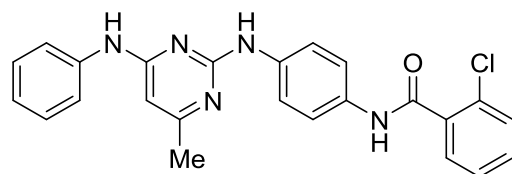


Figure 53 Glutor and CB-839 inhibited cancer cell growth synergistically. Synergy and antagonism scores were calculated using the software combenefit¹⁰⁵ employing the models Loewe¹⁰⁶ (a,b), highest single agent (HSA, c,d)¹⁰⁸ and Bliss¹⁰⁷ (e,f). The slopes calculated in Figure 50 b were used for the calculations. Synergy and antagonism scores are depicted in tables a,c,e or in the dose-response surface (Figure 51) within the applied concentration space of Glutor and CB-839. Data show mean values \pm s.d. (n=3, N=3). *: p<0.05; **: p<0.001.

8.3.9.2 Synergism with autophagy inhibitor Aumitin

The autophagy inhibitor Aumitin (Figure 54) was developed from a hit compound that was identified in a cell-based assay for autophagy modulators.



Aumitin
Mitochondrial complex I inhibitor
Autophagy inhibitor

Robke *et al.* 2018

Figure 54 Structure of the mitochondrial complex I and autophagy inhibitor Aumitin.

Aumitin inhibits starvation-induced autophagy with an $IC_{50}=1.4 \mu\text{M}$ in MCF7-GFP-LC3 cells.¹³⁶ Target identification revealed that complex I within the mitochondrial respiratory chain is the protein target of Aumitin.¹³⁶ Since the respiratory chain is involved in the generation of ATP and therefore closely connected to the TCA cycle, a combinatory treatment approach with **(S)-5n**, a less potent ($IC_{50}=0.38\pm 0.12 \mu\text{M}$) Glutor-derivative, and Aumitin was investigated. Of note, **(S)-5n** did not induce acute toxicity as monitored by the CellTiter-Glo® counterscreen.

HCT116 cells were treated with different concentrations **(S)-5n** and in the presence of different concentrations Aumitin (0 μM , 0.1 μM , 1 μM , 10 μM). The 13-fold less potent Glutor derivative **(S)-5n** ($IC_{50}=0.38\pm 0.12 \mu\text{M}$) showed no effect on the growth of HCT116 cells (Figure 56a). The presence of 100 nM Aumitin increased the cellular efficacy drastically to a GI_{50} value of $1.02\pm 0.63 \mu\text{M}$ (Figure 56a). Higher concentrations of Aumitin (1 μM and 10 μM) increased the potency of **(S)-5n** on cell growth by 3-5-fold, whereas no strong difference was observed between these both Aumitin concentrations (Figure 56a).

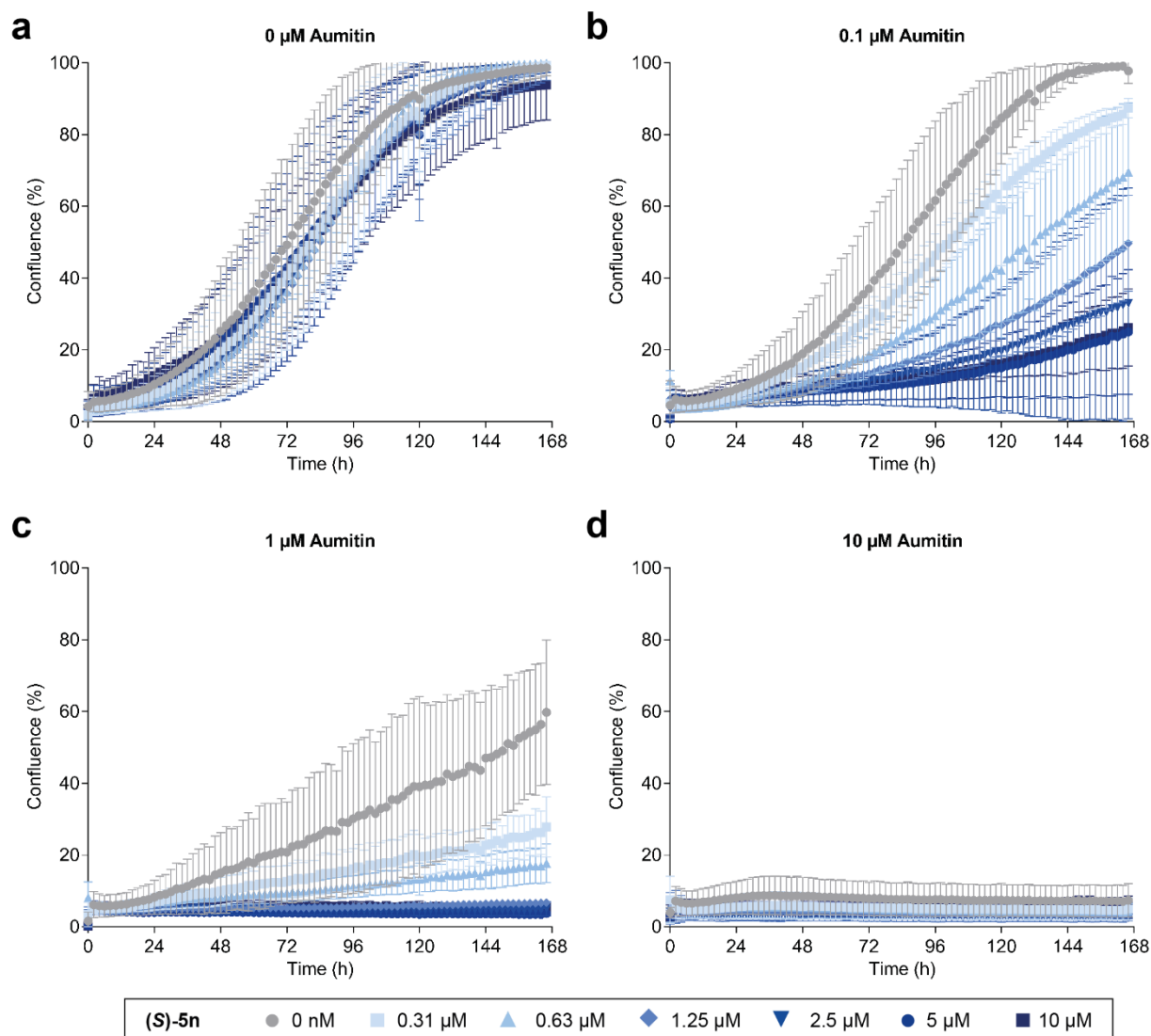


Figure 55 Co-treatment of HCT116 cells with (S)-5n and autophagy inhibitor Aumitin revealed a beneficial effect on growth inhibition. HCT116 cells were treated for 168 h simultaneously with (S)-5n and autophagy inhibitor Aumitin. Cell growth was monitored via live-cell imaging using the IncuCyte® ZOOM and cell confluence was assessed as a measure of growth. Data show mean values \pm s.d. ($n=3$, $N=3$).

The growth rates were normalized to DMSO-treated cells (Figure 56b) to reveal the dose-response shifts during co-treatment (Figure 57). The growth rates were further implemented in the software combenefit¹⁰⁵ to calculate synergy and antagonism scores.

Results

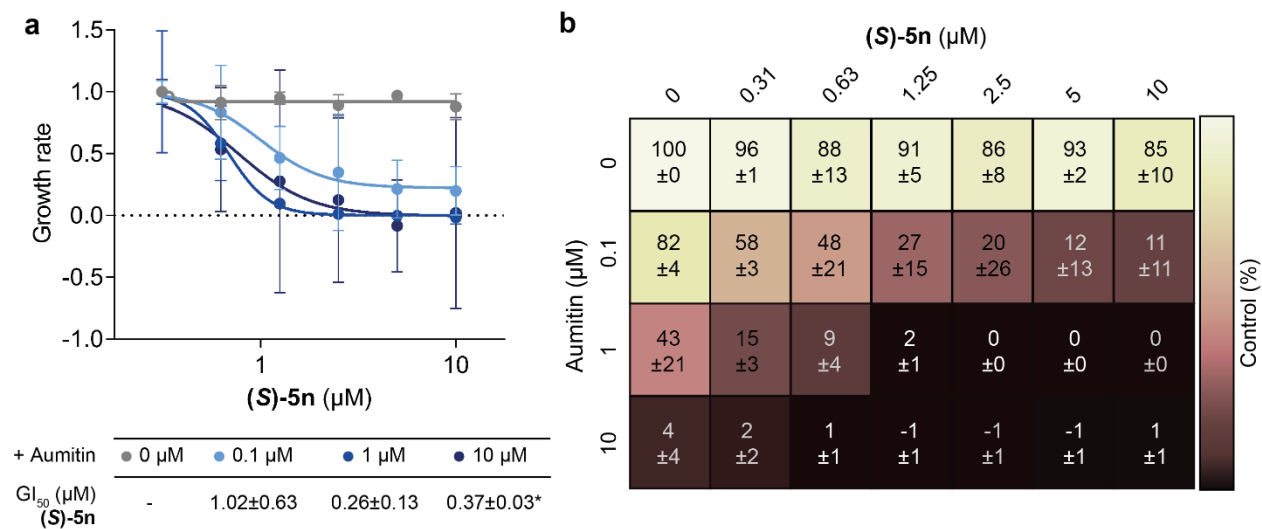


Figure 56 Dose-response curves for co-treatment of HCT116 cells with (S)-5n and Aumitin. Growth rates were calculated via determination of the linear regression during the exponential growth phase (Figure 55). a) Data of dose-response curves was normalized to the value cells treated with 0 μM (S)-5n. GI_{50} values are given in the adjacent table. Data show mean values \pm s.d. ($n=3$, $N=3$). * GI_{50} value was determined of $n=2$ due to incorrect fitting of one biological replicate. b) Growth rates are normalized to the value of DMSO-treated cells. Values were used for calculation of a potential synergistic effect (Figure 58). Data show mean values \pm ($n=3$, $N=3$).

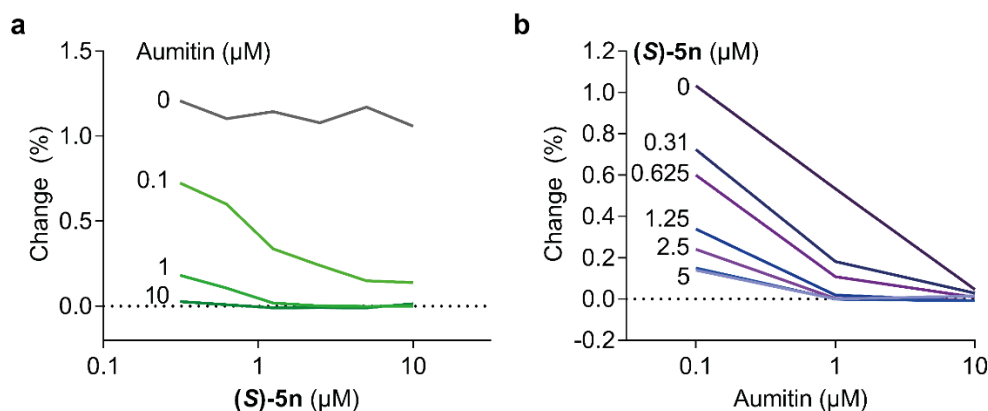


Figure 57 Dose-response shifts during co-treatment of HCT116 cells with (S)-5n and Aumitin. The growth rates (Figure 56) were plotted against the (S)-5n (a) or the Aumitin (b) concentration. Data show mean values ($n=3$, $N=3$).

Determination of the synergy and antagonism scores with the aforementioned established models Loewe,¹⁰⁶ HSA¹⁰⁸ and Bliss¹⁰⁷ revealed a clear synergistic effect between the compounds (S)-5n and Aumitin (Figure 58).

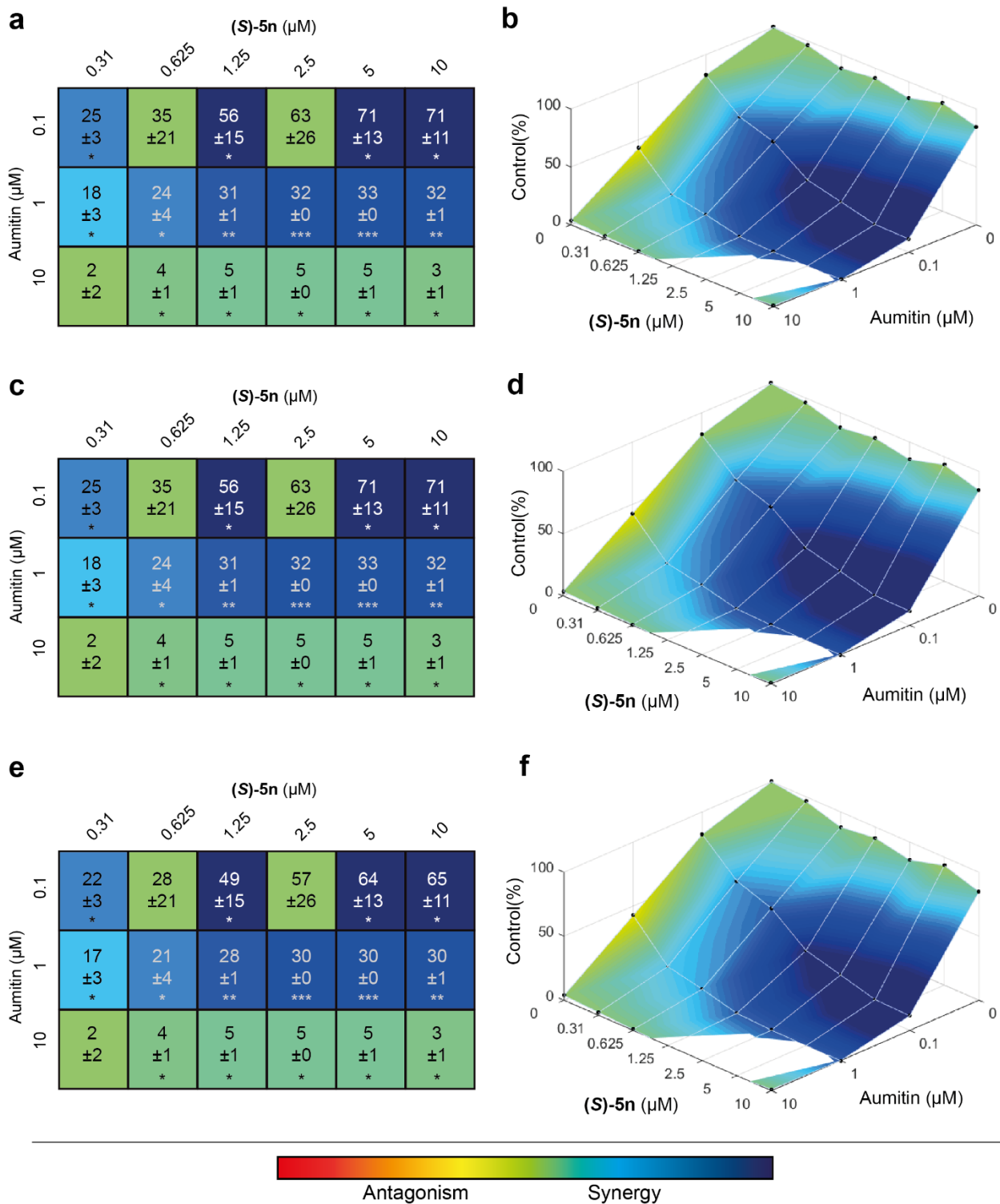


Figure 58 Overview of synergy and antagonism scores after co-treatment of HCT116 cells with (S)-5n and Aumitin. Synergy and antagonism scores were calculated using the software combenefit¹⁰⁵ employing the models Loewe¹⁰⁶ (a,b), highest single agent¹⁰⁸ (HSA, c,d) and Bliss¹⁰⁷ (e,f). The slopes calculated in **Figure 57** a were used for the calculations. Synergy and antagonism scores are depicted in tables a,c,e or in the dose-response surface (**Figure 57** b,c) within the applied concentration space of (S)-5n and Aumitin. Data show mean values ±s.d. (n=3, N=3). *: p<0.05; **: p<0.001; ***: p<0.0001.

All models identified the highest synergy between 5 μM and 10 μM **(S)-5n** and addition of 0.1 μM Aumitin (Figure 58a,c,e). The visualization of the synergy and antagonism scores in the dose-response surface within the concentration space of **(S)-5n** and Aumitin revealed also a strong synergy around 1 μM Aumitin (Figure 58b,d,f). Thus, also interference with the mitochondrial respiratory chain and glucose uptake inhibition synergistically inhibit cell growth. Collectively, HCT116 cancer cells show a high counter dependence on the two major building block- and energy-generating pathways, glycolysis and oxidative phosphorylation, including the TCA cycle. This reflects the metabolic plasticity of cancer cells and their adaptation to phases of nutrient shortage.

8.4 Biological characterization of other GLUT inhibitors

8.4.1 (+)-Glupin-1

(+)-Glupin-1 (Figure 59a) (GLucose Uptake Inhibitor) is a glucose uptake inhibitor that was developed by Melanie Schwalfenberg and Dr. Javier de Ceballos from an indomorphans-based hit substance from the semi-automated screening as described in chapter 8.1 (Figure 11).

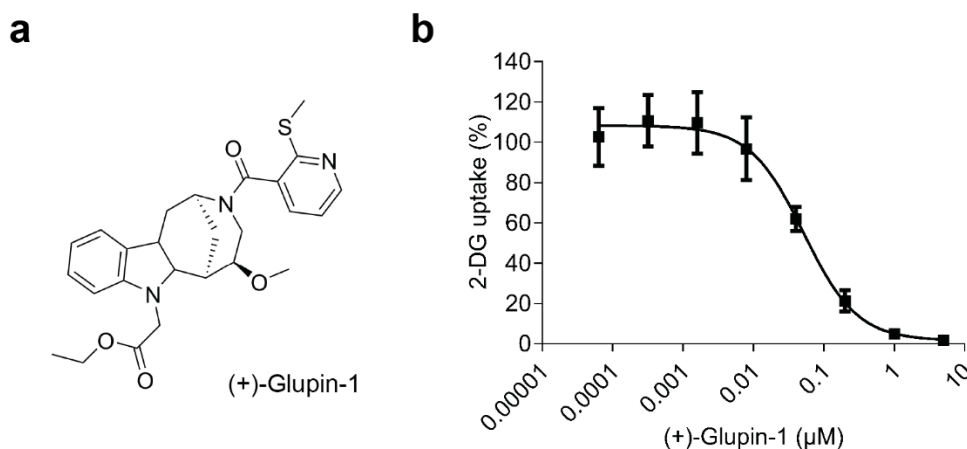


Figure 59 (+)-Glupin-1 inhibited 2-DG uptake with low nanomolar potency. a) Chemical structure of (+)-Glupin-1. b) Dose-response curve for (+)-Glupin-1 in the resazurin-coupled 2-DG uptake assay. Data show mean values \pm s.d. (n=3, N=3).

(+)-Glupin-1 inhibited the uptake of 2-DG in HCT116 cells with an IC_{50} value of 51.5 ± 7.6 nM (Figure 59b, as part of the Bachelor thesis of Aylin Binici). Furthermore, (+)-Glupin-1 did not inhibit the endogenous hexokinase activity in HCT116 whole cell lysates (Figure 60).

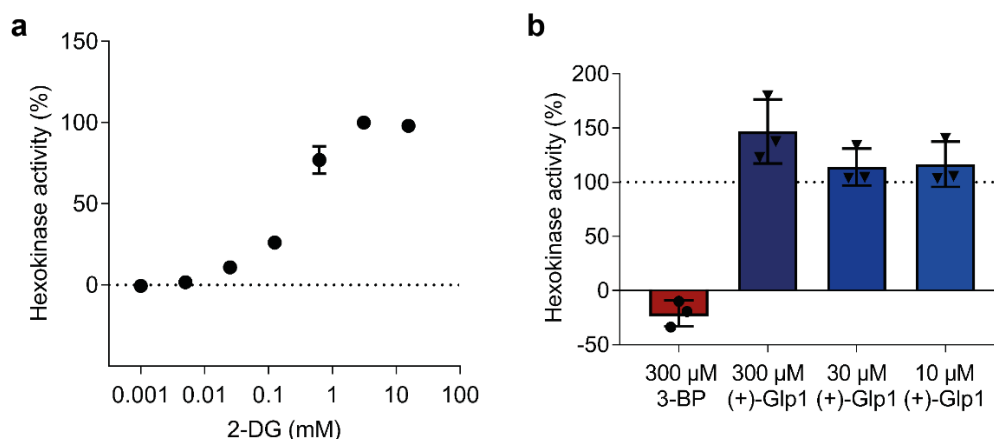


Figure 60 (+)-Glupin-1 did not interfere with endogenous hexokinase activity. NADP⁺ and glucose-6-phosphate dehydrogenase were supplemented to HCT116 whole cell lysates and NADPH+H⁺ generation was monitored at ex/em 340 nm/445 nm in the presence increasing 2-DG concentrations (a). b) (+)-Glupin-1 or DMSO was added to the cell lysates in presence of 3.12 mM 2-DG. 3-Bromopyruvate¹¹⁰ served as a control. Data is normalized to the highest 2-DG concentration (15.56 mM, a) or the prevalent 2-DG concentration upon compound addition (3.12 mM, b). Data show mean values \pm s.d. (n=3, N=3). (+)-Glp1=(+)-Glupin-1.

HCT116 cells that were cultured in the presence of 10 mM galactose showed a reduced growth behavior when treated with (+)-Glupin-1 compared to cells cultured with 25 mM glucose. This result indicates mitochondrial toxicity of the compound (Figure 61a). The control compound Oligomycin influences the cell growth in presence of galactose even stronger (Figure 61b). Therefore, the mitochondrial function seems to be only slightly impaired by (+)-Glupin-1.

Furthermore, (+)-Glupin-1 reduced the glycolysis rate in a concentration-dependent manner once glucose is added to MDA-MB-231 cells (Figure 62a). A high (+)-Glupin-1 concentration of 1 μ M led to complete inhibition of glycolysis (Figure 62a). The increase in glycolysis upon glucose addition in the absence or low concentration of (+)-Glupin-1 (0.01 μ M, 0.1 μ M) led to a decrease in oxidative phosphorylation at the same time (Figure 62b). In the presence of 1 μ M (+)-Glupin-1,

Results

the level of oxidative phosphorylation remains at a constant high level (Figure 62b), as observed for Glutor-treated HCT116 (Figure 24b,c) and UM-UC-3 cells (Figure 31a,b) before.

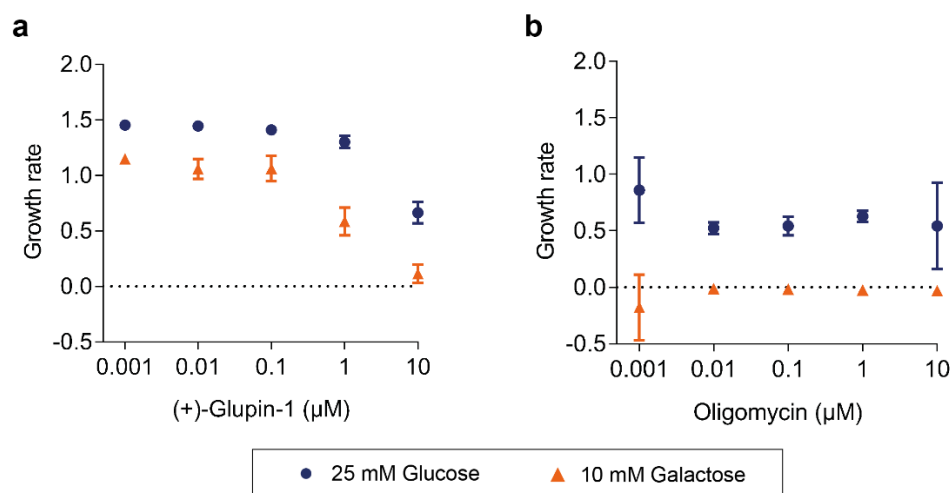


Figure 61 (+)-Glupin-1 showed slight mitochondrial toxicity. HCT116 cells were treated with (+)-Glupin-1 (a) or Oligomycin (b) in the presence of either 25 mM glucose or 10 mM galactose. Growth was monitored using the live-cell imaging device IncuCyte® ZOOM. Growth rates were calculated and normalized to the values of DMSO-treated cells. Data shown mean values \pm s.d. (n=3, N=3).

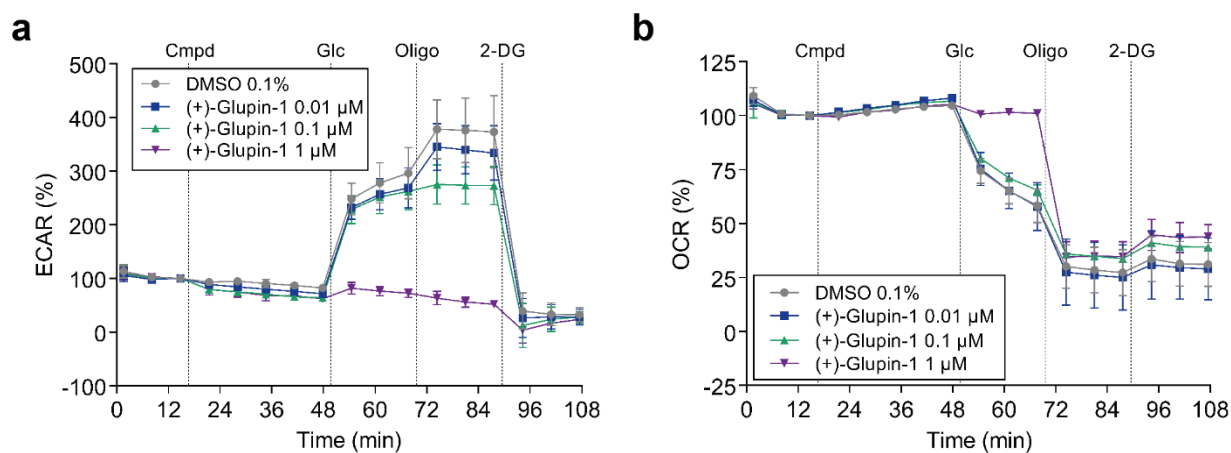


Figure 62 (+)-Glupin-1 inhibited glycolysis in MDA-MB-231 cells. MDA-MB-231 cells were starved of glucose for 45 min and subjected to a glycolysis stress test. The extracellular acidification rate (ECAR, a) as a measure of glycolysis and the oxygen consumption rate (OCR, b) as a measure of respiration were monitored using a Seahorse XFp device. Data show mean values \pm s.d. (n=3, N=2). Cmpd=compound/DMSO, Glc=10 mM glucose, Oligo=2 μM Oligomycin; 2-DG=100 mM 2-deoxy-D-glucose. Experiment was performed by Julian Wilke, MPI Dortmund.

Results

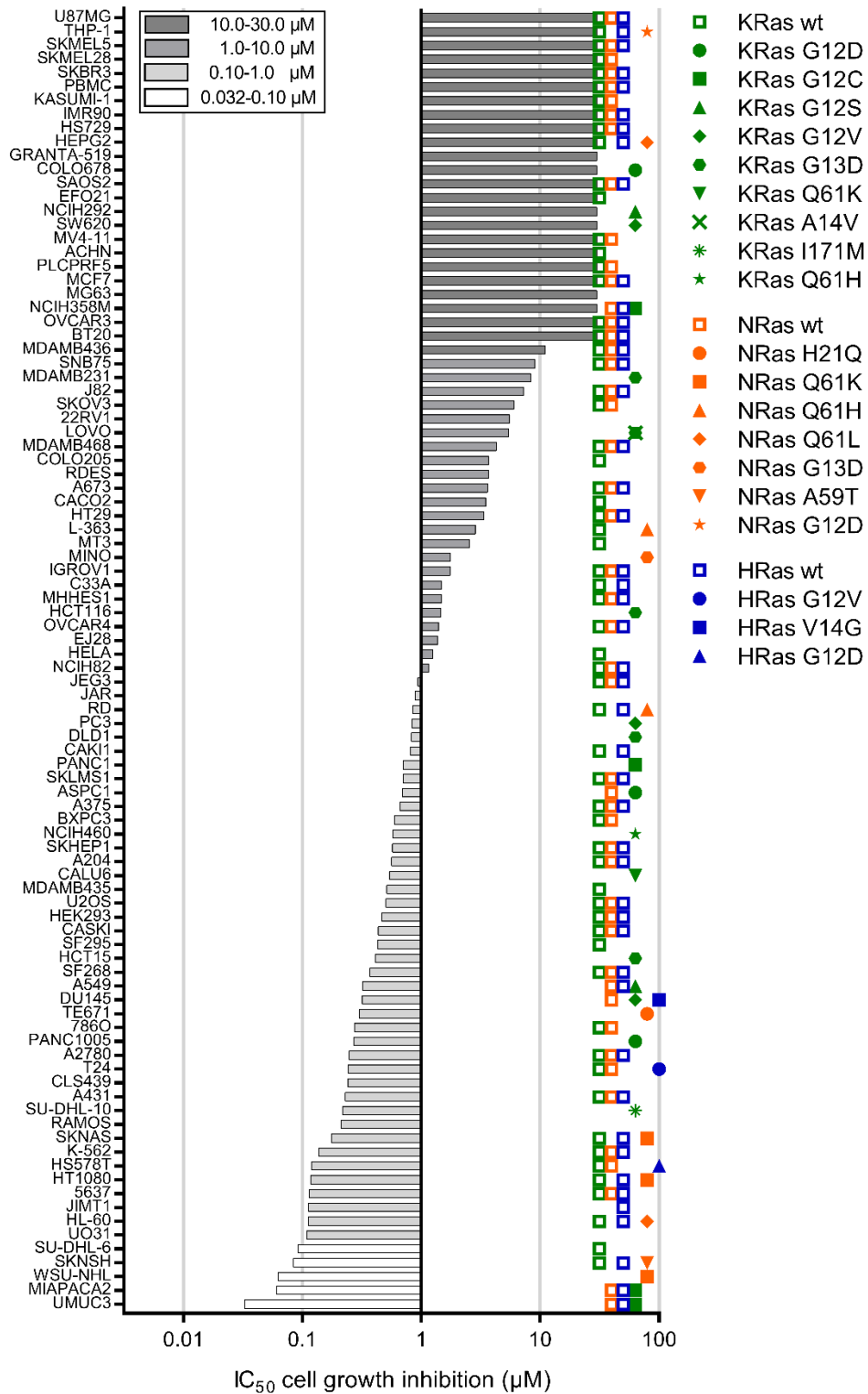


Figure 63 Growth inhibition of various cancer cell lines by (+)-Glupin-1. a) A panel of 94 cell lines was subjected to Sulforhodamine B assay after 72 h of (+)-Glupin-1 treatment. IC₅₀ values were determined after 72 h. The symbols indicate the mutational status of KRas, NRas and HRas as described in the Catalogue Of Somatic Mutations In Cancer (COSMIC)¹²¹. Sulforhodamine B assay was performed by Oncolead, Germany.

A panel of 94 different cell lines (Figure 63) was employed to test the range of (+)-Glupin-1 potency on cell growth as it was done for Glutor (Figure 27). Nearly half of the malignant cell lines (*i.e.*, 45 cell lines) exhibited IC_{50} values $<1 \mu\text{M}$ and 24 cell lines, including the non-malignant cell line IMR-90 as well as PBMCs, were resistant to (+)-Glupin-1 treatment ($IC_{50}>30 \mu\text{M}$, Figure 63). Analysis of the mutational status of KRas, NRas and HRas revealed an accumulation of point mutations among the more sensitive cell lines ($IC_{50} <1 \mu\text{M}$). Here, 23 out of 45 malignant cell lines bore a mutation in one of the three Ras isoforms (51%). In contrast, only 6 out of 22 resistant ($IC_{50}>30 \mu\text{M}$), malignant cell lines (27%) possessed a mutated form of one of the three Ras isoforms (Figure 63). Hence, a similar tendency toward accumulation of Ras mutation among the (+)-Glupin-1-sensitive cell lines was observed as it has been detected for Glutor-treated cells (Figure 27).

8.4.1.1 Target confirmation

GLUT-1 and GLUT-3 were identified as protein targets of (+)-Glupin-1 employing GLUT-1-4 overexpressing CHO cells (analog to chapter 8.3.6) that led to a partial rescue of 2-DG uptake inhibition in case of GLUT-1 and GLUT-3 overexpression (*work by Dr. George Karageorgis*). To confirm the proposed targets of (+)-Glupin-1, a proteome-wide CETSA® approach, thermal proteome profiling (TPP), was conducted using SW480 whole cell lysates that express high amounts of both GLUT isoforms. Compared to CETSA® that makes use of an immunoblot-based read-out of soluble protein fractions, TPP is predicated on the identification of the peptide mass finger prints via MS/MS analysis and database comparison to identify the corresponding proteins in the supernatant. TPP revealed a strong thermal stabilization of GLUT-3 ($\Delta T_m > 7.0 \text{ }^\circ\text{C}$) in the presence of $10 \mu\text{M}$ (+)-Glupin-1 (Figure 64b, Table 12). However, (+)-Glupin-1 exhibited only a slight influence on the thermal stability of GLUT-1 ($\Delta T_m = 2.6 \pm 0.5 \text{ }^\circ\text{C}$) and no influence on the reference protein $\text{Na}^+\text{-K}^+\text{-ATPase}$ ($\Delta T_m = -0.9 \pm 0.3 \text{ }^\circ\text{C}$) (Figure 64a,c, Table 12).

Results

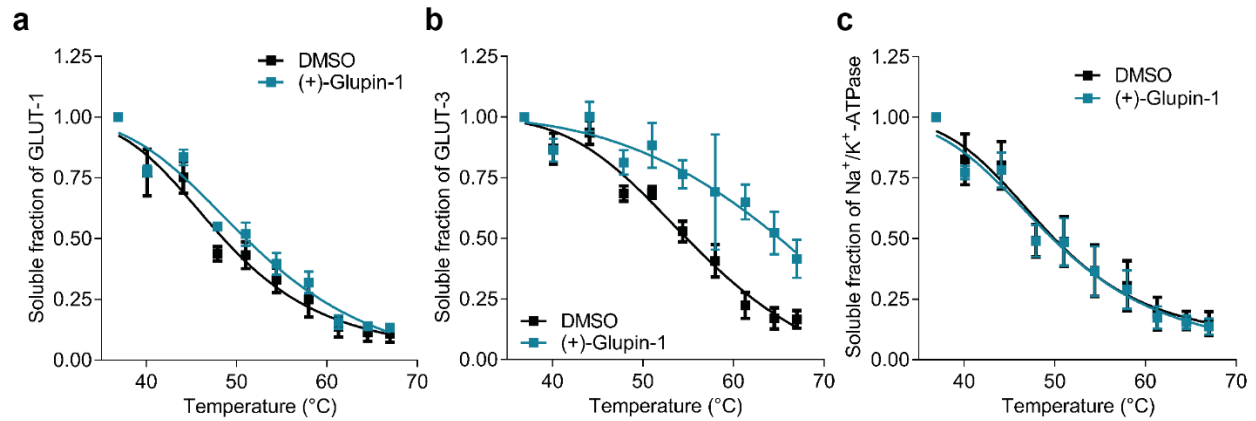


Figure 64 Melting curves of GLUT-1, GLUT-3 and Na⁺-K⁺-ATPase from TPP in the presence of (+)-Glupin-1. A thermal proteome profiling approach (TPP) was performed with SW480 whole cell lysates in the presence of 10 μM (+)-Glupin-1 or DMSO. The proteins GLUT-1 (a), GLUT-3 (b) and Na⁺-K⁺-ATPase (c) were identified in all three (GLUT-1/-3) or in two biological replicates (Na⁺-K⁺-ATPase) in the soluble fraction after heat treatment. Protein amount was normalized to the first temperature within the temperature gradient, *i.e.* 36.9 °C. The data was fitted using the Boltzmann equation. Data show mean values of n=3 ±s.d. (a,b) or n=2 ±s.d. (c).

Table 12 Overview of melting temperatures as determined in the TPP assay (Figure 64).

T _m (°C)	GLUT-1 (n=3)	GLUT-3 (n=3)	Na ⁺ /K ⁺ -ATPase (n=2)
(+)-Glupin-1	48.3±1.0	-	46.4±1.3
DMSO	45.7±0.9	53.1±0.5	47.3±1.0
ΔT _m	2.6±0.05	-	-0.9±0.3

A cellular thermal shift assay using immunoblot-based analysis was employed to confirm the observations of the TPP experiment using whole cell lysates of SW480 cells (Figure 65). As observed in the TPP assay, (+)-Glupin-1 altered the melting behavior of GLUT-3, which increased the T_m by >12 °C (Figure 65b, Table 13). GLUT-1 was stabilized by (+)-Glupin-1 with a ΔT_m of 6.5±0.6 °C (Figure 65a, Table 13), whereas the control protein Na⁺-K⁺-ATPase was not influenced in its melting behavior by (+)-Glupin-1 (Figure 65c, Table 13).

Results

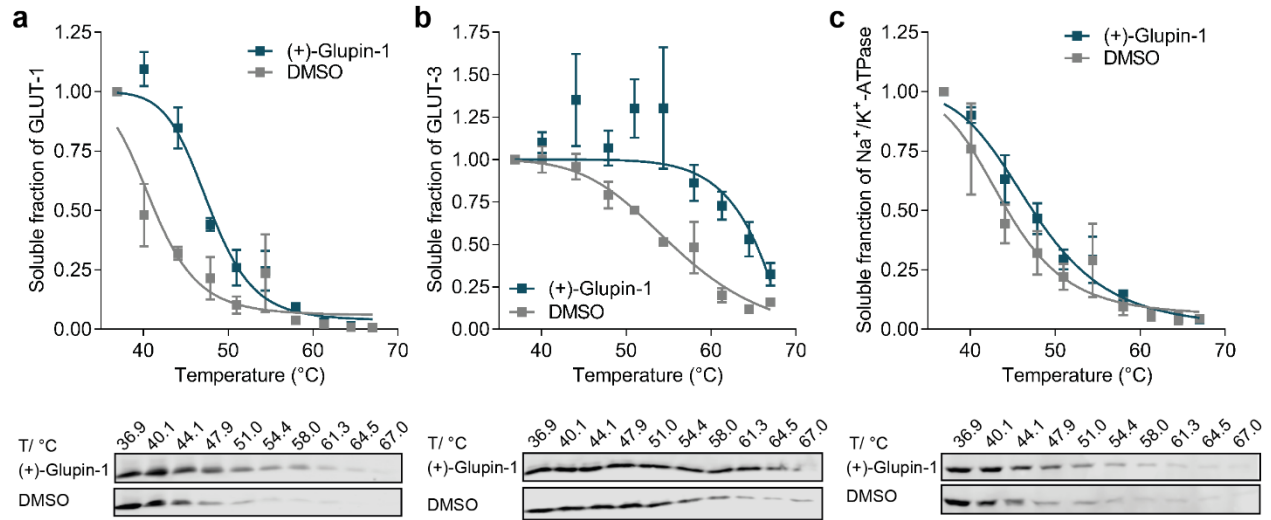


Figure 65 (+)-Glupin-1 stabilized GLUT-1 and GLUT-3 in a Cellular Thermal Shift Assay (CETSA®). A CETSA® approach was applied in SW480 whole cell lysate in the presence of 10 μ M (+)-Glupin-1 or DMSO. After ultracentrifugation, the supernatant was analyzed for GLUT-1 (a), GLUT-3 (b) or Na⁺/K⁺-ATPase (c) by means of immunoblotting and protein amount was quantified via densitometric analysis. Protein amount was normalized to the first temperature within the temperature gradient. The data was fitted using the Boltzmann equation. Data show mean values \pm s.d. (n=3). Blots are representative images of n=3.

Table 13 Overview of melting temperatures as determined in a CETSA® assay (Figure 65).

T _m (°C)	GLUT-1	GLUT-3	Na ⁺ /K ⁺ -ATPase
(+)-Glupin-1	47.2 \pm 0.8	-	45.8 \pm 1.8
DMSO	40.6 \pm 1.4	54.3 \pm 2.4	43.0 \pm 2.2
Δ T _m	6.5 \pm 0.6	-	2.8 \pm 1.5

8.4.1.2 Potential off-target effects of (+)-Glupin-1

The proteome-wide analysis of potential interaction partners for (+)-Glupin-1 revealed other proteins than GLUT-3 that were influenced in their thermal stability and could indicate potential off-target proteins (Figure 66, Figure 67, Appendix Figure 90, Figure 91 and Table 19). Selection of these proteins was based on a shift in melting temperature (same direction) in all three replicates and that the error bars of the mean values over all three replicates should not overlap in at least one temperature. In order to investigate if any of the identified off-targets are known interaction partners of each other, the STRING database was employed (Figure 66a). This

revealed that there are no known interactions between any of the identified off-target proteins. The proteins influenced strongest in their thermal stability by (+)-Glupin-1 are CDK2-associated and cullin domain-containing protein-1 (*CACUL1*), Canalicular multispecific organic anion transporter 2 (*ABCC3*), mitochondrial Trans-2-enoyl-CoA reductase (*MECR*) and PITH domain-containing protein 1 (*PITHD1*) (Figure 67). The mitochondrial Trans-2-enoyl-CoA reductase is a mitochondrial protein that is involved in the NAD⁺-dependent reduction of enoyl-CoA to acyl-CoA, which is an important step of fatty acid biosynthesis and is performed under anaerobic conditions.¹³⁷ An inhibition of this protein by (+)-Glupin-1 could explain the earlier observed mitotoxicity in HCT116 cells (Figure 61).

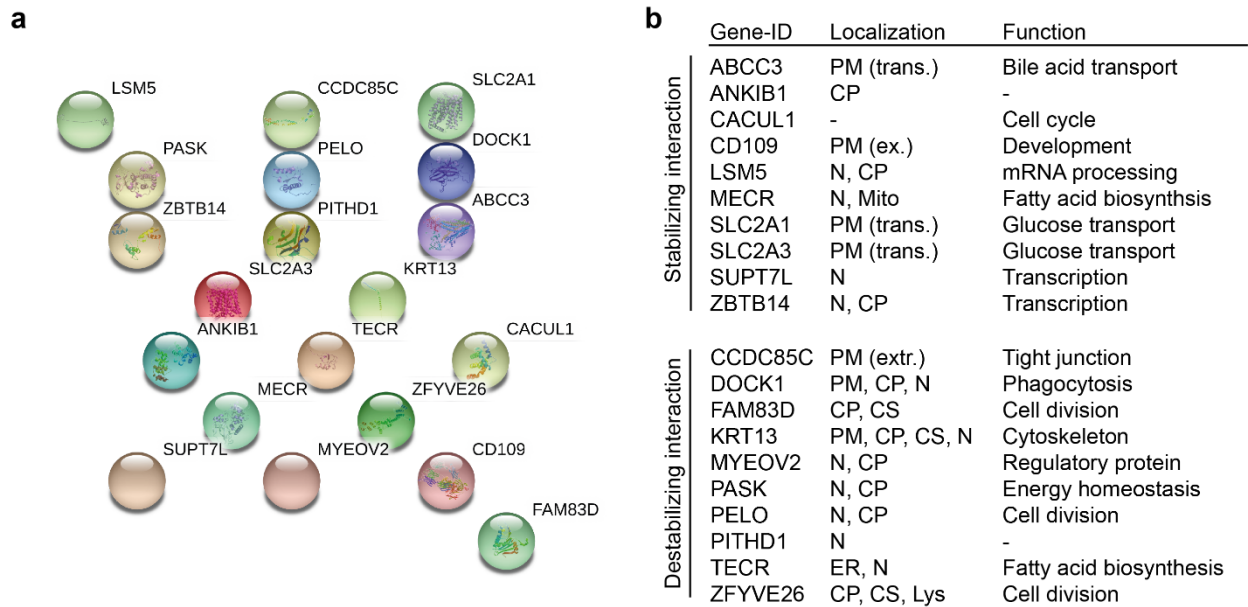


Figure 66 All interaction partners of (+)-Glupin-1 identified during thermal proteome profiling (TPP). a) Potential interaction partners among thermally influenced proteins by (+)-Glupin-1 were analyzed using the STRING database.¹³⁸ All proteins are named by their unique gene-ID. b) Overview of all proteins that are thermally stabilized or destabilized in the presence of 10 μ M (+)-Glupin-1. The protein's annotated localization as well as protein's function is given as indicated in the Uniprot database.¹³⁹ PM=Plasma membrane, CP=Cytoplasm, N=Nucleus, Mito=Mitochondrium, CS=Cytoskeleton, ER=Endoplasmic reticulum, Lys=Lysosome, trans.=transmembrane, ex.=extracellular.

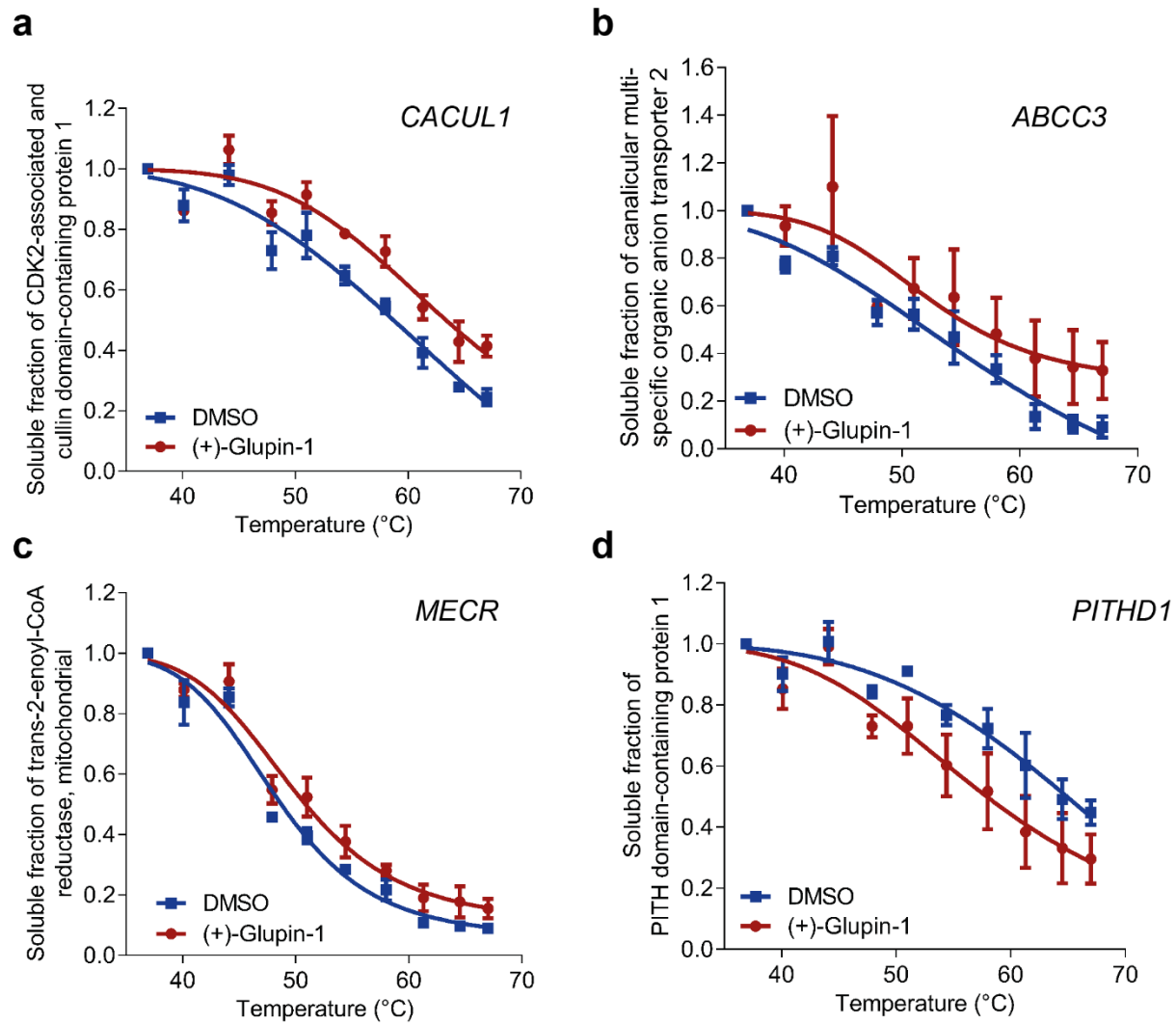


Figure 67 Further identified interaction partners of (+)-Glupin-1 from thermal proteome profiling (TPP). A thermal proteome profiling approach (TPP) was performed with SW480 whole cell lysates in presence of 10 μ M (+)-Glupin-1 or DMSO. The gene names (graph) and proteins names (y-axis) are given. The proteins CDK2-associated and cullin domain-containing protein 1 (a), canalicular multispecific organic anion transporter 2 (b), trans-2-enoyl-CoA reductase (c) and PITH domain-containing protein 1 (d) were identified in all three biological replicates in the soluble fraction after heat treatment. Protein amount was normalized to the first temperature within the temperature gradient. The data was fitted using the Boltzmann equation. Data show mean values \pm s.d. (n=3).

Table 14 Overview of melting temperatures as determined in a TPP approach (Figure 67).

T_m ($^{\circ}$ C)	<i>CACUL</i>	<i>ABCC3</i>	<i>MECR</i>	<i>PITHD1</i>
(+)-Glupin-1	58.9 \pm 1.3	50.6 \pm 2.4	48.1 \pm 0.6	53.1 \pm 1.8
DMSO	54.6 \pm 1.2	48.4 \pm 1.3	46.7 \pm 0.4	59.7 \pm 0.2
ΔT_m	4.3 \pm 2.2	2.2 \pm 2.8	1.4 \pm 0.8	-6.5 \pm 1.6

8.4.1.3 (+)-Glupin-1 induces GLUT-1 and GLUT-3 upregulation

In previous experiments, an upregulation of GLUT-1 and GLUT-3 after treatment of HCT116 cells with low glucose concentrations (0 mM, 1 mM) or Glutor of was observed (rescue mechanism, chapter 8.3.7). Hence, the influence of (+)-Glupin-1 on *GLUT1-4* mRNA level was investigated, in analogy to Glutor treatment. A slight increase of *GLUT1*, *GLUT3* and *B2M* could be observed in HCT116 cells after 24 h and 48 h of treatment with 0.5 μ M (+)-Glupin-1, even though this increase was not significant (Figure 68). *GLUT4* expression was slightly reduced after 24 h or 48 h of incubation with (+)-Glupin-1 (Figure 68). These results are in line with the effect of Glutor on the expression levels of *GLUT1*, *GLUT3*, *GLUT4* and *B2M* (Figure 38). *GLUT2* could not be detected and was not increased to detectable levels after (+)-Glupin-1 treatment. As GLUT-1 and GLUT-3 have been identified as the main targets of (+)-Glupin-1 in separate studies, the protein levels of these GLUT isoforms were investigated after treatment with the compound (Figure 69).

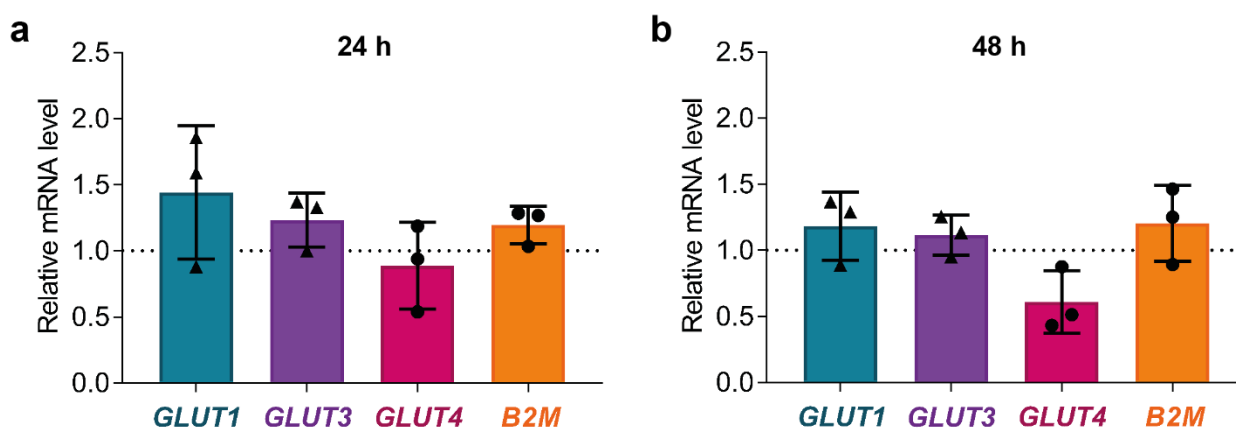


Figure 68 Influence of (+)-Glupin-1 on the *GLUT1*, *GLUT3*, *GLUT4* and *B2M* mRNA expression levels. DLD-1 cells were cultured in the presence of 0.5 μ M (+)-Glupin-1 over 24 h (a) or 48 h (b) at 25 mM glucose prior to extraction of total RNA for reverse transcription and RT-qPCR. *GLUT1,3,4* and *B2M* mRNA levels were normalized to the levels of *ATP1A1*, *ACTB* and *TUBB* and related to the value of DMSO-treated cells (which were set to 1). Data show mean values \pm s.d. (n=3). Statistical analysis was performed using an unpaired t-test with Welch's correction. All increases in mRNA level are non-significant.

On protein level, 0.5 μ M (+)-Glupin-1 increased the level of GLUT-1 to significant extent by about 2-fold after 24h and about 3.8-fold after 48 h (Figure 69a). GLUT-3 expression was also increased

significantly after 48 h of treatment by around 2.5-fold (Figure 69b). Thus, also the glucose uptake inhibitor (+)-Glupin-1 induces the upregulation of GLUT-1 and GLUT-3 in HCT116 cells as observed for Glutor (Figure 40). *These results are part of the Master thesis of Jessica Nowacki.*

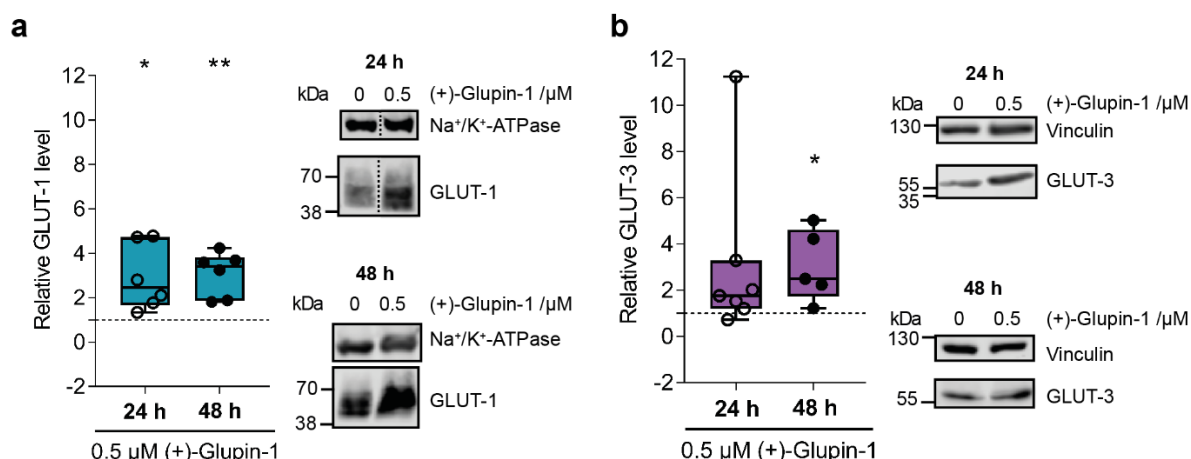


Figure 69 Influence of (+)-Glupin-1 on the GLUT-1 and GLUT-3 protein expression levels. DLD-1 cells were cultured for 24 h or 48 h in the presence of 0.5 μM (+)-Glupin-1 and 25 mM glucose before protein lysates were generated for SDS-PAGE and immunoblotting. $\text{Na}^+/\text{K}^+\text{-ATPase}$ (a) and vinculin (b) served as reference proteins for GLUT-1 (a) and GLUT-3 (b), respectively. Quantification was performed by means of densitometric analysis. Protein levels were normalized to the respective reference protein and related to values of DMSO-treated cells (which were set to 1). Data show median values with interquartile range of $n=7$. Representative immunoblots are depicted on the right side of each graph. Statistical analysis was performed using an unpaired t-Test with Welch's correction. $*=p<0.05$; $**=p<0.01$. Dashed lines indicate cropped images from the same blot.

8.4.2 Chromopyrones

The chromane-tetrahydropyriminones were identified in the cell-based semi-automated 2-DG uptake screening for glucose uptake inhibitors.¹⁰⁹ The compounds (*R,R*)-Chromopynone-1 and (*R,R*)-Chromopynone-2 (fused CHROMane- and tetrahydrOPYrimiNONE natural product fragments, Figure 70a) are potent structural, enantiomeric analogues of the hit substances *that were developed by Dr. George Karageorgis during an extensive SAR study.*¹⁰⁹ In the semi-automated resazurin-coupled 2-DG uptake assay, Chromopynone-1 inhibited the uptake of 2-DG with an IC_{50} value of $0.9\pm 0.4 \mu\text{M}$, whereas Chromopynone-2 exhibited an IC_{50} value of $0.60 \mu\text{M}$ in HCT116 cells. In the non-automated 2-DG uptake assay, the potency of (*R,R*)-Chromopynone-2 was investigated in four different cancerous cell lines (Figure 70b). (*R,R*)-Chromopynone-2

(Figure 70a) inhibited 2-DG uptake with IC_{50} values of 321.1 ± 105.8 nM in HCT116 cells, 751.3 ± 413.2 nM in UM-UC-3 cells, 703.7 ± 268.3 nM in UO-31 cells and most potently with an IC_{50} value of 172.6 ± 35.6 nM in MIA PaCa-2 cells (Figure 70b; *part of the Bachelor thesis of Aylin Binici*). Due to the sequential process of the SAR analysis, the experiments in this chapter were performed with (*R,R*)-Chromopynone-1 or (*R,R*)-Chromopynone-2.

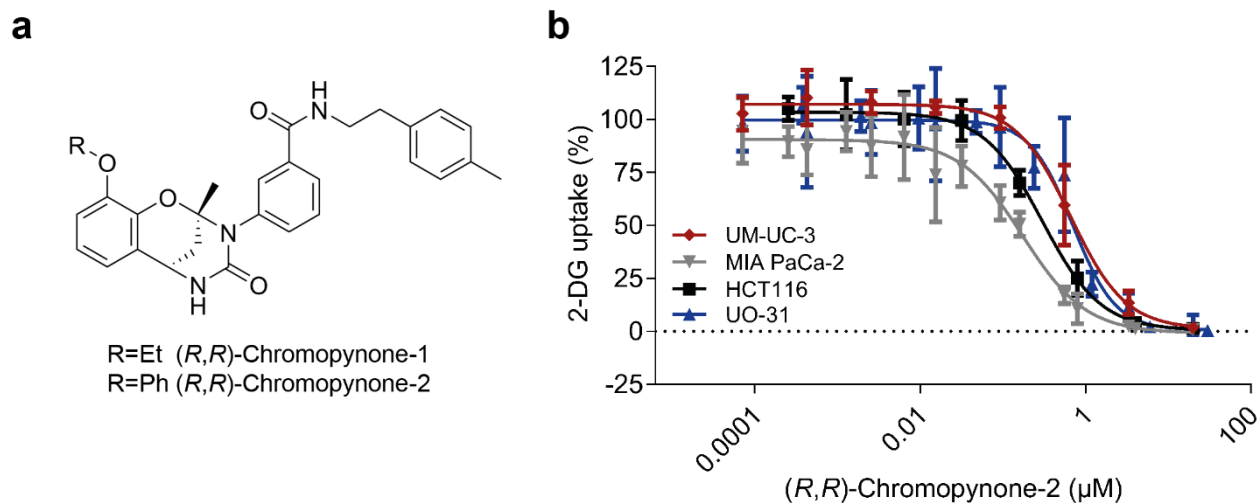


Figure 70 (*R,R*)-Chromopynone-2 inhibited 2-DG uptake with submicromolar potency. a) Chemical structure of (*R,R*)-Chromopynone-1 and -2. b) Dose-response curves of (*R,R*)-Chromopynone-2 in the resazurin-coupled 2-DG uptake assay in UM-UC-3, MIA PaCa-2, HCT116 and UO-31 cells. Data show mean values \pm s.d. ($n=4$, $N=3$) for HCT116 and UM-UC-3, ($n=5$, $N=3$) for UO-31 and ($n=6$, $N=3$) for MIA PaCa-2 cells.

8.4.2.1 Inhibition of cancer cell growth by (*R,R*)-Chromopynone-1

(*R,R*)-Chromopynone-1 was investigated for its efficacy to inhibit cell growth of HCT116 cells (Figure 71a) and MIA PaCa-2 cells (Figure 71b) in the presence of different glucose concentrations (1 mM, 5 mM, 25 mM). The compound inhibited the growth of MIA PaCa-2 cells to a higher degree ($GI_{50}=2.8 \pm 1.6$ μ M) than the growth of HCT116 cells ($GI_{50}>25$ μ M) (25 mM glucose) (Figure 71). The degree of potency was dependent on the prevalent glucose concentration. Lower glucose concentrations (1-5 mM) increased the potency of the compound in both cell lines to GI_{50} 0.6 ± 0.3 μ M (5 mM) and 0.6 ± 0.3 μ M (1 mM) in MIA PaCa-2 and GI_{50}

$3.5 \pm 0.7 \mu\text{M}$ (5 mM) and $2.8 \pm 1.0 \mu\text{M}$ (1 mM) in HCT116 cells. Thus, the potency of the compound on cell growth inhibition depends on the prevalent glucose concentration.

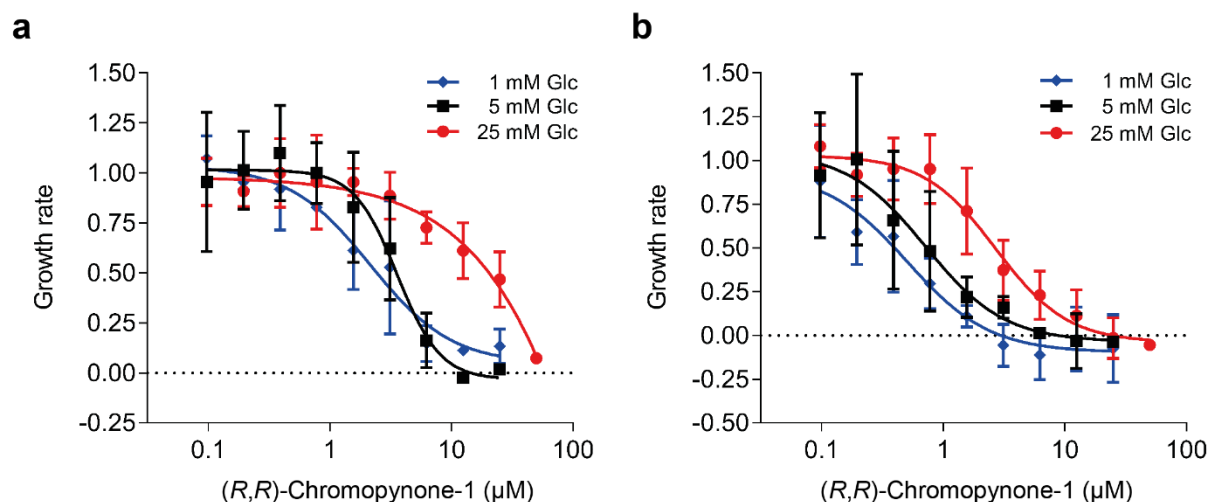


Figure 71 *(R,R)*-Chromopynone-1 inhibited cell growth of HCT116 cells stronger in the presence of low glucose concentrations. HCT116 (a) and MIA PaCa-2 cells (b) were cultured in the presence of *(R,R)*-Chromopynone-1 over 120 h. Glucose concentration was adjusted to either 1 mM, 5 mM or 25 mM in the presence of 4 mM glutamine. Growth rates were determined from the cell confluence via live-cell imaging using the IncuCyte® ZOOM. Data show mean values \pm s.d. ($n=3$, $N=3$). Glc=glucose.¹⁰⁹

The compound's efficacy to inhibit cell growth was investigated for a diverse collection of cancer cell lines (Figure 72a). *(R,R)*-Chromopynone-2 exhibited a moderate potency towards growth inhibition of most investigated cell lines. 58 malignant cell lines were inhibited with an IC_{50} value between 10 μM and 1 μM . The B cell lymphoma cell line WSU-NHL was the most sensitive cell line with an IC_{50} value of 105 nM. The non-malignant cell line IMR-90 and PBMCs were resistant ($\text{IC}_{50} > 30 \mu\text{M}$) towards *(R,R)*-Chromopynone-2 treatment. Investigation of the mutational status of the different Ras isoforms among the malignant cell lines, according to the previous analysis with Glutor (Figure 27a) and (+)-Glupin-1 (Figure 63), revealed an accumulation of Ras mutations in the sensitivity range 10 μM to 0.1 μM (42%). In contrast, only 25% of the resistant, malignant cell lines harbored a mutation in one of the three Ras isoforms.

Results

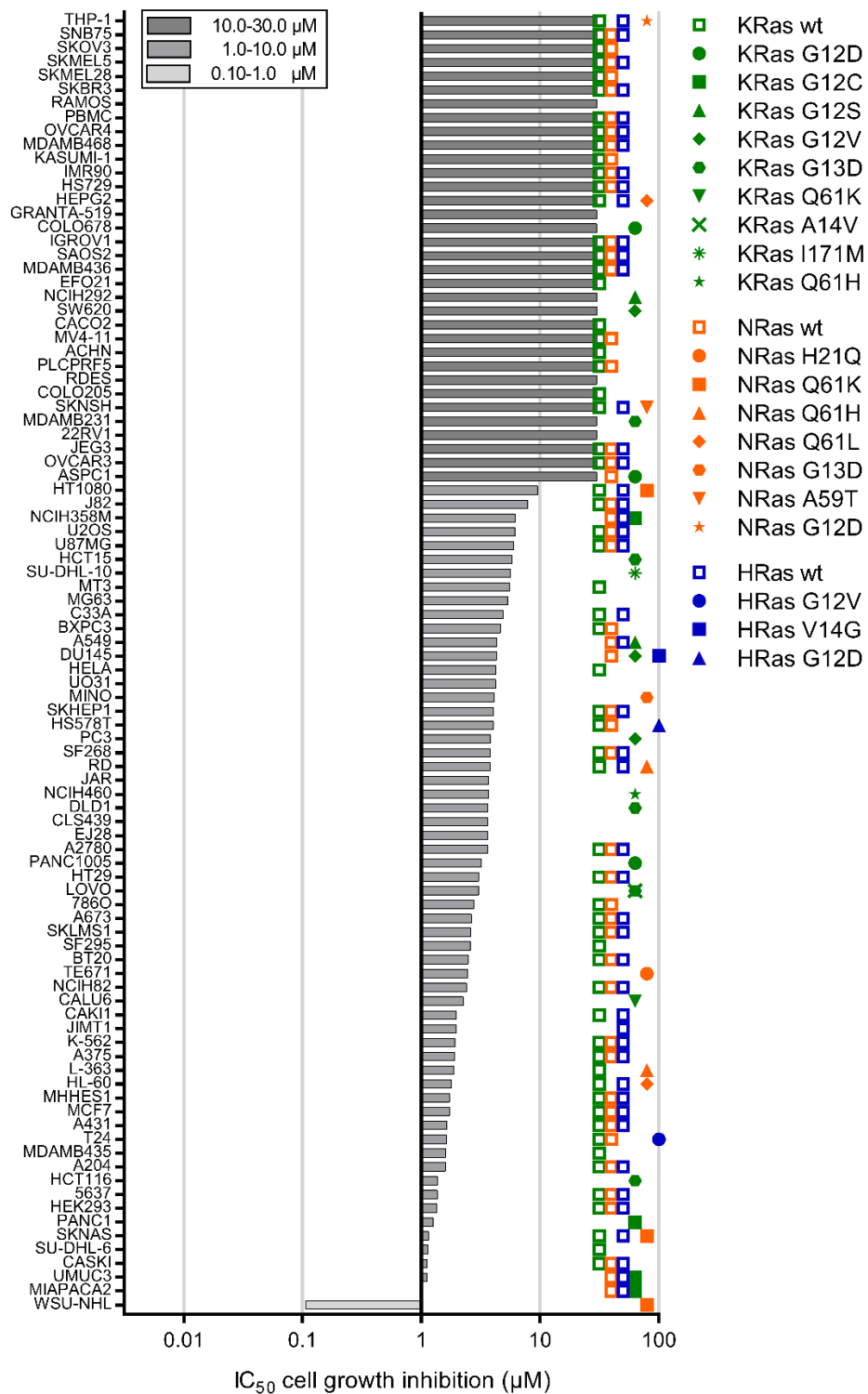


Figure 72 Growth inhibition by (R,R)-Chromopynone-2 of various different cancer cell lines. A panel of 94 cell lines was subjected to Sulforhodamine B assay after 72 h of (R,R)-Chromopynone-2 treatment. IC₅₀ values were determined after 72 h. The symbols indicate the mutational status of KRas, NRas and HRas as described in the Catalogue Of Somatic Mutations In Cancer (COSMIC)¹²¹. Sulforhodamine B assay was performed by Oncolead, Germany.

Hence, similar to Glutor and (+)-Glupin, also (*R,R*)-Chromopynone-2-sensitive cells show an accumulation of Ras mutations in their genotype.

Furthermore, the growth of a selected set of cell lines was validated using the live-cell imaging system IncuCyte® ZOOM as part of the Bachelor thesis of Aylin Binici (Figure 72b-e). Determination of the growth rate and calculation of the GI_{50} values revealed the cell line UM-UC-3 as most sensitive with a GI_{50} value of $2.0 \pm 0.2 \mu\text{M}$ (Figure 72d). The GI_{50} values of the cell lines MIA PaCa-2 and UO-31 were in a similar range with $3.0 \pm 1.3 \mu\text{M}$ and $3.2 \pm 0.9 \mu\text{M}$, respectively. The model cell line HCT116 exhibited a GI_{50} of $8.0 \pm 2.2 \mu\text{M}$ and showed the lowest sensitivity among the selected cell lines.

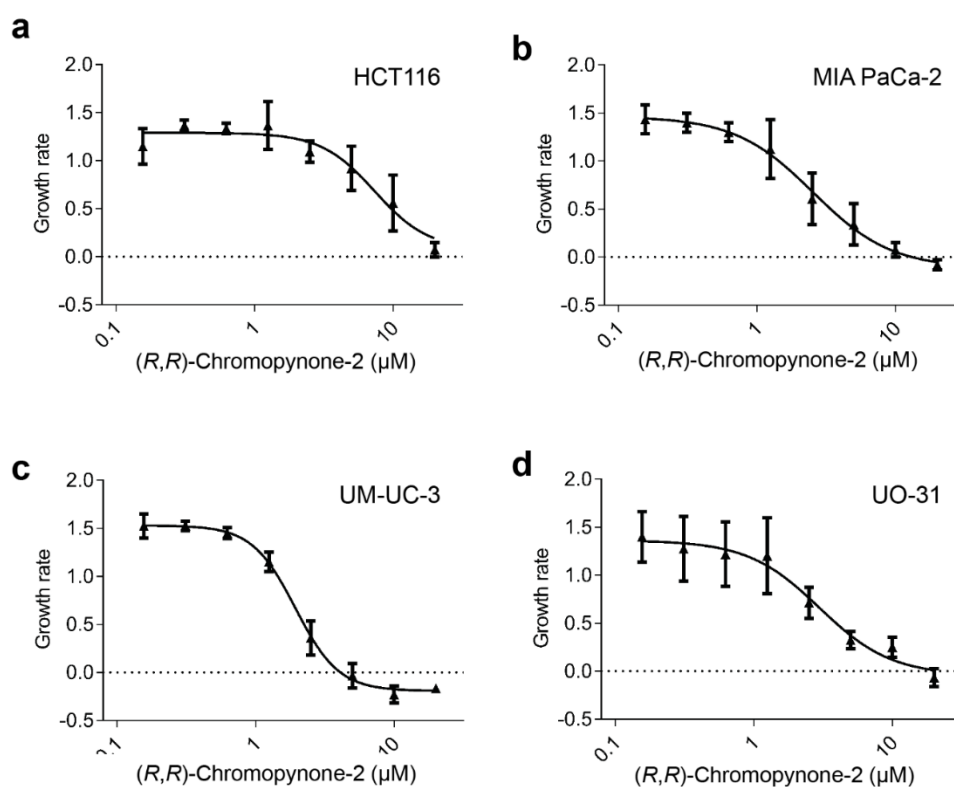


Figure 73 (*R,R*)-Chromopynone-2 inhibited the growth of different cancer cell lines in live-cell analysis. Growth inhibition curves of HCT116 (a), MIA PaCa-2 (b), UM-UC-3 (c) and UO-31 (d) upon (*R,R*)-Chromopynone-2 treatment as monitored during live-cell imaging by means of IncuCyte® ZOOM. Data show mean values \pm s.d. of $n=3$, $N=3$ (b,c,d) and $n=4$, $N=3$ (e). Bottom constrain was set to the growth rate at the highest compound concentration for HCT116.

Overall, the IC₅₀ values determined via Sulforhodamine B assay and the GI₅₀ values as determined via live-cell imaging were in the same concentration range between 10 μM and 1 μM. Even though the sensitivity nuances between the different cell lines were slightly different in both assays, HCT116 cells (Figure 72b) were less sensitive than UO-31 (Figure 72e) in the live-cell imaging system, but more sensitive in the Sulforhodamine B assay (Figure 72a).

8.4.2.2 Target validation of (R,R)-Chromopynone-1

The targets of the Chromopynone substance class were identified in GLUT-1-4 overexpressing CHO cells to be GLUT-1 and GLUT-3.¹⁰⁹ A cellular thermal shift assay (CETSA®) with (R,R)-Chromopynone-1 was employed to confirm these results using whole cell SW480 cell lysates (Figure 74).

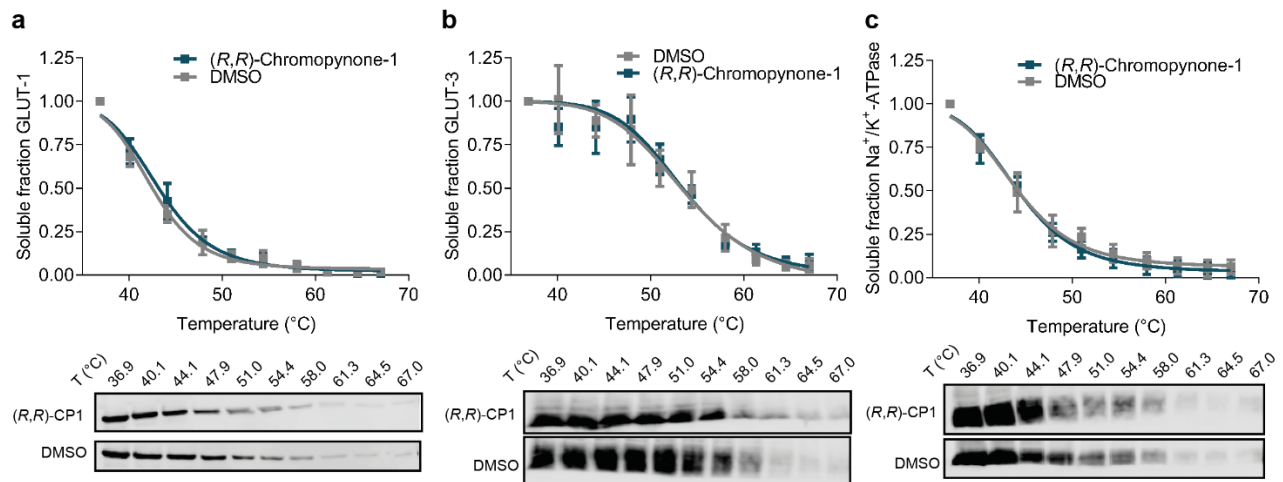


Figure 74 (R,R)-Chromopynone-1 did not show any influence on the thermal stability of GLUT-1 and GLUT-3 in the cellular thermal shift assay (CETSA®). SW480 whole cell lysate was subjected to ten different temperatures in the presence of 30 μM (R,R)-Chromopynone-1 or DMSO. After ultracentrifugation, the supernatant was analyzed for GLUT-1 (a), GLUT-3 (b) or Na⁺/K⁺-ATPase (c) by means of immunoblotting and protein amount was quantified via densitometric analysis. Protein amount was normalized to the first temperature within the temperature gradient, i.e. 36.9 °C. The data was fitted using the Boltzmann equation. Data show mean values ±s.d. (n=3, N=1). Blots are representative images of n=3. CP1=(R,R)-Chromopynone-1

Table 15 Overview of the melting temperatures as generated from the CETSA® experiment (Figure 74).

T _m (°C)	GLUT-1	GLUT-3	Na ⁺ /K ⁺ -ATPase
(<i>R,R</i>)-CP1	42.2±0.8	52.8±0.6	43.3±0.9
DMSO	42.1±0.4	51.7±3.0	43.2±0.9
ΔT _m	0.2±0.5	1.0±2.8	0.2±0.1

CP1=Chromopynone-1

Interestingly, the compound did not show any effect on the thermal stability of the target proteins GLUT-1 (Figure 74a) and GLUT-3 (Figure 74b), which behaved similar to the control protein Na⁺-K⁺-ATPase (Figure 74c). The melting temperature was altered between 0.2 °C and 1 °C for all investigated proteins (Table 15). These results thus cannot confirm, but do also not exclude (*R,R*)-Chromopynone-1 binding to GLUT-1 and GLUT-3, since not every binding site in the protein that is addressed by a small molecule must result in a change in thermal stability.

8.4.3 BAY-876

The compound BAY-876 (Figure 75a) was the first GLUT-1-selective inhibitor that was developed by Siebeneicher *et al.*²⁴ In most of the experiments conducted in this thesis, BAY-876 was implemented as a reference compound. In an alternative approach to the 2-DG uptake assay, BAY-876 was described to deplete ATP production with an IC₅₀ value of 6 nM in DLD-1 cells when oxidative phosphorylation is inhibited with Rotenone.²⁴ The potency of the GLUT-1-selective compound could be confirmed in the resazurin-coupled 2DG uptake assay in HCT116 and UM-UC-3 cells as part of the Bachelor thesis by Aylin Binici (Figure 75b). BAY-876 inhibited 2-DG uptake with IC₅₀=14.7±8.4 nM in HCT116 cells and with 40.33±23.10 nM in UM-UC-3 cells. The activity of BAY-876 was also tested in MIA PaCa-2 and UO-31 cells (Figure 75c). However, in these cell lines no IC₅₀ value could be determined but rather a linear dose-response was observed. One possible explanation might lay in the protein expression levels of GLUT-1 and GLUT-3 in the

investigated cell lines. The Cancer Cell Line Encyclopedia (CCLE) holds a database that reports the mRNA levels of various proteins in different cancer cell lines.¹²³ This revealed a distinct *GLUT1/GLUT3* ratio in the investigated cell lines HCT116, UM-UC-3 and MIA PaCa-2 (UO-31 cells are not reported in this database) (Table 16). The mRNA expression level ratios of *GLUT1* to *GLUT3* was 7.1 in UM-UC-3 and 9.6 in HCT116 cells, whereas MIA PaCa-2 cells exhibited a *GLUT1* to *GLUT3* ratio of 1.3 (Table 16). The relatively low *GLUT1* levels in MIA PaCa-2 cells might indicate a compensation of 2-DG uptake via GLUT-3 which is not inhibited by the GLUT-1-selective BAY-876. This might result in a linear dose-dependence instead of sigmoidal curve (Figure 75c).

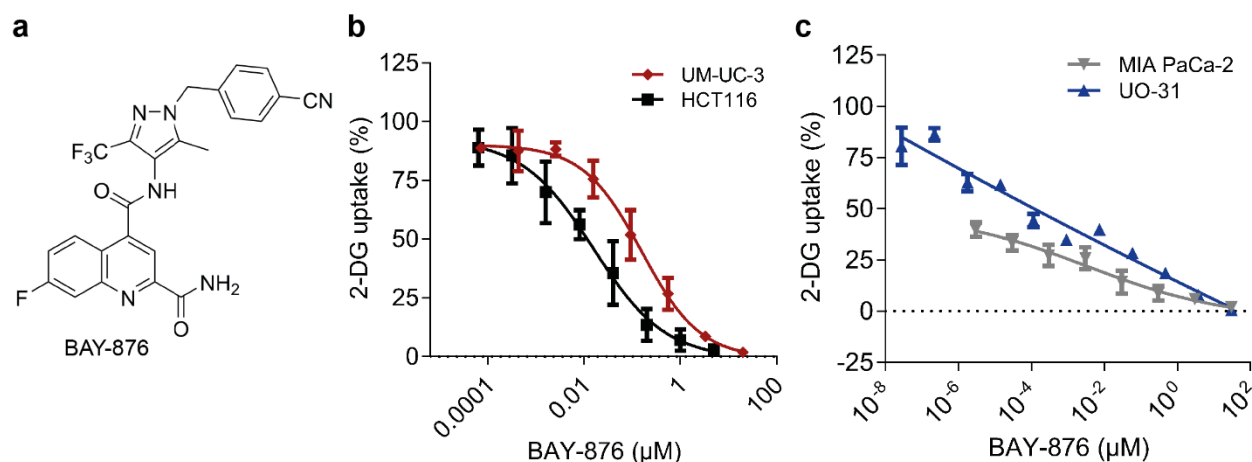


Figure 75 BAY-876 potently inhibited 2-DG uptake in UM-UC-3 and HCT116 cells. a) Chemical structure of BAY-876. b,c) Dose-response curves of BAY-876 in the resazurin-coupled 2-DG uptake assay. b) Data show mean values \pm s.d. $n=3$, $N=3$ (UM-UC-3), $n=4$, $N=3$ (HCT116). c) The graph shows representative data of $n=6$, $N=3$ (UO-31) and $n=12$, $N=3$ (MIA PaCa-2).

Table 16 Overview of the mRNA expression levels as reported by the Cancer Cell Line Encyclopedia.¹²³

Cell line	GLUT-1	GLUT-3	Ratio
HCT116	260.4	27.0	9.6
UM-UC-3	242.5	33.6	7.2
MIA PaCa-2	84.3	65.1	1.3

The mitochondrial toxicity of BAY-876 was tested in HCT116 cells that were cultured in the presence of 25 mM glucose or 10 mM galactose, as done previously for Glutor (Figure 25a) and (+)-Glupin-1 (Figure 61a). Oligomycin, an ATP-synthase inhibitor, served as a control (Figure 76b). The growth rates of HCT116 cells treated with BAY-876 in the presence of glucose are approximately 1.2-fold higher than the rate of cells treated in the presence of galactose (Figure 76a). Therefore, BAY-876 seemed to slightly impede the mitochondrial function of HCT116 cells.

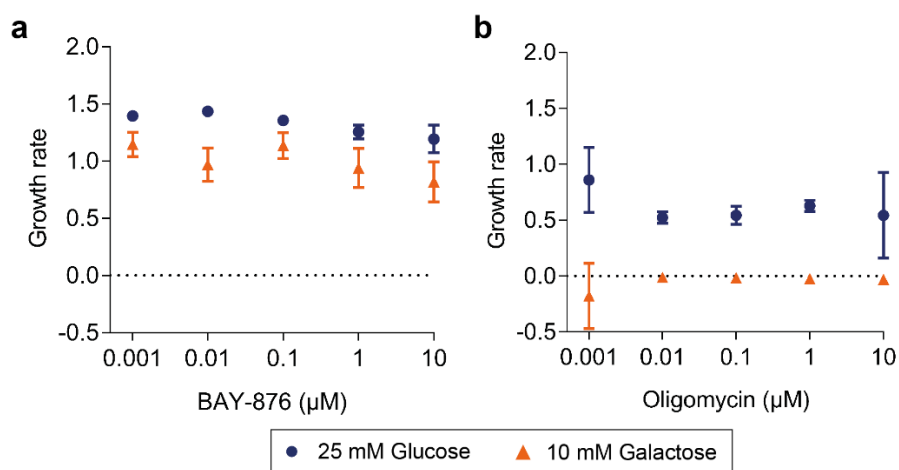


Figure 76 BAY-876 slightly impeded mitochondrial function. HCT116 cells were treated with BAY-876 (a) or Oligomycin (b) in the presence of either 25 mM glucose or 10 mM galactose. Growth was monitored using the live-cell imaging device IncuCyte® ZOOM. Growth rates were calculated and normalized to DMSO-treated cells. Data show mean values \pm s.d. (n=3, N=3).

8.4.3.1 Target validation for BAY-876

The reported target of BAY-876 is the GLUT isoform 1.²⁴ Therefore, BAY-876 was tested in a thermal proteome profiling approach in order to confirm GLUT-1 as the target protein. GLUT-1 was thermally stabilized in SW480 cell lysates by 10 μM BAY-876 with ΔT_m 8.5 ± 4.1 °C (Figure 77a, Table 17).

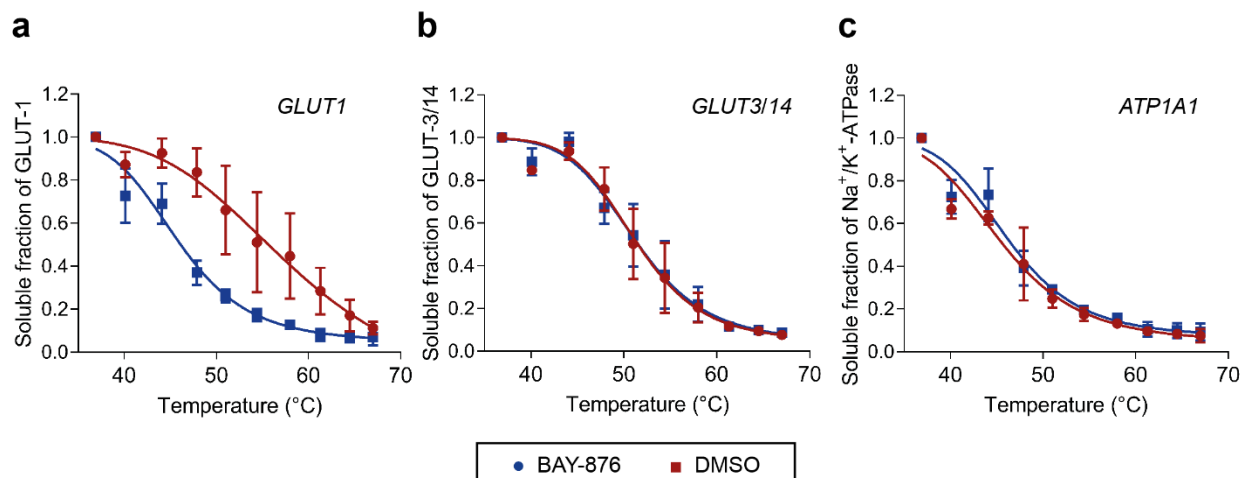


Figure 77 Melting curves of GLUT-1, GLUT-3 and Na⁺-K⁺-ATPase from TPP in the presence of BAY-876. A thermal proteome profilin approach (TPP) was performed with SW480 whole cell lysates in presence of 10 μM BAY-876 or DMSO. The proteins GLUT-1 (a), GLUT-3 (b) and Na⁺-K⁺-ATPase (c) were identified in the soluble fraction after heat treatment. Protein amount was normalized to the first temperature within the temperature gradient, *i.e.* 36.9 °C. The data was fitted using the Boltzmann equation. Data show mean values of \pm s.d.(n=3).

The GLUT isoform GLUT-3 and the control protein ATP1A1 were not influenced in their melting behavior by the presence of BAY-876 (Figure 77b,c, Table 17). Therefore, the results of the TPP assay are in line with the proposed isoform selectivity.²⁴

Table 17 Overview of melting temperatures as determined in a TPP assay (Figure 77).

T _m (°C)	GLUT-1	GLUT-3	Na ⁺ /K ⁺ -ATPase
BAY-876	53.2±2.9	50.5±0.7	44.0±1.0
DMSO	44.7±1.3	50.2±1.4	44.9±1.5
ΔT _m	8.5±4.1	0.2±1.2	-0.9±0.8

Data show mean values \pm s.d. (n=3).

8.4.3.2 Potential off-target effects of BAY-876

As previously shown for (+)-Glupin-1 (chapter 8.4.1.2), the TPP approach can be applied as an off-target identification strategy. Figure 78 presents an overview of all identified potential interaction partners of BAY-876 (see also Appendix, Figure 92, Figure 93 and Table 20). As described earlier, only proteins that show a thermal destabilization or stabilization over all three

Results

biological replicates (in the same direction), and where in at least one temperature the error bars of the BAY-876- or DMSO-treated lysates do not overlap, were considered to be potential off-targets (Figure 78, Figure 79).

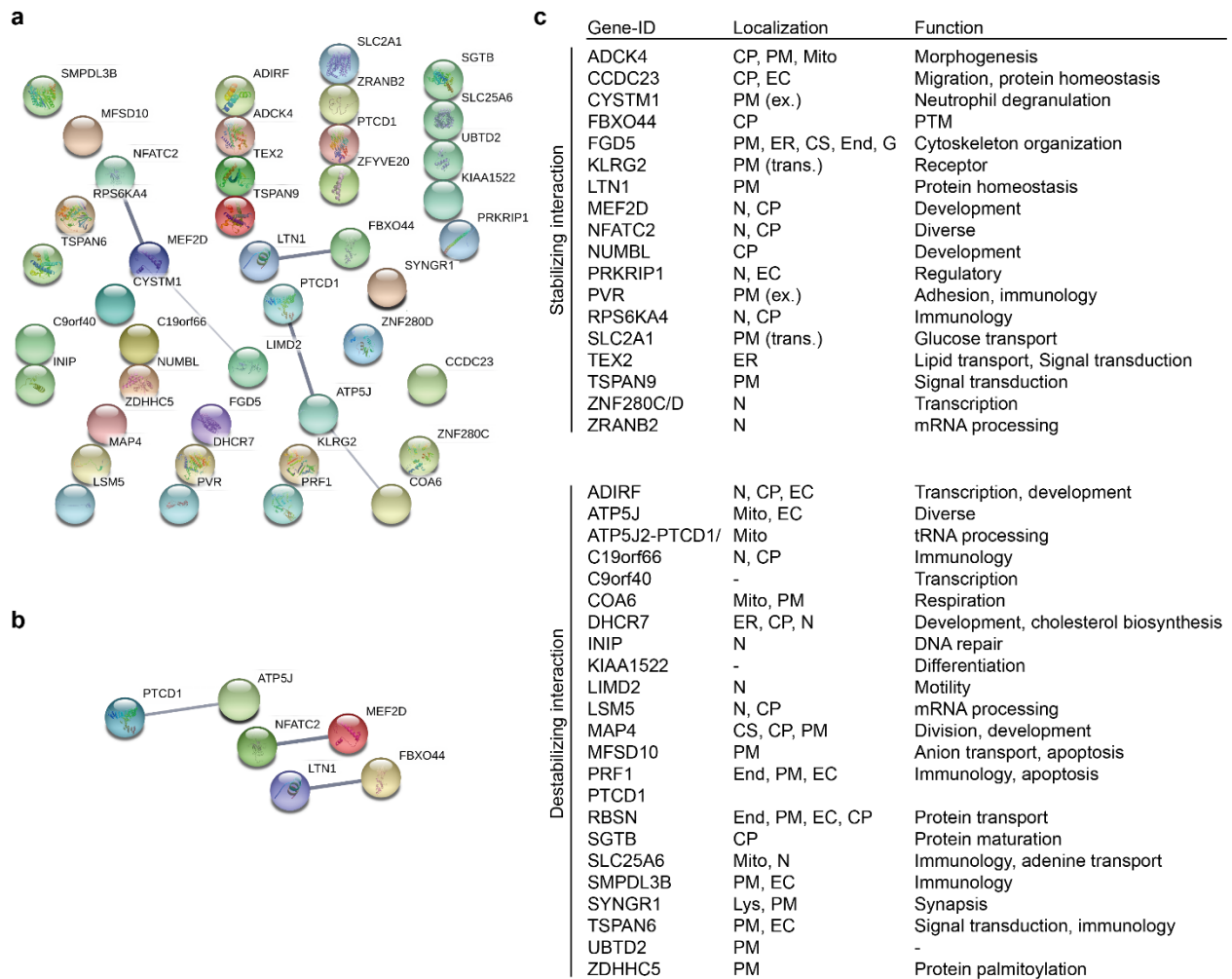


Figure 78 All interaction partners of BAY-876 that were identified during thermal proteome profiling (TPP). a) Potential interaction partners were analyzed using STRING database among each other.¹³⁸ All proteins are named by their unique gene-ID. b) Overview of all proteins that are thermally stabilized or destabilized in the presence of 10 μ M BAY-876. The protein's annotated localization as well as protein's function is given.¹³⁹ PM=Plasma membrane, CP=Cytoplasm, N=Nucleus, Mito=Mitochondrion, CS=Cytoskeleton, ER=Endoplasmic reticulum, Lys=Lysosome, trans.=transmembrane, ex.=extracellular.

The STRING database¹³⁸ was employed to find interaction partners among the identified proteins (Figure 78a,b). No large network, but three known protein-protein interactions were identified in the STRING database. Programmed cell death 1 (*PTCD1*) and ATP-synthase coupling factor 6

Results

(*ATP5J*) are known interaction partners as well as nuclear factor of activated T-cells (*NFATC2*) and myocyte enhancing factor 2D (*MEF2D*) and the proteins listerin E3 ubiquitin ligase 1 (*LTN1*) and F-box only protein 44 (*FBXO44*). *LTN1* and *FBXO44* are involved in protein homeostasis, whereas *NFATC2* and *MEF2D* can have diverse functions among other in developmental processes.¹³⁹ Moreover, Blaeser *et al.* reported a calcineurin-induced activation of MEF2D through NFAT. This interaction was further investigated by Youn *et al.* with regard to T cell apoptosis.^{140,141} *PTCD1* and *ATP5J* are both located in the mitochondria and their BAY-876-mediated inhibition could explain the observed mitochondrial toxicity in BAY-876 treated HCT116 cells (Figure 76a).

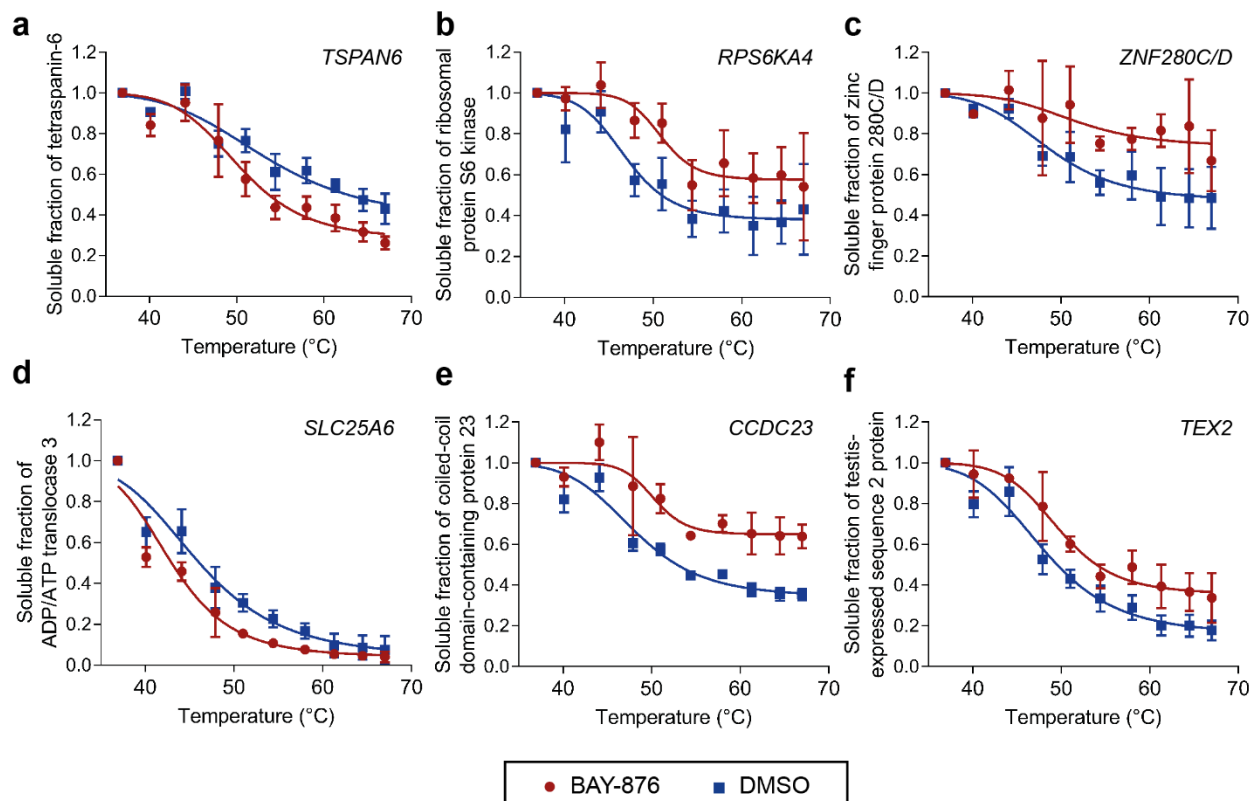


Figure 79 Other identified interaction partners of BAY-876 during thermal proteome profiling (TPP). A thermal proteome profiling approach (TPP) was performed with SW480 whole cell lysates in the presence of 10 μ M BAY-876 or DMSO. The gene names (graph) and protein names (y-axis) are given. These proteins were identified in all three biological replicates in the soluble fraction after heat treatment. Protein amount was normalized to the first temperature within the temperature gradient, *i.e.* 36.9 °C. The data was fitted using the Boltzmann equation. Data show mean values \pm s.d. (n=3).

The proteins that show the highest change in their melting behavior upon BAY-876 treatment are presented in Figure 79. The three proteins whose identity was best confirmed with the peptide mass finger print are GLUT-1 (*SLC2A1*, Figure 77a), Zinc finger Ran-binding protein (*ZRANB2*, Figure 91a) and the ADP/ATP translocase 3 (*SLC25A6*, Figure 79d). Among these proteins, ADP/ATP translocase 3 represents a mitochondrial protein that could explain the slight mitotoxicity of BAY-876 (Figure 76a).

Since multiple mitochondrial proteins were identified as potential off-targets, a mito stress test using the Seahorse XFp device was employed to further investigate this observation (Figure 80). BAY-876 behaved as expected for a glucose uptake inhibitor and inhibits the extracellular acidification rate (ECAR, glycolysis) in HCT116 cells when administered at 5 μM concentration (Figure 80a). At the same time, the cells increased oxidative phosphorylation (OCR) to counteract nutrient shortage, which shows their metabolic flexibility (Figure 80b).

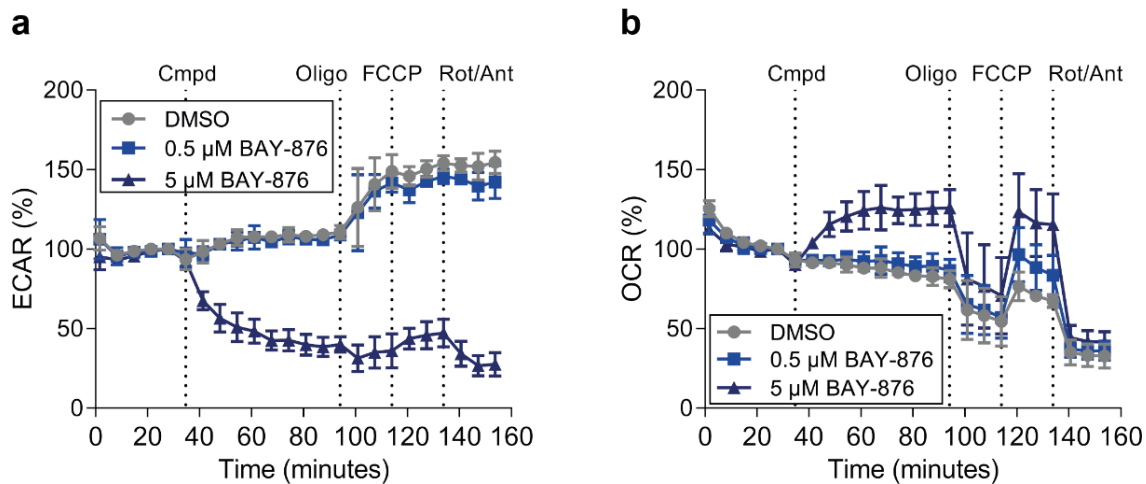


Figure 80 BAY-876 reduced glycolysis in HCT116 cells and uncoupled mitochondrial respiration. HCT116 cells were subjected to a mito stress test (Seahorse XFp). The extracellular acidification rate (ECAR) as measure of glycolysis and the oxygen consumption rate (OCR) as measure of respiration were monitored. Data show mean values \pm s.d. ($n=3$). Cmpd=compound, Oligo=1 μM Oligomycin; FCCP=0.5 μM Carbonyl cyanide 4-(trifluoromethoxy) phenylhydrazone, Rot/Ant=1 μM Rotenone/Antimycin A. Experiment was performed by Julian Wilke.

A lower concentration of the compound BAY-876 (0.5 μM) showed initially no effect on ECAR nor OCR (Figure 80). After addition of 1 μM Oligomycin, mitochondrial activity is impaired irrespective

of the previous treatment due to ATP-synthase inhibition. FCCP (carbonyl cyanide 4-(trifluoromethoxy) phenylhydrazone), a mitochondrial uncoupler, reveals the residual respiratory capacity of the HCT116 cell line. Interestingly, the compound BAY-876 increased concentration-dependent the spare respiratory capacity. This effect is most likely no counter effect due to glucose uptake inhibition, since no OCR increase was observed after treatment with 0.5 μM BAY-876. The inhibition of the ADP/ATP translocase 3 is known to reduce the OCR. Hence, the observed effect could be due to an activation effect of BAY-876 on the ADP/ATP translocase 3. The addition of 1 μM Rotenone and Antimycin A led to complete inactivation of the oxidative phosphorylation in the presence and the absence of BAY-876 (Figure 80b).

PD-1 is currently investigated in multiple clinical trials since it is involved in T-cell activation and inhibition of the interaction between the receptor and its ligand has been proven beneficial in immunooncology approaches (immune checkpoint inhibitors).¹⁴² Since 2014, the PD-1 antibody Nivolumab is approved for treatment of multiple cancers.¹⁴³ Nevertheless, the effect of PD-L1 inhibition using a PD-L1-specific antibody has been investigated using a mito stress test and no similar uncoupling effect was observed.¹⁴⁴ Also, PD-1 is known to be involved in glycolysis inhibition and promotion of fatty acid beta-oxidation.¹⁴⁵ Therefore, PD-1 was excluded as potential off-target of BAY-876.

ATP synthase-coupling factor 6 is part of the mitochondrial membrane ATP synthase and therefore involved in ATP generation in a present intermembrane proton gradient.¹³⁹ An inhibitor of this protein is Oligomycin that is supplemented to the cells during the mito stress test. BAY-876 does not mimic nor counteract the activity of Oligomycin which is why the ATP-synthase-coupling factor 6 can be excluded as off-target for the time being.

Thus, these studies revealed that the ADP/ATP translocase 3 could be a potential off-target of BAY-876.

8.4.3.3 Cell growth inhibition

The compound BAY-876 was also employed in the cell panel profiling to investigate its effect on the growth behavior of a variety of different cancer cell lines (Figure 81). Out of the whole panel, 42 cell lines were inhibited with an IC_{50} value $<1 \mu\text{M}$. The non-malignant cell line IMR-90 and PBMCs were resistant ($IC_{50}>30 \mu\text{M}$) against the treatment with BAY-876. Around 40% of the malignant cell lines with an IC_{50} value $<10 \mu\text{M}$ and only 19% of the resistant, malignant cell lines harbor a mutation in one of the three Ras isoforms. This observation is in line with the previous analysis, in which an accumulation of Ras mutations could also be observed among cell lines that show a high sensitivity towards glucose uptake inhibition (Figure 27, Figure 63, Figure 72).

As done previously for Glutor and (*R,R*)-Chromopynone-2 (Figure 26c, Figure 27b-e, Figure 72b-e), the sensitivity of selected cell lines was further analyzed against BAY-876 by means of live-cell imaging as part of the Bachelor thesis of Aylin Binici (Figure 82). BAY-876 could inhibit the growth of HCT116, MIA PaCa-2 and UO-31 to a similar extent and in the low micromolar range with GI_{50} values of $3.98\pm 0.94 \mu\text{M}$ (HCT116), $1.38\pm 0.06 \mu\text{M}$ (MIA PaCa-2) and $4.16\pm 1.76 \mu\text{M}$ (UO-31) (Figure 82a,b,d). In contrast, the IC_{50} values obtained in the Sulforhodamine B assay were 284 nM for HCT116 cells, 119 nM for UO-31 and 5 nM for the MIA PaCa-2 cell line which was also the most sensitive cell line within the panel (Figure 81). The second most sensitive cell line in the panel, UM-UC-3 (IC_{50} 6 nM) (Figure 81), displayed a GI_{50} value of $82.6\pm 45.4 \text{ nM}$ upon BAY-876 treatment (Figure 82c). Overall, the correlation between the Sulforhodamine B assay and the live-cell imaging analysis was weak for BAY-876 treatment. This can be explained by the different read-out of both assays. Whereas the Sulforhodamine B assay determines the cellular protein content, which is expected to correlate with the cell viability, the live-cell imaging approach takes the cell density into account. Discrepancies in the values are therefore not unexpected.

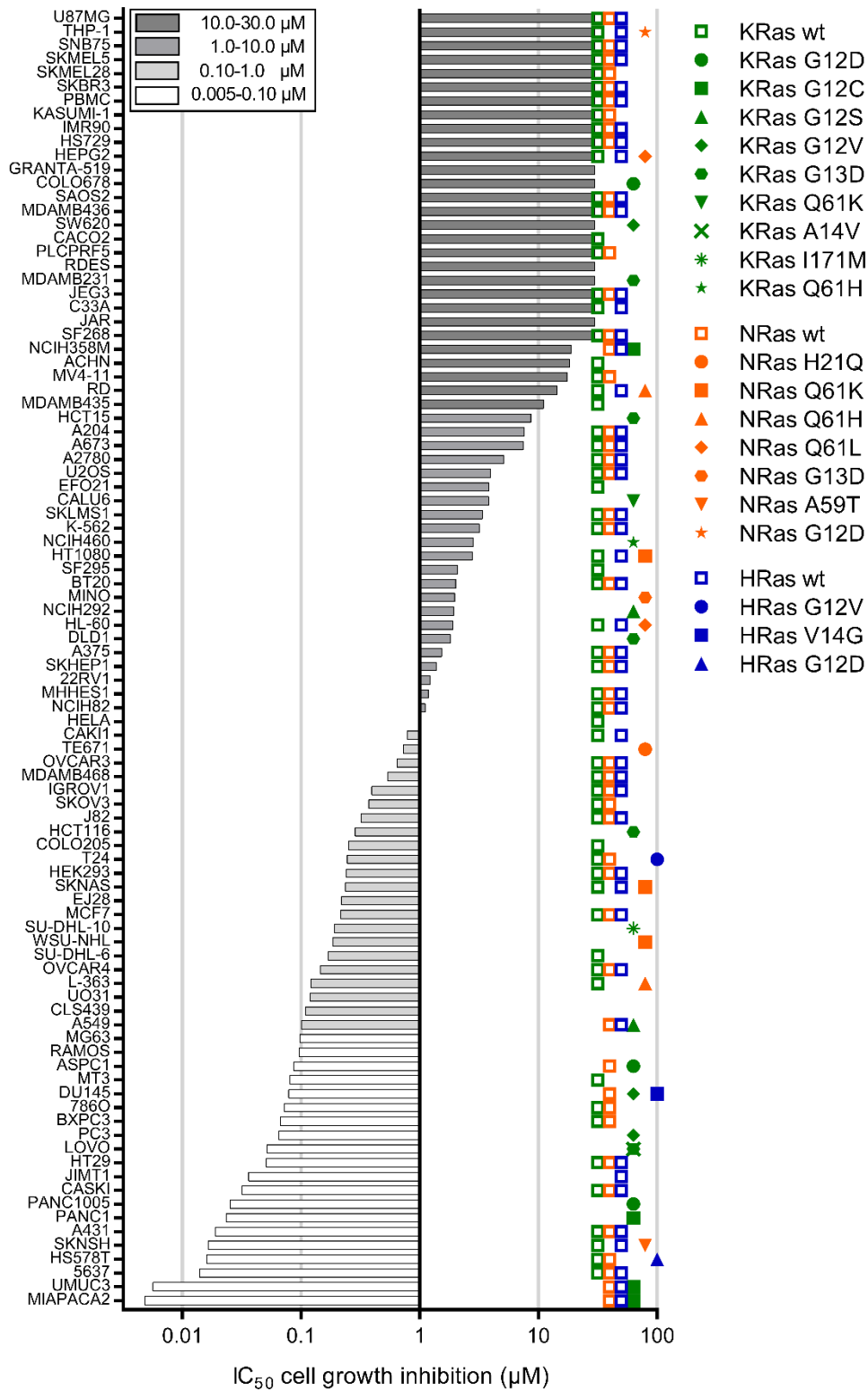


Figure 81 Growth inhibition of different cancer cell lines by means of BAY-876 treatment. A panel of 94 cell lines was subjected to Sulforhodamine B assay for IC₅₀ determination after 72 h of BAY-876 treatment. The symbols indicate the mutational status of KRas, NRas and HRas as described in the Catalogue Of Somatic Mutations In Cancer (COSMIC)¹²¹. *Sulforhodamine B* assay was performed by *Oncolead, Germany*.

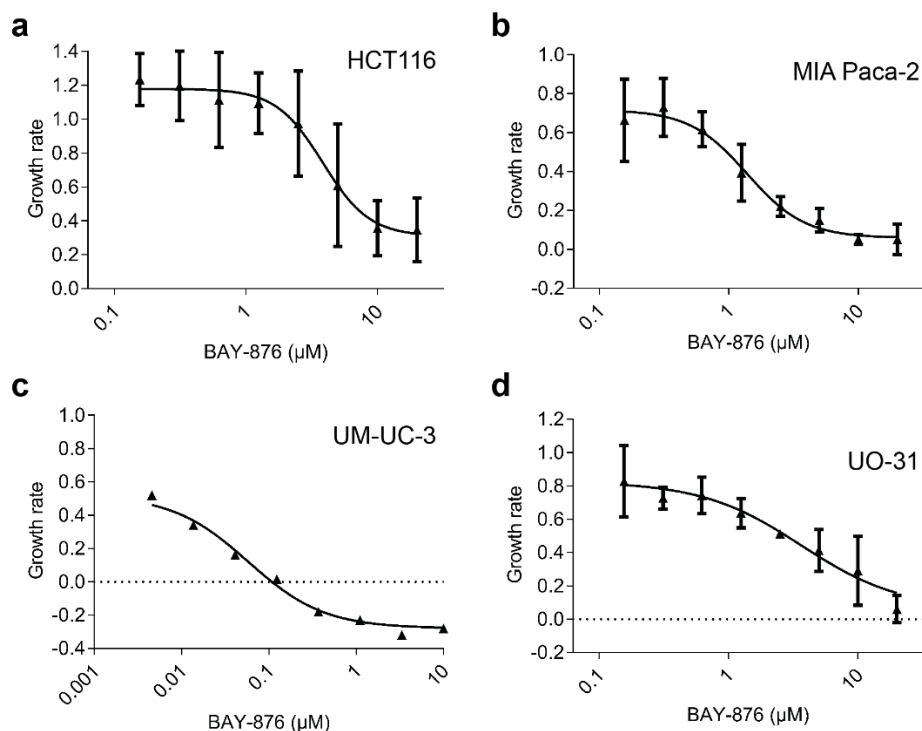


Figure 82 BAY-876 inhibited the growth of different cancer cell lines in live-cell analysis. Growth inhibition curves of HCT116 (a), MIA PaCa-2 (b), UM-UC-3 (c) and UO-31 (d) upon BAY-876 treatment as monitored during live-cell imaging by means of IncuCyte® ZOOM. Data show mean values \pm s.d. ($n=3$, $N=3$) for a,b,d or representative values ($n=3$, $N=3$) for c. Bottom constrain was set to the growth rate at the highest compound concentration and the top constrain to the growth rate at the lowest applied compound concentration for UM-UC-3 and UO-31 cells.

8.4.3.4 GLUT-1 and GLUT-3 upregulation upon BAY-876 treatment

In analogy to the other glucose uptake inhibitors, the upregulation of *GLUT1-4* was investigated upon BAY-876 treatment in DLD-1 cells (Figure 83). Low concentrations of BAY-876 (0.5 μM) induced a significant upregulation of *GLUT3* after 24 h and 48 h (Figure 83a,c). *GLUT1* was only slightly increased by 1.2- and 1.6-fold, respectively (Figure 83a,c). *B2M* mRNA levels correlated with *GLUT1* expression and *B2M* was therefore excluded as reference gene (Figure 83a,c). *GLUT4* mRNA levels were reduced after 48 h to a significant extent by nearly 50% (Figure 83c). *GLUT2* mRNA could not be detected in the samples and the level was also not increased to detectable amount after compound treatment. Interestingly, high concentrations of BAY-876

Results

(5 μ M) induced a significant upregulation of *GLUT1* by approximately 1.5-fold after 24 h and 48 h (Figure 83b,d), whereas the level of *GLUT3* mRNA was unaltered (Figure 83b,d). In analogy to *GLUT1* the gene expression, also *B2M* mRNA was upregulated after 24 h and 48 h of treatment with 5 μ M BAY-876 by 1.4- and 1.6.fold, respectively (Figure 83b,d). Due to insufficient sample volume, the influence of 5 μ M BAY-876 on *GLUT4* expression could not be analyzed (Figure 83b,d).

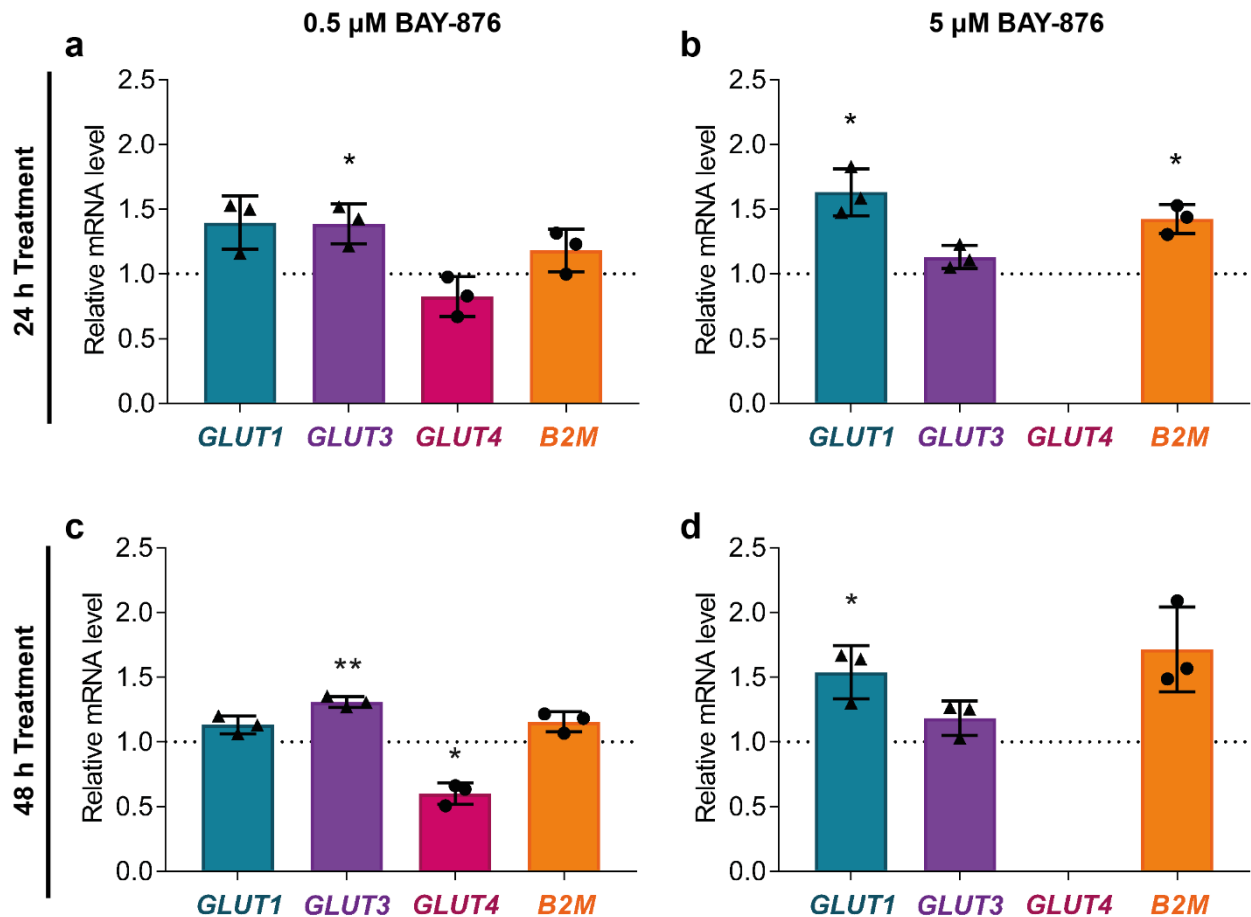


Figure 83 Influence of BAY-876 on the *GLUT1*, *GLUT3*, *GLUT4* and *B2M* mRNA expression levels. DLD-1 cells were cultured in the presence of 0.5 μ M (a,c) or 5 μ M BAY-876 (b,d) over 24 h (a,b) or 48 h (c,d) at 25 mM glucose prior to extraction of total RNA for reverse transcription and RT-qPCR. *GLUT1,3,4* and *B2M* mRNA levels were normalized to the levels of *ATP1A1*, *ACTB* and *TUBB* and related to the value of DMSO-treated cells (which were set to 1). Data show mean values \pm s.d. (n=3). Statistical analysis was performed using an unpaired t-test with Welch's correction. *= p <0.05; **= p <0.01.

Results

The protein levels of GLUT-1 and GLUT-3 were also analyzed to confirm the upregulation via transcription *as part of the Master thesis of Jessica Nowacki* (Figure 84). The immunoblot analysis showed that 0.5 μM BAY-876 mainly increased GLUT-3 protein level by around 4-fold after 48 h (Figure 84b), whereas GLUT-1 was only slightly increased by about 1.5-fold (Figure 84a). Increasing the concentration of BAY-876 to 5 μM also intensified the effect on GLUT-1 and GLUT-3 upregulation by nearly 2-fold and 6-fold, respectively (Figure 84a,b), but only the effect on GLUT-3 expression was determined to be significant. Collectively, also a GLUT-1-selective inhibitor induced an upregulation of not only its target isoform GLUT-1, but also and to an even higher extent of GLUT-3 protein level.

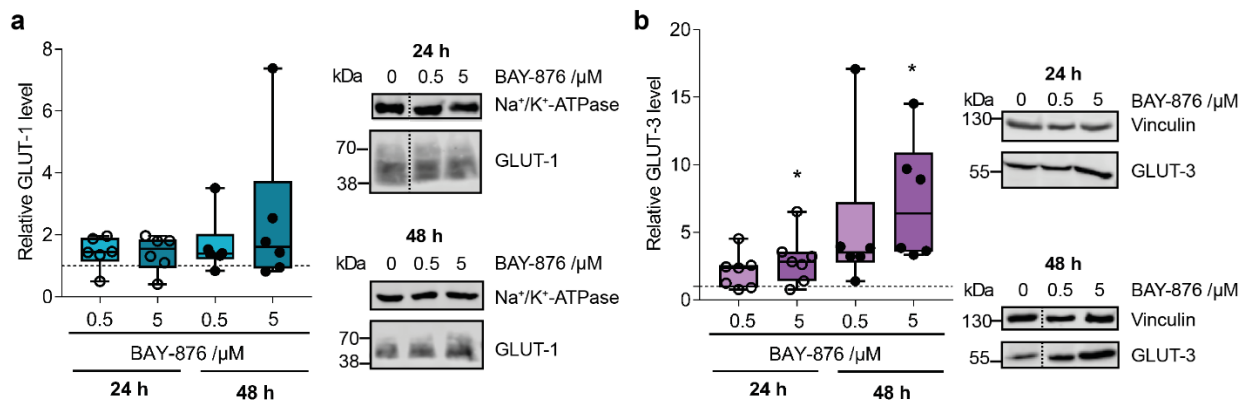


Figure 84 Influence of BAY-876 on the GLUT-1 and GLUT-3 protein expression levels. DLD-1 cells were cultured for 24 h or 48 h in the presence of 0.5 μM or 5 μM BAY-876 and 25 mM glucose before protein lysates were generated for SDS-PAGE and immunoblotting. Na⁺/K⁺-ATPase (a) and vinculin (b) served as reference proteins for GLUT-1 (a) and GLUT-3 (b), respectively. Quantification was performed by means of densitometric analysis. Protein levels were normalized to the respective reference protein and related to values of DMSO-treated cells (which were set to 1). Data show median values with interquartile range of n=6 (a) or n=7 (b). Representative immunoblots are depicted on the right side of each graph. Statistical analysis was performed using an unpaired t-Test with Welch's correction. *p<0.05. Dashed lines indicate cropped images from the same blot.

9 Discussion

Cancer, activated immune and stem cells exhibit an increased energy and nutrient demand due to accelerated proliferation rate.¹⁴⁶ This demand is met by increasing aerobic glycolysis, which is also known as the Warburg effect.¹⁴⁷ To increase the rate of glycolysis, facilitative glucose transporters are overexpressed and localized to the plasma membrane. In cancer, particularly the expression of GLUT-1 (class I GLUT) is enhanced and the development of small molecule inhibitors of glucose uptake was proposed as promising anti-cancer strategy. Numerous attempts to develop glucose uptake inhibitors were undertaken, yet specificity and potency remain major challenges. Since all class I GLUT isoforms are expressed tissue-specifically and are involved in central processes such as basal glucose uptake in all somatic cells (GLUT-1), glucose sensing in pancreas and liver (GLUT-2), neuronal glucose uptake (GLUT-3) and insulin-responsive glucose uptake in fat and muscle cells (GLUT-4), it was long deemed essential to develop GLUT-1-selective glucose transport inhibitors for cancer-targeted treatment to ensure a wide therapeutic window. Recently, Siebeneicher *et al.* developed the first GLUT-1-selective inhibitor with nanomolar potency.^{24,41} However, no information on its further clinical development nor its application have been reported to date. Moreover, not solely GLUT-1 but also GLUT-3 is upregulated in various cancers such as endometrial and breast cancers, head and neck tumors, thyroid carcinomas as well as colon, pancreatic and non-small cell lung cancer.^{25–30} These findings suggest that inhibition of both transporter isoforms might be necessary to completely block glucose supply of cancer cells. In this thesis, the development of the novel glucose uptake inhibitor Glutor and the elucidation of the required isoform specificity to successfully target glucose metabolism in cancer are described. Furthermore, one important aspect of this thesis was the investigation of the metabolic flexibility of cancer cells during glucose starvation with Glutor and how the cells might adapt to the state of nutrient reduction or starvation.

9.1 Structural optimization of Glutor

In the course of this work, the piperazin-2-one hit structure **1a** was identified in a cell-based screening for 2-DG uptake inhibitors. Subsequent studies revealed a narrow structure-activity relationship (SAR) at the core scaffold **B** that identified a phenylpyrazole as the best substituent (Figure 85). The benzylamine **A** required the introduction of a bulky substituent in 4-position in order to increase the biological potency. Hereby, substituents in 2- and 3-position or the exchange of an aliphatic substituent to a halogen led to compound inactivation (Figure 85). The benzylamide substituent **C** however allowed no substitution, except a methoxy group in 2-position. However, the exchange of the phenyl group by 3-pyridyl led to increased solubility and a boost in biological activity (Figure 85).

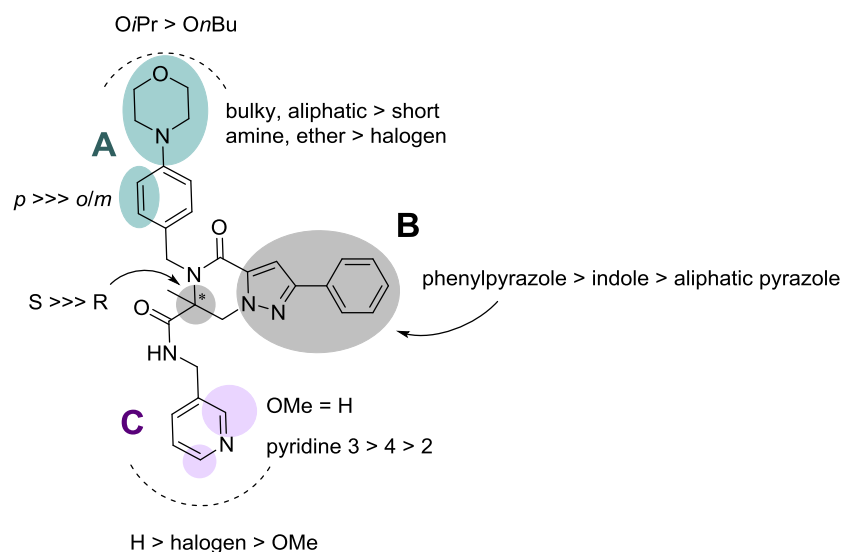


Figure 85 Reduced overview of the structure-activity relationship (SAR) for the piperazin-2-one inhibitor class. A reduced SAR is visualized on the structure of the piperazin-2-one derivative Glutor. Circles describe variation in the chemical structure.

The SAR studies led to the development of the highly potent and water-soluble enantiomeric compound Glutor ((**S**)-**5g**). Target validation approaches, that were only conducted for the most potent piperazin-2-one Glutor ((**S**)-**5g**), revealed selectivity for GLUT-1, GLUT-2 and GLUT-3.

Hence, analysis of the residual Glutor derivatives for their GLUT class I isoform selectivity might reveal a certain structure-selectivity relationship (SSR). This SSR would be useful for the generation of GLUT-1-, GLUT-2-, GLUT-3- and GLUT-4-selective tool compounds. The implementation of stably transfected GLUT-1-4-overexpressing cell lines, similar to the approaches of Siebeneicher *et al.* (Bayer corporation) and Cowley *et al.* (IOmet Pharma Ltd.), would be the method of choice for this approach.^{24,40} Since the function of class II and III GLUTs is largely unknown, new tool compounds with high isoform selectivity could help to elucidate their function. Therefore, SSR studies could be extended to the remaining GLUT isoforms as well.

The SAR could be furthermore extended to positions that revealed a certain tolerance towards minor structural modifications, *i.e.* the 4-position of the 3-phenylpyrazole (Figure 86, compare **19** and **20**) and the 2-position at the exocyclic benzyl amide (Figure 86, compare **1a** and **1o**).

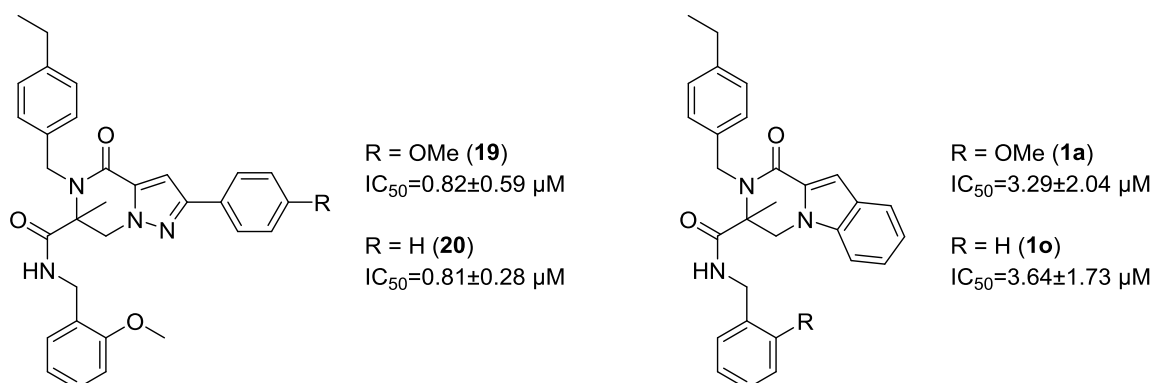


Figure 86 Selected piperazin-2-one derivatives and their biological activity on 2-DG uptake. HCT116 cells were employed in the resazurin-coupled 2-DG uptake assay. Data show mean values ±s.d. of n= 12 (**1a**), n=18 (**19**, **1o**) or n=21 (**20**) (N=3).

Functionalization can be employed for covalent modification of the target protein GLUT in order to identify the binding site of the piperazin-2-one substance class. Examples for this approach are affinity-guided 4-dimethylaminopyridine (DMAP) labeling and ligand-directed tosyl labeling of the target protein (Figure 87).^{148,149} DMAP serves as catalyst for the modification of nucleophilic residues nearby the binding site, *e.g.* arginine and lysine, of the target protein with a tag (*e.g.*

alkyne) that is mediated by an active ester.¹⁴⁸ The alkyne-tag of the tosyl modification is directly attached and transferred onto the target protein by nucleophilic attack of an adjacent nucleophilic amino acid at the tosyl group. The alkyne can afterwards be used for click chemistry of a biotin-labeled azide for solid support immobilization of the target protein in both approaches. After tryptic digest, the modification of the protein can be localized to the respective peptide sequences within the protein in order to locate the binding site of Glutor.

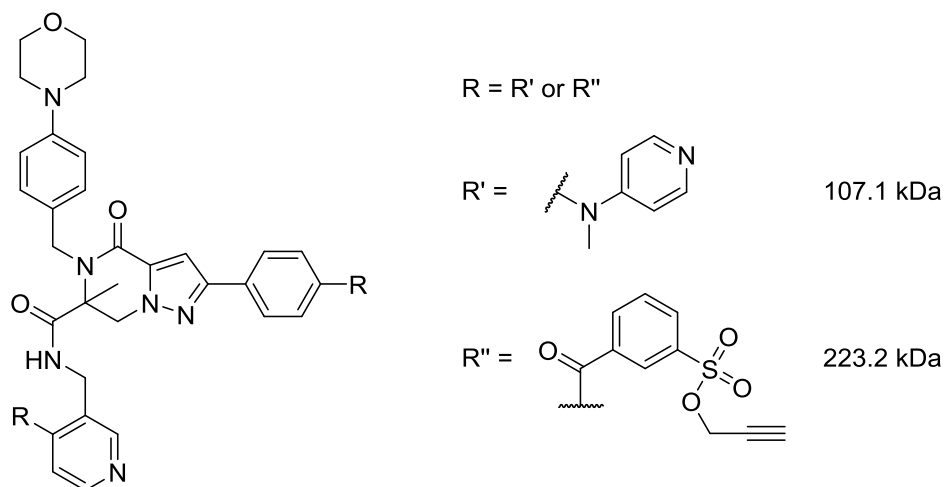


Figure 87 Proposed structural modifications of Glutor.

Even though the modifications are, depending on the linker size, with at least 107.1 kDa (DMAP) and 223.2 kDa (tosyl + alkyne-tag) rather small, they could still intervene with the interaction between Glutor and the GLUT. However, if this approach is applicable, it may also reveal off-targets that are bound by Glutor.

Since all results obtained within this doctoral thesis are highly promising for further development of a Glutor-derived drug candidate, the next steps would include structural optimization of the compound for *in vivo* application. This optimization phase is essential to ensure plasma and hepatic stability (metabolism), low renal clearance (excretion) and bioavailability (absorption) of the drug in an organism (ADME = absorption, distribution, metabolism and excretion).¹⁵⁰

Computational analysis of the drug-likeness of Glutor suggested that reduction of the number of aromatic rings and the downsizing of the structure to reduce the molecular weight would enhance the drug-likeness of the compound. These structural optimizations might be employed in the course of compound improvement. Nonetheless, the computational analysis evaluates the drug-likeness based on statistical parameters of marketed drugs.¹⁵⁰ Therefore, structural optimization does not ensure the probability or increase the chance of a drug candidate to enter clinical investigation.

9.2 GLUT isoform selectivity

The investigated compounds Glutor, (+)-Glupin-1 and (*R,R*)-Chromopynone as well as BAY-876 possess different GLUT isoform selectivity profiles. The conducted CETSA® experiments revealed target engagement of GLUT-1 and GLUT-3 for (+)-Glupin-1 as shown by the thermal stabilization of both GLUTs in the presence of the compound. Glutor, although inhibiting glucose uptake in a GLUT-1,-2,-3-selective manner, only influenced the melting behavior of GLUT-3 but not clearly of GLUT-1. The previously clarified targets of (*R,R*)-Chromopynone-1 are GLUT-1 and GLUT-3.¹⁰⁹ The interaction with both isoforms could not be confirmed in the conducted CETSA® experiments (Figure 74). These results suggest, that (*R,R*)-Chromopynone-1 might bind to a site of the GLUT-1 and GLUT-3 transporters that does not influence the thermal stability of these proteins. Hence, (*R,R*)-Chromopynone-1, Glutor and (+)-Glupin-1 bind most likely to different binding sites or different subsites of the same binding site. For comparability, the CETSA® approach should be also applied to BAY-876.

The difference in selectivity could be also due to the different scaffold and substitution patterns of the compounds. The substituents of each compound can be directed towards different amino acids within the same binding site. This can lead to distinct isoform selectivity, but also to different

melting behavior during CETSA® experiments. Competition experiments of e.g. fluorophore- or radioactive-labeled Glutor, (*R,R*)-Chrompynone-1/-2, (+)-Glupin-1 or BAY-876 by the respective other, non-labeled GLUT inhibitors should reveal if all compounds address the same or distinct binding sites of the GLUTs.

However, for localization of the respective binding site of all compounds further investigation should be considered. Two approaches for Glutor, involving the development of a chemical probe for affinity-guided DMAP labeling and ligand-directed tosyl labeling of the target protein GLUT-1/-2/-3 have been described previously. Co-crystallization studies of GLUT-1 (which is targeted by all inhibitors) together with the compounds should be conducted to elucidate the compounds' mode of binding. Since the glucose binding site of all class I GLUTs is identical, the compounds are expected to bind structurally distinct regions between the isoforms. The intracellular and the extracellular α -helices contain unique sequence stretches to GLUT-1. Therefore, one could propose the binding of the GLUT-1 selective compound BAY-876 to one of these regions. However, since Siebeneicher *et al.* reported structural analogs of the GLUT-1-selective BAY-876 with different GLUT isoform selectivity profiles, this is most likely not the binding site for BAY-876. Hence, the binding site of BAY-876 might also lay within the solute channel of GLUT-1, above or below the glucose binding site.

9.2.1 Target identification, validation and off-targets

TPP is a very powerful, label-free method for target identification that could be further used to propose potential off-targets for the compounds (+)-Glupin-1 and BAY-876. Since both compounds induced slight mitotoxicity in cells treated in the presence of galactose and the absence of glucose, potential off-targets could be associated to mitochondrial proteins. TPP identified the mitochondrial trans-2-enoyl-CoA reductase as potential off-target for (+)-Glupin-1. BAY-876 destabilized the ADP/ATP translocase 3, which is a mitochondrial protein that is shuttling

ADP in and ATP out of the mitochondria. Subsequent investigation of the cellular metabolism of HCT116 cells revealed a concentration-dependent mitochondrial uncoupling effect of BAY-876, which could be explained by an overactivation of the ADP/ATP translocase 3 and therefore suggested the protein as potential off-target. Schirris *et al.* described inhibition of the ADP/ATP translocase 3 as undesirable off-target effect of the cannabinoid receptor 1 antagonist Ibipinabant that resulted in myotoxicity during treatment of dogs *in vivo*.¹⁵¹ Consequences of the stimulation of ADP/ATP translocase 3 activity are unknown. However, Yang *et al.* linked the activity of the ADP/ATP translocase 3 to tumor necrosis factor- α (TNF- α)-induced apoptosis in MCF7 cells.¹⁵² This connection between ADP/ATP translocase 3 overexpression and apoptosis induction was also made by Zamora *et al.*¹⁵³ Additionally, Yang *et al.* associated the mitochondrial membrane potential and cytochrome c release to ADP/ATP translocase 3 function, which might explain the observed mitotoxic effect due to the overactivation of this enzyme.¹⁵² However, since Glutor, (+)-Glupin-1 and (*R,R*)-Chromopynone-1/-2 have not been examined in a mito stress test, the increased mitochondrial capacity cannot be definitely associated with an activation of the ADP/ATP translocase 3. As a matter of course, both proposed off-targets need further validation to make distinct conclusions.

9.3 Rescue effect

Glucose starvation of DLD-1 cells by means of Glutor treatment or in the absence of glucose increased GLUT-1 and GLUT-3 protein and mRNA level, but not *GLUT2* and *GLUT4* mRNA levels, after 24 h and 48 h. This observation indicated that cancer cells employ a rescue mechanism to increase the intake of glucose by means of transporter upregulation. Especially the upregulation of GLUT-3, which was also observed in HCT116 cells on mRNA level, is highly relevant because of two main reasons:

1) The neuronal glucose transporter GLUT-3 is a high-affinity glucose transporter with a K_m value of 1.4 mM for 2-DG.¹⁵⁴ This low K_m value is highly beneficial in a hypoglycemic environment and therefore ensures the uninterrupted supply of neurons with glucose. Under glucose starvation conditions, neuronal rat cells and mice brain tissue show an upregulation of GLUT-3 in order to ensure glucose influx.¹²⁹ The affinity of GLUT-1 for 2-DG is lower ($K_m=6.9$ mM)¹⁵⁴ than of GLUT-3, which gives cells with high GLUT-3 expression a survival advantage under hypoglycemic conditions (1-2 mM) compared to cells that exhibit high levels of GLUT-1.^{154,155} GLUT-3 upregulation has been already observed in the cervix carcinoma cell line HeLa *in vitro* under low glucose (2.5 mM) concentrations.¹³⁰

2) The upregulation of GLUT-3 was not only observed during treatment of DLD-1 cells with Glutor, but also with (+)-Glupin-1. This confirms the rescue effect during glucose uptake inhibition with a GLUT inhibitor. DLD-1 cells treated with the GLUT-1-selective inhibitor BAY-876 revealed the same rescue effect. Conclusively, upregulation of GLUT-1 and GLUT-3 expression upon glucose starvation in cancer requires treatment with a GLUT-1/GLUT-3 dual-selective inhibitor such as Glutor or (+)-Glupin-1 in order to inhibit glucose influx completely. The treatment with a solely GLUT-1-selective inhibitor puts cancer in a position to rescue itself from glucose depletion by upregulating GLUT-3, which might also drive clonal selection towards more adapted and, therefore, more malignant cancer cells. Hence, a GLUT-1/GLUT-3 dual-specific inhibitor holds great promise to efficiently and completely block glucose uptake in cancer since it can cope with the observed cellular rescue mechanism.^{129,130}

The mRNA level for the glucose transporter GLUT-4 is reduced upon Glutor, (+)-Glupin-1 and BAY-876 treatment. In resting insulin-responsive cells, GLUT-4 is stored in vesicles and only 1% of GLUT-4 proteins is exposed on the plasma membrane.¹⁸ Upon postprandial insulin secretion, the translocation of GLUT-4 to the plasma membrane is induced in insulin-responsive tissue, and GLUT-4 contributes to cellular glucose uptake. Interestingly, in 3T3L1 adipocytes, phases of

glucose deprivation increase the protein level of GLUT-1, whereas the GLUT-4 protein level remains unaltered while *GLUT4* mRNA level is reduced by 10-fold.¹⁵⁶ This mechanism might represent an adaptation mechanism under hypoglycemic conditions for adipose tissue that is also implemented by cancer. However, in HCT116 cells, *GLUT4* mRNA was increased significantly after 48 h of treatment under glucose deprivation (0 mM) and in the presence of Glutor which suggests a cell line-dependent adaptation to glucose starvation with respect to *GLUT4* expression.

Transcripts of the glucose transporter GLUT-2 were not detectable under fed and glucose-starved conditions after 24 h and 48 h in DLD-1 and HCT116 cells. The reason may be that both cell lines are not able to express and therefore regulate GLUT-2 expression. Alternatively, GLUT-2 is not relevant in this scenario of glucose starvation. In general, GLUT-2 is considered less relevant for cancer-targeted glucose uptake inhibition because of its function in glucose sensing and postprandial glucose (re)absorption, which makes GLUT-2 the primary target for diabetes.¹⁵⁷

9.3.1 Regulation of B2M

Beta-2-microglobulin (B2M) is part of the major histocompatibility complex (MHC) class I protein and is important for MHC I complex stability. The MHC I complex presents endogenous or exogenous peptide antigens to the immune system, more precisely to cytotoxic T cells and is expressed on the plasma membrane of nearly all nucleated cells. The complex is involved in T cell activation upon e.g. microbial infection.¹⁵⁸ *B2M*, which was often validated for the use as internal reference gene in RT-qPCR, served also as a reference gene in this thesis to normalize the expression level of the GLUT isoforms of interests.¹⁵⁹ Thereby, it was observed that *B2M* expression was elevated similar to *GLUT1* mRNA under low glucose levels or during GLUT inhibitor treatment. Granados *et al.* observed a decreased surface expression in MHC I upon glucose starvation that did not influence the mRNA level of MHC I proteins H2K and H2D.¹⁶⁰ Nonetheless, *B2M* mRNA was increased by nearly 2-fold although no significance was observed. The authors proposed that decreased overall protein synthesis hinders the correct presentation of

peptides on MHC I and the upregulation of B2M does not increase MHC I-peptide presentation. In conclusion, the observed link between glucose starvation and increased B2M expression does most probably not directly influence MHC I-peptide surface presentation and has therefore no direct relevance for this work.

9.4 Cancer cell growth inhibition

Glutor impedes the growth of a variety of cancer cell lines from different tissues and origin (metastatic vs. primary tumors). Nearly half of the 94 employed cell lines were inhibited with an IC_{50} value below 100 nM, which demonstrates the potentially broad application range of Glutor toward manifold cancer types. Compared to the other employed glucose uptake inhibitors (+)-Glupin-1, BAY-876 and (*R,R*)-Chromopynone-2, Glutor clearly possessed the strongest potency to inhibit cell growth. The cell lines with the highest Glutor sensitivity, UM-UC-3 and MIA PaCa-2, were also the most sensitive cell lines during (+)-Glupin-1 and BAY-876 treatment. (*R,R*)-Chromopynone-2 revealed the highest potency for the B cell lymphoma cell line WSU-NHL, followed by UM-UC-3 and MIA PaCa-2 cells. However, the glucose dependence of the cell line WSU-NHL is unknown, whereas UM-UC-3 and MIA PaCa-2 are highly glucose-dependent.^{161–163} Overall, urinary bladder carcinoma cell lines are overrepresented among the most sensitive 10% within the panel treated with Glutor. Indeed, high glucose dependence or sensitivity toward glycolytic inhibitors is described for all urinary bladder carcinoma cell lines within the most sensitive 10%.^{161,163} This might reveal a high glucose dependence of this cancer type, which makes urinary bladder carcinomas an interesting target for glucose uptake inhibition in cancer therapy.

The non-malignant cell line IMR-90 and peripheral blood mononuclear cells (PBMCs), which were employed to assess unspecific toxicity, were resistant against treatment with all employed glucose

uptake inhibitors. Furthermore, eight malignant cell lines were resistant against the treatment with all glucose uptake inhibitors, irrespective of their GLUT isoform selectivity profile. These cell lines included the leukemic cell line THP-1, the B lymphoma cell line GRANTA-579 and, the melanoma cell lines SKMEL5 and SKMEL28, the breast cancer cell line SKBR3, the sarcoma cell line HS729, the hepatic carcinoma cell line HEPG2 as well as the colorectal cancer cell line COLO678. However, the available literature points towards a glycolytic phenotype for THP-1 and HEPG2 cells, which are sensitive to glucose withdrawal, and SKBR3 cells, that are not addicted to glutamine.^{164–166} Hence, the nutrient dependence cannot explain the resistance of THP-1, HEPG2 and SKBR3 cells. No information on the metabolic phenotype of the other resistant cell lines were reported in the literature. Another reason might lay in the metabolic adaptation potential as seen previously during a glycolysis stress test of the Glutor-resistant cell line BxPC-3 versus the highly Glutor-sensitive cell line UM-UC-3. Hence, the metabolic profiles, *i.e.* respiratory reduction upon glucose addition and the glycolytic capacity, should be investigated for the eight GLUT inhibitor-resistant cell lines. Other reasons for the observed resistance might lay in the genetic background of these cell lines. For this, in-depth bioinformatic analysis is required.

Of note, the brain cell line SF268 and the placenta cell line JAR are resistant towards treatment with the GLUT-1-selective BAY-876, whereas the other glucose uptake inhibitors could reduce the growth of these cell lines. SF268 and JAR cell lines are not included in the *Cancer Cell Line Encyclopedia* (CCLE). Therefore, the expression levels of the different GLUT class I isoforms cannot be used to explain this observation. Hence, the expression of the GLUT isoforms and also the metabolic profiles of these cell lines should be investigated for possible explanation. However, it is known that SF268 cells are sensitive to glucose withdrawal whereas nothing is known about the metabolic phenotype of JAR cells.¹⁶⁷

Glutor could induce toxicity not only in monolayer-cultured HCT116 cells but also in a physiologically more relevant spheroid model. The core of the spheroid showed the highest

sensitivity to glucose starvation. Spheroids are recognized to more adequately represent physiological conditions by taking factors like three dimensional shape and small molecule penetration into account.¹²⁶ In addition, gene expression profiles of spheroids and therefore metabolic states like nutrient dependence resemble clinical expression profiles more closely.¹²⁶ In line with the results described in this work, Wenzel *et al.* treated spheroids of the breast cancer cell line T47D with 2-DG, which induced cell death in the inner part of the spheroid that has limited access to nutrients, *i.e.* glucose.¹⁶⁸ The outer circle of the spheroids stayed viable, as observed in the experiments described in this thesis. Only the treatment with an inhibitor of oxidative phosphorylation (Rotenone, Metformin, Oligomycin A, Antimycin A or Diphenyleneidonium) in the absence of glucose or as co-treatment with 2-DG led to cell death of the entire spheroid.¹⁶⁸ This result suggests that the outer region of the spheroid is capable to switch the metabolism to oxidative phosphorylation, whereas the inner dormant core cannot adapt to the glucose-depleted condition due to low oxygen availability. In addition, spheroids have a heterogeneous nature. Glycolytic cancer cells excrete the highly energetic nutrient lactate that can be further metabolized by cancer cells in less perfused regions. Corbet *et al.* revealed a high sensitivity of pharynx squamous cell carcinoma FaDU spheroids to lactate uptake inhibition with respect to cell growth.¹⁶⁹ Thus, the necrotic core of the inner spheroid might result from the glucose depletion and therefore metabolic switch of the outer spheroid to oxidative phosphorylation, which reduces the lactate supply in addition to the glucose depletion in the inner core. Hence, a co-treatment approach in spheroids addressing oxidative phosphorylation and glucose uptake promises to address the heterogeneity within the tumor and, furthermore, to reduce the metabolic adaptation potential.

9.5 Ras mutation and glucose addiction

Nearly all cancer cells within the panel that were resistant to Glutor carry the wild type proto-oncogene KRas, whereas the majority of cells possessing a KRas mutation were sensitive towards glucose deprivation induced by Glutor treatment. Moreover, mutations in the other Ras isoforms were detected among the most sensitive cancer cell lines. In general, Ras mutations were primarily detected in codons 12 (41%), 13 (18%) and 61 (26%). All of these codons are known to inhibit the GTP hydrolysis by reducing the GTPase activity, which renders Ras constitutively active.¹⁷⁰

Oncogenic Ras induces cancer metabolism rewiring (Warburg effect) and metabolic uncoupling of oxidative phosphorylation through two main pathways.^{5,124} Phosphatidylinositol-4,5-bisphosphate 3-kinase (PI3K)/ RAC- α serine/threonine-protein kinase (AKT1) signaling leads to HIF-1- α stabilization and thereby upregulation of glycolytic proteins that are involved in rate-limiting steps of glycolysis such as GLUT-1, which may explain the high glucose dependence KRas-mutated cell lines.⁶⁰ RAF/mitogen-activated protein kinase (MEK)/extracellular-signal-regulated kinase (ERK) signaling on the other hand induces the upregulation of the transcription factor Myc that directly activates glycolytic enzymes and proteins such as GLUT-1.⁵ However, sensitivity of cancer cell lines to Glutor was not restricted to cells with mutated KRas since several sensitive cell lines express the wild type protein. Investigation of the mutational status of all Ras isoforms KRas, NRas and KRas revealed an accumulation of oncogenic Ras in Glutor-sensitive cell lines. This observation was not restricted to Glutor treatment but also applied to cancer cells treated with (+)-Glupin-1, (*R,R*)-Chromopyrone-1 and BAY-876. These findings suggest that targeting glucose import may be a viable approach to inhibit cancer cell growth, especially of cancer types that possess oncogenic Ras such as pancreatic ductal adenocarcinomas (PDAC).¹²⁵ Furthermore, nearly all PDACs employed in the panel were sensitive to Glutor treatment, except for the cell line BxPC-3, which is known to possess a lipogenic and non-glycolytic phenotype.¹⁶²

Hence, this confirms the high sensitivity of PDACs against the treatment with the glucose uptake inhibitor Glutor.

This finding might reveal a potential opportunity to target very aggressive cancers by cutting their glucose supply since they often harbor KRas mutations. Most prominent are PDCA, which harbor a KRas mutation in 85% of the cases and a poor prognosis with a 5-year survival rate lower than 5%.¹⁷¹ Moreover, the treatment opportunities for PDAC are highly unsatisfactory since PDACs exhibit a highly heterogeneously mutated genome and a dense stromal environment that makes PDACs one of the most chemo-resistant cancers. Therefore, patients are mostly subjected to palliative treatment to decrease disease-associated symptoms.¹⁷² Further investigations addressing KRas-dependent tumors with glucose uptake inhibitors should employ studies with an isogenic cell lines harboring KRas wildtype and two genetically engineered KRas heterozygous and homozygous mutated cell lines similar to the approach of Kerr *et al.*⁶⁵ These three isogenic cell lines should exhibit a different degree of glucose addiction and therefore Glutor sensitivity, since Kerr *et al.* could prove a correlation between glucose addiction and KRas copy number in NSCLC.⁶⁵ Furthermore, a co-treatment approach could be also applied for KRas-dependent cancers employing Glutor and a small molecule that interrupts KRas signaling. Several biologically tested compounds have been described in the literature that target mutated KRas directly (e.g. KRas G12C) or are involved in the catalytic cycle of the protein (PDEdelta chaperon-mediated endomembrane cycling).¹⁷³⁻¹⁷⁷ The rapid clonal selection of superior cancer cell population results in a fast resistance towards compounds that are targeting KRas signaling. However, co-administration of Glutor might increase the sensitivity towards KRas inhibition since the lower proliferation rate in the absence of glucose also limits the possibility of resistance accumulation.

Additionally, the results obtained with the cell panel could be used to investigate differences in the genetic signature as well as the expression profile of the included cancer cell lines. Since possibly a combination of genetic (e.g. Ras) and expressional alterations (e.g. Myc) account for a high

sensitivity towards glucose depletion, computational analysis should be employed to investigate potential differences between the employed cell lines. The employment of available databases is of extreme importance for this approach. Ultimately, these genetic and expressional changes might also explain the different metabolic profiles of highly (Glutor-)sensitive cell lines, *i.e.* UM-UC-3 and (Glutor-)resistant cell lines, *i.e.* BxPC-3.

9.6 Metabolic flexibility and combinatory treatment approach

Glutamine is the most abundant amino acid in the human plasma and considered a non-essential amino acid since normal, non-dividing cells can synthesize glutamine *de novo*.⁷⁵ However, under stress conditions or during proliferation (*e.g.* T-cell activation)^{178,179} glutamine demand exceeds the supply and glutamine becomes an essential amino acid.⁷⁹ Glutamine can serve as a precursor for α -ketoglutarate, which fuels the TCA cycle for ATP production (mitochondrial respiration) and as anaplerotic starting material for nucleotide and amino acid synthesis, which makes glutamine metabolism an attractive target for cancer therapy.¹⁸⁰ The interplay between glucose and glutamine metabolism is highly complex and both metabolic pathways fuel ATP generation, maintenance of redox-balance and supply of biosynthetic precursors that are coordinated within the cell. Genetic alterations can influence the preference of cancer for one metabolic pathway. Glutamine metabolism and potential glutamine addiction is driven by Myc, KRas, HIF-1- α , receptor tyrosine-protein kinase erbB-2 (erbB-2), tyrosine-protein kinase JAK (JAK)/signal transducer and activator of transcription (STAT), serine/threonine-protein kinase mTOR (mTOR) and nuclear factor erythroid 2-related factor 2 (NRF2) activation as well as protein kinase C zeta type (PKC2), phosphatidylinositol 3,4,5-triphosphate 3-phosphatase and dual-specificity protein phosphatase PTEN (PTEN), retinoblastoma-associated protein (RB1) and p53 loss.¹⁸¹ Despite the fact that glutamine and glucose metabolism fulfill different functions in phases of high nutrient demand both pathways may compensate for one another.⁷⁵ This generates a certain metabolic plasticity that

enables cancer to quickly adapt to phases of nutrient reduction or depletion by upregulation of the other main metabolic pathway, as observed in the metabolic profile of BxPC-3 cells.¹⁸² Thus, it might be beneficial to target both metabolic pathways simultaneously to avoid clonal selection of highly flexible cancer cells. In this context, it has already been shown that reduced GLUT-1 expression sensitizes lung cancer cells to restricted glutamine supply.⁸² Furthermore, a beneficial effect on the inhibition of ovarian cancer cell growth was observed when the unspecific transaminase inhibitor aminooxyacetate (AOA), which interrupts glutaminolysis, and the glucose analogue and glycolysis inhibitor 2-DG were administered simultaneously.⁸³

Therefore, it seemed natural that the potency of Glutor would be enhanced if low glutamine concentrations were applied to monolayer cultured HCT116 cells, since these were highly sensitive to glutamine depletion. Of note, the administration of low glutamine concentrations to HCT116 spheroids did not alter the compound potency very much and interestingly, the nutrient dependence in spheroids compared to monolayer cultured cells seemed to be reversed. Whereas in monolayer culture, glutamine depletion reduced HCT116 cell growth more efficiently than glucose depletion, spheroids were far more sensitive to glucose than glutamine starvation, which resulted in the formation of a large necrotic core and in large spheroids even to spheroid bursting. It is known that the cellular microenvironment can have an immense impact on nutrient dependencies. Davidson *et al.* showed that KRas-driven non-small cell lung cancer (NSCLC) cells were highly glutamine-dependent when cultured *in vitro* in monolayer and switched to a highly glucose-addicted phenotype when the same cell line was inserted as xenograft in nude mice.⁶⁴ The described findings confirm the observations made by Davidson *et al.*

Since the nutrient dependence of HCT116 cells *in vivo* is unknown and in monolayer culture a clear glutamine addiction was observed, Glutor was co-administered with the glutaminase kidney isoform (GLS) inhibitor CB-839. Both compounds acted synergistically on cell growth inhibition and could increase Glutor potency by about 40-fold in presence of CB-839 at high glucose and

glutamine concentrations. Of note, the reported CB-839 sensitivity of triple negative breast cancer (TNBC) cell lines such as HCC1806 and MDA-MB-231 is extremely high (proliferation inhibition IC_{50} =20-55 nM), which at first sight disagrees with the low potency of CB-839 in HCT116 cells (interpolated IC_{50} 35.6 μ M). However, an NCI60 cell panel of CB-839 revealed a surprisingly low sensitivity towards CB-839 of most employed cell lines, including HCT116 cells.¹⁸³ HCT116 cells exhibited a GI_{50} of 16.2 μ M¹⁸³ which is in line with the IC_{50} of 35.6 μ M determined during live-cell experiments and in the absence of Glutor in this thesis. Therefore, the synergistic effect of Glutor and CB-839 is not only increasing the potency but clearly sensitized the treated cell line for CB-839 treatment in the first place. This sensitizing effect through Glutor might widen the therapeutic application of CB-839 that is currently only co-administered in clinical trials with, e.g., the poly [ADP-ribose] polymerase 1 (PARP1) inhibitor Talazoparib¹⁸⁴ and the epidermal growth factor receptor (EGFR) inhibitor Osimertinib¹⁸⁵, to a broader range of cancer types.⁸¹ These studies should be expanded to include other in-house or external GLUT inhibitors in co-administration with CB-839. Since spheroids showed a lower glutamine but high glucose dependence, it would be interesting to apply the combinatory treatment to spheroids to ensure a beneficial effect in physiologically more relevant model. The subsequent transfer to a mouse xenograft model would reveal the possibility for *in vivo* application.

Thus, targeting both major metabolic pathways simultaneously inhibits the growth of cancer cells very effectively that it clearly suggests further investigation of a co-treatment approach to avoid therapy resistance through metabolic plasticity.

9.6.1 Other combinatorial treatments

Furthermore, experiments of this thesis indicated that the dual targeting of glucose uptake via the less active Glutor derivative (**S**)-5n and oxidative phosphorylation with the use of the mitochondrial complex I inhibitor Aumitin showed a clear synergism with regard to cell growth inhibition.¹³⁶ This observation broadens the applicability of co-treatment approaches with glucose uptake inhibitors

and modulators of numerous targets within the TCA cycle, enzymes involved in precursor maturation for the TCA cycle or proteins within the respiratory chain.

Recently, the glutamate dehydrogenase inhibitor R162, a purpurin analog, was identified in a biochemical assay.¹⁸⁶ Since the glutamate dehydrogenase converts glutamate to α -ketoglutarate, which fuels the TCA cycle, R162 could be a well-suited tool compound for a co-treatment approach. R162 reduced the cell viability of multiple cancer cell lines with micromolar potency and was shown to be effective in mouse xenograft models.¹⁸⁶ The α -ketoglutarate dehydrogenase converts α -ketoglutarate to succinyl-CoA, which is part of the TCA cycle. CPI-613, a clinical candidate that inhibits the α -ketoglutarate dehydrogenase, shows promising results in patients with acute myeloid leukaemia.¹⁸⁷ Also the combinatorial treatment of patients with CPI-613 and a glucose uptake inhibitor will most likely show beneficial effects with regard to cancer cell growth inhibition. Corbet *et al.* reported promising effects for the disruption of mitochondrial pyruvate transport by the compound 7ACC2 in FaDu spheroids that led to the inhibition of lactate uptake, which is used as nutrient by less perfused cancer cells.¹⁶⁹ Also inhibition of mitochondrial pyruvate transport and glucose uptake inhibition might be interesting to explore as potential co-treatment strategy.

Amino acids other than glutamine, such as valine and serine, have been recognized to be important for cancer cell growth and biomass production.^{188,189} Furthermore, the influence of aspartate on glutamine dependency was recently examined on cell survival, which underlines the complex interplay between different amino acids.¹⁹⁰ The specific disruption of the anabolic or catabolic usage of alternative amino acids might reveal another advantageous susceptibility of cancer that could result in novel co-treatment opportunities with Glutor.

Furthermore, it has been shown that most cancer cells exhibit an increased glycogen metabolism, and hence glucose storage.¹⁹¹ Upon glucose starvation, cancer cell can mobilize glucose from intracellular glycogen stocks, and thereby span phases of glucose depletion. These phases could

support clonal selection of highly resistant cell lines. The liver isoform of the glycogen phosphorylase PYGL, that is involved in glucose mobilization, is overexpressed in cancer in response to hypoxia. Since PYGL is also a desirable treatment target for type II diabetes, different PYGL inhibitors such as CP-91149 (Pfizer Inc.) have been developed.¹⁹² CP-91149 inhibits PYGL with nanomolar potency and lowered plasma glucose levels in diabetic mice.¹⁹² A combinatory treatment approach that targets the depletion from extracellular and intracellular glucose pools simultaneously might reveal a beneficial effect on cancer cell line sensitivity towards glucose starvation. This strategy has not been reported so far.

Of note, no metabolic pathway is unique to malignant cells. Hence, targeting metabolism will not solely address cancer. However, many of the metabolic adaptations that cancer undergoes support cancer proliferation while the most non-malignant cells are differentiated and thus in a low proliferative state. Therefore, small molecules that target metabolic pathways, which drive proliferation, would preferentially target cancer.¹⁹³ Moreover, targeting multiple metabolic pathways at once reduces the dose of each single agent, thus decreasing potential side effects. Additionally, combinatorial treatment automatically addresses tumor heterogeneity, reduces the adaptation potential of cancer and therefore clonal selection.¹⁹⁴

Addressing cell proliferation by chemotherapeutics in combination with metabolic drugs sensitizes cancer to the chemotherapeutic agent. Promising results have been obtained in treatment of mouse xenograft models with chemotherapeutic DNA-damaging agent Etoposide and the glycolysis inhibitor 2-DG.¹⁹⁵ Additionally, this co-treatment approach resulted in a more efficient antitumor immune response, as observed in a slight manner during treatment with most DNA-damaging agents, due to the expression of danger-associated molecular patterns (DAMPs) on the plasma membrane of dying cancer cells.¹⁹⁵ Moreover, the combination of 2-DG and Doxorubicin was described to enhance the effect of radiotherapy of breast cancer cells *in vitro*.¹⁹⁶ These

examples show the vast range of co-treatment applications of compounds that interfere with glucose metabolism.

9.7 Further indications and applications of glucose uptake inhibitors

Glucose metabolism plays an important role in many physiological and pathophysiological events. Not only the overexpression of major GLUT isoforms and thereby glucose addiction in cancer is an attractive therapeutic strategy to investigate, but also other diseases that exhibit an increased glucose metabolism are of interest. Hereby, especially diseases that are related to inflammation as well as immunity and infection should be in focus of such ambitions. Whereas resting inflammatory cells rely primarily on fatty acid beta oxidation for homeostasis, activated inflammatory cells switch their metabolism to aerobic glycolysis. Macintyre *et al.* discovered in 2014 that GLUT-1 deficiency prevented activated CD4⁺ T cells from growth, proliferation, survival and differentiation to effector T cells, which cause inflammation *in vivo*.⁸⁷ Effector CD4⁺ T cells are enriched in inflammatory diseases, e.g. inflammatory bowel disease and graft-versus-host disease.^{197,198} However, GLUT-1-depleted effector CD4⁺ T cells were unable to induce graft-versus-host disease and colitis.⁸⁷ Resting T cells and activated regulatory T cells that rely mainly on lipid oxidation as energy source, were not influenced by GLUT-1 deficiency and furthermore suppressed effector T cells *in vivo*.⁸⁷ Hence, GLUT-1 depletion or glucose uptake inhibition may provide a layer for selective starvation of activated effector CD4⁺ T cells and therefore a novel therapeutic approach for this disease. Four years later, Jodeleit *et al.* investigated the treatment of ulcerative colitis in a mouse model with ritonavir, an HIV protease inhibitor, that impeded GLUT-4 function as off-target.¹⁹⁹ In the autoimmune disease systemic lupus erythemethus (SLE), autoreactive CD4⁺ T cells contribute to the malignant state of the patient.⁸⁸ These cells upregulate both, glycolysis and mitochondrial oxidative phosphorylation, and the combinatorial treatment of lupus murine models with metformin (inhibitor of mitochondrial metabolism) and 2-DG showed

promising results.⁸⁸ Hence, not only cancer but also other diseases that show deregulated immune response are highly relevant for combinatorial treatment approaches of oxidative phosphorylation and glycolysis.

Regulating keratinocytes are associated with up-regulated GLUT-1 protein expression upon wound damage, UV irradiation and hyperplasia. Furthermore, *GLUT1* deficiency led to impaired growth of keratinocytes *in vitro*. Psoriasis is an inflammatory skin disease associated with hyperplasia of the epidermis,⁸⁴ and glucose uptake inhibition of overactivated keratinocytes might offer a novel therapeutic approach for this indication. Hyperplasia is also a phenomenon of fibrosis. Stimulation of fibroblasts with the profibrotic cytokine TGF- β increases among others fibroblast proliferation²⁰⁰ and GLUT-1 expression *in vitro* and in lungs of patients with idiopathic pulmonary fibrosis as well as in a lung fibrosis mouse model.⁸⁶ Therefore, diseases associated with hyperplasia should be well suited for the application of glucose uptake inhibitors as potential therapeutic strategy.

Host cells that are infected by intracellular replicating bacteria adapt their metabolism, similar to cancer cells, to a Warburg-like phenotype (aerobic glycolysis).²⁰¹ Reports about these bacteria include *Mycobacterium tuberculosis*,^{202–206} *Legionella pneumophila*,⁸⁵ *Brucella abortus*,²⁰⁷ *Chlamydia trachomatis*^{208,209} and *Chlamydia pneumoniae*²¹⁰. Interestingly, 2-deoxy-2-(¹⁸F)fluoro-*D*-glucose (FDG)-positron emission tomography (PET) scanning has been successfully applied for diagnosis and monitoring of treatment efficacy of antimicrobial therapy, similar to FDG-PET application in cancer diagnosis.²¹¹ Escoll *et al.* proved that inhibition of glycolysis by 2-DG reduced the replication of *Legionella pneumophila* in primary human macrophages, whereas inhibition of mitochondrial ATP production by Oligomycin had no effect on bacterial replication.⁸⁵

Not only bacterial infections, but also viral infections are associated with metabolic reprogramming of their host cells. Rhinovirus-infected cells upregulate GLUT-1 protein in a PI3K-dependent manner.⁸⁹ Furthermore, Gualdoni *et al.* implemented in-depth metabolomics to reveal an

additional glucose mobilization from intracellular glycogen storage. Inhibition of glycolysis with 2-DG reduced the virus replication and reverted the metabolic reprogramming from aerobic glycolysis to lipogenic phenotype.⁸⁹ In a mouse model, 2-DG furthermore inhibited the viral infection and inflammation, which underlines the high potential of glucose uptake inhibitors also in this therapeutic application.⁸⁹ Furthermore, HIV-infected patients harbor an increased amount of CD4⁺ T cells that express high levels of GLUT-1 prior to treatment.⁹⁰ During antiretroviral therapy, the number of CD4⁺ T cells declined, albeit not to the level of uninfected people.⁹⁰ Therefore, inhibition of glycolysis by, e.g., glucose uptake inhibition could be a way to selectively target HIV-infected CD4⁺ T cells.

Moreover, upregulation of glycolytic enzymes and hence, increased glycolysis was observed in endothelial cells, which results in blood vessel branching and migration.²¹² Malignant vascularization is mainly associated with cancer and ocular neovascularization that may result in different diseases such as age-related macular degeneration (AMD). Kanako *et al.* demonstrated an increased lactate/pyruvate ratio in AMD patients, which indicates increased glycolysis and potentially mitochondrial impairment.²¹³ Therefore, ocular neovascularization diseases may provide an interesting novel therapeutic area for glucose uptake inhibitors that has not been investigated up till now.

In the field of progenitor differentiation, glycolytic control by means of e.g. small molecules has tremendous potential. Only recently, Izumi *et al.* revealed an increased differentiation from connective tissue progenitors to tendon cells and inhibition of chondrogenesis, which is associated with poor healing of injured tendons, when treated with 2-DG.²¹⁴ This may open up a field for directed differentiation for tissue repair to avoid excessive scar formation (fibrosis).

10 Outlook

In this thesis a novel, highly potent GLUT-1/-2/-3 inhibitor, called Glutor, was developed and its applicability was assessed in a range of different cancer cell lines as well as in a 3D cell culture model. Future investigations should address structural modification to metabolically stabilize the compound and hence pave the way for *in vivo* testing.

Combinatorial treatment approaches of glucose uptake inhibition and glutaminolysis restriction or oxidative phosphorylation blockage showed a strong synergism for impairment of cancer cell growth. Other co-treatment approaches addressing distinct metabolic events or cell division could be investigated. Also, the relevance of glutamine restriction and application together with a glucose uptake inhibitor should be addressed *in vivo*.

One important finding within the framework of this thesis was that among 91 Glutor-treated distinct cancer cell lines an accumulation of Ras (especially KRas) mutations was observed among the most sensitive cell lines. Interestingly, this perception held also true for (+)-Glupin-1-, (*R,R*)-Chromopynone-1- and BAY-876-treated cells, confirming the close linkage between KRas-driven cancers and metabolic reprogramming. The cause for this observation should be further investigated in genetic studies, since KRas-driven cancers are until today aggressive diseases with poor prognosis and treatment opportunities. Furthermore, the panel should be analyzed for correlation with gene expression and mutations of manifold genes in a bioinformatic approach.

Since glucose dependence is also highly relevant in immune-associated diseases such as bacterial infections⁸⁵, psoriasis⁸⁴ and colitis⁸⁷, the application range for glucose uptake inhibitors is not only restricted to cancer. Further disease models should be employed to investigate a potential application for other diseases. Hence, the potential that the glucose uptake inhibitor Glutor holds is high, and future studies will reveal its applicability for cancer treatment and other indications.

11 Abbreviations

Abbreviation	Explanation
(+)-Glp1	(+)-Glupin-1
2-DG	2-Deoxy- α -D-glucose, <i>German: 2-Desoxy-D-Glukose</i>
2-DG-P	2-Deoxy- α -D-glucose-6-phosphate
2-HG	2-Hydroxyglutarate
3-BP	3-Bromopyruvate
6P-2-DGA	6-Phospho-2-deoxyglucuronic acid
α -KG	α -Ketoglutarate
β -NG	<i>n</i> -Nonyl- β -D-glucopyraoside
Abs	Absolute
Ac-CoA	Acetyl-CoA
ACN	Acetonitrile
ADP	Adenosine diphosphate
AKT1	RAC- α serine/threonine-protein kinase
AlogP	Negative decadic logarithm of the calculated octanol-water partition coefficient
annul.	Annulated
AOA	Aminooxyacetate
APS	Ammoniumperoxodisulfate
Arom	Aromaticity
ASCT2	Alanine, serine, cystein-preferring transporter 2
ATCC	American Type Culture Collection
ATP	Adenosine triphosphate
B2M	Beta-2-microglobulin
bp	Basepairs
BP	Bisphosphate
bs	Broad singlet
BSA	<i>here: Bovine albumin fraction V</i>
C18	Octadecyl carbon chain
CCLE	Cancer cell line encyclopedia
CETSA®	Cellular thermal shift assay
CHAPS	(3-[3-Cholamidopropyl]-dimethyl-ammonio]-1-propansulfonat
Cmpd	Compound
COMAS	Compound Management and Screening Center
COSMIC	Catalogue Of Somatic Mutations In Cancer
CP	Cytoplasm
CP1	(<i>R,R</i>)-Chromopynone-1
CRC	Colorectal cancer
CS	Cytoskeleton
d	Doublet
dd	Doublet of doublets
ddd	Doublet of doublet of doublets
ddH ₂ O	Double-distilled water
DCM	Dichloromethane
DDM	Dodecyl- β -D-maltoside
DHA	Dehydroascorbic acid
DMEM	Dulbecco's Modified Eagle Medium

Abbreviations

Abbreviation	Explanation
DMSO	Dimethyl sulfoxide
DNA	Deoxyribonucleic acid
DSMZ	Deutsche Sammlung von Mikroorganismen und Zellkulturen
dt	Doublet of triplets
DTE	Dithioerythritol
EC ₅₀	Half-maximal effective concentration
ECAR	Extracellular acidification rate
EDTA	Ethylenediaminetetraacetic acid
EGFR	Epidermal growth factor receptor
ER	Endoplasmic reticulum
erbB-2	Receptor tyrosine-protein kinase erbB-2
ERK	Extracellular-signal-regulated kinase
ex.	Extracellular
FBS	Fetal bovine serum
FCCP	Carbonyl cyanide 4-(trifluoromethoxy) phenylhydrazone
FDA	Food and Drug Administration
FDG	2-Deoxy-2-(¹⁸ F)fluoro- <i>D</i> -glucose
Fru	Fructose
G6PDH	Glucose-6-phosphate dehydrogenase
GalN	Galactosamine
GDP	Guanosine diphosphate
GFPT1	Glucosamine-fructose-6-phosphate aminotransferase-1
GI ₅₀	Half-maximal growth inhibition
Glc	Glucose
GlcN	Glucosamine
Gln	Glutamine
GlpT	Glycerol-3-phosphate transporter
GLS	Glutaminase kidney isoform
GLUD1	Glutamate dehydrogenase 1
GLUT	Facilitative glucose transporter
GOT	Glutamate–oxaloacetate transaminase
GTP	Guanosine triphosphate
HBA	Hydrogen bond acceptors
HBD	Hydrogen bond donors
HBP	Hexosamine biosynthesis pathway
HEPES	4-(2-Hydroxyethyl)-1-piperazineethanesulfonic acid
HIF-1- α	Hypoxia-inducible factor 1-alpha
HIV	Human immunodeficiency virus
HK1/2	Hexokinase 1/2
HPLC	High-performance liquid chromatography
HRas	GTPase HRas
HR-MS	High resolution mass spectrometry
HRP	Horseradish peroxidase
IC ₅₀	Half-maximal inhibitory concentration
Inc.	Incorporated
Interp	Interpolated
<i>J</i>	Coupling constant
JAK	Tyrosine-protein kinase JAK
KRas	GTPase KRas

Abbreviations

Abbreviation	Explanation
KRB	Krebs-Ringer buffer
LogD	A _{LogP} at pH 7.4
Ltd.	limited
Lys	Lysosome
m	Multiplet
Man	Mannose
MAPK	MAP kinase
MEK	Mitogen-activated protein kinase
MEM	Minimum Essential Medium Eagle
Mito	Mitochondrium
mRNA	Messenger RNA
MS	Microsoft
MS	Mass spectrometry
MS	Molecular sieves
MscL	Large-conductance mechanosensitive ion channel
Mt	Maltose
mTOR	Serine/threonine-protein kinase mTOR
MW	Molecular weight
N	Nucleus
NAD ⁺	Nicotinamide adenine dinucleotide phosphate
NCE	New Chemical Entity
NCI	National Cancer Institute
NEAA	Non-essential amino acid
NMR	Nuclear magnetic resonance
NRas	GTPase NRas
NRF2	Nuclear factor erythroid 2-related factor 2
NP-40	Nonidet P-40
NSCLC	Non-small cell lung cancer
OAA	Oxaloacetate
OCR	Oxygen consumption rate
O.E.	Overexpression
Oligo	Oligomycin
P	Phosphate
p53	Cellular tumor antigen p53
PARP1	Poly [ADP-ribose] polymerase 1
PBS	Phosphate buffered saline
PCR	Polymerase chain reaction
PDAC	Pancreatic ductal adenocarcinoma
PDB	Protein Data Bank
PET	Positron emission tomography
PI3K	Phosphatidylinositol-4,5-bisphosphate 3-kinase
PI	Propidium iodide
PKC2	Protein kinase C zeta type
PM	Plasma membrane
PMSF	Phenylmethylsulfonyl fluoride
ppm	Parts per million
PPP	Pentose phosphate pathway
PSA	Polar surface area

Abbreviations

Abbreviation	Explanation
PTEN	Phosphatidylinositol 3,4,5-triphosphate 3-phosphatase and dual-specificity protein phosphatase PTEN
PVDF	Polyvinylidene difluoride membrane
PYGL	Glycogen phosphorylase
q	Quartet
QED	Quantitative Estimate of Drug-Likeness
RAF	RAF proto-oncogene serine/threonine-protein kinase
RB1	Retinoblastoma-associated protein
RCU	Bright-field objects red mean intensities
RIN	RNA Integrity Number
RIPA	Radioimmunoprecipitation assay
RNA	Ribonucleic acid
ROS	Reactive oxygen species
RotB	Rotatable bonds
RPMI	Roswell Park Memorial Institute
RT-qPCR	Reverse transcription-quantitative PCR
S	Singlet
SAR	Structure-activity relationship
s.d.	Standard deviation
SDS	Sodium dodecyl sulfate
SDS-PAGE	SDS-polyacrylamide gel electrophoresis
SLC	Solute carrier
SLE	Systemic lupus erythromethus
SRB	Sulforhodamine B
SSR	Structure-selectivity relationship
STAT	Signal transducer and activator of transcription
t	Triplet
TBS	Tris-buffered saline
TCA	Tricarboxylic acid cycle
TCA	Trichloroacetic acid
TCEP	Tris(2-carboxyethyl)phosphine
td	Triplet of doublets
TEAB	Triethylammonium bicarbonate
TEMED	<i>N,N,N,N</i> -Tetramethylethylenediamine
TFA	Trifluoroacetic acid
TGF β	Transforming growth factor β
TLC	Thin-layer chromatography
TMT	Tandem Mass Tag
TNBC	Tripple-negative breast cancer
TNF- α	tumor necrosis factor- α
TPP	Thermal proteome profiling
trans.	Transmembrane
UV	Ultraviolet
VHL	Von Hippel-Lindau disease tumor suppressor
w/o	without
WST	Water soluble tetrazolium
wt	Wildtype
Xyl	Xylose

12 Literature

1. World Health Organization. Cancer. Available at <https://www.who.int/news-room/fact-sheets/detail/cancer>. Accessed 23.04.2019.
2. Hanahan, D. & Weinberg, R. A. The hallmarks of cancer. *Cell* **100**, 57–70 (2000).
3. Hanahan, D. & Weinberg, R. A. Hallmarks of cancer: the next generation. *Cell* **144**, 646–674 (2011).
4. Warburg, O. ber den Stoffwechsel der Carcinomzelle. *Naturwissenschaften* **12**, 1131–1137 (1924).
5. Vander Heiden, M. G., Cantley, L. C. & Thompson, C. B. Understanding the Warburg effect. The metabolic requirements of cell proliferation. *Science* **324**, 1029–1033 (2009).
6. Liberti, M. V. & Locasale, J. W. The Warburg Effect: How Does it Benefit Cancer Cells? *Trends in biochemical sciences* **41**, 211–218 (2016).
7. Amann, T. *et al.* GLUT1 expression is increased in hepatocellular carcinoma and promotes tumorigenesis. *The American journal of pathology* **174**, 1544–1552 (2009).
8. Carvalho, K. C. *et al.* GLUT1 expression in malignant tumors and its use as an immunodiagnostic marker. *Clinics* **66**, 965–972 (2011).
9. Yu, M. *et al.* The prognostic value of GLUT1 in cancers: a systematic review and meta-analysis. *Oncotarget* **8**, 43356–43367 (2017).
10. Mortimer, J. E. *et al.* Positron emission tomography with 2-18FFluoro-2-deoxy-D-glucose and 16alpha-18FFluoro-17beta-estradiol in breast cancer: correlation with estrogen receptor status and response to systemic therapy. *Clinical cancer research* **2**, 933–939 (1996).
11. NIH. A Phase I/II Trial of 2-Deoxyglucose (2DG) for the Treatment of Advanced Cancer and Hormone Refractory Prostate Cancer (2-Deoxyglucose). Available at <https://clinicaltrials.gov/ct2/show/NCT00633087>. Accessed 07.05.2019.
12. Mohanti, B. K. *et al.* Improving cancer radiotherapy with 2-deoxy-d-glucose: phase I/II clinical trials on human cerebral gliomas. *International Journal of Radiation Oncology Biology Physics* **35**, 103–111 (1996).
13. Raez, L. E. *et al.* A phase I dose-escalation trial of 2-deoxy-D-glucose alone or combined with docetaxel in patients with advanced solid tumors. *Cancer chemotherapy and pharmacology* **71**, 523–530 (2013).
14. Nassereddine, S., Lap, C. J., Haroun, F. & Tabbara, I. The role of mutant IDH1 and IDH2 inhibitors in the treatment of acute myeloid leukemia. *Annals of hematology* **96**, 1983–1991 (2017).
15. Scheepers, A., Joost, H.-G. & Schürmann, A. The glucose transporter families SGLT and GLUT: molecular basis of normal and aberrant function. *JPEN. Journal of parenteral and enteral nutrition* **28**, 364–371 (2004).
16. Liu, Y. *et al.* A small-molecule inhibitor of glucose transporter 1 downregulates glycolysis, induces cell-cycle arrest, and inhibits cancer cell growth in vitro and in vivo. *Molecular cancer therapeutics* **11**, 1672–1682 (2012).
17. Amidon, G. L. & Sadée, W. *Membrane Transporters as Drug Targets* (Springer US, Boston, MA, 2002).
18. Szablewski, L. *Glucose Homeostasis and Insulin Resistance* (BENTHAM SCIENCE PUBLISHERS LTD., Sharjah, U.A.E., 2012).

19. Thorens, B. Glucose transporters in the regulation of intestinal, renal, and liver glucose fluxes. *The American journal of physiology* **270**, G541-53 (1996).
20. Deng, D. *et al.* Crystal structure of the human glucose transporter GLUT1. *Nature* **510**, 121–125 (2014).
21. Deng, D. *et al.* Molecular basis of ligand recognition and transport by glucose transporters. *Nature* **526**, 391–396 (2015).
22. Cheeseman, C. & Long, W. Structure of, and functional insight into the GLUT family of membrane transporters. *Cell Health and Cytoskeleton*, 167 (2015).
23. Zhao, F.-Q. & Keating, A. F. Functional properties and genomics of glucose transporters. *Current genomics* **8**, 113–128 (2007).
24. Siebeneicher, H. *et al.* Identification and Optimization of the First Highly Selective GLUT1 Inhibitor BAY-876. *ChemMedChem* **11**, 2261–2271 (2016).
25. Józwiak, P., Krześlak, A., Pomorski, L. & Lipińska, A. Expression of hypoxia-related glucose transporters GLUT1 and GLUT3 in benign, malignant and non-neoplastic thyroid lesions. *Molecular medicine reports* **6**, 601–606 (2012).
26. Krzeslak, A. *et al.* Expression of GLUT1 and GLUT3 glucose transporters in endometrial and breast cancers. *Pathology oncology research* **18**, 721–728 (2012).
27. Yamamoto, T. *et al.* Over-expression of facilitative glucose transporter genes in human cancer. *Biochemical and biophysical research communications* **170**, 223–230 (1990).
28. Mellanen, P., Minn, H., Grénman, R. & Härkönen, P. Expression of glucose transporters in head-and-neck tumors. *International journal of cancer* **56**, 622–629 (1994).
29. Ayala, F. R. R. *et al.* GLUT1 and GLUT3 as potential prognostic markers for Oral Squamous Cell Carcinoma. *Molecules* **15**, 2374–2387 (2010).
30. Younes, M., Brown, R. W., Stephenson, M., Gondo, M. & Cagle, P. T. Overexpression of Glut1 and Glut3 in stage I nonsmall cell lung carcinoma is associated with poor survival. *Cancer* **80**, 1046–1051 (1997).
31. Stockwell, B. R. Chemical genetics: ligand-based discovery of gene function. *Nature reviews. Genetics* **1**, 116–125 (2000).
32. Lehár, J., Stockwell, B. R., Giaever, G. & Nislow, C. Combination chemical genetics. *Nature chemical biology* **4**, 674–681 (2008).
33. La G de Torre, B. & Albericio, F. The Pharmaceutical Industry in 2018. An Analysis of FDA Drug Approvals from the Perspective of Molecules. *Molecules* **24** (2019).
34. Estensen, R. D. & Plagemann, P. G. Cytochalasin B: inhibition of glucose and glucosamine transport. *Proceedings of the National Academy of Sciences of the United States of America* **69**, 1430–1434 (1972).
35. Wood, T. E. *et al.* A novel inhibitor of glucose uptake sensitizes cells to FAS-induced cell death. *Molecular cancer therapeutics* **7**, 3546–3555 (2008).
36. Bloch, R. Inhibition of glucose transport in the human erythrocyte by cytochalasin B. *Biochemistry* **12**, 4799–4801 (1973).
37. Manel, N. *et al.* The Ubiquitous Glucose Transporter GLUT-1 Is a Receptor for HTLV. *Cell* **115**, 449–459 (2003).
38. MacLean-Fletcher, S. & Pollard, T. D. Mechanism of action of cytochalasin B on actin. *Cell* **20**, 329–341 (1980).
39. Wang, D. *et al.* Development of a novel class of glucose transporter inhibitors. *Journal of medicinal chemistry* **55**, 3827–3836 (2012).

40. Cowley, P. M., Wise, A., Brown, T. J., Isherwood, M. & Chakrabarti, A. SLC2A Transporter Inhibitors, WO/2014/187922 (2014).
41. Siebeneicher, H. *et al.* Identification of novel GLUT inhibitors. *Bioorganic & medicinal chemistry letters* **26**, 1732–1737 (2016).
42. Vera, J. C. *et al.* Genistein Is a Natural Inhibitor of Hexose and Dehydroascorbic Acid Transport through the Glucose Transporter, GLUT1. *The Journal of biological chemistry* **271**, 8719–8724 (1996).
43. Murata, H., Hruz, P. W. & Mueckler, M. Indinavir inhibits the glucose transporter isoform Glut4 at physiologic concentrations. *AIDS* **16**, 859–863 (2002).
44. Wu, C.-H. *et al.* In vitro and in vivo study of phloretin-induced apoptosis in human liver cancer cells involving inhibition of type II glucose transporter. *International journal of cancer* **124**, 2210–2219 (2009).
45. Zhan, T., Digel, M., Küch, E.-M., Stremmel, W. & Füllekrug, J. Silybin and dehydrosilybin decrease glucose uptake by inhibiting GLUT proteins. *Journal of cellular biochemistry* **112**, 849–859 (2011).
46. Melstrom, L. G. *et al.* Apigenin inhibits the GLUT-1 glucose transporter and the phosphoinositide 3-kinase/Akt pathway in human pancreatic cancer cells. *Pancreas* **37**, 426–431 (2008).
47. Park, J. B. Flavonoids are potential inhibitors of glucose uptake in U937 cells. *Biochemical and biophysical research communications* **260**, 568–574 (1999).
48. Kwon, O. *et al.* Inhibition of the intestinal glucose transporter GLUT2 by flavonoids. *Federation of American Societies for Experimental Biology* **21**, 366–377 (2007).
49. Strobel, P. *et al.* Myricetin, quercetin and catechin-gallate inhibit glucose uptake in isolated rat adipocytes. *The Biochemical journal* **386**, 471–478 (2005).
50. DeBerardinis, R. J., Lum, J. J., Hatzivassiliou, G. & Thompson, C. B. The biology of cancer: metabolic reprogramming fuels cell growth and proliferation. *Cell metabolism* **7**, 11–20 (2008).
51. Jones, R. G. & Thompson, C. B. Tumor suppressors and cell metabolism: a recipe for cancer growth. *Genes & development* **23**, 537–548 (2009).
52. Semenza, G. L. Regulation of cancer cell metabolism by hypoxia-inducible factor 1. *Seminars in cancer biology* **19**, 12–16 (2009).
53. Cairns, R. A., Harris, I. S. & Mak, T. W. Regulation of cancer cell metabolism. *Nature reviews. Cancer* **11**, 85–95 (2011).
54. Yun, J. *et al.* Glucose deprivation contributes to the development of KRAS pathway mutations in tumor cells. *Science* **325**, 1555–1559 (2009).
55. Telang, S. *et al.* Small molecule inhibition of 6-phosphofructo-2-kinase suppresses t cell activation. *Journal of Translational Medicine* **10**, 95 (2012).
56. Le, A. *et al.* Inhibition of lactate dehydrogenase A induces oxidative stress and inhibits tumor progression. *Proceedings of the National Academy of Sciences of the United States of America* **107**, 2037–2042 (2010).
57. Vander Heiden, M. G. Targeting cancer metabolism: a therapeutic window opens. *Nature reviews. Drug discovery* **10**, 671–684 (2011).
58. Bos, J. L. ras oncogenes in human cancer: a review. *Cancer research* **49**, 4682–4689 (1989).

59. Karapetis, C. S. *et al.* K-ras mutations and benefit from cetuximab in advanced colorectal cancer. *The New England journal of medicine* **359**, 1757–1765 (2008).
60. Ying, H. *et al.* Oncogenic Kras maintains pancreatic tumors through regulation of anabolic glucose metabolism. *Cell* **149**, 656–670 (2012).
61. Hobbs, G. A., Der, C. J. & Rossman, K. L. RAS isoforms and mutations in cancer at a glance. *Journal of cell science* **129**, 1287–1292 (2016).
62. Kawada, K., Toda, K. & Sakai, Y. Targeting metabolic reprogramming in KRAS-driven cancers. *International journal of clinical oncology* **22**, 651–659 (2017).
63. Chiaradonna, F., Gaglio, D., Vanoni, M. & Alberghina, L. Expression of transforming K-Ras oncogene affects mitochondrial function and morphology in mouse fibroblasts. *Biochimica et biophysica acta* **1757**, 1338–1356 (2006).
64. Davidson, S. M. *et al.* Environment Impacts the Metabolic Dependencies of Ras-Driven Non-Small Cell Lung Cancer. *Cell metabolism* **23**, 517–528 (2016).
65. Kerr, E. M., Gaude, E., Turrell, F. K., Frezza, C. & Martins, C. P. Mutant Kras copy number defines metabolic reprogramming and therapeutic susceptibilities. *Nature* **531**, 110–113 (2016).
66. Mayers, J. R. *et al.* Tissue of origin dictates branched-chain amino acid metabolism in mutant Kras-driven cancers. *Science* **353**, 1161–1165 (2016).
67. Ratnikov, B. I., Scott, D. A., Osterman, A. L., Smith, J. W. & Ronai, Z. A. Metabolic rewiring in melanoma. *Oncogene* **36**, 147–157 (2017).
68. Zhou, B., Der, C. J. & Cox, A. D. The role of wild type RAS isoforms in cancer. *Seminars in cell & developmental biology* **58**, 60–69 (2016).
69. Karnoub, A. E. & Weinberg, R. A. Ras oncogenes: split personalities. *Nature reviews. Molecular cell biology* **9**, 517–531 (2008).
70. Semenza, G. L. Defining the role of hypoxia-inducible factor 1 in cancer biology and therapeutics. *Oncogene* **29**, 625–634 (2010).
71. Kroemer, G. & Pouyssegur, J. Tumor cell metabolism: cancer's Achilles' heel. *Cancer cell* **13**, 472–482 (2008).
72. Gaglio, D. *et al.* Oncogenic K-Ras decouples glucose and glutamine metabolism to support cancer cell growth. *Molecular systems biology* **7**, 523 (2011).
73. DeBerardinis, R. J. & Chandel, N. S. Fundamentals of cancer metabolism. *Science advances* **2**, e1600200 (2016).
74. Hensley, C. T. *et al.* Metabolic Heterogeneity in Human Lung Tumors. *Cell* **164**, 681–694 (2016).
75. Daye, D. & Wellen, K. E. Metabolic reprogramming in cancer: unraveling the role of glutamine in tumorigenesis. *Seminars in cell & developmental biology* **23**, 362–369 (2012).
76. DeBerardinis, R. J. *et al.* Beyond aerobic glycolysis: transformed cells can engage in glutamine metabolism that exceeds the requirement for protein and nucleotide synthesis. *Proceedings of the National Academy of Sciences of the United States of America* **104**, 19345–19350 (2007).
77. Csibi, A. *et al.* The mTORC1/S6K1 pathway regulates glutamine metabolism through the eIF4B-dependent control of c-Myc translation. *Current biology* **24**, 2274–2280 (2014).
78. Michoudet, C., Chauvin, M. F. & Baverel, G. Glutamine synthesis from glucose and ammonium chloride by guinea-pig kidney tubules. *The Biochemical journal* **297**, 69–74 (1994).

79. Still, E. R. & Yuneva, M. O. Hopefully devoted to Q: targeting glutamine addiction in cancer. *British journal of cancer* **116**, 1375–1381 (2017).
80. Gross, M. I. *et al.* Antitumor activity of the glutaminase inhibitor CB-839 in triple-negative breast cancer. *Molecular cancer therapeutics* **13**, 890–901 (2014).
81. National Cancer Institute. Clinical Trials Using GLutaminase Inhibitor CB-839. Available at <https://www.cancer.gov/about-cancer/treatment/clinical-trials/intervention/glutaminase-inhibitor-cb-839>. Accessed 15.04.2019.
82. Lee, Y.-M. *et al.* Inhibition of glutamine utilization sensitizes lung cancer cells to apigenin-induced apoptosis resulting from metabolic and oxidative stress. *International journal of oncology* **48**, 399–408 (2016).
83. Sun, L. *et al.* Dual inhibition of glycolysis and glutaminolysis as a therapeutic strategy in the treatment of ovarian cancer. *Oncotarget* **8**, 63551–63561 (2017).
84. Zhang, Z. *et al.* Differential glucose requirement in skin homeostasis and injury identifies a therapeutic target for psoriasis. *Nature medicine* **24**, 617–627 (2018).
85. Escoll, P. *et al.* Legionella pneumophila Modulates Mitochondrial Dynamics to Trigger Metabolic Repurposing of Infected Macrophages. *Cell host & microbe* **22**, 302–316 (2017).
86. Andrianifahanana, M. *et al.* Profibrotic up-regulation of glucose transporter 1 by TGF- β involves activation of MEK and mammalian target of rapamycin complex 2 pathways. *Federation of American Societies for Experimental Biology* **30**, 3733–3744 (2016).
87. Macintyre, A. N. *et al.* The glucose transporter Glut1 is selectively essential for CD4 T cell activation and effector function. *Cell metabolism* **20**, 61–72 (2014).
88. Yin, Y. *et al.* Normalization of CD4+ T cell metabolism reverses lupus. *Science translational medicine* **7**, 274ra18 (2015).
89. Gualdoni, G. A. *et al.* Rhinovirus induces an anabolic reprogramming in host cell metabolism essential for viral replication. *Proceedings of the National Academy of Sciences of the United States of America* **115**, E7158–E7165 (2018).
90. Palmer, C. S., Cherry, C. L., Sada-Ovalle, I., Singh, A. & Crowe, S. M. Glucose Metabolism in T Cells and Monocytes: New Perspectives in HIV Pathogenesis. *EBioMedicine* **6**, 31–41 (2016).
91. Fulmer, G. R. *et al.* NMR Chemical Shifts of Trace Impurities. Common Laboratory Solvents, Organics, and Gases in Deuterated Solvents Relevant to the Organometallic Chemist. *Organometallics* **29**, 2176–2179 (2010).
92. Neochoritis, C. G., Stotani, S., Mishra, B. & Dömling, A. Efficient isocyanide-less isocyanide-based multicomponent reactions. *Organic letters* **17**, 2002–2005 (2015).
93. Ilyn, A. P., Trifilenkov, A. S., Tsurulnikov, S. A., Kurashvily, I. D. & Ivachtchenko, A. V. Synthesis of 4-Oxo-4,5,6,7-tetrahydropyrazolo[1,5-*a*]pyrazine-6-carboxamides using a modification of Ugi condensation. *Journal of combinatorial chemistry* **7**, 806–808 (2005).
94. Creedon, S. M., Crowley, H. K. & McCarthy, D. G. Dehydration of formamides using the Burgess Reagent. A new route to isocyanides. *Journal of the Chemical Society*, 1015–1018 (1998).
95. Dolomanov, O. v., Bourhis, L. J., Gildea, R. J., Howard, J. A. K. & Puschmann, H. OLEX2 : a complete structure solution, refinement and analysis program. *Journal of Applied Crystallography* **42**, 339–341 (2009).
96. Sheldrick, G. M. SHELXT - integrated space-group and crystal-structure determination. *Acta crystallographica. Section A, Foundations and advances* **71**, 3–8 (2015).

97. Sheldrick, G. M. A short history of SHELX. *Acta crystallographica. Section A, Foundations of crystallography* **64**, 112–122 (2008).
98. Tyanova, S. *et al.* Visualization of LC-MS/MS proteomics data in MaxQuant. *Proteomics* **15**, 1453–1456 (2015).
99. McLellan, A. C., Phillips, S. A. & Thornalley, P. J. Fluorimetric assay of D-lactate. *Analytical biochemistry* **206**, 12–16 (1992).
100. Vichai, V. & Kirtikara, K. Sulforhodamine B colorimetric assay for cytotoxicity screening. *Nature protocols* **1**, 1112–1116 (2006).
101. Marroquin, L. D., Hynes, J., Dykens, J. A., Jamieson, J. D. & Will, Y. Circumventing the Crabtree effect. Replacing media glucose with galactose increases susceptibility of HepG2 cells to mitochondrial toxicants. *Toxicological sciences* **97**, 539–547 (2007).
102. Livak, K. J. & Schmittgen, T. D. Analysis of relative gene expression data using real-time quantitative PCR and the 2⁻(-Delta Delta C(T)) Method. *Methods* **25**, 402–408 (2001).
103. Reckzeh, E. S., Brockmeyer, A., Metz, M., Waldmann, H. & Janning, P. Target Engagement of Small Molecules: Thermal Profiling Approaches on Different Levels. *Methods in molecular biology* **1888**, 73–98 (2019).
104. Matsushita, K. *et al.* Glycolysis inhibitors as a potential therapeutic option to treat aggressive neuroblastoma expressing GLUT1. *Journal of pediatric surgery* **47**, 1323–1330 (2012).
105. Di Veroli, G. Y. *et al.* Combenefit. An interactive platform for the analysis and visualization of drug combinations. *Bioinformatics* **32**, 2866–2868 (2016).
106. LOEWE, S. The problem of synergism and antagonism of combined drugs. *Arzneimittel-Forschung* **3**, 285–290 (1953).
107. BLISS, C. I. THE TOXICITY OF POISONS APPLIED JOINTLY¹. *Annals of Applied Biology* **26**, 585–615 (1939).
108. Tan, X. *et al.* Systematic identification of synergistic drug pairs targeting HIV. *Nature biotechnology* **30**, 1125–1130 (2012).
109. Karageorgis, G. *et al.* Chromopyrones are pseudo natural product glucose uptake inhibitors targeting glucose transporters GLUT-1 and -3. *Nature chemistry* **10**, 1103–1111 (2018).
110. Cardaci, S., Desideri, E. & Ciriolo, M. R. Targeting aerobic glycolysis: 3-bromopyruvate as a promising anticancer drug. *Journal of bioenergetics and biomembranes* **44**, 17–29 (2012).
111. Chrostowska, A. *et al.* Are unsaturated isocyanides so different from the corresponding nitriles? *Chemphyschem* **13**, 226–236 (2012).
112. Kajanus, J. *et al.* Isoindolinone compounds active as Kv1.5 blockers identified using a multicomponent reaction approach. *Bioorganic & medicinal chemistry letters* **26**, 2023–2029 (2016).
113. Allen, C. L., Atkinson, B. N. & Williams, J. M. J. Transamidation of primary amides with amines using hydroxylamine hydrochloride as an inorganic catalyst. *Angewandte Chemie (International Edition)* **51**, 1383–1386 (2012).
114. Wu, J.-W., Wu, Y.-D., Dai, J.-J. & Xu, H.-J. Benzoic Acid-Catalyzed Transamidation Reactions of Carboxamides, Phthalimide, Ureas and Thioamide with Amines. *Advanced Synthesis & Catalysis* **356**, 2429–2436 (2014).

115. Hong, S. & Pedersen, P. L. ATP synthase and the actions of inhibitors utilized to study its roles in human health, disease, and other scientific areas. *Microbiology and molecular biology reviews* **72**, 590-641, Table of Contents (2008).
116. Dykens, J. A. & Will, Y. The significance of mitochondrial toxicity testing in drug development. *Drug discovery today* **12**, 777–785 (2007).
117. Ghose, A. K., Viswanadhan, V. N. & Wendoloski, J. J. Prediction of Hydrophobic (Lipophilic) Properties of Small Organic Molecules Using Fragmental Methods. An Analysis of ALOGP and CLOGP Methods. *The Journal of Physical Chemistry A* **102**, 3762–3772 (1998).
118. Bickerton, G. R., Paolini, G. V., Besnard, J., Muresan, S. & Hopkins, A. L. Quantifying the chemical beauty of drugs. *Nature chemistry* **4**, 90–98 (2012).
119. Lipinski, C. A., Lombardo, F., Dominy, B. W. & Feeney, P. J. Experimental and computational approaches to estimate solubility and permeability in drug discovery and development settings. *Advanced Drug Delivery Reviews* **64**, 4–17 (2012).
120. Ertl, P., Rohde, B. & Selzer, P. Fast Calculation of Molecular Polar Surface Area as a Sum of Fragment-Based Contributions and Its Application to the Prediction of Drug Transport Properties. *Journal of medicinal chemistry* **43**, 3714–3717 (2000).
121. Tate, J. G. *et al.* COSMIC. The Catalogue Of Somatic Mutations In Cancer. *Nucleic acids research* **47**, D941-D947 (2019).
122. Lin, Y.-C. *et al.* Genome dynamics of the human embryonic kidney 293 lineage in response to cell biology manipulations. *Nature communications* **5**, 4767 (2014).
123. Barretina, J. *et al.* The Cancer Cell Line Encyclopedia enables predictive modelling of anticancer drug sensitivity. *Nature* **483**, 603–607 (2012).
124. Zeitouni, D., Pylayeva-Gupta, Y., Der, C. J. & Bryant, K. L. KRAS Mutant Pancreatic Cancer. No Lone Path to an Effective Treatment. *Cancers* **8** (2016).
125. Blum, R. & Kloog, Y. Metabolism addiction in pancreatic cancer. *Cell death & disease* **5**, e1065 (2014).
126. Friedrich, J., Seidel, C., Ebner, R. & Kunz-Schughart, L. A. Spheroid-based drug screen. Considerations and practical approach. *Nature protocols* **4**, 309–324 (2009).
127. Schmidt, T. *et al.* ProteomicsDB. *Nucleic acids research* **46**, D1271-D1281 (2018).
128. Jafari, R. *et al.* The cellular thermal shift assay for evaluating drug target interactions in cells. *Nature protocols* **9**, 2100–2122 (2014).
129. Nagamatsu, S. *et al.* Gene expression of GLUT3 glucose transporter regulated by glucose in vivo in mouse brain and in vitro in neuronal cell cultures from rat embryos. *The Biochemical journal* **300**, 125–131 (1994).
130. Marín-Hernández, A. *et al.* Modeling cancer glycolysis under hypoglycemia, and the role played by the differential expression of glycolytic isoforms. *Federation of American Societies for Experimental Biology* **281**, 3325–3345 (2014).
131. Güemes, M., Rahman, S. A. & Hussain, K. What is a normal blood glucose? *Archives of disease in childhood* **101**, 569–574 (2016).
132. Hensley, C. T., Wasti, A. T. & DeBerardinis, R. J. Glutamine and cancer: cell biology, physiology, and clinical opportunities. *The Journal of clinical investigation* **123**, 3678–3684 (2013).
133. Wise, D. R. & Thompson, C. B. Glutamine addiction: a new therapeutic target in cancer. *Trends in biochemical sciences* **35**, 427–433 (2010).

134. Scriver, C. R. & Rosenberg, L. E. Amino acid metabolism and its disorders. *Major problems in clinical pediatrics* **10**, 1–478 (1973).
135. Mayers, J. R. & Vander Heiden, M. G. Nature and Nurture: What Determines Tumor Metabolic Phenotypes? *Cancer research* **77**, 3131–3134 (2017).
136. Robke, L. *et al.* Discovery of the novel autophagy inhibitor aumitin that targets mitochondrial complex I. *Chemical science* **9**, 3014–3022 (2018).
137. Hoffmeister, M., Piotrowski, M., Nowitzki, U. & Martin, W. Mitochondrial trans-2-enoyl-CoA reductase of wax ester fermentation from *Euglena gracilis* defines a new family of enzymes involved in lipid synthesis. *The Journal of biological chemistry* **280**, 4329–4338 (2005).
138. Szklarczyk, D. *et al.* STRING v11: protein-protein association networks with increased coverage, supporting functional discovery in genome-wide experimental datasets. *Nucleic acids research* **47**, D607–D613 (2019).
139. UniProt: a worldwide hub of protein knowledge. *Nucleic acids research* **47**, D506–D515 (2019).
140. Blaeser, F., Ho, N., Prywes, R. & Chatila, T. A. Ca(2+)-dependent gene expression mediated by MEF2 transcription factors. *The Journal of biological chemistry* **275**, 197–209 (2000).
141. Youn, H. D., Chatila, T. A. & Liu, J. O. Integration of calcineurin and MEF2 signals by the coactivator p300 during T-cell apoptosis. *The EMBO journal* **19**, 4323–4331 (2000).
142. Freeman, G. J. *et al.* Engagement of the PD-1 immunoinhibitory receptor by a novel B7 family member leads to negative regulation of lymphocyte activation. *The Journal of experimental medicine* **192**, 1027–1034 (2000).
143. U.S. Food & Drug Administration. Available at <https://www.fda.gov/Drugs/InformationOnDrugs/ApprovedDrugs/ucm617370.htm>. Accessed 16.04.2019.
144. Tkachev, V. *et al.* Programmed death-1 controls T cell survival by regulating oxidative metabolism. *Journal of immunology* **194**, 5789–5800 (2015).
145. Patsoukis, N. *et al.* PD-1 alters T-cell metabolic reprogramming by inhibiting glycolysis and promoting lipolysis and fatty acid oxidation. *Nature communications* **6**, 6692 (2015).
146. Cliff, T. S. & Dalton, S. Metabolic switching and cell fate decisions: implications for pluripotency, reprogramming and development. *Current opinion in genetics & development* **46**, 44–49 (2017).
147. Jones, W. & Bianchi, K. Aerobic glycolysis: beyond proliferation. *Frontiers in immunology* **6**, 227 (2015).
148. Tsukiji, S. & Hamachi, I. Ligand-directed tosyl chemistry for in situ native protein labeling and engineering in living systems: from basic properties to applications. *Current opinion in chemical biology* **21**, 136–143 (2014).
149. Tsukiji, S., Miyagawa, M., Takaoka, Y., Tamura, T. & Hamachi, I. Ligand-directed tosyl chemistry for protein labeling in vivo. *Nature chemical biology* **5**, 341–343 (2009).
150. Hughes, J. P., Rees, S., Kalindjian, S. B. & Philpott, K. L. Principles of early drug discovery. *British journal of pharmacology* **162**, 1239–1249 (2011).
151. Schirris, T. J. J. *et al.* Mitochondrial ADP/ATP exchange inhibition: a novel off-target mechanism underlying ibipinabant-induced myotoxicity. *Scientific reports* **5**, 14533 (2015).

152. Yang, Z. *et al.* Adenine nucleotide (ADP/ATP) translocase 3 participates in the tumor necrosis factor induced apoptosis of MCF-7 cells. *Molecular biology of the cell* **18**, 4681–4689 (2007).
153. Zamora, M., Granell, M., Mampel, T. & Viñas, O. Adenine nucleotide translocase 3 (ANT3) overexpression induces apoptosis in cultured cells. *Federation of American Societies for Experimental Biology* **563**, 155–160 (2004).
154. Augustin, R. The protein family of glucose transport facilitators: It's not only about glucose after all. *IUBMB life* **62**, 315–333 (2010).
155. Simpson, I. A. *et al.* The facilitative glucose transporter GLUT3: 20 years of distinction. *American journal of physiology. Endocrinology and metabolism* **295**, E242-53 (2008).
156. Tordjman, K. M., Leingang, K. A. & Mueckler, M. Differential regulation of the HepG2 and adipocyte/muscle glucose transporters in 3T3L1 adipocytes. Effect of chronic glucose deprivation. *The Biochemical journal* **271**, 201–207 (1990).
157. Olson, A. L. & Pessin, J. E. Structure, function, and regulation of the mammalian facilitative glucose transporter gene family. *Annual review of nutrition* **16**, 235–256 (1996).
158. Li, L., Dong, M. & Wang, X.-G. The Implication and Significance of Beta 2 Microglobulin: A Conservative Multifunctional Regulator. *Chinese medical journal* **129**, 448–455 (2016).
159. Zhang, X., Ding, L. & Sandford, A. J. Selection of reference genes for gene expression studies in human neutrophils by real-time PCR. *BMC molecular biology* **6**, 4 (2005).
160. Granados, D. P. *et al.* ER stress affects processing of MHC class I-associated peptides. *BMC immunology* **10**, 10 (2009).
161. Lea, M. A., Altayyar, M. & desBordes, C. Inhibition of Growth of Bladder Cancer Cells by 3-(3-Pyridinyl)-1-(4-pyridinyl)-2-propen-1-one in Combination with Other Compounds Affecting Glucose Metabolism. *Anticancer research* **35**, 5889–5899 (2015).
162. Daemen, A. *et al.* Metabolite profiling stratifies pancreatic ductal adenocarcinomas into subtypes with distinct sensitivities to metabolic inhibitors. *Proceedings of the National Academy of Sciences of the United States of America* **112**, E4410-7 (2015).
163. Massari, F. *et al.* Metabolic phenotype of bladder cancer. *Cancer treatment reviews* **45**, 46–57 (2016).
164. Delgado-Goni, T. *et al.* The BRAF inhibitor vemurafenib activates mitochondrial metabolism and inhibits hyperpolarized pyruvate-lactate exchange in BRAF mutant human melanoma cells. *Molecular cancer therapeutics* **15**, 2987–2999 (2016).
165. Lampa, M. *et al.* Glutaminase is essential for the growth of triple-negative breast cancer cells with a deregulated glutamine metabolism pathway and its suppression synergizes with mTOR inhibition. *PloS one* **12**, e0185092 (2017).
166. Iyer, V. V., Yang, H., Ierapetritou, M. G. & Roth, C. M. Effects of glucose and insulin on HepG2-C3A cell metabolism. *Biotechnology and bioengineering* **107**, 347–356 (2010).
167. Graham, N. A. *et al.* Glucose deprivation activates a metabolic and signaling amplification loop leading to cell death. *Molecular systems biology* **8**, 589 (2012).
168. Wenzel, C. *et al.* 3D high-content screening for the identification of compounds that target cells in dormant tumor spheroid regions. *Experimental cell research* **323**, 131–143 (2014).
169. Corbet, C. *et al.* Interruption of lactate uptake by inhibiting mitochondrial pyruvate transport unravels direct antitumor and radiosensitizing effects. *Nature communications* **9**, 1208 (2018).

170. Castellano, E. & Santos, E. Functional Specificity of Ras Isoforms: So Similar but So Different. *Genes & Cancer* **2**, 216–231 (2011).
171. Vincent, A., Herman, J., Schulick, R., Hruban, R. H. & Goggins, M. Pancreatic cancer. *The Lancet* **378**, 607–620 (2011).
172. Adamska, A., Domenichini, A. & Falasca, M. Pancreatic Ductal Adenocarcinoma: Current and Evolving Therapies. *International Journal of Molecular Sciences* **18** (2017).
173. Patricelli, M. P. *et al.* Selective Inhibition of Oncogenic KRAS Output with Small Molecules Targeting the Inactive State. *Cancer discovery* **6**, 316–329 (2016).
174. Zeng, M. *et al.* Potent and Selective Covalent Quinazoline Inhibitors of KRAS G12C. *Cell chemical biology* **24**, 1005-1016.e3 (2017).
175. Martín-Gago, P. *et al.* A PDE6 δ -KRas Inhibitor Chemotype with up to Seven H-Bonds and Picomolar Affinity that Prevents Efficient Inhibitor Release by Arl2. *Angewandte Chemie (International Edition)* **56**, 2423–2428 (2017).
176. Janes, M. R. *et al.* Targeting KRAS Mutant Cancers with a Covalent G12C-Specific Inhibitor. *Cell* **172**, 578-589.e17 (2018).
177. Zimmermann, G. *et al.* Small molecule inhibition of the KRAS-PDE δ interaction impairs oncogenic KRAS signalling. *Nature* **497**, 638–642 (2013).
178. Ardawi, M. S. Glutamine and glucose metabolism in human peripheral lymphocytes. *Metabolism: clinical and experimental* **37**, 99–103 (1988).
179. Carr, E. L. *et al.* Glutamine uptake and metabolism are coordinately regulated by ERK/MAPK during T lymphocyte activation. *Journal of immunology* **185**, 1037–1044 (2010).
180. Akins, N. S., Nielson, T. C. & Le, H. V. Inhibition of Glycolysis and Glutaminolysis: An Emerging Drug Discovery Approach to Combat Cancer. *Current topics in medicinal chemistry* **18**, 494–504 (2018).
181. Altman, B. J., Stine, Z. E. & Dang, C. V. From Krebs to clinic: glutamine metabolism to cancer therapy. *Nat. Rev. Cancer* **16**, 619–634 (2016).
182. Lukey, M. J., Katt, W. P. & Cerione, R. A. Targeting Therapy Resistance: When Glutamine Catabolism Becomes Essential. *Cancer cell* **33**, 795–797 (2018).
183. National Cancer Institute. Available at <http://dtp.cancer.gov>. Accessed 04.04.2019.
184. NIH. Study of CB-839 (Telaglenastat) in Combination With Talazoparib in Patients With Solid Tumors. Available at <https://clinicaltrials.gov/ct2/show/NCT03875313>. Accessed 09.05.2019.
185. NIH. Glutaminase Inhibitor CB-839 Hydrochloride and Osimertinib in Treating Patients With EGFR-Mutated Stage IV Non-small Cell Lung Cancer. Available at <https://clinicaltrials.gov/ct2/show/NCT03831932>. Accessed 09.05.2019.
186. Jin, L. *et al.* Glutamate dehydrogenase 1 signals through antioxidant glutathione peroxidase 1 to regulate redox homeostasis and tumor growth. *Cancer cell* **27**, 257–270 (2015).
187. Pardee, T. S. *et al.* A Phase I Study of the First-in-Class Anti-Mitochondrial Metabolism Agent, CPI-613, in Patients with Advanced Hematologic Malignancies. *Clinical cancer research* **20**, 5255–5264 (2014).
188. Hosios, A. M. *et al.* Amino Acids Rather than Glucose Account for the Majority of Cell Mass in Proliferating Mammalian Cells. *Developmental cell* **36**, 540–549 (2016).

189. Labuschagne, C. F., van den Broek, N. J. F., Mackay, G. M., Vousden, K. H. & Maddocks, O. D. K. Serine, but not glycine, supports one-carbon metabolism and proliferation of cancer cells. *Cell reports* **7**, 1248–1258 (2014).
190. Alkan, H. F. *et al.* Cytosolic Aspartate Availability Determines Cell Survival When Glutamine Is Limiting. *Cell metabolism* **28**, 706-720.e6 (2018).
191. Zois, C. E. & Harris, A. L. Glycogen metabolism has a key role in the cancer microenvironment and provides new targets for cancer therapy. *Journal of molecular medicine* **94**, 137–154 (2016).
192. Martin, W. H. *et al.* Discovery of a human liver glycogen phosphorylase inhibitor that lowers blood glucose in vivo. *Proceedings of the National Academy of Sciences of the United States of America* **95**, 1776–1781 (1998).
193. Fendt, S.-M. Is There a Therapeutic Window for Metabolism-Based Cancer Therapies? *Frontiers in endocrinology* **8**, 150 (2017).
194. Chen, S.-H. & Lahav, G. Two is better than one; toward a rational design of combinatorial therapy. *Current opinion in structural biology* **41**, 145–150 (2016).
195. Bénéteau, M. *et al.* Combination of glycolysis inhibition with chemotherapy results in an antitumor immune response. *Proceedings of the National Academy of Sciences of the United States of America* **109**, 20071–20076 (2012).
196. Islamian, J. P., Aghaee, F., Farajollahi, A., Baradaran, B. & Fazel, M. Combined Treatment with 2-Deoxy-D-Glucose and Doxorubicin Enhances the in Vitro Efficiency of Breast Cancer Radiotherapy. *Asian Pacific Journal of Cancer Prevention* **16**, 8431–8438 (2016).
197. Davidson, N. J. *et al.* T helper cell 1-type CD4+ T cells, but not B cells, mediate colitis in interleukin 10-deficient mice. *The Journal of experimental medicine* **184**, 241–251 (1996).
198. Hu, H. Z., Li, G. L., Lim, Y. K., Chan, S. H. & Yap, E. H. Kinetics of interferon-gamma secretion and its regulatory factors in the early phase of acute graft-versus-host disease. *Immunology* **98**, 379–385 (1999).
199. Jodeleit, H. *et al.* Targeting ulcerative colitis by suppressing glucose uptake with ritonavir. *Disease models & mechanisms* **11** (2018).
200. Nakerakanti, S. & Trojanowska, M. The Role of TGF- β Receptors in Fibrosis. *The Open Rheumatology Journal* **6**, 156–162 (2012).
201. Escoll, P. & Buchrieser, C. Metabolic reprogramming of host cells upon bacterial infection: Why shift to a Warburg-like metabolism? *Federation of American Societies for Experimental Biology* **285**, 2146–2160 (2018).
202. Appelberg, R. *et al.* The Warburg effect in mycobacterial granulomas is dependent on the recruitment and activation of macrophages by interferon- γ . *Immunology* **145**, 498–507 (2015).
203. Gleeson, L. E. *et al.* Cutting Edge: Mycobacterium tuberculosis Induces Aerobic Glycolysis in Human Alveolar Macrophages That Is Required for Control of Intracellular Bacillary Replication. *Journal of immunology* **196**, 2444–2449 (2016).
204. Lachmandas, E. *et al.* Rewiring cellular metabolism via the AKT/mTOR pathway contributes to host defence against Mycobacterium tuberculosis in human and murine cells. *European journal of immunology* **46**, 2574–2586 (2016).
205. Shi, L. *et al.* Infection with Mycobacterium tuberculosis induces the Warburg effect in mouse lungs. *Scientific reports* **5**, 18176 (2015).

206. Somashekar, B. S. *et al.* Metabolic profiling of lung granuloma in Mycobacterium tuberculosis infected guinea pigs: ex vivo ¹H magic angle spinning NMR studies. *Journal of proteome research* **10**, 4186–4195 (2011).
207. Czyż, D. M., Willett, J. W. & Crosson, S. Brucella abortus Induces a Warburg Shift in Host Metabolism That Is Linked to Enhanced Intracellular Survival of the Pathogen. *Journal of Bacteriology* **199** (2017).
208. Ojcius, D. M., Degani, H., Mispelster, J. & Dautry-Varsat, A. Enhancement of ATP Levels and Glucose Metabolism during an Infection by Chlamydia. *The Journal of biological chemistry* **273**, 7052–7058 (1998).
209. Siegl, C., Prusty, B. K., Karunakaran, K., Wischhusen, J. & Rudel, T. Tumor suppressor p53 alters host cell metabolism to limit Chlamydia trachomatis infection. *Cell reports* **9**, 918–929 (2014).
210. Rupp, J. *et al.* Chlamydia pneumoniae directly interferes with HIF-1alpha stabilization in human host cells. *Cellular microbiology* **9**, 2181–2191 (2007).
211. Davis, S. L. *et al.* Noninvasive pulmonary ¹⁸F-2-fluoro-deoxy-D-glucose positron emission tomography correlates with bactericidal activity of tuberculosis drug treatment. *Antimicrobial agents and chemotherapy* **53**, 4879–4884 (2009).
212. Bock, K. de *et al.* Role of PFKFB3-driven glycolysis in vessel sprouting. *Cell* **154**, 651–663 (2013).
213. Yokosako, K. *et al.* Glycolysis in patients with age-related macular degeneration. *The open ophthalmology journal* **8**, 39–47 (2014).
214. Izumi, S., Otsuru, S., Adachi, N., Akabudike, N. & Enomoto-Iwamoto, M. Control of glucose metabolism is important in tenogenic differentiation of progenitors derived from human injured tendons. *PloS one* **14**, e0213912 (2019).
215. Chung, C. K. *et al.* Process Development of C–N Cross-Coupling and Enantioselective Biocatalytic Reactions for the Asymmetric Synthesis of Niraparib. *Organic Process Research & Development* **18**, 215–227 (2014).

13 Appendix

13.1 Supplementary Figures

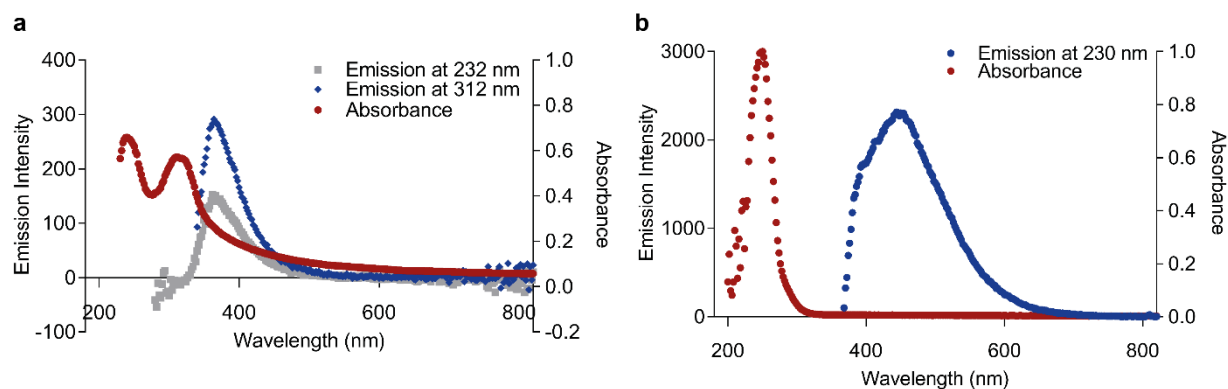


Figure 88 Absorption and emission spectra for hit compound 1a and Glutator (related to Figure 14 and Figure 23). Absorption spectra was measured at 100 μ M hit compound 1a (a) or Glutator (b) concentration. Excitation spectra were recorded at the wavelength where a local absorption maximum was observed. The background spectra (DMSO) were subtracted from the compound spectra.

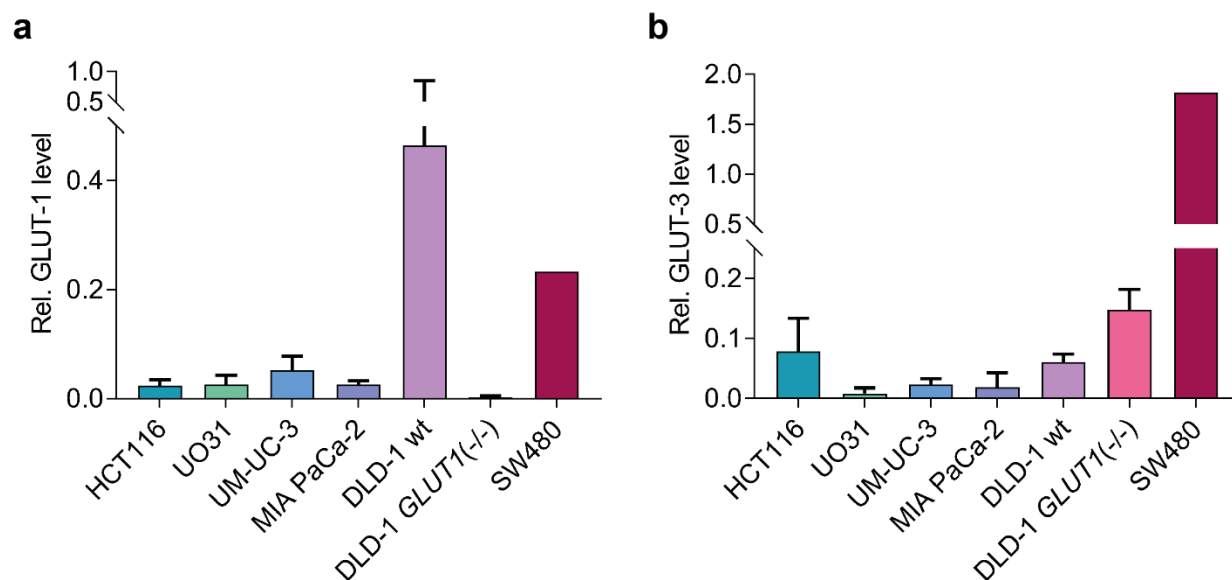


Figure 89 GLUT-1 and GLUT-3 protein expression level of selected cancer cell lines. Immunoblot-based analysis of whole cell lysates was conducted to assess the protein levels of GLUT-1 (a) and GLUT-3 (b). a) Data show mean values \pm s.d. of n=2 (HCT116, UO-31, UM-UC-3, MIA PaCa-2, DLD-1 wt, DLD-1 GLUT1(-/-)) or n=1 (SW480). b) Data show mean values \pm s.d. of n=3 (HCT116, UO-31, UM-UC-3, MIA PaCa-2, DLD-1 wt, DLD-1 GLUT1(-/-)) or n=1 (SW480). Data was normalized to the reference protein Na⁺/K⁺-ATPase (a) or vinculin (b).

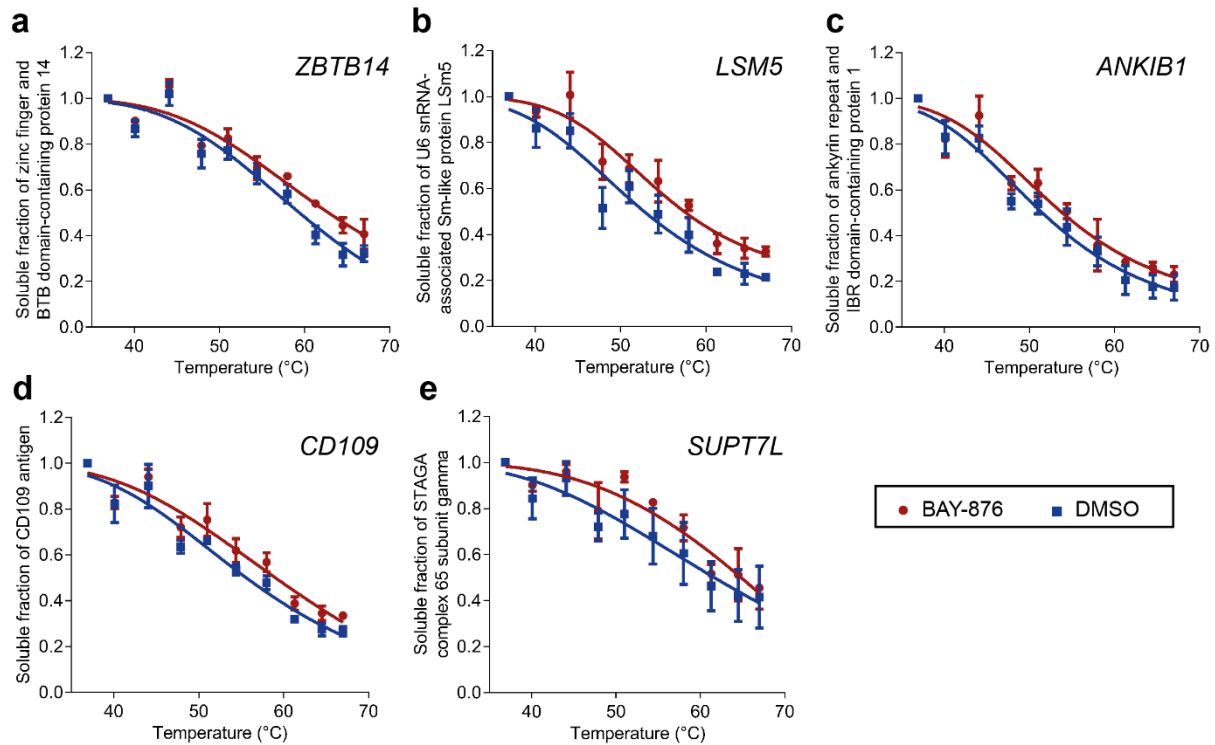


Figure 90 Further identified stabilized interaction partners of (+)-Glupin-1 during thermal proteome profiling (TPP) (related to Figure 66, Figure 67 and Table 19). Thermal proteome profiling (TPP) was performed with SW480 whole cell lysates in presence of 10 μ M (+)-Glupin-1 or DMSO. The gene names (graph) and proteins names (y-axis) are given. The proteins zinc finger and BTB domain-containing protein 14 (a), U6 snRNA-associated Sm-like protein LSM5 (b), ankyrin repeat and IBR domain-containing protein 1 (c), CD109 antigen (d) and STAGA complex 65 subunit gamma (e) were identified in all three biological replicates in the soluble fraction after heat treatment. Protein amount was normalized to the first temperature within the temperature gradient, *i.e.* 36.9 $^{\circ}$ C. The data was fitted using the Boltzmann equation. Data show mean values \pm s.d. (n=3).

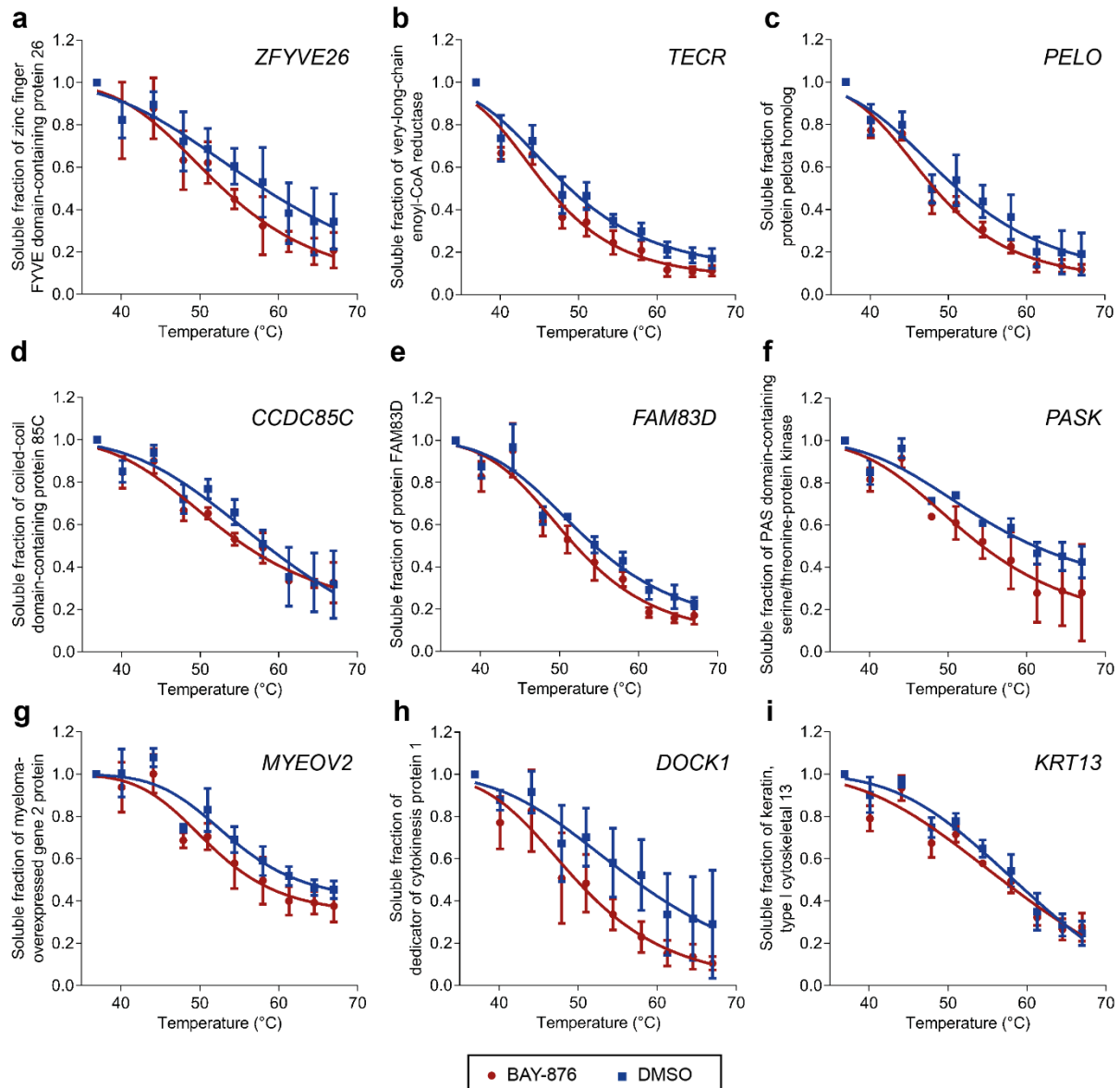
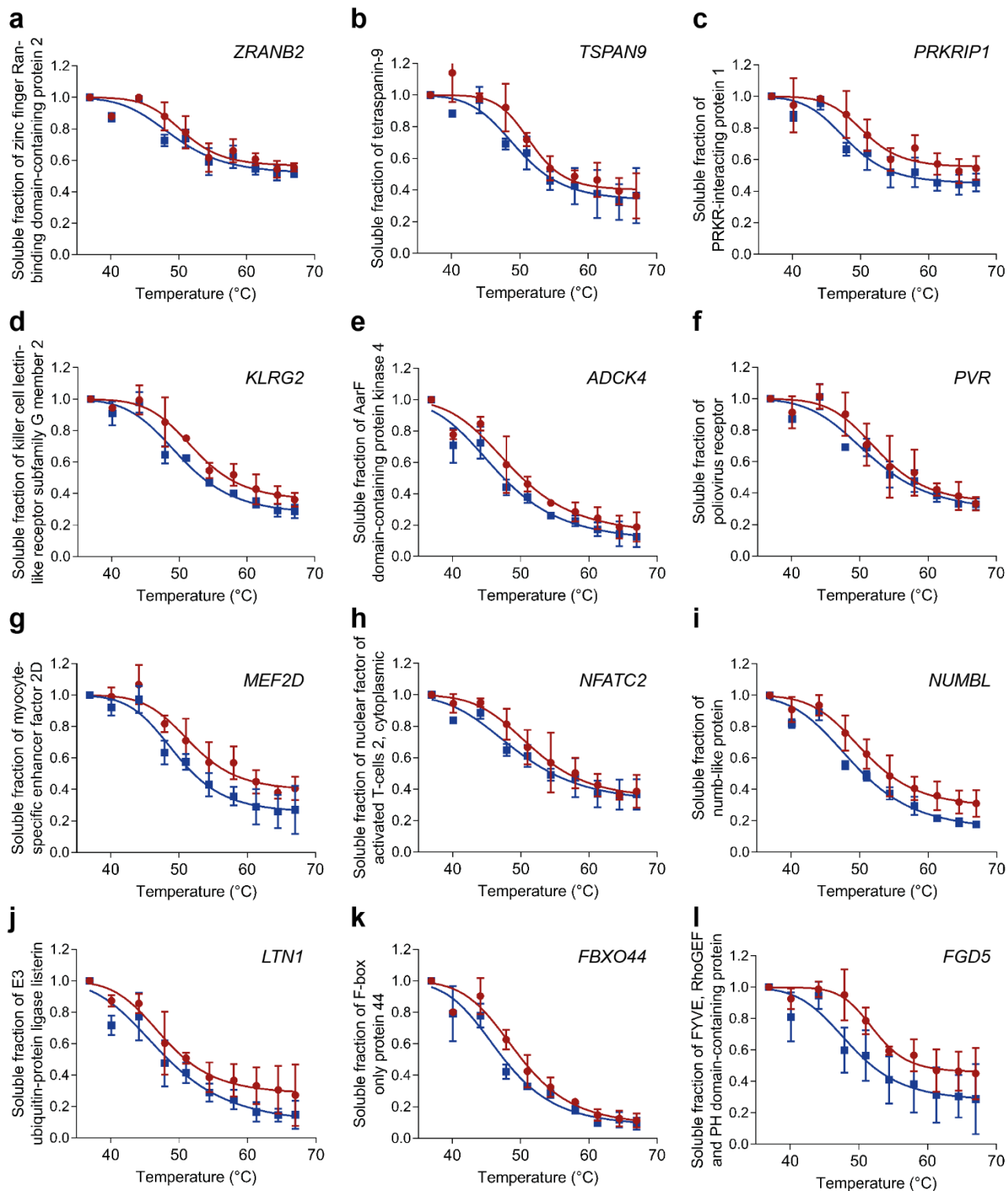


Figure 91 Further identified destabilized interaction partners of (+)-Glupin-1 during thermal proteome profiling (TPP) (related to Figure 66, Figure 67 and Table 19). Thermal proteome profiling (TPP) was performed with SW480 whole cell lysates in presence of 10 μ M (+)-Glupin-1 or DMSO. The gene names (graph) and proteins names (y-axis) are given. The proteins zinc finger FYVE domain-containing protein 26 (a), very-long-chain enoyl-CoA reductase (b), protein pelota homolog (c), coiled-coil domain-containing protein 85C (d), protein FAM83D (e), PAS domain-containing serine/threonine-protein kinase (f), myeloma-overexpressed gene 2 protein (g), dedicator of cytokinesis protein 1 (h) and keratin, type I cytoskeletal 13 (i) were identified in all three biological replicates in the soluble fraction after heat treatment. Protein amount was normalized to the first temperature within the temperature gradient, *i.e.* 36.9 °C. The data was fitted using the Boltzmann equation. Data show mean values \pm s.d. (n=3).



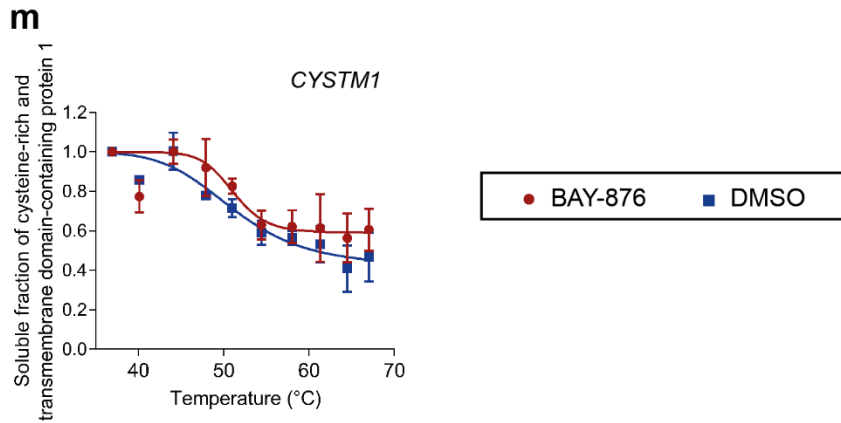
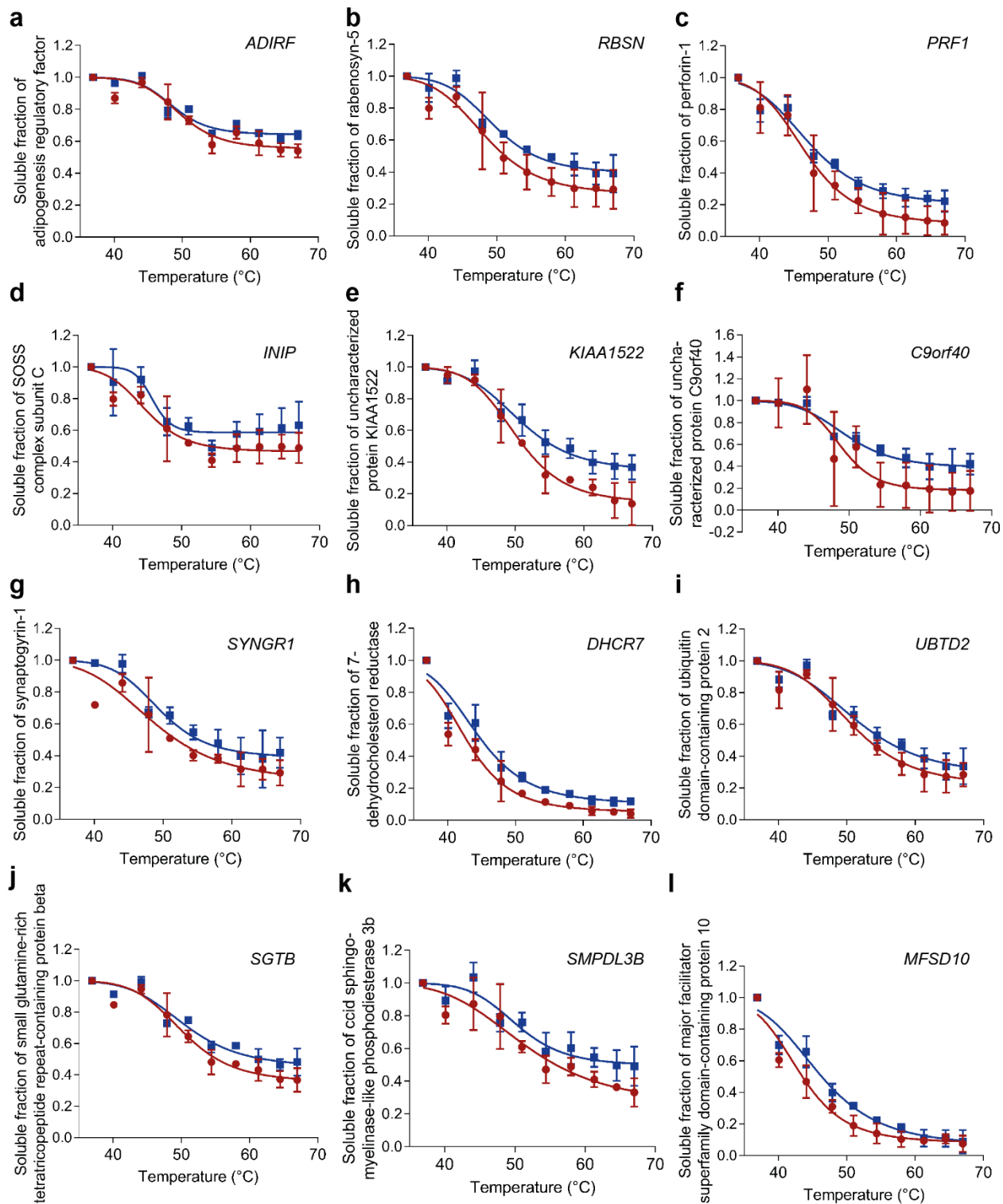


Figure 92 Further identified stabilized interaction partners of BAY-876 during thermal proteome profiling (TPP) (related to Figure 78, Figure 79 and Table 20). Thermal proteome profiling (TPP) was performed with SW480 whole cell lysates in presence of 10 μ M BAY-876 or DMSO. The gene names (graph) and proteins names (y-axis) are given. The proteins zinc finger Ran-binding domain-containing protein 2 (a), tetraspanin-9 (b), PPKR-interacting protein 1 (c), killer cell lectin-like receptor subfamily G member 2 (d), AarF domain-containing protein kinase 4 (e), poliovirus receptor (f), myocyte-specific enhancer factor 2D (g), nuclear factor of activated T-cells (h), numb-like protein (i), E3 ubiquitin-protein ligase listerin (j), F-box only protein 44 (k), FYVE, RhoGEF and PH domain-containing protein (l), cysteine-rich and transmembrane domain-containing protein 1 (m) were identified in all three biological replicates in the soluble fraction after heat treatment. Protein amount was normalized to the first temperature within the temperature gradient, *i.e.* 36.9 °C. The data was fitted using the Boltzmann equation. Data show mean values \pm s.d. (n=3).

Appendix



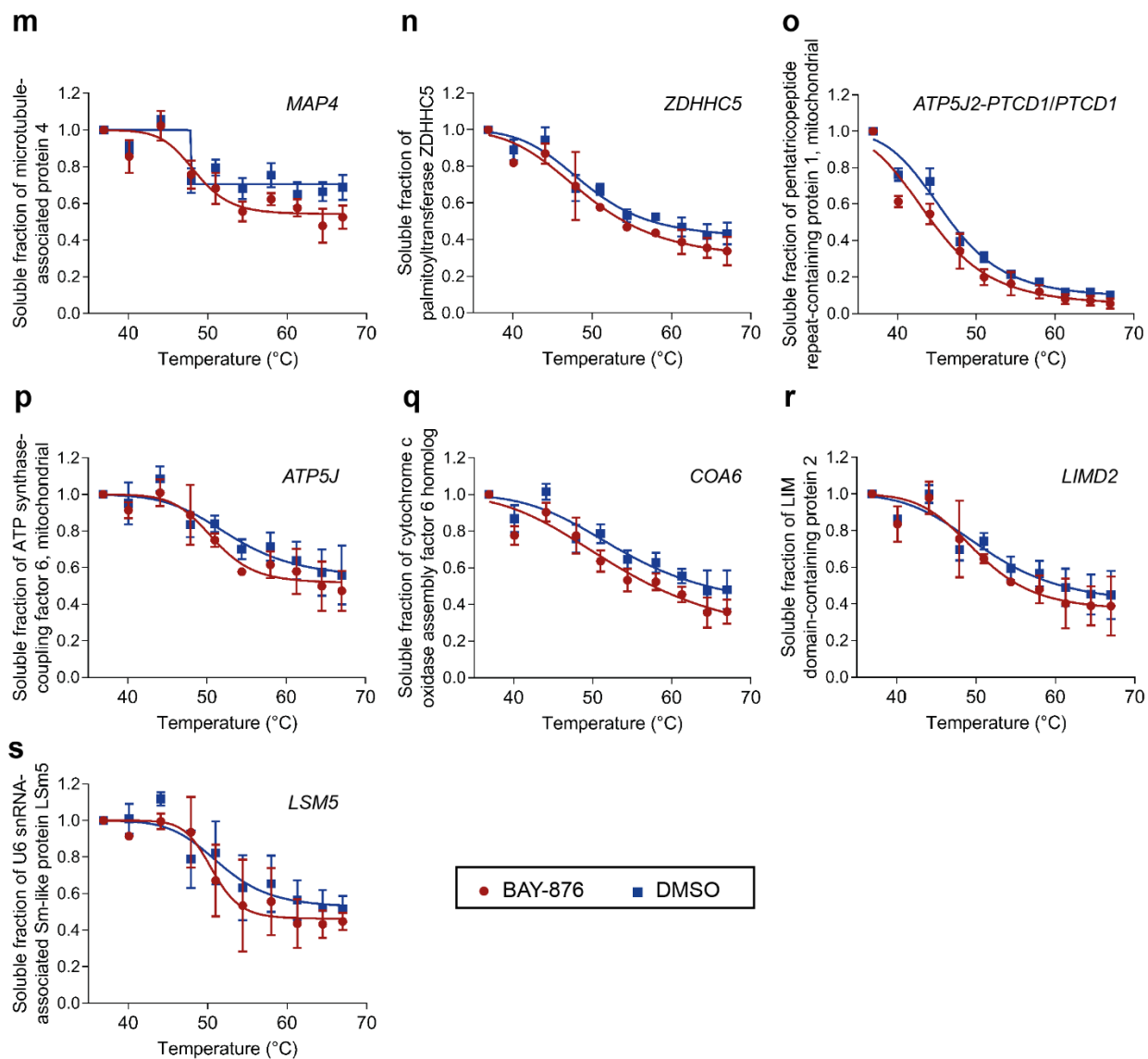


Figure 93 Further identified destabilized interaction partners of BAY-876 during thermal proteome profiling (TPP) (related to Figure 78, Figure 79 and Table 20). Thermal proteome profiling (TPP) was performed with SW480 whole cell lysates in presence of 10 μ M BAY-876 or DMSO. The gene names (graph) and proteins names (y-axis) are given. The proteins adipogenesis regulatory factor (a), rabenosyn-5 (b), perforin-1 (c), SOSS complex subunit C (d), uncharacterized protein KIAA 1522 (e), uncharacterized protein c9orf140 (f), synaptogyrin-1 (g), 7-dehydrocholesterol reductase (h), ubiquitin-domain containing protein 2 (i), small glutamine-rich tetratricopeptide repeat-containing protein beta (j), acid sphingomyelinase-like phosphodiesterase 3b (k), major facilitator superfamily domain-containing protein 10 (l), microtubule-associated protein 4 (m), palmitoyltransferase ZDHHC5 (n), pentatricopeptide repeat-containing protein 1 (o), ATP-synthase-coupling factor 6 (p), cytochrome c oxidase assembly factor 6 homolog (q), LIM domain-containing protein 2 (r) and U6 snRNA-associated Sm-like protein LSM5 (s) were identified in all three biological replicates in the soluble fraction after heat treatment. Protein amount was normalized to the first temperature within the temperature gradient, *i.e.* 36.9 °C. The data was fitted using the Boltzmann equation. Data show mean values \pm s.d. (n=3).

13.2 Supplementary Tables

Table 18 Overview of Sulforhodamine B assay cell panel after Glutor treatment (related to Figure 27).

Cell line	IC ₅₀ (μM)	Tissue of origin	Origin
UM-UC-3	0.004	bladder	primary
MIA PACA-2	0.004	pancreas	primary
TE671	0.005	muscle	primary
SK-N-AS	0.006	brain	bone marrow
5637	0.006	bladder	primary
WSU-NHL	0.007	hematological	primary
A431	0.009	skin	primary
T-24	0.011	bladder	primary
SU-DHL-6	0.011	hematological	peritoneal cavity
K-562	0.012	hematological	primary
JIMT1	0.013	breast	primary
L363	0.014	hematological	-
HEK293	0.015	kidney	-
A549	0.015	lung	primary
BT-20	0.015	breast	primary
HL-60	0.016	hematological	primary
DU145	0.017	prostate	brain
CASKI	0.018	endometrial	small intestine
CLS-439	0.018	bladder	primary
ASPC1	0.019	pancreas	ascites
A375	0.019	skin	primary
SF-268	0.019	brain	-
PANC1005	0.023	pancreas	primary
786O	0.023	kidney	primary
PANC1	0.026	pancreas	primary
RD	0.027	muscle	primary
HT29	0.027	colon	primary
MHH-ES-1	0.032	bone	peritoneal cavity
A2780	0.036	ovary	primary
HCT116	0.040	colon	primary
CALU6	0.047	lung	-
MDA-MB-435	0.048	skin	pleural effusion
U2OS	0.049	bone	-
DLD1	0.050	colon	primary
LOVO	0.052	colon	supraclavicular region
A673	0.058	muscle	primary
CAKI1	0.062	kidney	skin
SF-295	0.068	brain	-
OVCAR3	0.076	ovary	primary
SU-DHL-10	0.083	hematological	peritoneal effusion
HT1080	0.086	connective tissue	primary
JAR	0.089	placenta	primary
NCI-H82	0.090	lung	pleural effusion
HCT15	0.092	colon	primary
J82	0.099	bladder	-

Appendix

Cell line	IC ₅₀ (µM)	Tissue of origin	Origin
EJ28	0.105	bladder	primary
NCI-H460	0.131	lung	pleural effusion
PC-3	0.138	prostate	bone
C-33-A	0.151	endometrial	primary
MT-3	0.198	breast	-
MINO	0.201	hematological	-
HELA	0.224	endometrial	primary
JEG3	0.243	placenta	primary
SKHEP1	0.258	liver	-
22RV1	0.276	prostate	-
UO31	0.304	kidney	primary
NCI-H358M	0.310	lung	alveolus
MDA-MB-231	0.325	breast	pleural effusion
MG-63	0.343	bone	primary
SKNSH	0.381	brain	bone marrow
COLO205	0.412	colon	ascites
MCF-7	0.429	breast	pleural effusion
RDES	0.474	bone	primary
PLCPRF5	0.483	liver	primary
A204	0.484	muscle	-
ACHN	0.641	kidney	pleural effusion
MV4-11	1.003	hematological	primary
CACO2	1.428	colon	primary
SW620	1.701	colon	lymphnode
NCIH292	3.273	lung	primary
EFO21	4.140	ovary	-
MDA-MB-436	7.158	breast	pleural effusion
SAOS-2	8.429	bone	primary
IGROV-1	10.548	ovary	-
BXPC3	30.000	pancreas	primary
COLO678	30.000	colon	lymphnode
GRANTA-519	30.000	hematological	primary
HEPG2	30.000	liver	primary
HS578T	30.000	breast	primary
HS729	30.000	muscle	primary
IMR90	30.000	lung	-
KASUMI-1	30.000	hematological	primary
MDA-MB-468	30.000	breast	pleural effusion
OVCAR4	30.000	ovary	primary
PBMC	30.000	hematological	-
RAMOS	30.000	hematological	primary
SKBR3	30.000	breast	pleural effusion
SKLMS1	30.000	uterus	primary
SKMEL28	30.000	skin	primary
SKMEL5	30.000	skin	axillarynode
SKOV3	30.000	ovary	ascites
SNB75	30.000	brain	primary
THP-1	30.000	hematological	primary
U87MG	30.000	brain	primary

Experiment was conducted by Oncolead, Germany.

Appendix

Table 19 Overview of melting temperatures as determined in a TPP assay with (+)-Glupin-1 (related to Figure 66, Figure 90 and Figure 91).

T_m (°C)	(+)-Glupin-1	DMSO	ΔT_m
<i>ANKIB1</i>	49.5±1.7	47.8±1.2	1.7±0.5
<i>CCDC85C</i>	49.1±0.3	52.1±3.1	-3.0±3.4
<i>CD109</i>	52.9±1.7	49.7±1.3	3.2±1.2
<i>FAM83D</i>	49.0±1.9	50.1±0.8	-1.1±1.2
<i>LSM5</i>	52.0±2.1	48.3±2.1	3.7±1.1
<i>PASK</i>	48.0±2.7	50.2±2.4	-2.1±0.7
<i>PELO</i>	45.4±0.7	46.7±1.5	-1.3±1.0
<i>SUPT7L</i>	57.6±1.5	52.5±2.0	5.1±1.8
<i>TECR</i>	43.4±0.7	44.7±1.2	-1.2±0.6
<i>ZBTB14</i>	56.6±1.6	54.9±1.3	1.7±2.6
<i>ZFYVE26</i>	48.6±2.6	51.9±2.8	-3-2±0.3

Proteins are described according to their gene name. Data show mean values ±s.d. (n=3).

Table 20 Overview of melting temperatures as determined in a TPP assay with BAY-876 (related to Figure 78, Figure 92 and Figure 93).

T_m (°C)	BAY-876	DMSO	ΔT_m
<i>ADCK4</i>	47.2±1.3	44.9±1.1	2.3±1.1
<i>ADIRF</i>	49.1±2.1	48.1±0.5	1.0±2.0
<i>ATP5J2-PTCD1/PTCD1</i>	42.8±0.6	44.9±1.0	-2.1±0.4
<i>ATP5J</i>	50.5±0.3	52.1±2.4	-1.6±2.5
<i>C9orf40</i>	48.2±0.9	48.6±1.1	-0.4±1.9
<i>COA6</i>	50.2±1.7	52.2±2.7	-2.0±1.7
<i>CYSTM1</i>	51.2±1.7	49.6±1.1	1.6±0.6
<i>DHCR7</i>	41.7±0.8	43.3±1.7	-1.6±1.0
<i>FBXO44</i>	48.3±1.3	45.7±0.7	2.6±1.0
<i>FGD5</i>	51.8±1.4	47.7±1.5	4.1±2.7
<i>INIP</i>	45.4±2.3	47.4±4.2	-1.2±0.8
<i>KIAA1522</i>	49.2±0.7	49.5±1.7	-0.3±1.9
<i>KLRG2</i>	51.1±0.4	48.9±0.6	2.2±0.2
<i>LIMD2</i>	49.2±0.7	49.4±1.3	-0.2±1.8
<i>LSM5</i>	53.2±2.0	52.5±3.7	0.7±1.9
<i>LTN1</i>	47.1±1.9	45.5±2.0	1.5±2.6
<i>MAP4</i>	47.8±0.5	48.7±3.1	0.3±1.0
<i>MEF2D</i>	51.7±1.9	48.6±1.2	3.1±1.1
<i>MFS10</i>	41.9±0.4	44.4±1.0	-2.4±0.9
<i>NFATC2</i>	51.2±1.9	47.6±1.1	3.5±1.2
<i>NUMBL</i>	49.8±1.3	47.4±0.5	2.4±1.3
<i>PRF1</i>	45.4±0.2	45.7±0.8	-0.3±0.9
<i>PRKRIP1</i>	51.2±2.3	47.7±0.6	3.5±1.9
<i>PVR</i>	53.6±2.2	50.6±1.4	3.0±1.4
<i>RBSN</i>	47.1±1.8	48.7±0.8	-1.6±2.5
<i>SGTB</i>	49.7±0.6	49.3±1.0	0.4±1.3
<i>SMPDL3B</i>	48.9±1.8	49.3±0.5	-0.4±1.3
<i>SYNGR1</i>	46.8±2.4	46.9±0.5	-0.2±2.0

Appendix

T_m (°C)	BAY-876	DMSO	ΔT_m
TSPAN9	51.7±0.6	48.6±0.8	3.1±0.6
UBTD2	49.0±1.8	49.7±2.2	-0.7±3.7
ZDHHC5	47.4±1.7	47.7±1.3	-0.3±2.4
ZRANB2	50.9±1.0	48.2±0.4	2.7±1.1

Proteins are described according to their gene name. Data show mean values \pm s.d. (n=3).

Table 21 Overview of the used amines and isocyanides (related to Figure 15). Amines, isocyanides that were utilized in and *in situ* generated isocyanides generated during the synthesis of a piperazin-2-one-based library.

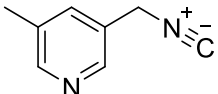
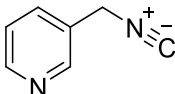
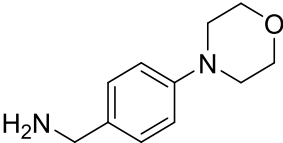
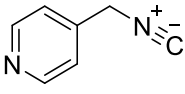
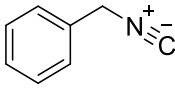
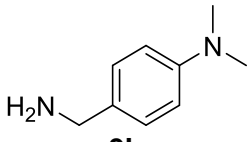
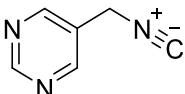
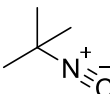
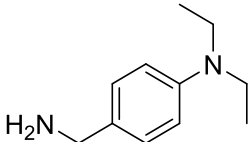
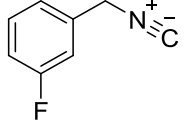
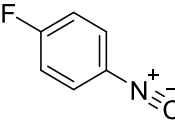
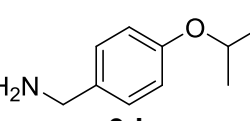
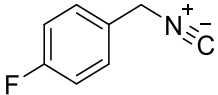
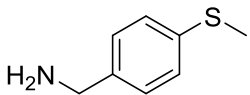
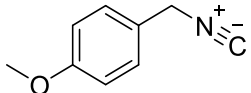
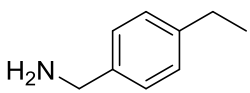
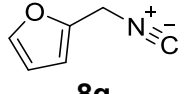
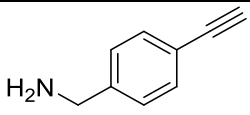
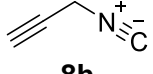
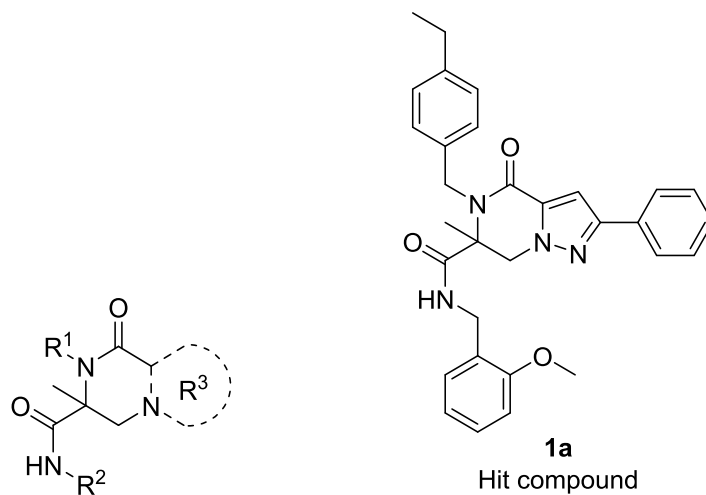
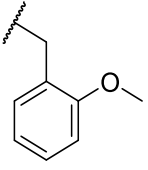
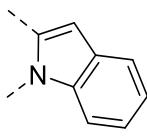
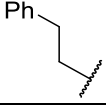
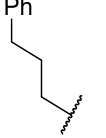
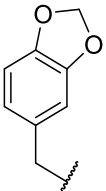
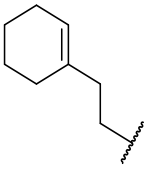
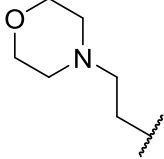
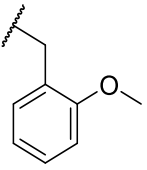
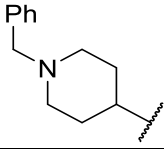
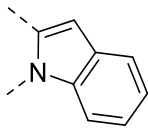
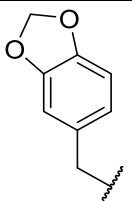
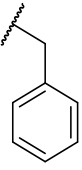
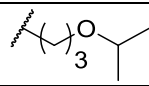
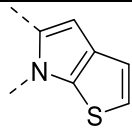
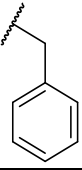
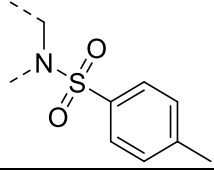
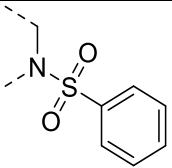
<i>In situ</i> generated isocyanides	Isocyanides	Amines
 8a	 8j	 9a
 8b	 8k	 9b
 8c	 8l	 9c
 8d	 8m	 9d
 8e		 9e
 8f		 9f
 8g		 9g
 8h		

Table 22 Inhibition of 2-DG import by Glutor derivatives (part I). Glutor derivatives and their respective activity as determined by the semi-automated resazurin-coupled 2-DG uptake assay. Values are mean values of all biological experiments (n=3-18) \pm s.d. n=biological replicates; n.a. not active at 30 μ M; Cmpd compound.



Entry	Cmpd	R ¹	R ²	R ³	IC ₅₀ (\pm s.d.) / μ M	n
1	1a	4-Et-Bn			3.29 (\pm 2.04)	12
2	1b	4-Me-Bn			10.67 (\pm 5.92)	15
3	1c	4-OMe-Bn			3.67 (\pm 1.40)	15
4	1d	3-OMe-Bn			25.63 (\pm 4.37)	6
5	1e	2-OMe-Bn			n.a.	3
6	1f	4-F-Bn			n.a.	3
7	1g	4-Cl-Bn			n.a.	3
8	1h	3-Cl-Bn			n.a.	3
9	1i	2-Cl-Bn			n.a.	3
10	1j	CH ₂ -(2-furyl)			25.90 (\pm 4.10)	6
11	1k	CH ₂ -(3-pyridyl)			> 30	6
12	1l	4-Et-Ph			n.a.	3
13	1m	Ph 			n.a.	3
14	1n	Ph 			n.a.	3
15	26	4-OEt-Bn			2.21 (\pm 1.03)	18
16	27	2-OEt-Bn			n.a.	3
17	28	CH ₂ -(2-thiophenyl)			21.67 (\pm 8.33)	6
18	29	2,4-(OMe) ₂ -Bn			20.06 (\pm 6.44)	6
19	30	CH ₂ -(2,4-(OMe) ₂ -Bn)			n.a.	3
20	31	CH ₂ -(3,4-(OMe) ₂ -Bn)			n.a.	3
21	32	3-Br-Bn			n.a.	3

Appendix

Entry	Cmpd	R ¹	R ²	R ³	IC ₅₀ (±s.d.) / μM	n
22	33				23.41 (±6.60)	6
23	34				n.a.	3
24	35				n.a.	3
25	36				n.a.	3
26	37	Et			n.a.	3
27	1o	4-Et-Bn			3.64 (±1.73)	18
28	21	2-OEt-Bn			n.a.	3
29	38	Bn			> 30	6
30	39	2-Br-Bn			n.a.	3
31	40	3-Br-Bn			n.a.	3
32	41				24.28 (±5.73)	6
33	1p	4-Et-Bn			> 30	3
34	42	4-F-Bn			n.a.	3
35	18	4-Et-Bn	2-OMe-Bn		5.09 (±1.40)	15
36	43	CH ₂ -(2-thiophenyl)			n.a.	3
37	44	CH ₂ -(2-furyl)			n.a.	3

Appendix

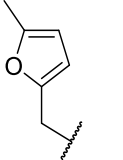
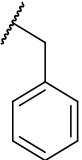
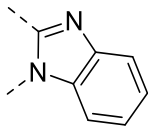
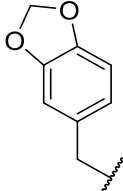
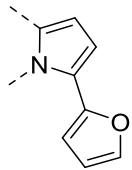
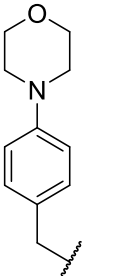
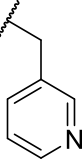
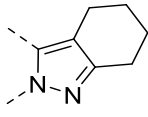
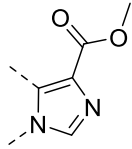
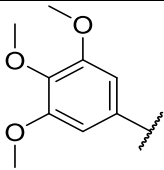
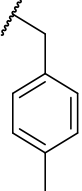
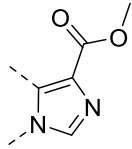
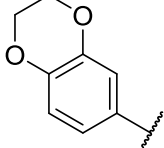
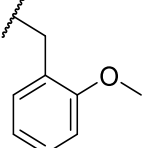
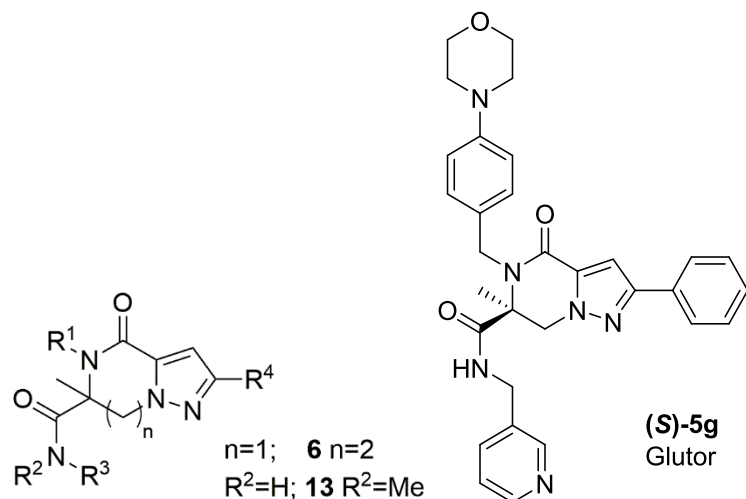
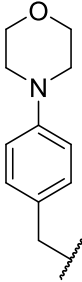
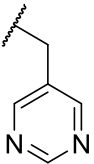
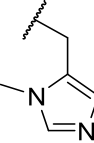
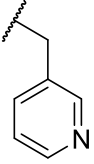
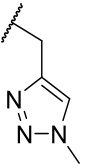
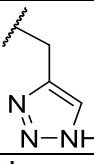
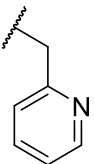
Entry	Cmpd	R ¹	R ²	R ³	IC ₅₀ (±s.d.) / μM	n
38	45				> 30	3
39	24	2-OEt-Bn			15.22 (±5.10)	15
40	46					22.24 (±7.77)
41	7					14.04 (±2.32)
42	47	2-OMe-Bn			4-F-Bn	21.14 (±7.47)
43	48	2-OMe-Bn	4-Me-Bn	> 30	9	
44	23	2-OEt-Bn	Bn		> 30	3
45	49	CH ₂ -(2-furyl)			n.a.	3
46	50	4-SMe-Bn			n.a.	3
47	51				n.a.	3
48	52					n.a.

Table 23 Inhibition of 2-DG import by Glutor derivatives (part II). Glutor-derivatives and their respective biological activities as determined by the semi-automated resazurin-coupled 2-DG uptake assay. Values are mean values of all biological experiments (n=3-21) \pm s.d.; n=biological replicates; n.a. not active at 30 μ M.

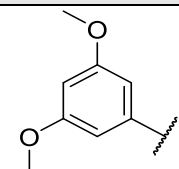
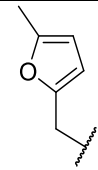


Entry	Cmpd	R ¹	R ³	R ⁴	IC ₅₀ (\pm s.d.) / μ M	n
1	5a	4-SMe-Bn	Bn	Ph	1.65 (\pm 1.10)	21
2	(S)-5a	4-SMe-Bn	Bn	Ph	0.88 (\pm 0.23)	12
3	(R)-5a	4-SMe-Bn	Bn	Ph	n.a.	6
4	5b	4-NEt ₂ -Bn	Bn	Ph	0.33 (\pm 0.09)	3
5	5c	4-NMe ₂ -Bn	Bn	Ph	0.42 (\pm 0.27)	12
6	5d	4-O <i>i</i> Pr-Bn	Bn	Ph	0.19 (\pm 0.06)	12
7	5e	4-Et-Bn	Bn	Ph	0.23 (\pm 0.11)	6
8	5f	4-(CCH)-Bn	Bn	Ph	6.77 (\pm 1.39)	3
9	5u	4-OEt-Bn	Bn	Ph	0.46 (\pm 0.27)	15
10	5v	4- <i>Or</i> nBu-Bn	Bn	Ph	1.94 (\pm 1.60)	15
11	5w	CH ₂ -(4-OEt-Bn)	Bn	Ph	> 30	3
12	13	4-SMe-Bn	Bn	Ph	n.a.	3
13	25	2-OEt-Bn	Bn	Ph	8.04 (\pm 1.47)	8
14	5g			Ph	0.03 (\pm 0.01)	12
15	(S)-5g			Ph	0.019 (\pm 0.002)	12
16	(R)-5g			Ph	n.a.	9
17	5h				Ph	0.48 (\pm 0.09)
18	5i			Ph	0.12 (\pm 0.01)	6

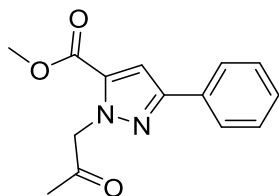
Appendix

Entry	Cmpd	R ¹	R ³	R ⁴	IC ₅₀ (±s.d.) / μM	n
19	5j			Ph	4.00 (±1.31)	6
20	5k			Ph	0.75 (±0.02)	6
21	5l		tBu	Ph	n.a.	3
22	5m		CH ₂ -CCH	Ph	> 30	6
23	5n		Bn	Ph	0.16 (±0.09)	9
24	5o		4-F-Bn	Ph	2.98 (±0.09)	6
25	5p		3-F-Bn	Ph	1.15 (±0.60)	3
26	5q		4-F-Ph	Ph	n.a.	9
27	5r		4-OMe-Bn	Ph	19.22 (±9.53)	9
28	5s		CH ₂ -(2-furyl)	Ph	1.17 (±0.05)	6
29	6			Ph	1.33 (±0.5)	6
30	15			Ph	6.64 (±0.91)	6
31	14			Ph	17.95 (±3.03)	3
32	16		H	Ph	n.a.	3
33	17		Ph	21.82 (±2.14)	3	
34	19	4-Et-Bn	2-OMe-Bn	Ph	0.82 (±0.59)	18
35	20	4-Et-Bn	2-OMe-Bn	4-OMe-Ph	0.81 (±0.28)	21
36	53	4-OEt-Bn	2-OMe-Bn	Ph	0.90 (±0.60)	15
37	54	4-Et-Bn	PrOMe	Ph	14.93 (±4.11)	12
38	24	2-OEt-Bn	Bn	tBu	> 30	3
39	55	4-OMe-Bn	Bn	Me	12.82 (±4.42)	12
40	56	3-F-Bn	Bn	tBu	> 30	3
41	57	CH ₂ -(2-furyl)	Cyclooctan	4-Et-Ph	n.a.	3

Appendix

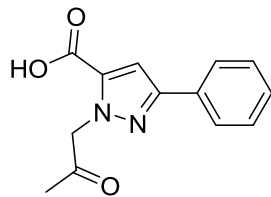
Entry	Cmpd	R ¹	R ³	R ⁴	IC ₅₀ (±s.d.) / μM	n
42	58		2-OMe-Bn	CO ₂ Et	> 30	3
43	59		4-Cl-Bn	CO ₂ Et	n.a. ³	3
44	60	2-Br-Bn	Bn	CO ₂ Et	22.61 (±5.28)	9
45	61	C ₂ H ₄ -(2-furyl)	Bn	4-OMe-Ph	> 30	6

13.3 Compound characterization



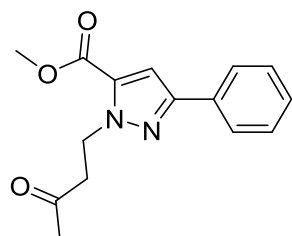
13.3.1.1 Methyl 1-(2-oxopropyl)-3-phenyl-1H-pyrazole-5-carboxylate (3a)

Methyl 3-phenyl-1H-pyrazole-5-carboxylate **2a** (30.0 mg, 0.15 mmol, 1.0 equiv.), 3-chloroacetone (11.9 μ L, 0.15 mmol, 1.0 equiv.), K_2CO_3 (24.6 mg, 0.18 mmol, 1.2 equiv.) and 18-crown-6-ether (0.4 mg, 1.5 μ mol, 0.01 equiv.) were suspended in 1,4-dioxane (1 mL) and vigorously stirred under reflux conditions for 6 h. Afterwards, water (50 mL) and DCM (50 mL) were added to the reaction mixture and the layers were separated. The aqueous phase was extracted two more times with DCM (2x 50 mL) and the combined organic layers were dried over $MgSO_4$, filtrated and evaporated under reduced pressure. The residue was purified by means of silica gel column chromatography (elute: cyclohexane / EtOAc) and obtained as white solid (23.0 mg, 0.15 mmol, quant.). $R_f = 0.24$ (cyclohexane / EtOAc = 3:1). 1H NMR (400 MHz, $CDCl_3$) δ 7.79 (d, $J = 7.3$ Hz, 2H), 7.41 (t, $J = 7.3$ Hz, 2H), 7.33 (t, $J = 7.3$ Hz, 1H), 7.19 (s, 1H), 5.39 (s, 2H), 3.88 (s, 3H), 2.23 ppm (s, 3H). ^{13}C NMR (100 MHz, $CDCl_3$) δ 201.3, 162.9, 146.5, 143.9, 129.9, 129.4, 129.4, 129.1, 109.6, 59.8, 52.5, 27.4 ppm. HR-MS: calc. for $[M+H]^+$ $C_{14}H_{15}N_2O_3$ 259.1077 found 259.1075.



13.3.1.2 1-(2-Oxopropyl)-3-phenyl-1H-pyrazole-5-carboxylic acid (4a)

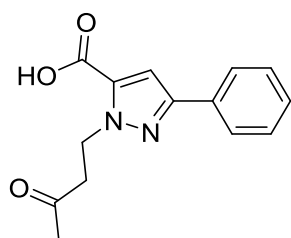
Methyl 1-(2-oxopropyl)-3-phenyl-1H-pyrazole-5-carboxylate **3a** (30.0 mg, 0.12 mmol, 1.0 equiv.) was suspended in water (1 mL) and NaOH was added slowly (5.6 mg, 0.14 mmol, 1.2 equiv.) and stirred thoroughly at 70 °C for 3 h. Afterwards, HCl (0.5 mL, 1 M) was added to the crude reaction mixture. Water (40 mL) and EtOAc (40 mL) were added to the crude reaction and the phases were separated. The aqueous phase was extracted two more times with EtOAc (2x 40 mL) and the combined organic layers were dried over Na₂SO₄, filtered and concentrated under reduced pressure. The product was obtained as light yellow solid (28.3 mg, 0.12 mmol, quant.). $R_f = 0.41$ (dichloromethane / MeOH = 7:3). ¹H NMR (400 MHz, CDCl₃) δ 7.88 (d, $J = 7.3$ Hz, 2H), 7.42 (t, $J = 7.3$ Hz, 2H), 7.35 (t, $J = 7.3$ Hz, 1H), 7.31 (s, 1H), 5.41 (s, 2H), 2.23 ppm (s, 3H). ¹³C NMR (100 MHz, CDCl₃) δ 201.2, 163.6, 151.4, 133.4, 132.0, 128.9, 128.6, 125.9, 110.0, 61.5, 27.0 ppm. HR-MS: calc. for [M+H]⁺ C₁₃H₁₃N₂O₃ 245.0921 found 245.0929.



13.3.1.3 Methyl 1-(3-oxobutyl)-3-phenyl-1H-pyrazole-5-carboxylate (3b)

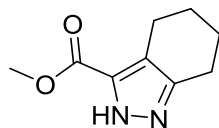
Methyl 3-phenyl-1-pyrazole-5-carboxylate **2a** (100 mg, 495 μ mol, 1.0 equiv.) was dissolved in 1,4-dioxane (1.5 mL) and potassium carbonate (82 mg, 593 μ mol, 1.2 equiv.), 18-Crown-6 ether

(1.5 mg, 5 μ mol, 0.01 equiv.) and 4-chlorobutan-2-one (47.3 μ L, 495 μ mol, 1.0 equiv.) were added. The solution was stirred thoroughly at 140 °C for 4 h. The product was purified by means of silica gel column chromatography (elute: cyclohexane / EtOAc) and obtained as white solid (55 mg, 202 μ mol, 40%). R_f = 0.30 (cyclohexane / EtOAc = 3:1). ^1H NMR (700 MHz, CDCl_3) δ 7.77 (dd, J = 8.0, 1.2 Hz, 2H), 7.40 (t, J = 8.0 Hz, 2H), 7.34 – 7.30 (m, 1H), 7.11 (s, 1H), 4.86 (t, J = 7.2 Hz, 2H), 3.92 (s, 3H), 3.09 (t, J = 7.2 Hz, 2H), 2.21 ppm (s, 3H). ^{13}C NMR (176 MHz, CDCl_3) δ 206.0, 160.3, 150.3, 133.4, 132.6, 128.9, 128.3, 125.7, 108.3, 52.2, 46.9, 43.5, 30.3 ppm. HR-MS: calc. for $[\text{M}+\text{H}]^+$ $\text{C}_{15}\text{H}_{17}\text{N}_2\text{O}_3$ 273.12337 found 273.12343.



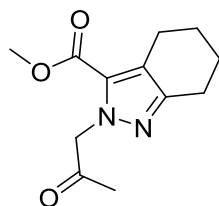
13.3.1.4 1-(3-Oxobutyl)-3-phenyl-1H-pyrazole-5-carboxylic acid (4b)

Methyl 1-(3-oxobutyl)-3-phenyl-1H-pyrazole-5-carboxylate **3b** (70 mg, 0.26 mmol, 1.0 equiv.) was subjected to NaOH (2% w/v in water, 617 μ L, 0.31 mmol, 1.2 equiv.) and stirred at 70 °C for 4 h. The crude was acidified to pH 2 using 1 M HCl and extracted with EtOAc. The combined organic layers were dried over Na_2SO_4 , filtered and concentrated under reduced pressure. The product was purified by means of silica gel column chromatography (elute: cyclohexane / EtOAc +2% v/v acetic acid) and obtained as crystalline white solid (58 mg, 0.22 mmol, 87%). R_f = 0.37 (EtOAc +2% v/v acetic acid). ^1H NMR (700 MHz, CDCl_3) δ 7.80-7.76 (m, 2H), 7.41 (t, J = 7.7 Hz, 2H), 7.36 – 7.31 (m, 1H), 7.22 (s, 1H), 4.87 (t, J = 7.2 Hz, 2H), 3.12 (t, J = 7.2 Hz, 2H), 2.23 ppm (s, 3H). ^{13}C NMR (176 MHz, CDCl_3) δ 206.2, 162.8, 150.5, 132.7, 132.4, 128.9, 128.4, 125.7, 109.6, 46.9, 43.4, 30.3 ppm. HR-MS: calc. for $[\text{M}+\text{H}]^+$ $\text{C}_{14}\text{H}_{15}\text{N}_2\text{O}_3$ 259.10772 found 259.10779.



13.3.1.5 Methyl 4,5,6,7-tetrahydro-2H-indazole-3-carboxylate (2b)

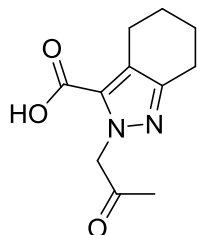
4,5,6,7-Tetrahydro-2H-indazole-3-carboxylate (324 mg, 2.13 mmol, 1.0 equiv.) was dissolved in 7.8 mL methanol and cooled to -10 °C before thionyl chloride (278.3 μ L, 3.84 mmol, 1.8 equiv.) was added dropwise to the solution. The reaction was vigorously stirred at room temperature for 5 days. The crude reaction mixture was concentrated under reduced pressure. The product was extracted thrice with EtOAc (20 mL) from water (20 mL) and the combined organic layers were dried over Na₂SO₄ and filtered. The filtrate was concentrated under reduced pressure and the residual was purified by means of silica gel column chromatography (elute: DCM / MeOH) and obtained as white solid (161.7 mg, 0.9 mmol, 42%). R_f = 0.23 (DCM +4% v/v MeOH). ¹H NMR (500 MHz, CDCl₃) δ 3.89 (s, 3H), 2.72 (td, J = 25.9, 6.1 Hz, 4H), 1.84-1.71 ppm (m, 4H). ¹³C NMR (126 MHz, CDCl₃) δ 162.5, 119.9, 51.8, 22.9, 22.6, 22.2, 21.5 ppm. HR-MS: calc. for [M+H]⁺ C₉H₁₃N₂O₂ 181.09715 found 181.09697.



13.3.1.6 Methyl 2-(2-oxopropyl)-4,5,6,7-tetrahydro-2H-indazole-3-carboxylate (3c)

Methyl-4,5,6,7-tetrahydro-2H-indazol-3-carboxylate **2b** (90.4 mg, 0.5 mmol, 1.0 equiv.) and 1-chloroactone (161.44 μ L, 2.01 mmol, 4.0 equiv.) were dissolved in 2.3 mL acetone and K₂CO₃

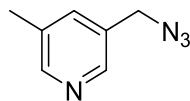
(153.22 mg, 1.1 mmol, 2.2 equiv.) was added. The reaction mixture was vigorously stirred at 60 °C for 2 days. The crude reaction mixture was adjusted to pH 7 with 0.5 M HCl. The solvent was evaporated under reduced pressure. The crude reaction was extracted thrice with EtOAc (3x 50 mL) from water (50 mL) and the combined organic layers were dried over Na₂SO₄ and filtered. The filtrate was evaporated under reduced pressure and purified by means of silica gel column chromatography (elute: DCM / MeOH). The isomers were separated using preparative HPLC. The 2-alkylated product was obtained as white solid (24 mg, 0.1 mmol, 20%). $R_f = 0.66$ (DCM +5% v/v MeOH). ¹H NMR (500 MHz, CDCl₃) δ 4.88 (s, 2H), 3.90 (s, 3H), 2.77 (t, $J = 6.0$ Hz, 2H), 2.45 (t, $J = 6.2$ Hz, 2H), 2.14 (s, 3H), 1.84 – 1.74 ppm (m, 4H). ¹³C NMR (126 MHz, CDCl₃) δ 201.0, 163.1, 141.0, 139.8, 120.7, 58.7, 52.0, 26.9, 22.3, 22.0, 21.3, 21.1 ppm. HR-MS: calc. for [M+H]⁺ C₁₂H₁₇N₂O₃ 237.12547 found 237.12337.



13.3.1.7 2-(2-Oxopropyl)-4,5,6,7-tetrahydro-2H-indazole-3-carboxylate (4c)

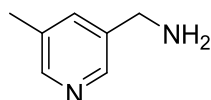
Methyl 2-(2-oxopropyl)-4,5,6,7-tetrahydro-2H-indazole-3-carboxylate **3c** (24 mg, 0.1 mmol, 1.0 equiv.) was solved in 0.8 mL water and NaOH (4.9 mg, 0.12 mmol, 1.2 equiv.) was added subsequently to the solution. The reaction mixture was stirred at 70 °C for 5 h. The crude was acidified to pH 4-5 using 1 M HCl and extracted thrice with EtOAc (3x 50 mL) from water (50 mL). The combined organic layers were dried over Na₂SO₄, filtered and concentrated under reduced pressure. The product was obtained as white solid (12.2 mg, 0.05 mmol, 54%). $R_f = 0.56$ (DCM +35% v/v MeOH). ¹H NMR (500 MHz, CD₃CN) δ 5.23 (s, 2H), 4.44 (s, 1H), 2.71 (t, $J = 6.1$ Hz, 2H), 2.62 – 2.57 (m, 2H), 2.13 (s, 3H), 1.82 – 1.70 ppm (m, 4H). ¹³C NMR (126 MHz, CD₃CN) δ 203.4,

161.9, 149.5, 129.7, 62.0, 27.3, 23.9, 23.8, 23.8, 23.1 ppm. HR-MS: calc. for $[M+H]^+$ $C_{11}H_{15}N_2O_3$ 223.10772 found 223.1080.



13.3.1.8 3-(Azidomethyl)-5-methylpyridine

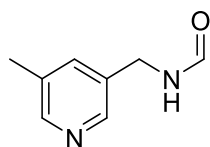
3-(Chloromethyl)-5-methylpyridine (300 mg, 1.7 mmol, 1.0 equiv.) and sodium azide (470 mg, 7.2 mmol, 4.2 equiv.) were dissolved in ACN (6.2 mL). *N,N*-Diisopropylethylamide (287 μ L, 1.7 mmol, 1.0 equiv.), tetrabutylammonium iodide (6 mg, 20 μ mol, 0.1 equiv.) and 18-crown-6 (4 mg, 20 μ mol, 0.1 equiv.) were added. The reaction mixture was stirred at room temperature overnight. EtOAc was added to the crude product and the mixture was extracted with saturated $NaHCO_3$. The aqueous layer was extracted twice with EtOAc and the combined organic layers were concentrated under reduced pressure. The product was obtained as white crystalline solid (238 mg, 1.61 mmol, 95%) and used in the following step without further purification. $R_f = 0.71$ (EtOAc / MeOH / TEA = 9:1:0.1). 1H NMR (500 MHz, $CDCl_3$) δ 8.43 (d, $J = 2.0$ Hz, 1H), 8.38 (d, $J = 2.0$ Hz, 1H), 7.47 (m, 1H), 4.35 (s, 2H), 2.37 ppm (s, 3H). ^{13}C NMR (126 MHz, $CDCl_3$) δ 150.5, 146.6, 136.4, 133.5, 130.7, 52.2, 18.5 ppm. HR-MS: calc. for $[M+H]^+$ $C_7H_9N_4$ 149.08217 found 149.08198.



13.3.1.9 (5-Methylpyridin-3-yl)methanamine (12a)

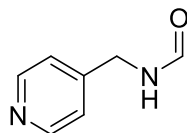
3-(Azidomethyl)-5-methylpyridine (244 mg, 1.7 mmol, 1.0 equiv.) was dissolved in 55 mL EtOAc / MeOH (2:1) and Pd/C (175 mg, 0.17 mmol, 0.1 equiv.) was added. The solution was stirred under

inert hydrogen atmosphere for 1 h. The reaction mixture was filtered over Celite® and the filtrate was concentrated under reduced pressure. The residual was purified by means of silica gel column chromatography (elute: EtOAc / MeOH +1% v/v TEA) and the product was obtained as pale yellow oil (108.6 mg, 0.89 mmol, 54%). $R_f = 0.23$ (DCM / EtOH / sat.NH₄OH = 50:8:1). ¹H NMR (500 MHz, CDCl₃) δ 8.35 (d, $J = 1.5$ Hz, 1H), 8.33 (d, $J = 1.5$ Hz, 1H), 7.49 – 7.47 (m, 1H), 3.87 (s, 2H), 2.33 ppm (s, 3H). ¹³C NMR (126 MHz, CDCl₃) δ 149.0, 146.2, 137.7, 135.6, 133.1, 43.9, 18.5 ppm. HR-MS: m/z calculated for [M+H]⁺ C₇H₁₁N₂ 123.09167 found 123.09139.



13.3.1.10 *N-((5-methylpyridin-3-yl)methyl)formamide (13a)*

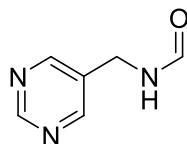
(5-Methylpyridin-3-yl)methanamine **12a** (100 mg, 0.82 mmol, 1.0 equiv.) was dissolved in ethyl formate (200 μ L, 2.5 mmol, 3.0 equiv.) and the solution was vigorously stirred at 60 °C for 24 h. The solvent was removed under reduced pressure and the residual was purified by means of silica gel column chromatography (elute: EtOAc / MeOH +1% v/v TEA). The product was obtained as yellow oil (111 mg, 0.74 mmol, 90%). ¹H NMR (500 MHz, CDCl₃) δ 8.34 (d, $J = 14.4$ Hz, 2H), 8.29 (s, 1H), 7.46 (s, 1H), 4.47 (d, $J = 6.1$ Hz, 2H), 2.33 ppm (s, 3H). ¹³C NMR (126 MHz, CDCl₃) δ 161.2, 149.7, 146.3, 136.4, 133.5, 133.0, 39.6, 18.5 ppm. HR-MS: m/z calculated for [M+H]⁺ C₈H₁₁N₂O 151.08659 found 151.08616.



13.3.1.11 *N*-(4-Picolyl)formamide (13b)

4-Picolylamine **12b** (305 μ L, 3.0 mmol, 1.0 equiv.) was dissolved in ethyl formate (724 μ L, 9.0 mmol, 3 equiv.) and the solution was vigorously stirred at 60 °C for 24 h. The reaction mixture was evaporated under reduced pressure and the product was obtained as yellow oil (398 mg, 2.9 mmol, 97%). R_f = 0.21 (EtOAc / MeOH / TEA = 90:10:1). ^1H NMR (500 MHz, DMSO- d_6) mixture of rotamers is observed, major rotamer is given; δ 8.62 (bs, 1H), 8.50 (d, J = 6.0 Hz, 2H), 8.19 (s, 1H), 7.26 (d, J = 6.0 Hz, 2H), 4.33 ppm (d, J = 6.2 Hz, 2H). ^{13}C NMR (126 MHz, DMSO- d_6) δ 161.5, 149.6, 148.0, 122.2, 39.8* ppm. LC-MS: m/z calculated for $[\text{M}+\text{H}]^+$ $\text{C}_7\text{H}_9\text{N}_2\text{O}$ 137 found 137.

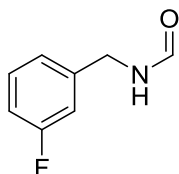
*Under solvent signal, determined by HSQC



13.3.1.12 *N*-(Pyrimidine-5-ylmethyl)formamide (13c)

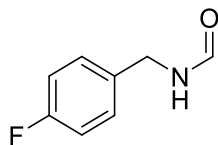
Prepared according to general procedure 1A with pyrimidine-5-carbaldehyde **11a** (300 mg, 2.8 mmol, 1.0 equiv.), formic acid (838 μ L, 22 mmol, 7.9 equiv.) and formamide (1.6 mL, 33 mmol, 11.8 equiv.) under conventional heating at 180 °C for 30 min. The product was purified by means of silica gel column chromatography (elute: EtOAc / MeOH +1% v/v TEA) to obtain the product as colorless oil (41 mg, 0.3 mmol, 10%). R_f = 0.17 (EtOAc / MeOH / TEA = 90:10:1). ^1H NMR (600 MHz, CDCl_3) mixture of rotamers is observed, major rotamer is given; δ 9.15 (s, 1H), 8.71 (s, 2H), 8.32 (s, 1H), 6.16 (bs, 1H), 4.51 ppm (d, J = 6.2 Hz, 2H). ^{13}C NMR (151 MHz, CDCl_3) δ 161.3,

158.3, 156.6, 131.5, 37.6 ppm. HR-MS: m/z calculated for $[M+H]^+$ $C_6H_8N_3O$ 138.0662 found 138.06579.



13.3.1.13 *N*-(3-Fluorobenzyl)formamide (13d)

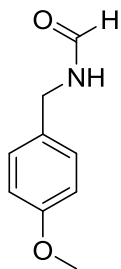
Prepared according to general procedure 1A with 3-fluorobenzaldehyde **11b** (300 μ L, 2.8 mmol, 1.0 equiv.), formic acid (530 μ L, 14 mmol, 5.0 equiv.) and formamide (1.3 mL, 28 mmol, 10.0 equiv.) under conventional heating. The product was obtained by means of flash silica gel column chromatography (elute: cyclohexane / EtOAc) as pale yellow oil (244 mg, 1.6 mmol, 56%). R_f = 0.27 (cyclohexane / EtOAc = 1:1). 1H NMR (400 MHz, DMSO- d_6) mixture of rotamers is observed, major rotamer is given; δ 8.54 (bs, 1H), 8.15 (d, J = 0.8 Hz, 1H), 7.41-7.33 (m, 1H), 7.14 – 7.03 (m, 3H), 4.32 ppm (d, J = 6.2 Hz, 2H). ^{13}C NMR (101 MHz, DMSO- d_6) δ 165.0, 163.4, 161.2, 142.1, 142.0, 130.3, 130.3, 123.3, 123.2, 114.0, 113.8, 113.7, 113.5, 40.2 ppm. LC-MS: m/z calculated for $[M+H]^+$ C_8H_9FNO 154.0 found 154.0.



13.3.1.14 *N*-(4-Fluorobenzyl)formamide (13e)

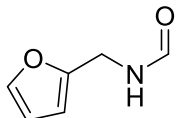
Prepared according to general procedure 1A with 4-fluorobenzaldehyde **11c** (300 μ L, 2.8 mmol, 1.0 equiv.), formic acid (530 μ L, 14 mmol, 5.0 equiv.) and formamide (1.3 mL, 28 mmol,

10.0 equiv.) under conventional heating. The product was obtained by means of flash silica gel column chromatography (elute: cyclohexane / EtOAc) as white crystalline solid (254 mg, 1.7 mmol, 59%). $R_f = 0.23$ (cyclohexane / EtOAc = 1:1). $^1\text{H NMR}$ (400 MHz, DMSO- d_6) mixture of rotamers is observed, major rotamer is given; δ 8.50 (bs, 1H), 8.12 (s, 1H), 7.34-7.25 (m, 2H), 7.21-7.10 (m, 2H), 4.28 ppm (d, $J = 6.2$ Hz, 2H). $^{13}\text{C NMR}$ (101 MHz, DMSO- d_3) δ 161.1, 129.3, 129.3, 115.2, 115.0, 40.0 ppm. LC-MS: m/z calculated for $[\text{M}+\text{H}]^+$ $\text{C}_8\text{H}_9\text{FNO}$ 154.0 found 154.0.



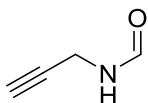
13.3.1.15 *N*-(4-Methoxybenzyl)formamide (13f)

Prepared according to general procedure 1A using 4-methoxybenzaldehyde **11d** (44.6 μL , 0.37 mmol, 1.0 equiv.), formic acid (72.9 μL , 1.84 mmol, 5.0 equiv.) and formamide (731.9 μL , 18.36 mmol, 50.0 equiv.) using microwave irradiation. The product was purified by means of flash silica gel column chromatography (elute: cyclohexane / EtOAc) and obtained as off-white solid (29.9 mg, 0.18 mmol, 49%). $R_f = 0.24$ (cyclohexane / EtOAc 1:3). $^1\text{H NMR}$ (400 MHz, CDCl_3 , mixture of rotamers, only major rotamer given) δ 8.24 (s, 1H), 7.22 (d, $J = 8.7$ Hz, 2H), 6.87 (d, $J = 8.7$ Hz, 2H), 5.75 (bs, 1H), 4.42 (d, $J = 5.8$ Hz, 2H), 3.80 ppm (s, 3H). $^{13}\text{C NMR}$ (100 MHz, CDCl_3 , mixture of rotamers, only major rotamer given) δ 160.9, 159.4, 129.4, 128.5, 114.3, 55.5, 41.9 ppm. MS-EI: m/z (%): 165 (100) $[\text{M}]^+$, 136 (56), 121 (85), 109 (20), 91 (18), 77 (26).



13.3.1.16 *N*-(Furan-2-ylmethyl)formamide (13g)

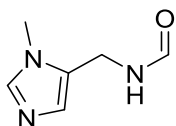
Prepared according to general procedure 1A with furfural **11e** (300 μ L, 3.6 mmol, 1.0 equiv.), formic acid (683 μ L, 18 mmol, 5.0 equiv.) and formamide (1.7 mL, 36 mmol, 10.0 equiv.) under conventional heating. The product was obtained by means of flash silica gel column chromatography (elute: cyclohexane / EtOAc) as brown oil (164 mg, 1.3 mmol, 36%). R_f = 0.11 (cyclohexane / EtOAc = 1:1). ^1H NMR (600 MHz, DMSO- d_6) mixture of rotamers is observed, major rotamer is given; δ 8.47 (bs, 1H), 8.06 (s, 1H), 7.62-7.55 (m, 1H), 6.39 (dd, J = 3.0, 1.9 Hz, 1H), 6.25 (d, J = 3.2 Hz, 1H), 4.28 ppm (d, J = 5.8 Hz, 2H). ^{13}C NMR (151 MHz, DMSO- d_6) δ 160.9, 151.8, 142.2, 110.5, 107.0, 34.0 ppm. MS-EI: m/z (%): 125 (100) $[\text{M}]^+$, 108 (5), 96 (50), 81 (48), 68 (20), 53 (20).



13.3.1.17 *N*-(Propargyl)formamide (13h)

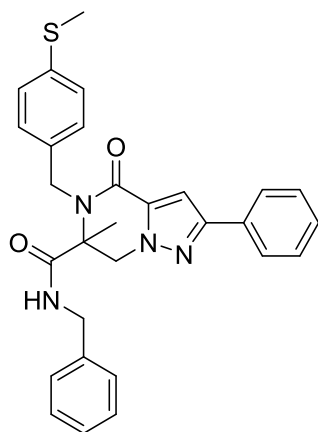
Propargylamine **12c** (500 μ L, 9.1 mmol, 1.0 equiv.) and formamide (360 μ L, 9.1 mmol, 1.0 equiv.) were dissolved in toluene (8 mL) and hydroxylamine hydrochloride (63 mg, 0.9 mmol, 0.1 equiv.) was added. The reaction mixture was stirred to reflux for 24 h. The reaction mixture was allowed to cool down to room temperature and concentrated under reduced pressure.¹¹³ The crude reaction was extracted with DCM and the organic layer was washed twice with water. The combined organic layers were dried over Na_2SO_4 , filtered and concentrated under reduced pressure. The product was obtained by means of silica gel column chromatography (elute: cyclohexane / EtOAc) as white crystalline solid (367 mg, 4.4 mmol, 48%). R_f = 0.28 (cyclohexane

/ EtOAc = 1:1). ^1H NMR (500 MHz, CDCl_3) mixture of rotamers is observed, major rotamer is given; δ 8.19 (s, 1H), 5.86 (bs, 1H), 4.10 (ddd, $J = 5.4, 2.6, 0.8$ Hz, 2H), 2.26 ppm (t, $J = 2.6$ Hz, 1H). ^{13}C NMR (126 MHz, CDCl_3) δ 160.7, 78.9, 72.1, 28.0 ppm.



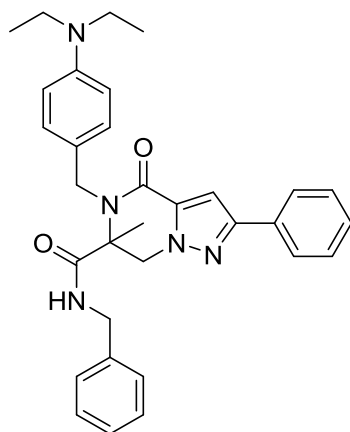
13.3.1.18 *N*-((1-Methyl-1H-imidazol-5-yl)methyl)formamide (13i)

(1-Methyl-1H-imidazol-5-yl)methanamine **12d** (233 mg, 2.1 mmol, 1.0 equiv.) was dissolved in ethyl formate (505 μL , 6.3 mmol, 3.0 equiv.) and the solution was transferred into a sealed glass vial. The reaction was vigorously stirred at 60 $^\circ\text{C}$ for 24 h. After completion of the reaction, the reaction mixture was evaporated under reduced pressure and purified by means of silica gel column chromatography (EtOAc / MeOH). The product was obtained as colorless oil (252 mg, 1.81 mmol, 86%). $R_f = 0.16$ (EtOAc / MeOH / TEA = 90:10:1). ^1H NMR (700 MHz, DMSO-d_6) mixture of rotamers is observed, major rotamer is given; δ 8.36 (bs, 1H), 8.04 (s, 1H), 7.53 (s, 1H), 6.78 (s, 1H), 4.28 (d, $J = 5.7$ Hz, 2H), 3.55 ppm (s, 3H). ^{13}C NMR (176 MHz, DMSO-d_6) δ 160.8, 138.4, 128.6, 127.6, 30.9, 30.5 ppm. LC-MS: m/z calculated for $[\text{M}+\text{H}]^+$ $\text{C}_6\text{H}_{10}\text{N}_3\text{O}$ 140; found, 140.



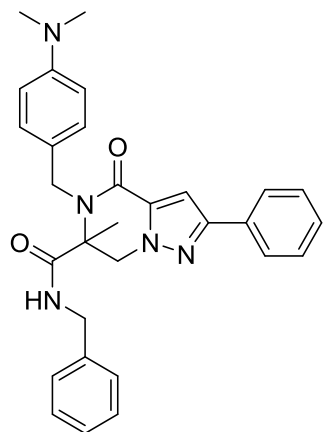
13.3.1.19 *N*-Benzyl-6-methyl-5-(4-(methylthio)benzyl)-4-oxo-2-phenyl-4,5,6,7-tetrahydropyrazolo[1,5-a]pyrazine-6-carboxamide (**5a**)

Prepared according to general procedure 2 using 1-(2-oxopropyl)-3-phenyl-1*H*-pyrazole-5-carboxylic acid **4a** (200.0 mg, 0.82 mmol, 1.0 equiv.), 4-(methylthio)benzylamine **9e** (144.1 μ L, 0.82 mmol, 1.0 equiv.) and benzylisocyanide **8k** (99.7 μ L, 0.82 mmol, 1.0 equiv.). The product was obtained as white solid (382.4 mg, 0.77 mmol, 94%). Enantiomers were separated by means of chiral preparative HPLC. Optical rotation after enantiomer separation: *R* -0.250 $^{\circ}$; *S* +0.258 $^{\circ}$. Crystals for X-ray structure determination were grown in Et₂O / DCM (5:1). R_f = 0.45 (cyclohexane / EtOAc = 1:1). ¹H NMR (500 MHz, CDCl₃) δ 7.77 (d, *J* = 7.4 Hz, 2H), 7.41 (t, *J* = 7.4 Hz, 2H), 7.35 (t, *J* = 7.4 Hz, 1H), 7.27 (d, *J* = 7.9 Hz, 1H), 7.16 (d, *J* = 8.3 Hz, 2H), 7.12 – 7.08 (m, 3H), 7.06 (s, 1H), 6.78 (d, *J* = 6.4 Hz, 2H), 6.31 (s, 1H), 5.15 (d, *J* = 15.5 Hz, 1H), 5.06 (d, *J* = 13.0 Hz, 1H), 4.61 (d, *J* = 15.5 Hz, 1H), 4.37 (dd, *J* = 14.9, 6.7 Hz, 1H), 4.19 (d, *J* = 13.0 Hz, 1H), 4.01 (dd, *J* = 14.9, 5.0 Hz, 1H), 2.45 (s, 3H), 1.70 ppm (s, 3H). ¹³C NMR (126 MHz, CDCl₃) δ 170.7, 159.1, 152.4, 138.5, 137.1, 134.6, 134.1, 132.3, 128.9, 128.7, 128.5, 128.2, 127.6, 127.1, 127.0, 125.8, 105.4, 66.0, 55.8, 45.7, 44.1, 22.0, 15.8 ppm. HR-MS: calc. for [M+H]⁺ C₂₉H₂₉N₄O₂S 497.2006 found 497.2002.



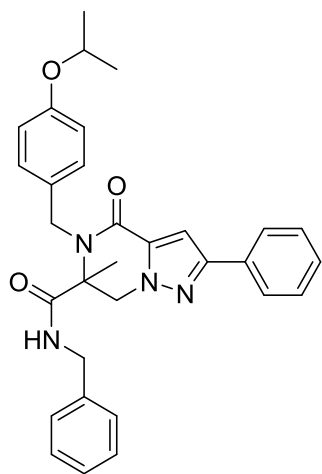
13.3.1.20 *N*-Benzyl-5-(4-(diethylamino)benzyl)-6-methyl-4-oxo-2-phenyl-4,5,6,7-tetrahydropyrazolo[1,5-a]pyrazine-6-carboxamide (**5b**)

Prepared according to general procedure 2 using 1-(2-oxopropyl)-3-phenyl-1*H*-pyrazole-5-carboxylic acid **4a** (20.0 mg, 0.08 mmol, 1.0 equiv.), (4-aminomethyl)-*N,N*-diethylaniline **9c** (13.3 μ L, 0.07 mmol, 0.9 equiv.) and benzyl isocyanide **8k** (10.0 μ L, 0.08 mmol, 1.0 equiv.). The product was obtained as light yellow solid (11.5 mg, 0.02 mmol, 27%). R_f = 0.42 (cyclohexane / EtOAc = 1:1). ^1H NMR (500 MHz, CDCl_3) δ 7.80 (d, J = 7.4 Hz, 2H), 7.41 (t, J = 7.4 Hz, 2H), 7.34 (t, J = 7.4 Hz, 1H), 7.28 (s, 1H), 7.13 – 7.02 (m, 4H), 6.70 (d, J = 7.0 Hz, 2H), 6.55 – 6.56 (m, 2H), 6.20 – 6.13 (m, 1H), 5.10 (d, J = 12.8 Hz, 1H), 4.95 (d, J = 15.0 Hz, 1H), 4.70 (d, J = 15.0 Hz, 1H), 4.32 (dd, J = 15.0, 7.0 Hz, 1H), 4.17 (d, J = 12.8 Hz, 1H), 3.80 (dd, J = 15.0 Hz, 1H), 3.31 (q, J = 7.0 Hz, 4H), 1.80 (s, 3H), 1.13 ppm (t, J = 7.0 Hz, 6H). ^{13}C NMR (126 MHz, CDCl_3) δ 171.2, 159.1, 152.1, 147.5, 137.2, 134.5, 132.5, 129.8, 128.9, 128.6, 128.4, 127.4, 127.0, 125.8, 123.8, 112.1, 105.2, 65.9, 55.9, 45.4, 44.4, 44.0, 21.8, 12.6 ppm. HR-MS: calc. for $[\text{M}+\text{H}]^+$ $\text{C}_{32}\text{H}_{36}\text{N}_5\text{O}_2$ 522.2864 found 522.2873, calc. for $[\text{M}+\text{Na}]^+$ $\text{C}_{32}\text{H}_{35}\text{N}_5\text{O}_2\text{Na}$ 544.2694 found 544.2694.



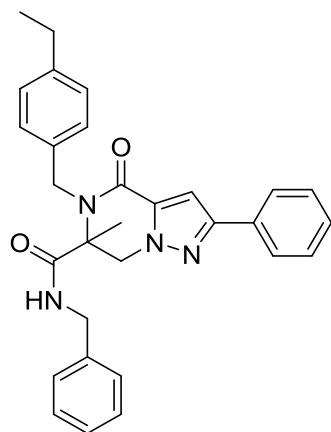
13.3.1.21 *N*-Benzyl-5-(4-(dimethylamino)benzyl)-6-methyl-4-oxo-2-phenyl-4,5,6,7-tetrahydropyrazolo[1,5-a]pyrazine-6-carboxamide (**5c**)

Prepared according to the general procedure 2 using 1-(2-oxopropyl)-3-phenyl-1*H*-pyrazole-5-carboxylic acid **4a** (36.7 mg, 0.15 mmol, 1.0 equiv.), (4-aminomethyl)-*N,N*-dimethylaniline **9b** (22.2 μ L, 0.15 mmol, 1.0 equiv.) and benzyl isocyanide **8k** (18.3 μ L, 0.15 mmol, 1.0 equiv.). The product was obtained as light-yellow solid (44.4 mg, 0.09 mmol, 60%). R_f = 0.38 (cyclohexane / EtOAc = 1:1). ^1H NMR (500 MHz, CDCl_3) δ 7.81 – 7.79 (m, 2H), 7.42 (t, J = 7.5 Hz, 2H), 7.35 (t, J = 7.5 Hz, 1H), 7.29 (d, J = 8.6 Hz, 2H), 7.14 – 7.03 (m, 5H), 6.72 (d, J = 7.1 Hz, 2H), 6.61 (bs, 1H), 6.14 (t, J = 5.4 Hz, 1H), 5.10 (d, J = 12.8 Hz, 1H), 4.91 (d, J = 14.7 Hz, 1H), 4.77 (d, J = 14.7 Hz, 1H), 4.28 (dd, J = 14.9, 7.0 Hz, 1H), 4.17 (d, J = 12.8 Hz, 1H), 3.88 (dd, J = 14.9, 4.6 Hz, 1H), 2.92 (s, 6H), 1.78 ppm (s, 3H). ^{13}C NMR (126 MHz, CDCl_3) δ 171.1, 159.1, 152.2, 137.2, 134.4, 132.4, 129.4, 128.9, 128.6, 128.4, 127.4, 127.1, 125.8, 112.9, 105.2, 77.4, 65.9, 60.6, 55.9, 45.4, 44.1, 21.8 ppm. HR-MS: calc. for $[\text{M}+\text{H}]^+$ $\text{C}_{30}\text{H}_{32}\text{N}_5\text{O}_2$ 494.2551 found 494.2561, calc. for $[\text{M}+\text{Na}]^+$ $\text{C}_{30}\text{H}_{31}\text{N}_5\text{O}_2\text{Na}$ 516.2370 found 516.2382.



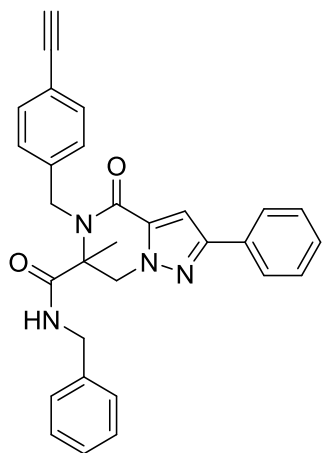
13.3.1.22 *N*-Benzyl-5-(4-isopropoxybenzyl)-6-methyl-4-oxo-2-phenyl-4,5,6,7-tetrahydropyrazolo[1,5-a]pyrazine-6-carboxamide (**5d**)

Prepared according to general procedure 2 using 1-(2-oxopropyl)-3-phenyl-1*H*-pyrazole-5-carboxylic acid **4a** (20.0 mg, 0.08 mmol, 1.0 equiv.), (4-isopropoxyphenyl)-methanamine **9d** (13.7 μ L, 0.08 mmol, 1.0 equiv.) and benzyl isocyanide **8k** (10.0 μ L, 0.08 mmol, 1.0 equiv.). The product was obtained as brown solid (24.9 mg, 0.05 mmol, 60%). R_f = 0.55 (cyclohexane / EtOAc = 1:1). ^1H NMR (500 MHz, CDCl_3) δ 7.99 (d, J = 7.2 Hz, 2H), 7.71 – 7.45 (m, 5H), 7.31 (d, J = 7.2 Hz, 3H), 6.98 – 7.03 (m, 4H), 6.65 – 6.77 (m, 1H), 5.55 – 5.23 (m, 2H), 4.88 (d, J = 15.0 Hz, 1H), 4.73 (hept, J = 6.0 Hz, 1H), 4.59 (d, J = 15.0 Hz, 1H), 4.39 – 4.44 (m, 1H), 4.22 (d, J = 15.0 Hz, 1H), 1.94 (s, 3H), 1.55 ppm (d, J = 6.0 Hz, 6H). ^{13}C NMR (126 MHz, CDCl_3) δ 170.9, 159.1, 157.6, 152.2, 137.2, 134.3, 132.3, 129.6, 129.2, 128.9, 128.6, 128.4, 127.5, 127.0, 125.8, 116.3, 105.3, 69.9, 65.9, 55.8, 45.5, 44.0, 22.1, 21.9 ppm. HR-MS: calc. for $[\text{M}+\text{H}]^+$ $\text{C}_{31}\text{H}_{33}\text{N}_4\text{O}_3$ 509.2547 found 509.2561, calc. for $[\text{M}+\text{Na}]^+$ $\text{C}_{31}\text{H}_{32}\text{N}_4\text{O}_3\text{Na}$ 531.2367 found 531.2382.



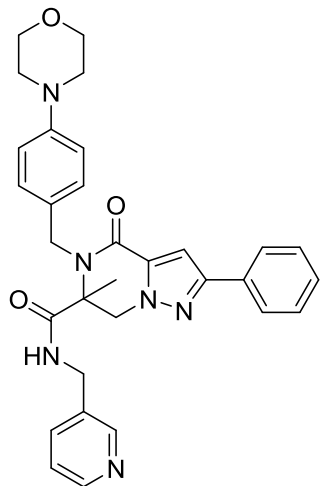
13.3.1.23 *N*-Benzyl-5-(4-ethylbenzyl)-6-methyl-4-oxo-2-phenyl-4,5,6,7-tetrahydropyrazolo[1,5-a]pyrazine-6-carboxamide (**5e**)

Prepared according to the general procedure 2 using 1-(2-oxopropyl)-3-phenyl-1*H*-pyrazole-5-carboxylic acid **4a** (50.0 mg, 0.20 mmol, 1.0 equiv.), (4-ethylphenyl)methanamine **9f** (29.2 μ L, 0.20 mmol, 1.0 equiv.) and benzyl isocyanide **8k** (24.9 μ L, 0.20 mmol, 1.0 equiv.). The product was obtained as light-yellow solid (72.8 mg, 0.15 mmol, 74%). R_f = 0.56 (cyclohexane / EtOAc = 1:1). ^1H NMR (400 MHz, CDCl_3) δ 7.96 (d, J = 7.3 Hz, 2H), 7.58 (t, J = 7.3 Hz, 2H), 7.52 (d, J = 7.3 Hz, 1H), 7.49 – 7.41 (m, 2H), 7.33 – 7.23 (m, 5H), 6.93 (d, J = 7.1 Hz, 2H), 6.38 (t, J = 5.6 Hz, 1H), 5.24 (dd, J = 15.0, 5.4 Hz, 2H), 4.89 (d, J = 15.0 Hz, 1H), 4.53 (dd, J = 15.0, 5.1 Hz, 1H), 4.37 (d, J = 15.0 Hz, 1H), 4.10 (dd, J = 15.0, 5.1 Hz, 1H), 2.78 (q, J = 7.7 Hz, 2H), 1.89 (s, 3H), 1.38 ppm (t, J = 7.7 Hz, 3H). ^{13}C NMR (101 MHz, CDCl_3) δ 170.9, 159.1, 152.4, 144.2, 137.2, 135.2, 134.3, 132.4, 128.9, 128.8, 128.7, 128.4, 127.8, 127.6, 127.1, 125.9, 105.4, 66.0, 55.9, 45.9, 44.1, 28.6, 21.9, 15.6 ppm. HR-MS: calc. for $[\text{M}+\text{H}]^+$ $\text{C}_{30}\text{H}_{31}\text{N}_4\text{O}_2^+$ 479.2442 found 479.2454, calc. for $[\text{M}+\text{Na}]^+$ $\text{C}_{30}\text{H}_{30}\text{N}_4\text{O}_2\text{Na}$ 501.2261 found 501.2273.



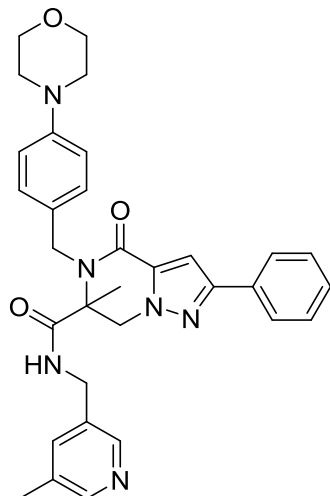
13.3.1.24 *N*-Benzyl-5-(4-ethynylbenzyl)-6-methyl-4-oxo-2-phenyl-4,5,6,7-tetrahydropyrazolo[1,5-a]pyrazine-6-carboxamide (**5f**)

Prepared according to general procedure 2 using 1-(2-oxopropyl)-3-phenyl-1*H*-pyrazole-5-carboxylic acid **4a** (20.0 mg, 0.08 mmol, 1.0 equiv.), (4-ethynylphenyl)methanamine **9g** (10.7 μ L, 0.08 mmol, 1.0 equiv.) and benzyl isocyanide **8k** (10.0 μ L, 0.08 mmol, 1.0 equiv.). The product was obtained as white solid (13.4 mg, 0.03 mmol, 34%). R_f = 0.56 (cyclohexane / EtOAc = 3:7). ^1H NMR (500 MHz, CDCl_3 , major rotamer given) δ 7.99 (d, J = 7.2 Hz, 2H), 7.69 – 7.62 (m, 4H), 7.60 (d, J = 7.2 Hz, 1H), 7.53 – 7.48 (m, 2H), 7.36 – 7.31 (m, 3H), 7.07 – 6.99 (m, 2H), 6.80 (t, J = 5.1 Hz, 1H), 5.56 (d, J = 15.9 Hz, 1H), 5.29 (d, J = 13.1 Hz, 1H), 4.74 (d, J = 15.9 Hz, 1H), 4.63 (dd, J = 14.9 Hz, 1H), 4.43 (d, J = 13.1 Hz, 1H), 4.33 (dd, J = 14.9, 5.1 Hz, 1H), 3.35 (s, 1H), 1.91 ppm (s, 3H). ^{13}C NMR (126 MHz, CDCl_3) δ 170.6, 159.2, 152.4, 138.7, 137.2, 134.1, 132.9, 132.2, 128.9, 128.7, 128.5, 127.6, 127.3, 127.1, 125.8, 121.8, 105.5, 83.1, 78.0, 66.0, 55.8, 46.0, 44.1, 22.0 ppm. HR-MS: calc. for $[\text{M}+\text{H}]^+$ $\text{C}_{30}\text{H}_{27}\text{N}_4\text{O}_2$ 475.2129 found 475.2124, calc. for $[\text{M}+\text{Na}]^+$ $\text{C}_{30}\text{H}_{26}\text{N}_4\text{O}_2\text{Na}$ 497.1948 found 497.1943.



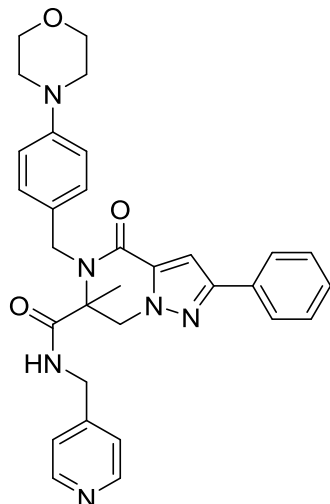
13.3.1.25 **6-Methyl-5-(4-morpholinobenzyl)-4-oxo-2-phenyl-N-(pyridin-3-ylmethyl)-4,5,6,7-tetrahydropyrazolo[1,5-a]pyrazine-6-carboxamide (5g)**

Prepared according to general procedure 2 using 1-(2-oxopropyl)-3-phenyl-1*H*-pyrazole-5-carboxylic acid **4a** (100.0 mg, 0.41 mmol, 1.0 equiv.), 4-(morpholinophenyl)methanamine **9a** (78.7 mg, 0.41 mmol, 1.0 equiv.) and 3-(isocyanomethyl)pyridine **8j** (48.4 mg, 0.41 mmol, 1.0 equiv.). The product was obtained as white solid (97.2 mg, 0.18 mmol, 44%). Enantiomers were separated by means of chiral preparative HPLC. Optical rotation after enantiomer separation: *R* -0.431 °; *S* +0.390 °. $R_f = 0.51$ (dichloromethane / MeOH = 4:1). $^1\text{H NMR}$ (400 MHz, CDCl_3) δ 8.33 (dd, $J = 4.7, 1.4$ Hz, 1H), 8.19 (d, $J = 1.4$ Hz, 1H), 7.81 – 7.68 (m, 2H), 7.46 – 7.30 (m, 3H), 7.27 (s, 1H), 6.98 (s, 1H), 6.97 (dt, $J = 7.8, 1.9$ Hz, 1H), 6.90 (dd, $J = 7.8, 4.7$ Hz, 1H), 6.79 (d, $J = 8.7$ Hz, 2H), 6.64 (t, $J = 5.5$ Hz, 1H), 5.06 (d, $J = 13.0$ Hz, 1H), 4.97 (d, $J = 15.3$ Hz, 1H), 4.73 (d, $J = 15.3$ Hz, 1H), 4.25 (dd, $J = 15.1, 6.5$ Hz, 1H), 4.16 (d, $J = 13.0$ Hz, 1H), 4.00 (dd, $J = 15.1, 5.5$ Hz, 1H), 3.84 (t, $J = 4.8$ Hz, 4H), 3.10 (t, $J = 4.8$ Hz, 4H), 1.72 ppm (s, 3H). $^{13}\text{C NMR}$ (101 MHz, CDCl_3) δ 171.3, 159.1, 152.3, 151.0, 148.9, 148.8, 134.8, 134.3, 133.1, 132.2, 129.0, 128.9, 128.7, 128.5, 125.8, 123.6, 115.9, 105.2, 66.9, 65.9, 55.8, 48.9, 45.5, 41.5, 21.8 ppm. HR-MS: calc. for $[\text{M}+\text{H}]^+$ $\text{C}_{31}\text{H}_{33}\text{N}_6\text{O}_3$ 537.2609 found 537.2601.



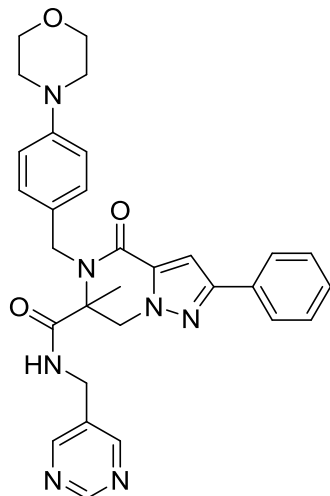
13.3.1.26 *6-Methyl-N-((5-methylpyridin-3-yl)methyl)-5-(4-morpholinobenzyl)-4-oxo-2-phenyl-4,5,6,7-tetrahydropyrazolo[1,5-a]pyrazine-6-carboxamide (5h)*

Prepared according to general procedure 3B using Burgess reagent (95 mg, 400 μ mol, 2.0 equiv.), *N*-((5-methylpyridin-3-yl)methyl)formamide **13a** (30 mg, 200 μ mol, 1.0 equiv.), 1-(2-oxopropyl)-3-phenyl-1*H*-pyrazole-5-carboxylic acid **4a** (49 mg, 200 μ mol, 1.0 equiv.) and 4-(morpholinophenyl)methanamine **9a** (35 mg, 180 μ mol, 1.0 equiv.) in MeOH (1.2 mL) and ACN (5.5 mL). The product was purified by means of silica gel column chromatography (DCM / EtOH / sat. NH_4OH) and obtained as white crystalline solid (13 mg, 24 μ mol, 13%). ^1H NMR (700 MHz, CDCl_3) δ 8.18 (d, J = 2.1 Hz, 1H), 7.99 (d, J = 2.1 Hz, 1H), 7.77 (d, J = 7.1 Hz, 2H), 7.42 – 7.36 (m, 2H), 7.34 – 7.29 (m, 3H), 7.07 (s, 1H), 6.83 – 6.81 (m, 2H), 6.81 – 6.79 (m, 1H), 6.34 (t, J = 6.3 Hz, 1H), 5.08 (d, J = 12.8 Hz, 1H), 4.91 (d, J = 15.3 Hz, 1H), 4.81 (d, J = 15.3 Hz, 1H), 4.26 (dd, J = 15.1, 6.3 Hz, 1H), 4.16 (d, J = 12.8 Hz, 1H), 3.90 (dd, J = 15.1, 6.3 Hz, 1H), 3.85 (t, J = 4.9 Hz, 4H), 3.11 (td, J = 4.3, 1.5 Hz, 4H), 2.02 (s, 3H), 1.75 ppm (s, 3H). ^{13}C NMR (176 MHz, CDCl_3) δ 171.3, 159.0, 152.3, 151.1, 149.6, 145.8, 135.3, 134.3, 133.3, 132.5, 132.2, 129.2, 128.9, 128.7, 128.5, 125.8, 116.0, 105.1, 66.9, 65.9, 55.8, 49.0, 45.5, 41.4, 21.9, 18.2 ppm. HR-MS: calc. for $[\text{M}+\text{H}]^+$ $\text{C}_{32}\text{H}_{35}\text{N}_6\text{O}_3$ 551.27652 found 551.27602.



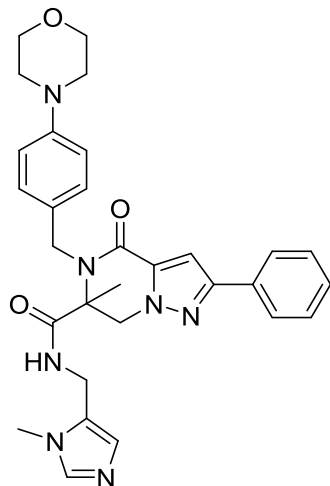
13.3.1.27 *6-Methyl-5-(4-morpholinobenzyl)-4-oxo-2-phenyl-N-(pyridin-4-ylmethyl)-4,5,6,7-tetrahydropyrazolo[1,5-a]pyrazine-6-carboxamide (5i)*

Prepared according to general procedure 3B using Burgess reagent (83 mg, 348 μmol , 1.6 equiv.), *N*-(4-picolyl)formamide **13b** (30 mg, 220 μmol , 1.0 equiv.), 1-(2-oxopropyl)-3-phenyl-1*H*-pyrazole-5-carboxylic acid **4a** (54 mg, 220 μmol , 1.0 equiv.) and 4-(morpholinophenyl)methanamine **9a** (38 mg, 198 μmol , 0.9 equiv.) in MeOH (1.2 mL) and ACN (5.5 mL). The product was purified twice by means of silica gel column chromatography (1st elute: DCM / MeOH; 2nd elute: DCM / EtOH / sat. NH_4OH) and obtained as white solid (12 mg, 22 μmol , 11%). R_f = 0.29 (DCM / EtOH / sat. NH_4OH = 75:4:0.5). ^1H NMR (700 MHz, CD_2Cl_2) δ 8.27-8.22 (m, 2H), 7.85 – 7.80 (m, 2H), 7.46 – 7.41 (m, 2H), 7.38 – 7.35 (m, 1H), 7.34 (d, J = 8.7 Hz, 2H), 7.15 (s, 1H), 6.84 – 6.80 (m, 2H), 6.60 – 6.57 (m, 2H), 6.31 (t, J = 6.2 Hz, 1H), 5.03 (d, J = 12.8 Hz, 1H), 4.88 (s, 2H), 4.26 (dd, J = 16.0, 6.2 Hz, 1H), 4.22 (d, J = 12.8 Hz, 1H), 3.94 (dd, J = 16.0, 6.2 Hz, 1H), 3.83 – 3.78 (m, 4H), 3.07 (m, 4H), 1.76 ppm (s, 3H). ^{13}C NMR (176 MHz, CD_2Cl_2) δ 171.9, 159.2, 152.4, 151.5, 150.1, 146.7, 134.9, 132.7, 129.4, 129.2, 129.0, 128.7, 125.9, 121.8, 116.1, 105.2, 67.1, 66.2, 56.2, 49.2, 45.6, 43.0, 21.8 ppm. HR-MS: calc. for $[\text{M}+\text{H}]^+$ $\text{C}_{31}\text{H}_{33}\text{N}_6\text{O}_3$ 537.26087 found 537.26006.



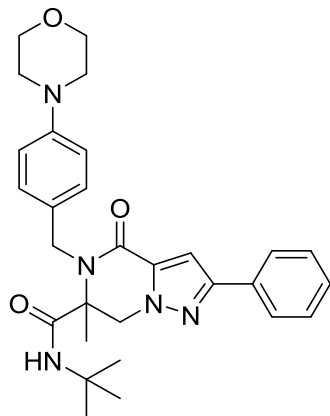
13.3.1.28 *6-Methyl-5-(4-morpholinobenzyl)-4-oxo-2-phenyl-N-(pyrimidin-5-ylmethyl)-4,5,6,7-tetrahydropyrazolo[1,5-a]pyrazine-6-carboxamide (5j)*

Prepared according to general procedure 3B using Burgess reagent (143 mg, 602 μmol , 2.6 equiv.), *N*-(pyrimidin-5-ylmethyl)formamide **13c** (32 mg, 233 μmol , 1.0 equiv.), 1-(2-oxopropyl)-3-phenyl-1*H*-pyrazole-5-carboxylic acid **4a** (53 mg, 218 μmol , 0.9 equiv.) and 4-(morpholinophenyl)methanamine **9a** (38 mg, 196 μmol , 0.8 equiv.) in MeOH (1.2 mL) and ACN (5.5 mL). The product was purified twice by means of silica gel column chromatography (1st elute: DCM / MeOH; 2nd elute: DCM / EtOH / sat. NH_4OH) and obtained as white solid (12 mg, 22 μmol , 12%). $R_f = 0.21$ (DCM / EtOH / sat. $\text{NH}_4\text{OH} = 150:8:1$). ^1H NMR (700 MHz, CD_2Cl_2) δ 8.96 (s, 1H), 8.21 (s, 2H), 7.82 – 7.79 (m, 2H), 7.42 (dd, $J = 7.0, 8.4$ Hz, 2H), 7.37 – 7.32 (m, 3H), 7.11 (s, 1H), 6.81 – 6.79 (m, 2H), 6.26 (t, $J = 6.2$ Hz, 1H), 5.03 (d, $J = 12.8$ Hz, 1H), 4.99 (d, $J = 15.4$ Hz, 1H), 4.71 (d, $J = 15.4$ Hz, 1H), 4.18 (d, $J = 12.8$ Hz, 1H), 4.08 (dd, $J = 15.4, 6.2$ Hz, 1H), 3.99 (dd, $J = 15.4, 6.2$ Hz, 1H), 3.82 (m, 4H), 3.10 (m, 4H), 1.75 ppm (s, 3H). ^{13}C NMR (176 MHz, CD_2Cl_2) δ 172.0, 159.2, 158.3, 156.3, 152.3, 151.5, 134.8, 132.7, 131.4, 129.6, 129.1, 128.8, 128.6, 126.0, 116.0, 105.2, 67.1, 66.1, 56.0, 49.0, 45.6, 39.6, 21.8 ppm. HR-MS: calc. for $[\text{M}+\text{H}]^+$ $\text{C}_{30}\text{H}_{32}\text{N}_7\text{O}_3$ 538.25611 found 538.25529.



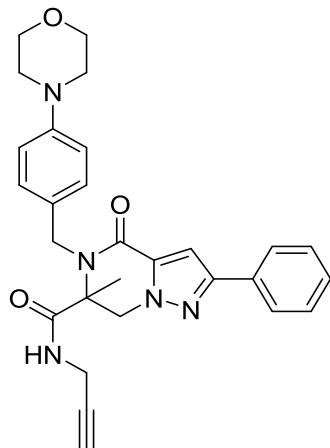
13.3.1.29 **6-Methyl-N-((1-methyl-1H-imidazol-5-yl)methyl)-5-(4-morpholinobenzyl)-4-oxo-2-phenyl-4,5,6,7-tetrahydropyrazolo[1,5-a]pyrazine-6-carboxamide (5k)**

Prepared according to general procedure 3B using Burgess reagent (128 mg, 539 μmol , 2.5 equiv.), *N*-((1-methyl-1*H*-imidazol-5-yl)methyl)formamide **13i** (30 mg, 216 μmol , 1.0 equiv.), 1-(2-oxopropyl)-3-phenyl-1*H*-pyrazole-5-carboxylic acid **4a** (53 mg, 216 μmol , 1.0 equiv.) and 4-(morpholinophenyl)methanamine **9a** (37 mg, 194 μmol , 0.9 equiv.) in MeOH (1.2 mL) and ACN (5.5 mL). The product was purified twice by means of silica gel column chromatography (1st elute: EtOAc / MeOH / TEA = 90:10:1; 2nd elute: DCM / EtOH / sat. NH_4OH = 125:4:0.5) and obtained as white solid (13 mg, 24 μmol , 12%). R_f = 0.40 (DCM / EtOH / sat. NH_4OH = 125:4:0.5). ^1H NMR (700 MHz, CD_2Cl_2) δ 7.80 (d, J = 7.5 Hz, 2H), 7.42 (t, J = 7.5 Hz, 2H), 7.35 (t, J = 7.5 Hz, 1H), 7.30 (d, J = 8.5 Hz, 2H), 7.23 (s, 1H), 7.10 (s, 1H), 6.81 (d, J = 8.5 Hz, 2H), 6.64 (s, 1H), 5.98 (s, 1H), 5.03 (d, J = 12.5 Hz, 1H), 4.89 (d, J = 15.4 Hz, 1H), 4.75 (d, J = 15.4 Hz, 1H), 4.23 (dd, J = 15.6, 6.2 Hz, 1H), 4.18 (d, J = 12.5 Hz, 1H), 3.93 (dd, J = 15.5, 6.2 Hz, 1H), 3.83 (t, J = 5.0 Hz, 4H), 3.14 (m, 4H), 3.09 (s, 3H), 1.74 ppm (s, 3H). ^{13}C NMR (176 MHz, CD_2Cl_2) δ 171.2, 159.1, 152.2, 151.4, 139.1, 135.0, 132.7, 129.4, 129.2, 128.9, 128.7, 128.7, 127.7, 125.9, 116.0, 105.0, 67.2, 66.1, 56.1, 49.2, 45.6, 33.8, 31.3, 21.7 ppm. HR-MS: calc. for $[\text{M}+\text{H}]^+$ $\text{C}_{30}\text{H}_{34}\text{N}_7\text{O}_3$ 540.27176 found 540.27094.



13.3.1.30 *N*-(*Tert*-butyl)-6-methyl-5-(4-morpholinobenzyl)-4-oxo-2-phenyl-4,5,6,7-tetrahydropyrazolo[1,5-*a*]pyrazine-6-carboxamide (**5l**)

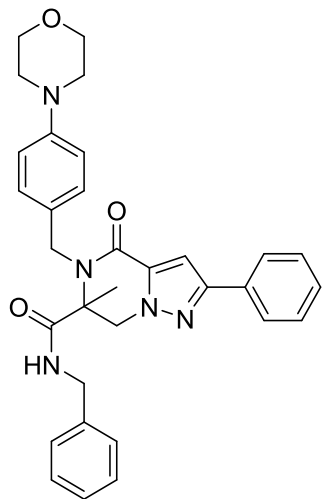
Prepared according to general procedure 2 using 1-(2-oxopropyl)-3-phenyl-1*H*-pyrazole-5-carboxylic acid **4a** (108 mg, 0.44 mmol, 1.0 equiv.), 4-(morpholinophenyl) methanamine **9a** (85 mg, 0.44 mmol) and *tert*-butylisocyanide **8l** (50 μ L, 0.44 mmol, 1.0 equiv.). The product was purified by means of silica gel column chromatography (elute: pentane / EtOAc) and obtained as yellow solid (126 mg, 0.25 mmol, 57%). R_f = 0.21 (cyclohexane / EtOAc = 1:1). ^1H NMR (700 MHz, CDCl_3) δ 7.82 – 7.79 (m, 2H), 7.42 – 7.39 (m, 4H), 7.35 – 7.31 (m, 1H), 7.17 (s, 1H), 6.91 – 6.88 (m, 2H), 5.41 (s, 1H), 4.97 (d, J = 12.9 Hz, 1H), 4.94 (d, J = 15.2 Hz, 1H), 4.69 (d, J = 15.2 Hz, 1H), 4.14 (d, J = 12.8 Hz, 1H), 3.87 – 3.84 (m, 4H), 3.17 – 3.10 (m, 4H), 1.74 (s, 3H), 0.94 ppm (s, 9H). ^{13}C NMR (176 MHz, CDCl_3) δ 169.8, 159.2, 152.1, 151.3, 134.3, 132.6, 129.8, 129.0, 128.9, 128.4, 125.9, 116.3, 104.9, 67.0, 66.2, 56.1, 51.7, 49.3, 45.4, 28.2, 21.6 ppm. HR-MS: calc. for $[\text{M}+\text{H}]^+$ $\text{C}_{29}\text{H}_{36}\text{N}_5\text{O}_3$ 502.28127 found 502.28028.



13.3.1.31 **6-Methyl-5-(4-morpholinobenzyl)-4-oxo-2-phenyl-N-(prop-2-yn-1-yl)-4,5,6,7-tetrahydropyrazolo[1,5-a]pyrazine-6-carboxamide (5m)**

A round bottom flask was charged with formamide **13h** (106 mg, 1.3 mmol, 1 equiv.), benzenesulfonyl chloride (327 μ L, 2.6 mmol, 2.0 equiv.) and trioctylamine (1.12 mL, 2.6 mmol, 2.0 equiv.). The flask was connected to a glass distillation tube and heated to 80 $^{\circ}$ C. A two-neck receiver flask was cooled to -80 $^{\circ}$ C to collect formed isocyanide under reduced pressure over 2 h according to the procedure described by Chrostowska *et al.*¹¹¹ Subsequently, 4-(morpholinophenyl)methanamine **9a** (80 mg, 415 μ mol, 0.3 equiv) and 1-(2-oxopropyl)-3-phenyl-1*H*-pyrazole-5-carboxylic acid **4a** (113 mg, 461 μ mol, 0.4 equiv.) were added in MeOH (2.4 mL) to the freshly distilled isocyanide. The resulting mixture was stirred vigorously at room temperature for two days. Thereafter, the reaction mixture was diluted with EtOAc and washed with saturated NaHCO₃. The aqueous layer was extracted twice with EtOAc and the combined organic layers were dried over Na₂SO₄ and filtered. The filtrate was concentrated under reduced pressure and the product was purified by means of silica gel column chromatography (DCM / EtOH / sat. NH₄OH) and obtained as white crystalline solid (80 mg, 170 μ mol, 40%). *R*_f = 0.5 (DCM / EtOH / sat. NH₄OH = 125:4:0.5). ¹H NMR (500 MHz, CDCl₃) δ 7.78 – 7.73 (m, 2H), 7.39 – 7.34 (m, 2H), 7.34 – 7.28 (m, 3H), 7.14 (s, 1H), 6.90 – 6.86 (m, 2H), 6.28 (q, *J* = 4.8 Hz, 1H), 5.11 (d, *J* = 15.4 Hz, 1H), 5.03 (d, *J* = 13.0 Hz, 1H), 4.66 (d, *J* = 15.4 Hz, 1H), 4.15 (d, *J* = 13.0 Hz, 1H), 3.87 – 3.80 (m,

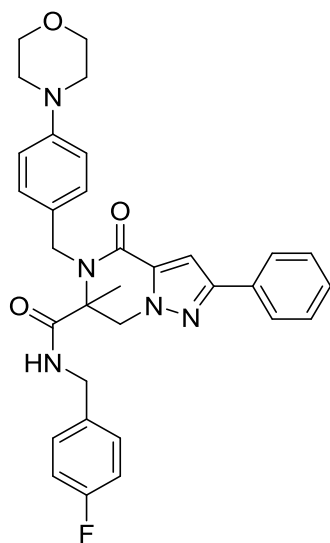
5H), 3.72 (ddd, $J = 17.5, 5.0, 2.6$ Hz, 1H), 3.17 – 3.11 (m, 4H), 2.08 (t, $J = 2.6$ Hz, 1H), 1.69 ppm (s, 3H). ^{13}C NMR (126 MHz, CDCl_3) δ 170.8, 159.0, 152.3, 151.0, 134.2, 132.2, 128.9, 128.9, 128.8, 128.4, 125.8, 116.2, 105.4, 78.6, 72.1, 66.9, 65.7, 55.6, 49.2, 45.6, 30.1, 22.1 ppm. HR-MS: calc. for $[\text{M}+\text{H}]^+ \text{C}_{28}\text{H}_{30}\text{N}_5\text{O}_3$ 484.23432 found 484.23387.



13.3.1.32 *N*-Benzyl-6-methyl-5-(4-morpholinobenzyl)-4-oxo-2-phenyl-4,5,6,7-tetrahydropyrazolo[1,5-a]pyrazine-6-carboxamide (**5n**)

Prepared according to general procedure 2 using 1-(2-oxopropyl)-3-phenyl-1*H*-pyrazole-5-carboxylic acid **4a** (30.0 mg, 0.12 mmol, 1.0 equiv.), (4-morpholino-phenyl)methanamine **9a** (21.2 μL , 0.12 mmol, 1.0 equiv.) and benzyl isocyanide **8k** (15.0 μL , 0.12 mmol, 1.0 equiv.). The product was obtained as brown solid (44.3 mg, 0.08 mmol, 67%). Enantiomers were separated by means of chiral preparative HPLC. Optical rotation after enantiomer separation: *R* -0.252 $^\circ$; *S* +0.260 $^\circ$. $R_f = 0.25$ (cyclohexane / EtOAc = 3:7). ^1H NMR (500 MHz, CDCl_3) δ 7.79 (d, $J = 7.3$ Hz, 2H), 7.41 (t, $J = 7.3$ Hz, 2H), 7.35 (t, $J = 7.3$ Hz, 1H), 7.30 (d, $J = 8.7$ Hz, 2H), 7.13 – 7.07 (m, 4H), 6.80 (d, $J = 8.7$ Hz, 2H), 6.75 (d, $J = 6.4$ Hz, 2H), 6.21 (t, $J = 5.4$ Hz, 1H), 5.08 (d, $J = 12.9$ Hz, 1H), 4.98 (d, $J = 15.0$ Hz, 1H), 4.74 (d, $J = 15.0$ Hz, 1H), 4.35 (dd, $J = 15.0, 6.8$ Hz, 1H), 4.18 (d, $J = 12.9$ Hz, 1H), 3.94 (dd, $J = 15.0, 5.4$ Hz, 1H), 3.85 (t, $J = 4.8$ Hz, 4H), 3.11 (t, $J = 4.8$ Hz, 4H), 1.74 ppm (s, 3H). ^{13}C NMR (126 MHz, CDCl_3) δ 171.0, 159.1, 152.3, 150.9, 137.2, 134.3, 132.4,

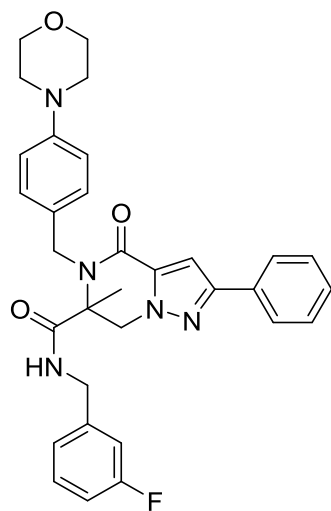
129.1, 128.9, 128.7, 128.4, 127.5, 127.0, 125.8, 116.0, 105.3, 66.9, 65.9, 55.9, 49.1, 45.5, 44.1, 29.8, 21.9 ppm. HR-MS: calc. for $[M+H]^+$ $C_{32}H_{34}N_5O_3$ 536.2656 found 536.2668, calc. for $[M+Na]^+$ $C_{32}H_{33}N_5O_3Na$ 558.2476 found 558.2487.



13.3.1.33 *N*-(4-Fluorobenzyl)-6-methyl-5-(4-morpholinobenzyl)-4-oxo-2-phenyl-4,5,6,7-tetrahydropyrazolo[1,5-a]pyrazine-6-carboxamide (**5o**)

Prepared according to general procedure 3B using Burgess reagent (70 mg, 293 μ mol, 2.0 equiv.), *N*-(4-fluorobenzyl)formamide **13e** (30 mg, 196 μ mol, 1.0 equiv.), 1-(2-oxopropyl)-3-phenyl-1*H*-pyrazole-5-carboxylic acid **4a** (48 mg, 196 μ mol, 1.0 equiv.) and 4-(morpholinophenyl)methanamine **9a** (34 mg, 176 μ mol, 0.9 equiv) in MeOH (1.2 ml) and ACN (5.5 ml). The crude was filtered and the remaining product was washed thrice with cold ACN. The product was obtained as a white solid (15 mg, 27 μ mol, 15%). R_f = 0.47 (cyclohexane / EtOAc = 1:4). 1H NMR (500 MHz, $CDCl_3$) δ 7.77 (d, J = 7.3 Hz, 2H), 7.41 (t, J = 7.3 Hz, 2H), 7.35 (t, J = 7.3 Hz, 1H), 7.30 (d, J = 8.6 Hz, 2H), 7.06 (s, 1H), 6.80 (d, J = 8.6 Hz, 2H), 6.75 (t, J = 8.3 Hz, 2H), 6.73-6.68 (m, J = 8.3 Hz, 2H), 6.25 (s, 1H), 5.07 (d, J = 12.9 Hz, 1H), 4.94 (d, J = 15.2 Hz, 1H), 4.76 (d, J = 15.2 Hz, 1H), 4.27 (dd, J = 14.9, 6.7 Hz, 1H), 4.18 (d, J = 12.9 Hz, 1H), 3.91 (dd,

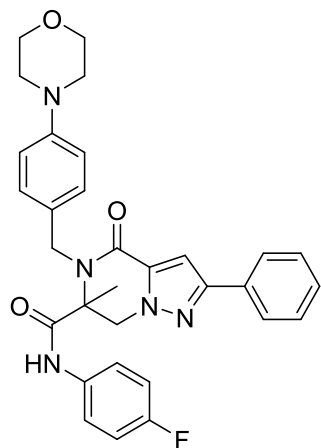
$J = 14.9, 5.1$ Hz, 1H), 3.88-3.81 (m, 4H), 3.17-3.06 (m, 4H), 1.74 ppm (s, 3H). ^{13}C NMR (126 MHz, CDCl_3) C-F-coupling observed; δ 171.0, 163.1, 161.1, 159.1, 152.3, 151.0, 134.3, 133.0, 132.2, 129.1, 128.9, 128.8, 128.8, 128.5, 125.8, 115.9, 115.6, 115.4, 105.3, 66.9, 65.9, 55.9, 49.0, 45.5, 43.4, 21.8 ppm. HR-MS: calc. for $[\text{M}+\text{H}]^+$ $\text{C}_{32}\text{H}_{33}\text{FN}_5\text{O}_3$ 554.25619 found 554.25544.



13.3.1.34 *N*-(3-Fluorobenzyl)-6-methyl-5-(4-morpholinobenzyl)-4-oxo-2-phenyl-4,5,6,7-tetrahydropyrazolo[1,5-a]pyrazine-6-carboxamide (**5p**)

Prepared according to general procedure 3B using Burgess reagent (70 mg, 293 μmol , 2.0 equiv.), *N*-(3-fluorobenzyl)formamide **13d** (30 mg, 196 μmol , 1.0 equiv.), 1-(2-oxopropyl)-3-phenyl-1*H*-pyrazole-5-carboxylic acid **4a** (48 mg, 196 μmol , 1.0 equiv.) and 4-(morpholinophenyl)methanamine **9a** (34 mg, 176 μmol , 1.0 equiv.) in MeOH (1.2 mL) and ACN (5.5 mL). The product was purified by means of recrystallization from MeOH and obtained as brown solid (20 mg, 35 μmol , 20%). $R_f = 0.50$ (cyclohexane / EtOAc = 1:4). ^1H NMR (700 MHz, CDCl_3) δ 7.77 (dd, $J = 7.6, 1.3$ Hz, 2H), 7.39 (t, $J = 7.6$ Hz, 2H), 7.35 – 7.32 (m, 1H), 7.30 (d, $J = 8.5$ Hz, 2H), 7.08 (s, 1H), 7.02 (td, $J = 7.9, 5.8$ Hz, 1H), 6.81 – 6.77 (m, 3H), 6.53 – 6.51 (m, 1H), 6.48 (dt, $J = 9.5, 2.0$ Hz, 1H), 6.39 (t, $J = 6.1$ Hz, 1H), 5.08 (d, $J = 12.8$ Hz, 1H), 4.94 (d, $J =$

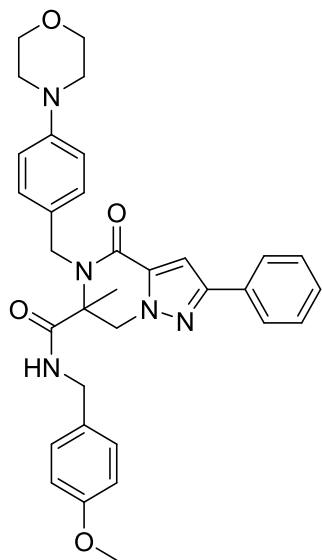
15.4 Hz, 1H), 4.79 (d, $J = 15.4$ Hz, 1H), 4.27 (dd, $J = 15.2, 6.1$ Hz, 1H), 4.17 (d, $J = 12.8$ Hz, 1H), 3.95 (dd, $J = 15.2, 6.1$ Hz, 1H), 3.84 (m, 4H), 3.13 – 3.08 (m, 4H), 1.75 ppm (s, 3H). ^{13}C NMR (176 MHz, CDCl_3) C-F-coupling observed; δ 171.1, 163.5, 162.1, 159.1, 152.4, 151.0, 139.9, 139.8, 134.3, 132.3, 130.2, 130.1, 129.1, 128.8, 128.8, 128.4, 125.9, 122.6, 122.6, 115.9, 114.5, 114.4, 114.1, 114.0, 105.3, 66.9, 65.9, 55.9, 49.0, 45.5, 43.5, 43.5, 21.9 ppm. HR-MS: calc. for $[\text{M}+\text{H}]^+$ $\text{C}_{32}\text{H}_{33}\text{FN}_5\text{O}_3$ 554.25619 found 554.25561.



13.3.1.35 *N*-(4-fluorophenyl)-6-methyl-5-(4-morpholinobenzyl)-4-oxo-2-phenyl-4,5,6,7-tetrahydropyrazolo[1,5-a]pyrazine-6-carboxamide (**5q**)

Prepared according to general procedure 2 using 1-(2-oxopropyl)-3-phenyl-1*H*-pyrazole-5-carboxylic acid **4a** (50.0 mg, 0.20 mmol, 1.0 equiv.), (4-morpholino-phenyl)methanamine **9a** (35.4 μL , 0.20 mmol, 1.0 equiv.) and *N*-(4-fluorophenyl)formamide **8m** (25 mg, 0.20 mmol, 1.0 equiv.). The product was obtained as light brown solid (33.7 mg, 0.06 mmol, 31%). $R_f = 0.18$ (cyclohexane / EtOAc = 1:9). ^1H NMR (500 MHz, CDCl_3) δ 7.77 (d, $J = 7.5$ Hz, 2H), 7.51 (d, $J = 8.5$ Hz, 2H), 7.38 (t, $J = 7.5$ Hz, 3H), 7.31 (t, $J = 7.5$ Hz, 1H), 7.14 (s, 1H), 6.91 (d, $J = 8.5$ Hz, 2H), 6.88 – 6.75 (m, 4H), 5.22 (d, $J = 15.1$ Hz, 1H), 5.17 (d, $J = 12.9$ Hz, 1H), 4.64 (d, $J = 15.1$ Hz, 1H), 4.22 (d, $J = 12.9$ Hz, 1H), 3.86 (t, $J = 4.8$ Hz, 4H), 3.14 (t, $J = 4.8$ Hz, 4H), 1.86 ppm (s, 3H). ^{13}C

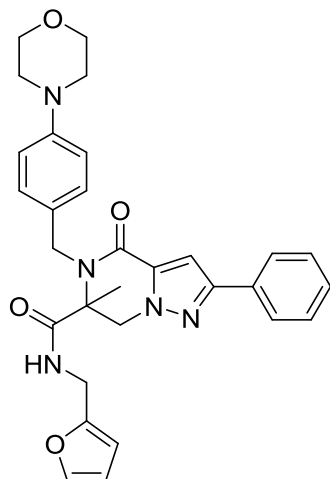
NMR (126 MHz, CDCl₃) δ 169.2, 159.1, 152.4, 151.4, 134.2, 132.2, 130.3, 128.8, 128.5, 128.5, 125.8, 122.4, 122.3, 116.3, 115.5, 115.3, 105.4, 66.9, 66.3, 55.7, 49.0, 45.6, 22.0 ppm. HR-MS: calc. for [M+H]⁺ C₃₁H₃₁FN₅O₃ 540.2405 found 540.2413.



13.3.1.36 *N*-(4-Methoxybenzyl)-6-methyl-5-(4-morpholinobenzyl)-4-oxo-2-phenyl-4,5,6,7-tetrahydropyrazolo[1,5-a]pyrazine-6-carboxamide (**5r**)

Prepared according to general procedure 3A using *N*-(4-methoxybenzyl)formamide **13f** (10.0 mg, 0.07 mmol, 1.0 equiv.), 1-(2-oxopropyl)-3-phenyl-1*H*-pyrazole-5-carboxylic acid **4a** (16.6 mg, 0.07 mmol, 1.0 equiv.) and (4-morpholinophenyl)methanamine **9a** (11.8 mg, 0.06 mmol, 0.9 equiv.). The product was obtained as light yellow solid (13.2 mg, 0.02 mmol, 34%). *R*_f = 0.39 (cyclohexane / EtOAc = 1:9). ¹H NMR (400 MHz, CDCl₃) δ 7.83 – 7.79 (m, 2H), 7.45 – 7.38 (m, 2H), 7.37 – 7.32 (m, 1H), 7.32 – 7.27 (m, 2H), 6.84 – 6.78 (m, 2H), 6.70 – 6.65 (m, 2H), 6.62 – 6.57 (m, 2H), 6.10 – 6.00 (m, 1H), 5.06 (d, *J* = 12.9 Hz, 1H), 4.98 (d, *J* = 15.3 Hz, 1H), 4.71 (d, *J* = 15.3 Hz, 1H), 4.31 (dd, *J* = 14.8 Hz, 1H), 4.18 (d, *J* = 12.9 Hz, 1H), 3.87 – 3.84 (m, 4H), 3.83 – 3.82 (m, 1H), 3.59 (s, 3H), 3.17 – 3.08 (m, 4H), 1.74 ppm (s, 3H). ¹³C NMR (126 MHz, CDCl₃) δ 170.7, 159.0, 158.8, 152.1, 150.9, 134.2, 132.3, 129.1, 129.0, 128.8, 128.3, 128.3, 125.7, 115.9,

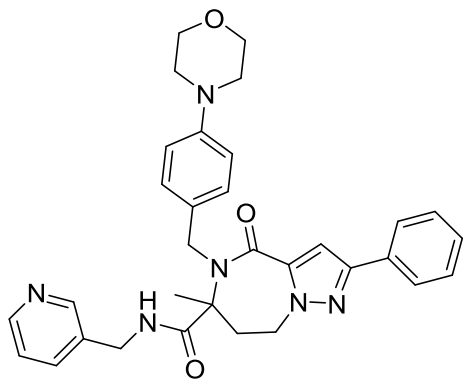
113.9, 105.2, 66.8, 65.8, 55.8, 55.1, 49.0, 45.3, 43.4, 26.9, 21.7 ppm. HR-MS: calc. for $[M+H]^+$ $C_{33}H_{36}N_5O_4$ 566.2762 found 566.2759, calc. for $[M+Na]^+$ $C_{33}H_{35}N_5O_4Na$ 588.2581 found 588.2579.



13.3.1.37 *N*-(Furan-2-ylmethyl)-6-methyl-5-(4-morpholinobenzyl)-4-oxo-2-phenyl-4,5,6,7-tetrahydropyrazolo[1,5-a]pyrazine-6-carboxamide (**5s**)

Prepared according to general procedure 3B using Burgess reagent (43 mg, 180 μ mol, 1.5 equiv.), *N*-(furan-2-ylmethyl)formamide **13g** (15 mg, 120 μ mol, 1.0 equiv.), 1-(2-oxopropyl)-3-phenyl-1*H*-pyrazole-5-carboxylic acid **4a** (29 mg, 121 μ mol, 1.0 equiv.) and 4-(morpholinophenyl)methanamine **9a** (21 mg, 109 μ mol, 0.9 equiv.) in MeOH (0.6 mL) and ACN (2.75 mL). After work-up of the crude reaction mixture, the product was purified using preparative HPLC-MS followed by silica gel column chromatography (elute: DCM / EtOH / sat. NH_4OH) as white solid (10 mg, 19 μ mol, 17%). R_f = 0.51 (cyclohexane / EtOAc = 1:4). 1H NMR (500 MHz, CD_2Cl_2) δ 7.82 – 7.78 (m, 2H), 7.41 (t, J = 7.6 Hz, 2H), 7.36 – 7.32 (m, 1H), 7.30 (d, J = 8.5 Hz, 2H), 7.21 (d, J = 1.9 Hz, 1H), 7.11 (s, 1H), 6.92 – 6.88 (m, 2H), 6.17 (dd, J = 3.3, 1.9 Hz, 2H), 5.87 (d, J = 3.3 Hz, 1H), 5.02 (d, J = 15.5 Hz, 1H), 4.98 (d, J = 13.0 Hz, 1H), 4.65 (d, J = 15.5 Hz, 1H), 4.23 – 4.16 (m, 2H), 4.11 (dd, J = 15.6, 5.6 Hz, 1H), 3.85 – 3.81 (m, 4H), 3.16 – 3.12 (m, 4H), 1.68 ppm (s, 3H). ^{13}C NMR (126 MHz, CD_2Cl_2) δ 171.1, 159.2, 152.2, 150.9, 150.5, 142.5, 134.8,

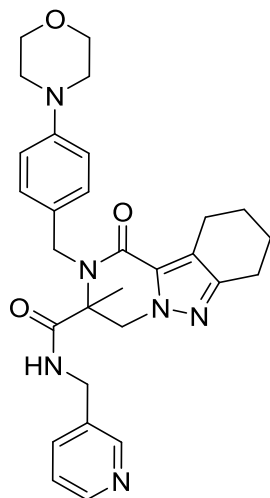
132.7, 130.1, 129.9, 129.1, 128.6, 125.9, 116.6, 110.6, 107.3, 105.1, 66.9, 66.0, 55.9, 49.8, 45.7, 37.4, 21.9 ppm. HR-MS: calc. for $[M+H]^+$ $C_{30}H_{32}N_5O_4$ 526.24488 found 526.24402.



13.3.1.38 **6-Methyl-5-(4-morpholinobenzyl)-4-oxo-2-phenyl-N-(pyridin-3-ylmethyl)-5,6,7,8-tetrahydro-4H-pyrazolo[1,5-a][1,4]diazepine-6-carboxamide (6)**

Prepared according to general procedure 2 using 1-(3-oxobutyl)-3-phenyl-1H-pyrazole-5-carboxylic acid **4b** (50 mg, 190 μ mol, 1.0 equiv.), 4-(morpholinophenyl)methanamine **9a** (34 mg, 170 μ mol, 0.9 equiv.) and 3-(isocyanomethyl)pyridine **8j** (23 mg, 190 μ mol, 1.0 equiv.). The product was purified by means of silica gel column chromatography (elute: DCM / EtOH / sat. NH_4OH) and obtained as off-white solid (7 mg, 13 μ mol, 7%). R_f = 0.39 (DCM / EtOH / sat. NH_4OH = 175:4:0.5). 1H NMR (700 MHz, $CDCl_3$) δ 8.39 (dd, J = 4.8, 2.0 Hz, 1H), 8.29 (d, J = 2.0 Hz, 1H), 7.77 – 7.74 (m, 2H), 7.44 – 7.39 (m, 2H), 7.34 – 7.29 (m, 3H), 7.23 (dt, J = 7.8, 2.0 Hz, 1H), 6.97 (ddd, J = 7.8, 4.8, 0.9 Hz, 1H), 6.87 (s, 1H), 6.83 – 6.80 (m, 2H), 6.07 (t, J = 6.0 Hz, 1H), 4.92 (d, J = 128.0 Hz, 2H), 4.60 (ddd, J = 14.2, 7.2, 4.5 Hz, 1H), 4.26 (ddd, J = 14.2, 9.2, 6.2 Hz, 1H), 4.10 (dd, J = 14.8, 5.9 Hz, 1H), 4.00 (dd, J = 14.8, 5.9 Hz, 1H), 3.86 (t, J = 4.8 Hz, 4H), 3.21 (ddd, J = 14.4, 9.2, 7.3 Hz, 1H), 3.16 – 3.09 (m, 4H), 2.07 (ddd, J = 14.4, 6.2, 4.6 Hz, 1H), 1.69 ppm (s, 3H). ^{13}C NMR (176 MHz, $CDCl_3$) δ 172.5, 163.0, 151.1, 156.0, 149.3, 149.2, 138.2, 135.9, 133.1, 132.6,

129.8, 128.9, 128.8, 128.2, 125.8, 123.7, 115.9, 107.9, 67.0, 65.8, 49.1, 47.3, 47.1, 41.7, 38.7, 27.4 ppm. HR-MS: calc. for $[M+H]^+$ $C_{32}H_{35}N_6O_3$ 551.27652 found 551.27590.

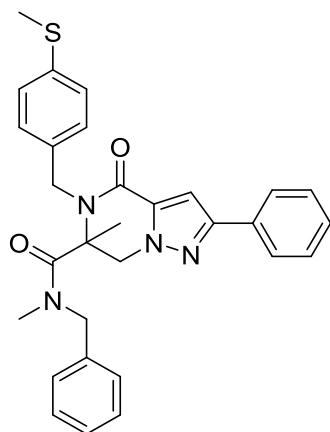


13.3.1.39 *3-Methyl-2-(4-morpholinobenzyl)-1-oxo-N-(pyridin-3-ylmethyl)-1,2,3,4,7,8,9,10-octahydropyrazino[1,2-b]indazole-3-carboxamide (7)*

Prepared according to general procedure 2 using 2-(2-oxopropyl)-4,5,6,7-tetrahydro-2*H*-indazol-3-carboxylic acid **4c** (11.6 mg, 0.05 mmol, 1.0 equiv.), 4-morpholino-benzylamine **9a** (18.1 mg, 0.9 mmol, 1.8 equiv.) and 3-isocyanomethylpyridine **8j** (5.71 μ L, 0.05 mmol, 1.0 equiv.). The product was purified by means of silica gel column chromatography (elute: DCM / MeOH) and obtained as white solid (9.9 mg, 0.02 mmol, 37%). R_f = 0.27 (DCM / MeOH = 95:5). 1H NMR (500 MHz, $CDCl_3$) δ 8.46 (d, J = 4.6 Hz, 1H), 8.16 (s, 1H), 7.28 (d, J = 8.7 Hz, 2H), 7.09 (d, J = 7.8 Hz, 1H), 7.03 (d, J = 7.8 Hz, 1H), 6.79 (d, J = 8.7 Hz, 2H), 6.25 (t, J = 5.5 Hz, 1H), 4.93 – 4.88 (m, 2H), 4.71 (d, J = 15.3 Hz, 1H), 4.30 (dd, J = 15.3, 6.9 Hz, 1H), 4.04 (d, J = 12.7 Hz, 1H), 3.97 (dd, J = 15.3 Hz, 5.5 Hz, 1H), 3.85 (t, J = 4.8 Hz, 4H), 3.10 (t, J = 4.8 Hz, 4H), 2.91 – 2.80 (m, 1H), 2.72 – 2.65 (m, 2H), 2.65 – 2.59 (m, 1H), 1.85 – 1.78 (m, 2H), 1.78 – 1.71 (m, 2H), 1.69 ppm (s, 3H). ^{13}C NMR (126 MHz, $CDCl_3$) δ 171.7, 160.0, 150.9, 150.3, 149.0, 148.8, 134.8, 133.2, 129.0,

128.2, 123.5, 121.0, 115.9, 66.9, 65.9, 55.7, 49.0, 45.0, 41.4, 23.4, 23.0, 22.9, 21.7, 21.3 ppm.

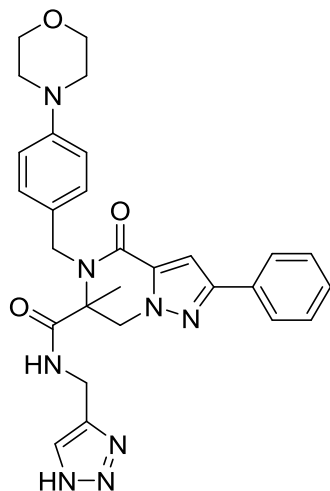
HR-MS: calc. for $[M+H]^+$ $C_{29}H_{35}N_6O_3$ 515.27652 found 515.27724.



13.3.1.40 *N*-Benzyl-*N*,6-dimethyl-5-(4-(methylthio)benzyl)-4-oxo-2-phenyl-4,5,6,7-tetrahydropyrazolo[1,5-*a*]pyrazine-6-carboxamide (**13**)

N-Benzyl-6-methyl-5-(4-(methylthio)benzyl)-4-oxo-2-phenyl-4,5,6,7-tetrahydropyrazolo[1,5-*a*]pyrazine-6-carboxamide **5a** (11 mg, 22 μ mol, 1.0 equiv.) was dissolved in DMF (0.5 mL) and cooled to 0 °C. Sodium hydride (1.8 mg, 44 μ mol, 2.0 equiv.) was thereto added and the solution was stirred at 0 °C for 10 min. Subsequently, methyl iodide (1.7 μ L, 27 μ mol, 1.2 equiv.) was added and the solution was allowed to warm up to room temperature overnight. The excess of sodium hydride was quenched by addition of 1 mL water at 0 °C. The product was extracted thrice with EtOAc and the combined organic layers were concentrated under reduced pressure. The product was purified by means of silica gel column chromatography (elute: cyclohexane / EtOAc) and obtained as white solid (4 mg, 8 μ mol, 35%). R_f = 0.67 (cyclohexane / EtOAc = 1:1). 1H NMR (600 MHz, $CDCl_3$) δ 7.81 – 7.77 (m, 2H), 7.42 (d, J = 7.2 Hz, 2H), 7.36 – 7.33 (m, 1H), 7.31 – 7.27 (m, 5H), 7.23 (s, 1H), 7.21 – 7.18 (m, 2H), 7.10 (d, J = 7.2 Hz, 2H), 4.77 – 4.67 (m, 2H), 4.61 (d, J = 15.4 Hz, 2H), 4.36 (d, J = 13.5 Hz, 2H), 2.79 (s, 3H), 2.48 (s, 3H), 1.65 ppm (s, 3H). ^{13}C NMR (151 MHz, $CDCl_3$) δ 168.2, 158.6, 152.7, 138.3, 135.9, 134.7, 134.3, 132.3, 129.5, 129.0, 129.0,

128.6, 128.0, 127.8, 126.6, 125.8, 105.6, 66.5, 53.8, 53.7, 47.3, 36.6, 23.8, 16.0 ppm. HR-MS: calc. for $[M+H]^+$ $C_{30}H_{31}N_4O_2S$ 511.21622 found 511.21567.

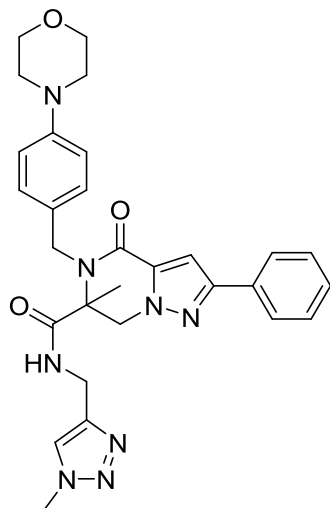


13.3.1.41 *N-((1H-1,2,3-triazol-4-yl)methyl)-6-methyl-5-(4-morpholinobenzyl)-4-oxo-2-phenyl-4,5,6,7-tetrahydropyrazolo[1,5-a]pyrazine-6-carboxamide (14)*

To a suspension of 6-methyl-5-(4-morpholinobenzyl)-4-oxo-2-phenyl-*N*-(prop-2-yn-1-yl)-4,5,6,7-tetrahydropyrazolo[1,5-a]pyrazine-6-carboxamide **5m** (30 mg, 62 μ mol, 1.0 equiv.), copper(I)iodide (1.3 mg 6.9 μ mol, 0.1 equiv.), and sodium ascorbate (4.9 mg 25 μ mol, 0.4 equiv.) in a DMF-water mixture (4:1, 1.0 mL) was added trimethylsilylazide (9 mg, 76 μ mol, 1.2 equiv.). The resulting mixture was stirred at heating on 100 °C overnight. The mixture was allowed to cool down to room temperature and was subsequently extracted between saturated NH_4Cl and DCM. The combined organic layers were dried over Na_2SO_4 , filtered and concentrated under reduced pressure. The product was purified by means of silica gel column chromatography (elute: DCM / EtOH / sat. NH_4OH) and obtained as white crystalline solid (18 mg, 34 μ mol, 55%). R_f = 0.27 (Pentane / DCM / EtOH / sat. NH_4OH = 60:50:8:1). 1H NMR (700 MHz, $CDCl_3$) δ 12.79 (bs, 1H), 7.74 (dd, J = 7.5, 1.3 Hz, 2H), 7.37 (t, J = 7.5 Hz, 2H), 7.32 – 7.29 (m, 1H), 7.27 (s, 1H), 7.24 (d, J = 8.6 Hz, 2H), 7.08 (s, 1H), 6.87 (s, 1H), 6.82-6.78 (m, 2H), 5.13 (d, J = 15.7 Hz, 1H), 5.05 (d, J

= 12.9 Hz, 1H), 4.57 (d, J = 15.7 Hz, 1H), 4.33 – 4.26 (m, 2H), 4.17 (d, J = 12.9 Hz, 1H), 3.85 – 3.81 (m, 4H), 3.12 – 3.08 (m, 4H), 1.68 ppm (s, 3H). ^{13}C NMR (176 MHz, CDCl_3) δ 171.4, 159.3, 152.4, 150.9, 144.8*, 134.4, 132.2, 128.9, 128.9, 128.8, 128.5, 125.9, 116.0, 105.4, 66.9, 65.8, 55.7, 49.1, 45.7, 35.4**, 21.9 ppm. HR-MS: calc. for $[\text{M}+\text{H}]^+$ $\text{C}_{28}\text{H}_{31}\text{N}_8\text{O}_3$ 527.25136 found 527.25070.

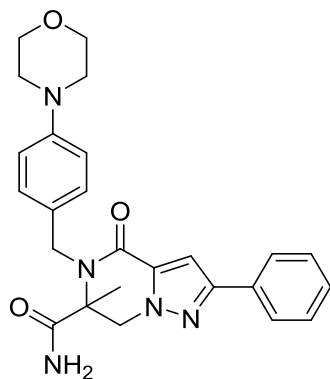
only observed in HMBC* or HSQC**



13.3.1.42 **6-Methyl-N-((1-methyl-1H-1,2,3-triazol-4-yl)methyl)-5-(4-morpholinobenzyl)-4-oxo-2-phenyl-4,5,6,7-tetrahydropyrazolo[1,5-a]pyrazine-6-carboxamide (15)**

Copper(I)iodide (2.4 mg, 12.4 μmol , 0.2 equiv.) and sodium azide (8.8 mg, 136 μmol , 2.4 equiv.) were dissolved in H_2O / EtOH (400 μL , 1:1). To the reaction mixture methyl iodide (4.3 μL , 68 μmol , 1.2 equiv.) and sodium ascorbate (11 mg, 60 μmol , 0.9 equiv.) were added and the resulting mixture and stirred for 1 h at room temperature. Subsequently, 6-methyl-5-(4-morpholinobenzyl)-4-oxo-2-phenyl-N-(prop-2-yn-1-yl)-4,5,6,7-tetrahydropyrazolo[1,5-a]pyrazine-6-carboxamide **5m** (27 mg, 56 μmol , 1.0 equiv.) was added and the mixture was stirred at 50 $^\circ\text{C}$ for 2 days. The product was purified by means of silica gel column chromatography (DCM / EtOH / sat. NH_4OH)

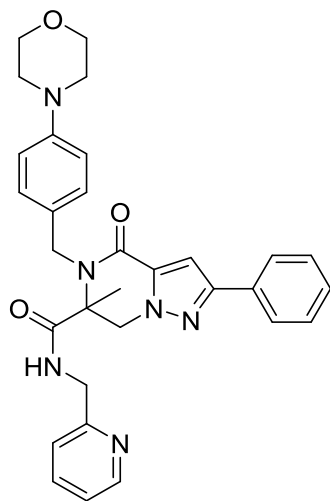
followed by MS-assisted preparative HPLC. After basic extraction between saturated NaHCO_3 and DCM the product was obtained as white solid (12 mg, 22 μmol , 40%). $R_f = 0.11$ (DCM / EtOH / sat. $\text{NH}_4\text{OH} = 175:4:0.5$). ^1H NMR (700 MHz, CDCl_3) δ 7.79 (dd, $J = 8.2, 1.3$ Hz, 2H), 7.44 – 7.39 (m, 2H), 7.37 – 7.31 (m, 1H), 7.29 (d, $J = 8.7$ Hz, 2H), 7.08 (s, 1H), 6.89 – 6.84 (m, 2H), 6.78 (s, 1H), 6.64 (t, $J = 6.2$ Hz, 1H), 5.12 (d, $J = 15.5$ Hz, 1H), 5.02 (d, $J = 12.8$ Hz, 1H), 4.63 (d, $J = 15.5$ Hz, 1H), 4.43 (dd, $J = 15.3, 6.6$ Hz, 1H), 4.17 (d, $J = 12.8$ Hz, 1H), 4.05 (dd, $J = 15.3, 5.4$ Hz, 1H), 3.87 – 3.83 (m, 4H), 3.58 (s, 3H), 3.16 – 3.11 (m, 4H), 1.71 ppm (s, 3H). ^{13}C NMR (176 MHz, CDCl_3) δ 171.4, 159.0, 151.9, 151.0, 144.6, 134.6, 132.2, 129.0, 129.0, 128.9, 128.6, 125.7, 122.6, 116.1, 105.0, 67.0, 65.9, 56.1, 49.2, 45.5, 36.3, 36.0, 21.6 ppm. HR-MS: calc. for $[\text{M}+\text{H}]^+$ $\text{C}_{29}\text{H}_{33}\text{N}_8\text{O}_3$ 541.26701 found 541.26642.



13.3.1.43 *6-Methyl-5-(4-morpholinobenzyl)-4-oxo-2-phenyl-4,5,6,7-tetrahydropyrazolo[1,5-a]pyrazine-6-carboxamide (16)*

N-(*tert*-butyl)-6-methyl-5-(4-morpholinobenzyl)-4-oxo-2-phenyl-4,5,6,7-tetrahydropyrazolo[1,5-a]pyrazine-6-carboxamide **5I** (52 mg, 104 μmol , 1.0 equiv.) was dissolved in *p*-xylene (0.5 mL) and methanesulfonic acid (1.0 mL, 15.4 mmol, 148 equiv.) was slowly added. The biphasic mixture was stirred vigorously for 5 min at room temperature and an additional hour at 40 °C. The reaction mixture was allowed to cool down to room temperature and carefully transferred to a

container with 25 mL saturated NaHCO₃.²¹⁵ The resulting mixture was extracted thrice with EtOAc and the combined organic layers were dried over Na₂SO₄, filtered and concentrated under reduced pressure. The product was obtained as white solid (46 mg, 100 μmol, 99%). R_f = 0.60 (EtOAc / MeOH / TEA = 90:10:1). ¹H NMR (700 MHz, CDCl₃) δ 7.77 (dd, *J* = 7.6, 1.4 Hz, 2H), 7.38 (t, *J* = 7.6 Hz, 2H), 7.34 – 7.30 (m, 1H), 7.29 (d, *J* = 8.5 Hz, 2H), 7.14 (s, 1H), 6.87 – 6.84 (m, 2H), 5.93 (s, 1H), 5.63 (s, 1H), 5.16 (d, *J* = 15.5 Hz, 1H), 4.99 (d, *J* = 13.0 Hz, 1H), 4.57 (d, *J* = 15.5 Hz, 1H), 4.15 (d, *J* = 13.0 Hz, 1H), 3.88 – 3.83 (m, 4H), 3.16 – 3.11 (m, 4H), 1.68 ppm (s, 3H). ¹³C NMR (176 MHz, CDCl₃) δ 173.6, 159.1, 152.4, 150.9, 134.4, 132.3, 129.0, 128.9, 128.9, 128.4, 125.8, 116.0, 105.4, 66.9, 65.5, 55.6, 49.2, 45.5, 22.0 ppm. HR-MS: calc. for [M+H]⁺ C₂₅H₂₈N₅O₃ 446.31867 found 446.21830.



13.3.1.44 *6-Methyl-5-(4-morpholinobenzyl)-4-oxo-2-phenyl-N-(pyridin-2-ylmethyl)-4,5,6,7-tetrahydropyrazolo[1,5-a]pyrazine-6-carboxamide (17)*

6-Methyl-5-(4-morpholinobenzyl)-4-oxo-2-phenyl-4,5,6,7-tetrahydropyrazolo[1,5-a]pyrazine-6-carboxamide **16** (30 mg, 67 μmol, 1.0 equiv.) was dissolved in DMF (0.50 mL) and cooled to 0 °C. Solid sodiumhydride (60% dispersion in mineral oil, 3 mg, 75 μmol, 1.1 equiv.) was added and the resulting suspension was stirred at 0 °C for half an hour. 2-Picolyl chloride (basic workup of the

commercially obtained HCl salt with saturated NaHCO₃ yielded the free chloride derivative) (7.2 μL, 75 μmol, 1.1 equiv.) was added to via a syringe and the vial was allowed to warm up to room temperature overnight. Afterwards, the mixture was cooled to 0 °C and water (1 mL) was added. The mixture was extracted thrice with EtOAc, the combined organic layers were washed with brine, dried over Na₂SO₄, filtered and concentrated under reduced pressure. The product was purified by means of silica gel column chromatography (elute: EtOAc/ MeOH / TEA) and obtained as white solid (7 mg, 13 μmol, 19%). R_f = 0.53 (EtOAc / MeOH / TEA = 90:10:1). ¹H NMR (700 MHz, CDCl₃) δ 8.43 (d, *J* = 4.9 Hz, 1H), 7.81 – 7.76 (m, 2H), 7.45 (td, *J* = 7.7, 1.8 Hz, 1H), 7.40 (t, *J* = 7.7 Hz, 2H), 7.35 – 7.30 (m, 1H), 7.28 (d, *J* = 8.7 Hz, 2H), 7.22 (t, *J* = 4.9 Hz, 1H), 7.15 (s, 1H), 7.10 – 7.06 (m, 1H), 6.83 (t, *J* = 8.1 Hz, 3H), 5.38 (d, *J* = 15.6 Hz, 1H), 5.04 (d, *J* = 13.0 Hz, 1H), 4.53 (d, *J* = 15.6 Hz, 1H), 4.45 (dd, *J* = 16.6, 4.9 Hz, 1H), 4.28 (dd, *J* = 16.6, 4.9 Hz, 1H), 4.20 (d, *J* = 13.0 Hz, 1H), 3.86 – 3.82 (m, 4H), 3.13 – 3.07 (m, 4H), 1.71 ppm (s, 3H). ¹³C NMR (176 MHz, CDCl₃) δ 171.0, 159.1, 155.3, 152.2, 150.8, 149.1, 136.8, 134.5, 132.5, 129.4, 128.9, 128.7, 128.4, 125.8, 122.5, 121.4, 116.0, 105.3, 67.0, 65.8, 55.8, 49.3, 45.7, 44.8, 22.2 ppm. HR-MS: calc. for [M+H]⁺ C₃₁H₃₃N₆O₃ 537.26087 found 537.26033.

14 Curriculum vitae

PERSONAL INFORMATION

Elena Sabrina Reckzeh (née Heider)

Date of birth: 27th of June, 1990

Place of birth: Hilden, Germany

Citizenship: German

EDUCATION

Max Planck Institute of Molecular Physiology Dortmund, Germany

PhD student, Chemical Biology 03/2015 – 06/2019

Thesis: *Synthesis and biological evaluation of small molecule GLUT-inhibitors that cause glucose starvation in cancer*

Supervisor: Prof. Herbert Waldmann

TU Dortmund University Dortmund, Germany

MSc, Chemical Biology 10/2012 – 12/2014

Thesis: *Computer-based design, synthesis and biological evaluation of new inhibitors of the TGF β -signaling pathway.*

Supervisors: Prof. Dennis Schade, Prof. Daniel Rauh

Advanced Training: *Ligand-based pharmacophore model, scaffold hopping and QSAR-analysis of TGF β II-inhibitory 1,4-dihydropyridines.*

Supervisors: Dr. Oliver Koch, Prof. Dennis Schade, Prof. Daniel Rauh

University of Bonn, LIMES institute Bonn, Germany

BSc, Molecular Biomedicine 10/2009 – 06/2012

Thesis: *Characterization of ERK2-binding aptamers C5, C3 and TRA.*

Supervisor: Prof. Günter Mayer

Advanced Training: *Isolation of MDSCs from tumor-bearing mice by means of MACS and characterization of their immunomodulatory properties against antigen-specific T cells.*

Supervisor: Prof. Thomas Tüting, clinical center, dermatology, Bonn

The Bromfield School	Harvard, MA, USA
Exchange student	08/2006 – 07/2007

RELATED WORK EXPERIENCE

Adtracon GmbH	Hilden, Germany
Internship in R&D, personal assistance	02/2015 – 03/2015
<i>Synthesis and analytic of reactive hotmelt adhesives</i>	08/2011 – 09/2011
	09/2010 – 10/2010

Bayer Pharma AG	Berlin, Germany
Internship in R&D Common Mechanism Research for Inflammation	05/2012 – 07/2012
<i>Characterization of immune-modulatory properties of development substances on proliferation and activation of T cells.</i>	

Phenion (Henkel AG)	Düsseldorf, Germany
Internship in R&D skin model technologies	09/2007 – 10/2007

RELATED PROFESSIONAL EXPERIENCE

International Chemical Biology Society Students' Chapter Dortmund	Dortmund, Germany
Founder and President	09/2018 – present

International Max Planck Research School Students' Symposium	Dortmund, Germany
Symposium organizing committee	11/2018

International Max Planck Research School in Chemical and Molecular Biology	Dortmund, Germany
PhD student representative	05/2017 – 04/2019

Poppelsdorfer Schlossgespräche	Bonn, Germany
Students organized lecture series with internationally renowned scientists	05/2011 – 04/2012
Finances	

CERTIFICATES

High-school graduate prize of the *Gesellschaft Deutscher Chemiker* (GDCh)
Certificate in Advanced English C1
Diplôme d'Études en Langue Française A2

CONFERENCES / CONTRIBUTIONS / PRIZES

ICBS2018 – Annual Conference of the International Chemical Biology Society Vancouver, BC, Canada

September 24-27, 2018

- Organizing committee of the pre-conference trainee day
- Poster presentation
- Travel grant awardee

DECHEMA – Advances in Chemical Biology

Frankfurt a.M., Germany

- Poster presentation
- Poster prize awardee

January 30-31, 2018

ICBS2017 – Annual Conference of the International Chemical Biology Society

Shanghai, China

October 17-20, 2017

- Poster presentation
- Podium flash presentation
- Poster prize awardee
- Travel grant awardee

CEWIS – Cologne Excellent Women in Science International Symposium

Cologne, Germany

October 5-6, 2017

- Poster presentation

Keystone Symposia Conference on Tumor Metabolism

Whistler, BC, Canada

- Poster presentation

March 5-10, 2017

International Max Planck Research School (IMPRS-CMB) Students' Symposium

Dortmund, Germany

- Poster presentation
- Poster presentation

November 12-14, 2018

October 24-26, 2017

INVITED TALKS

Drug Discovery India 2019, Rathnam Chaguturu, Mumbai, India, January 17-18, 2019 (declined).

Academia meets Boehringer Ingelheim High Throughput Biology, talk title: "Cutting the energy supply of cancer cells by means of novel glucose uptake inhibitors", Boehringer Ingelheim, Biberach an der Riss, Germany, January 14-15, 2019 (accepted).

ICBS2018 – Annual Conference of the International Chemical Biology Society, talk title: "Thermal Proteome Profiling for Target Identification", Vancouver, Canada, September 24-27, 2018.

15 Publication list

Reckzeh ES, Karageorgis G, Schwalfenberg M, Ceballos J, Nowacki J, Stroet MCM, Binici A, Knauer A, Brand S, Strohmann C, Ziegler S, Waldmann H. "Inhibition of Glucose Transporters and Glutaminase Synergistically Impairs Tumor Cell Growth." *Cell Chemical Biology*, *in print*.

Laengle D, Werner TR, Wesseler F, Reckzeh ES, Schaumann N, Drowley L, Polla M, Plowright AT, Hirt MN, Eschenhagen T, Schade D. "Towards second generation cardiomyogenic and anti-cardiofibrotic 1,4-dihydropyridine-class of TGF β inhibitors." *ChemMedChem*, **2019**, *14*(8), 810-822.

Reckzeh ES, Brockmeyer A, Metz M, Waldmann H, Janning P, "Target Engagement of Small Molecules: Thermal Profiling Approaches on Different Levels", *Methods in Molecular Biology, Systems Chemical Biology*, Ed. Ziegler S, Ed. Waldmann H, New York: Humana Press, **2019**, *Vol. 1888*, 73-98.

Karageorgis G, Reckzeh ES, Ceballos J, Schwalfenberg M, Sievers S, Ostermann C, Pahl A, Ziegler S, Waldmann H. Chromopyrones are "Pseudo Natural Product" Glucose Uptake Inhibitors Targeting Glucose Transporters GLUT-1 and -3" *Nature Chemistry*, **2018**, *10*, 1103-11.

Längle D, Marquardt V, Heider E, Vigante B, Duburs G, Luntena I, Flötgen D, Golz C, Strohmann C, Koch O, Schade D. "Design, synthesis and 3D-QSAR studies of novel 1,4-dihydropyridines as TGF β /Smad inhibitors", *European Journal of Medicinal Chemistry*, **2015**, *95*, 249-66.

Lennarz S, Heider E, Blind M, Mayer G. "An Aptamer to the MAP Kinase Insert Region" *ACS Chemical Biology*, **2015**, *10*(1), 320-7.